OKINAWA INSTITUTE OF SCIENCE AND TECHNOLOGY GRADUATE UNIVERSITY
沖縄科学技術大学院大学

Astrocyte calcium activity mapping in behaving mice using anterograde axo-astrocytic AAV transfer

Author	Leonidas Georgiou
Degree Conferral Date	2020-03-31
Degree	Doctor of Philosophy
Degree Referral Number	38005甲第48号
Copyright Information	(C) 2020 The Author.
URL	http://doi.org/10.15102/1394.00001528

Creative Commons Attribution 4.0 International(https://creativecommons.org/licenses/by/4.0/)

Okinawa Institute of Science and Technology
Graduate University

Thesis submitted for the degree

Doctor of Philosophy

Astrocyte calcium activity mapping in behaving mice using anterograde axo-astrocytic AAV transfer

---

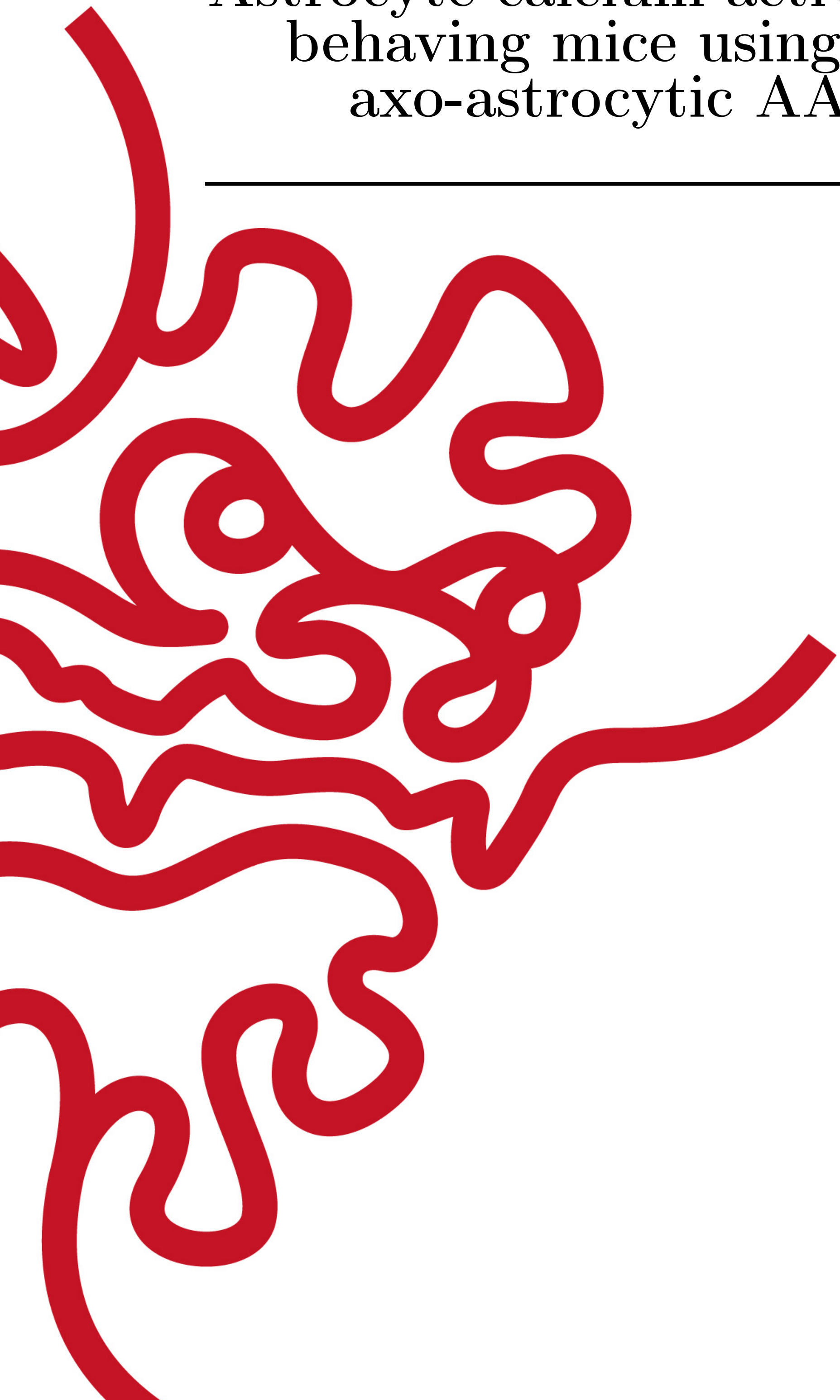

by

Leonidas Georgiou

Supervisor: **Bernd Kuhn**

March, 2020

Declaration of Original and Sole Authorship

I, Leonidas Georgiou, declare that this thesis entitled *Astrocyte calcium activity mapping in behaving mice using anterograde axo-astrocytic AAV transfer* and the data presented in it are original and my own work.

I confirm that:

- No part of this work has previously been submitted for a degree at this or any other university.
- References to the work of others have been clearly acknowledged. Quotations from the work of others have been clearly indicated, and attributed to them.
- In cases where others have contributed to part of this work, such contribution has been clearly acknowledged and distinguished from my own work.
- None of this work has been previously published elsewhere, with the exception of the following: (provide list of publications or presentations, or delete this part). (If the work of any co-authors appears in this thesis, authorization such as a release or signed waiver from all affected co-authors must be obtained prior to publishing the thesis. If so, attach copies of this authorization to your initial and final submitted versions, as a separate document for retention by the Graduate School, and indicate on this page that such authorization has been obtained).

Date: March, 2020
Signature:

Abstract

Astrocyte calcium activity mapping in behaving mice using anterograde axo-astrocytic AAV transfer

Astrocytes are considered active partners to neurons in information processing. Heterogeneous, bidirectional interaction between neurons and astrocytes alludes to circuit specific communication. However, the role of astrocytes in information processing, primarily established through *ex vivo* experiments, has been challenged by a series of controversies that highlighted the importance of studying astrocytes under fully physiological conditions in behaving mice. Astrocytes extend highly ramified processes that cradle synapses. They form functionally independent microdomains where they exhibit a rich repertoire of localized calcium signals. How astrocyte Ca^{2+} microdomain signals relate to neuronal activity and behaviour *in vivo* is still unclear. My objective was to investigate circuit specific, single-astrocyte Ca^{2+} microdomain activity in mice during behavioural states and sensory stimuli. I found that adeno-associated viruses (AAVs) can transfer anterogradely along thalamocortical projections to transduce cortical astrocytes and neurons. This axo-astrocytic AAV transfer enables the study of astrocytes and neurons embedded in specific neuronal circuits. Intersectional approaches, using anterograde axo-astrocytic AAV transfer in combination with membrane tagged genetically encoded calcium indicators (GECIs), enabled sparse, high contrast labelling of cortical astrocytes embedded in the somatosensory system of mice. Continuous imaging with two-photon microscopy of single astrocytes for about ≈1 hour combined with automatic, unbiased extraction of Ca^{2+} activity revealed a rich repertoire of subsecond, μm scale, localized Ca^{2+} signals. The number, size and duration of astrocytic Ca^{2+} signals were modulated with locomotion but not with intermittent whisker-touch stimulation. Locomotion and whisker stimuli evoked rapid $[Ca^{2+}]_i$ elevation in thalamocortical axon boutons, whose activity was not correlated with nearby astrocyte Ca^{2+} microdomain signalling. Astrocyte fine processes exhibit heterogeneous, non-random, Ca^{2+} signalling patterns giving rise to hotspots of higher activity that are stable over time. Hotspot patterns allude to subcellular specialization. Our study: a) provides a new toolkit for studying neuron-astrocyte interactions within brain circuits, b) extends our understanding of astrocyte Ca^{2+} microdomain signalling and relationship to neuronal activity in behaving animals and c) suggests that there are astrocyte Ca^{2+} activity maps in the brain.

Acknowledgment

First, I would like to express my gratitude to my supervisor, Dr. Bernd Kuhn, who has supported me throughout the PhD as a mentor but also as a friend. I would like to thank you for the helpful discussions and feedback, continuous support whenever it was necessary, giving me the freedom to pursue my ideas, and letting me grow throughout the PhD. You were there anytime I had a problem (which was most of the time) and I never had to worry about access to equipment. Most importantly, I would like to thank you for being not just a good supervisor but also a great person. Science is a human endeavour in great need of people like you.

I would also like to thank Achilleas, who helped me with data processing and analysis during his internship and beyond. Without your ongoing support and exemplary skills in programming this project wouldn't have been completed on time. The fact that you continued supporting this project while doing your military service tells a great deal about your character, and it will be an honor to work with you again.

I would especially like to thank my lab members for supporting me and mentoring me. Thank you Sigita for teaching me how to perform surgeries when I just started. It has been instrumental for this project. Kazuo, thank you for keeping us alive in the lab and making sure everything was available when it was needed. Every glass pipette I used was your own creation. Also thank you Chris, Claudia, Hiroko, Lina, Neil, Ray, Shinobu, Soumen and Tabbal for the support, conversations, feedback, fun and all the sweets over the years.

Bernd, Audrey, Claudia and Neil, thank you for taking the time to read over this thesis and give me feedback, especially considering the time constraints. Also, Audrey, I really enjoy our discussion about astrocytes. They have been very helpful.

To my close friends. You were perhaps the most important aspect of my experience in OIST. I will never forget the endless philosophical conversations of 224 from 2-4am with you. I will always treasure our treasure hunts in the jungles, adventures on the island and the beautiful ocean, cooking experiments and board games among many others. You gave life to PhD life. You know who you are. To all the amazing people I met at OIST, it was a great honor getting to know you and being part of this beautiful community.

A special thanks to my family. You have always been there for me, and without you I would never have reached this stage. Despite 8724 km you have always been in touch.

Finally I am grateful to the graduate school for all the support over the years, and to OIST for the generous funding, facilities, and welcoming us here. Of course this wouldn't be possible without the initiative of the Japanese government and generous support of the Okinawan people. Through your support, I had the opportunity to complete this project and travel abroad to learn and present my work. In particular I especially appreciated the International Astrocyte School in Bertinoro, where I met amazing people and got introduced to the field.

Abbreviations

1P	single photon excitation microscopy
2P	two photon excitation microscopy
Aldh1l1	aldehyde dehydrogenase 1 family, member L1
AM	acetoxymethyl
AU	Airy Unit
AQP4	aquaporin 4
BTC	brainstem trigeminal complex
CaM	Calmodulin
CI	95% confidence interval
Cx	Connexin
DREADD	designer receptors exclusively activated by designer drug
dsDNA	double stranded DNA
EAAT	excitatory amino acid transporter
EE	early endosome
ER	endoplasmic reticulum
GABA	gamma aminobutyric acid
GAT	GABA transporter
GC	genome copies
GECI	Genetically encoded calcium indicator
GFAP	Glial fibrillary acidic protein
GLAST	Glutamate aspartate transporter
GLT1	glutamate transporter 1
GNR	glia to neuron ratio
GPCR	G-protein coupled receptor
IHC	immunohistochemistry
i.p	intraperitoneal
IP_3	inositol triphosphate
IP3R	Inositol trisphosphate receptor
$K_{ir}4.1$	inward rectifying potassium channel 4.1
KCC	K^+/Cl^- co-transporter
LE	late endosome
LC	locus coeruleus
LTD	long-term depression
LTP	long-term potentiation
MAPK	mitogen activated protein kinase
MCT	monocarboxylate transporters

MCU	mitochondrial calcium uniporter
mGluR	metabotropic glutamate receptor
MVB	multivesicular body
N.A.	numerical aperture
NA	noradrenaline
NBM	nucleus basalis of Maynert
NCX	Na^+/Ca^{2+} exchanger
NKA	Na^+/ K^+ ATPase
NKCC	$Na^+/ K^+/Cl^-$ co-transporter
NLCX	$Na^+/Li^+/Ca^{2+}$ exchanger
NO	nitric oxide
OCT	optimal cutting temperature
PAPs	perisynaptic astrocytic processes
PI3K	phosphoinositide 3-kinase
PIP_2	phosphatidylinositol bisphosphate
PLC	phospholipase C
PMCA	plasma membrane Ca^{2+} ATPase
PMT	photomultiplier tube
POm	posterior medial nucleus
PrV	principal sensory nucleus
PSF	point spread function
PV	parvalbumin
RYR	ryanodine receptor
S1	primary somatosensory cortex
SBF-SEM	serial block-face scanning electron microscopy
SD	standard deviation
SERCA	sarco-endoplasmic reticulum ATPase
SNR	signal to noise ratio
SpV	spinal nucleus
SpVc	spinal nucleus subnucleus caudalis
SPVi	spinal nucleus subnucleus interpolaris
SpVo	spinal nucleus subnucleus oralis
SR101	sulforhodamine 101
ssDNA	single stranded DNA
SST	somatostatin
TGN	trans-golgi network
TLL	"Traffic Light Labelling"
TNFα	tumor necrosis factor alpha
TRP	transient receptor potential cation channel
V1	primary visual cortex
VPM	ventral posterior medial nucleus
xcorr	cross correlation

To Dienekes, Maron, Alpheus, Eurytus,
Aristodemus and the rest of the 300 mice sacrificed.

Contents

Declaration of Original and Sole Authorship iii

Abstract v

Acknowledgment vii

Abbreviations ix

Contents xiii

List of Figures xvii

Motivation 1

1 Introduction 3
- 1.1 What are astrocytes? 3
  - 1.1.1 Historical perspective 3
  - 1.1.2 Distribution of astrocytes in the brain 3
  - 1.1.3 Morphology 5
  - 1.1.4 Molecular characteristics 5
  - 1.1.5 Astrocyte networks 7
- 1.2 Multifunctional role of astrocytes 8
  - 1.2.1 Homeostasis 8
  - 1.2.2 K^+ homeostasis 8
  - 1.2.3 Water homeostasis, aquaporins and the glymphatic system 10
  - 1.2.4 Neurotransmitter homeostasis 10
  - 1.2.5 Metabolic support 11
  - 1.2.6 Perspective 12
  - 1.2.7 Control of synapse form and function 12
  - 1.2.8 Reactive astrocytes and pathology 13
- 1.3 Astrocyte calcium signalling 14
  - 1.3.1 Calcium: the ubiquitous second messenger 15
  - 1.3.2 Generation of Ca^{2+} signals 17
  - 1.3.3 Spatiotemporal organization of Ca^{2+} signals 17
  - 1.3.4 Diverse types of astrocyte Ca^{2+} signals 19

1.4 Astrocyte calcium responses to neuronal activity 20
  1.4.1 Early studies revealed reliable astrocytic Ca^{2+} responses to neuronal stimulation 20
  1.4.2 Do astrocytes respond with transient elevation of $[Ca^{2+}]_i$ to neuronal activity? 21
  1.4.3 Astrocytes respond reliably to neuromodulators 26
  1.4.4 Perspective 27
1.5 Astrocyte modulation of neuronal activity 27
  1.5.1 Mechanisms of gliotransmitter release 29
  1.5.2 Modulation of gliotransmitter release 29
  1.5.3 Role of astrocyte $[Ca^{2+}]_i$ elevation and gliotransmission in neuronal circuits 30
  1.5.4 Controversies 33
1.6 Methods for investigating astrocyte calcium signals 34
  1.6.1 General principles for optical measurements of Ca^{2+} signals . . . 34
  1.6.2 Organic Ca^{2+} indicator dyes 36
  1.6.3 Genetically encoded calcium indicators (GECI) 36
  1.6.4 Fluorescent microscopy: focus on two photon microscopy 37
  1.6.5 Molecular toolkit for probing astrocyte physiology 39
1.7 AAV biology 40
  1.7.1 Cell specific gene expression using AAVs 42
  1.7.2 AAVs exhibit anterograde and retrograde properties 44
1.8 The mouse somatosensory system 45
  1.8.1 The whisker somatosensory circuit 45
  1.8.2 Whisker touch increases neuronal activity in barrel cortex . . . 46
  1.8.3 VPM drives cortical states 46
  1.8.4 Locomotion modulates sensory responses 46
  1.8.5 Astrocytes of the barrel cortex 47

2 Anterograde axo-astrocytic AAV transfer to astrocytes 49
2.1 Motivation 49
  2.1.1 Hypothesis 49
2.2 Methods 49
  2.2.1 Animals 49
  2.2.2 Surgery 51
  2.2.3 Adeno associated viruses 51
  2.2.4 Slice preparation and immunohistochemistry 52
  2.2.5 Confocal imaging and analysis 52
  2.2.6 Whisker removal 54
  2.2.7 Exosome inhibition 54
2.3 Results 55
  2.3.1 AAV1 vectors injected in the VPM mediate astrocytic and neuronal labelling in S1 55
  2.3.2 AAV capsids are found in astrocytes and neurons in the cortex following VPM injection 57
  2.3.3 Mechanisms of intercellular AAV transfer 60

2.4 Discussion 64
2.4.1 A small number of AAV particles is anterogradely transferred to transduce 2nd-order astrocytes and neurons 64
2.4.2 Axo-astrocytic AAV transfer offers a flexible toolkit for studying brain circuits 66
2.4.3 The mechanisms involved in anterograde AAV transfer remain unknown 68
2.4.4 Summary 69
2.5 Summary of findings 70

3 Single-astrocyte [Ca^{2+}]$_i$ microdomain mapping in behaving mice 71
3.1 Motivation 71
3.1.1 Hypotheses 72
3.2 Methods 72
3.2.1 Animals 72
3.2.2 Surgery 72
3.2.3 Adeno-associated viruses 73
3.2.4 Two photon imaging in awake animals 73
3.2.5 Data analysis 74
3.3 Results 79
3.3.1 Single-astrocyte Ca^{2+} microdomain 2-photon imaging in awake mice 79
3.3.2 State dependent astrocyte Ca^{2+} activity 81
3.3.3 Astrocyte Ca^{2+} event changes during state transitions 84
3.3.4 Astrocyte Ca^{2+} signals are not random 86
3.3.5 Astrocytes display Ca^{2+} activity hotspots that are stable over time 88
3.3.6 Axon-astrocyte interaction 91
3.4 Discussion 94
3.4.1 Anterograde axo-astrocytic rAAV transfer can be used for functional studies in barrel cortex astrocytes 94
3.4.2 Unbiased investigation of astrocytic Ca^{2+} microdomains during behaviour 95
3.4.3 Diversity of astrocyte Ca^{2+} microdomain signals 96
3.4.4 Locomotion modulates astrocyte Ca^{2+} microdomain signals . . . 97
3.4.5 Whisker stimulation does not modulate microdomain Ca^{2+} signals in L2/3 S1 astrocytes 98
3.4.6 Thalamocortical axon Ca^{2+} activity increases with whisker stimulation and locomotion 100
3.4.7 Astrocyte Ca^{2+} microdomain activity is not random 101
3.4.8 Astrocyte Ca^{2+} activity maps in the brain 102
3.4.9 Summary of findings 103

Conclusion 105

Bibliography **107**

List of Figures

1.1 Heterogeneous distribution and identity of astrocytes in the brain . . . 4
1.2 Astrocyte morphology 6
1.3 Astrocytes are connected to each other via gap junctions 8
1.4 Astrocytes maintain homeostasis in the brain 9
1.5 Astrocyte regulate the energy supply of the brain 11
1.6 Astrocytes control synaptic form, function and elimination 13
1.7 Ca^{2+} sources and sinks 16
1.8 A diverse Ca^{2+} signalling toolkit allows versatile control of cellular processes 18
1.9 Localized Ca^{2+} microdomains in astrocyte processes 20
1.10 Astrocytes responding to neuronal stimulation with Ca^{2+} microdomain signals 24
1.11 Neuromodulators modulate astrocyte Ca^{2+} signalling 25
1.12 Current model of bidirectional communication between astrocytes and neurons 28
1.13 Functions of astrocyte Ca^{2+} elevation 31
1.14 Heterogeneity in astrocyte - neuron interactions 32
1.15 Multiscale spatiotemporal relationship between astrocytes and neurons 35
1.16 Optical imaging 38
1.17 Schematic of AAV transduction pathway 41
1.18 rAAV construct building strategy for cell specific gene delivery 43
1.19 Whisker somatosensory system of mice 47

2.1 Hypothetical schematic of trans-synaptic AAV transfer to astrocytes and neurons. 50
2.2 Intercellular AAV transfer injection strategies. 56
2.3 AAV capsids enter thalamic cells within 24 hours after injection 58
2.4 AAV capsids are found in cortical astrocytes and neurons 12 days after injection in the thalamus. 59
2.5 "Traffic light labelling" 61
2.6 Number of labelled 2nd order cells in S1 was not affected by the exosome inhibitor GW4869. 63
2.7 Number of labelled 2nd order cells in S1 was not affected by contralateral whisker removal. 65

3.1 Experimental design 80

3.2 State dependent modulation of astrocyte membrane Ca^{2+} signal characteristics . . . 82
3.3 State dependent astrocyte Ca^{2+} event characteristics . . . 83
3.4 Astrocyte Ca^{2+} signal changes during state transitions . . . 85
3.5 Astrocyte calcium activity is not random . . . 87
3.6 Astrocyte activity heatmaps are stable over time . . . 89
3.7 Axon-astrocyte interactions . . . 92

Motivation

The human brain contains ≈100 billion neurons, connected through trillions of synapses involved in information processing. A tantalizing modern theory is that glial cells, such as astrocytes, may be active partners to neurons in information processing through active mechanisms supplementing their established homeostatic roles. This is a revolutionary idea in our understanding of brain function. These traditionally thought star-shaped cells arborize into nanoscopic processes that are in contact with synapses and blood vessels giving them a characteristics spongiform, cloud-like appearance. Considering their proximity to synapses, are astrocytes involved in synaptic information processing? Astrocytes possess receptors that can sense chemical signals in their environment, including neurotransmitters and neuromodulators. A large body of evidence, suggests bidirectional communication between neurons and astrocytes. Astrocytes can respond to neuronal activity with Ca^{2+} signals that can in-turn drive mechanisms that modulate neurons. Reported mechanisms include astrocytic release of chemical messengers, termed "gliotransmitters". However, fast, bidirectional communication between neurons and astrocytes under physiological conditions is controversial. On one hand the spatiotemporal dynamics (whole astrocyte, multiple seconds) of Ca^{2+} signals are not compatible with precise and fast signalling between synapses. The bidirectional communication between astrocytes and neurons was also questioned on the grounds of pathology, since most of the supporting evidence was accumulated from *ex-vivo* preparations. Since the identity and functions of astrocytes identity changes with pathology, age and the conditions of their environment it is important to minimize their perturbation in experimental preparations if we want to derive conclusions about physiology. *In-vivo* preparations in awake, adult animals provides a more physiological platform to test these ideas. Modern research, suggests that astrocytic function and Ca^{2+} signaling are heterogeneous. For example, improved labelling techniques revealed a rich repertoire of fast (hundreds of milliseconds) Ca^{2+} signals localized in thin astrocytic processes that were previously unsampled. In addition, a heterogeneous and dynamic identity of astrocytes within different neuronal circuits starts emerging where astrocytes - neuron interaction exhibit circuit specificity. Therefore, functional tools for probing neuron - astrocyte interactions within specific circuits under physiological conditions, along with high spatiotemporal extraction of the rich Ca^{2+} activity at astrocytic thin processes, are bound to revolutionize our understanding about the role of astrocytes in information processing in the brain.

My aim was to develop a system for studying the function of astrocytes embed within specific circuits, at high spatiotemporal resolution, in behaving mice. Then use this system to investigate how Ca^{2+} signals in astrocytic fine processes are modulated by neuronal activity and characterize them.

Chapter 1

Introduction

1.1 What are astrocytes?

1.1.1 Historical perspective

Astrocytes are neuroglial cells. Rudolf Virchow (1858) coined the term neuroglia, referring to the passive 'connective tissue' holding neurons together. About a decade later Camillo Golgi (1873) stained this glia 'goo' with the 'black reaction' to reveal its cellular attributes. The 'star like' subset of these glial cells was termed astrocytes by Michael von Lenhossék (1891). Cajal's pioneering modifications to the Golgi stain with gold chloride demonstrated the morphology of astrocytes [107]. Interestingly, the gold chloride stain targets intermediate filaments [178], consisting primarily of (GFAP) today used as an astrocytic marker.

1.1.2 Distribution of astrocytes in the brain

The human brain consists of ≈1:1 glia to neuron ratio (GNR) [24]. The GNR ratio was a controversial topic in neuroscience for decades [5] [163]. It was thought that there were 10 times more glia than neurons until it was recently disproved by Herculano-Houzel's group using the isotropic fractionator method [24] [26]. The GNR generally increases with brain size and varies between brain regions (Figure 1.1 A) and species [24] [380] [371]. The majority of glial cells in the human brain are oligodendrocytes (45-75%) followed by astrocytes (19-40%) and microglia (10%) [380]. Astrocyte tile the entire brain with little overlap to each other (Figure 1.2 A, B, C), thus occupying distinct territorial domains [58]. They were classically divided based on their morphology and astrocyte enriched proteins into: fibrous astrocytes of the white matter, protoplasmic astrocytes of the gray matter and specialized astrocytes. Specialized astrocytes include: radial glia, retinal Muller cells, Bergman cells, velate astrocytes, tanycytes, pituicytes, Gomori astrocytes, ependymocytes and surface associated astrocytes [373]. Some of these types of astrocytes are illustrated in Figure 1.1 C. Although this rough classification of astrocytes was helpful, defining the heterogeneity of astrocytes is still a work in progress. Astrocytes are defined by their morphology, molecular markers and function. Here, we will focus on protoplasmic astrocytes.

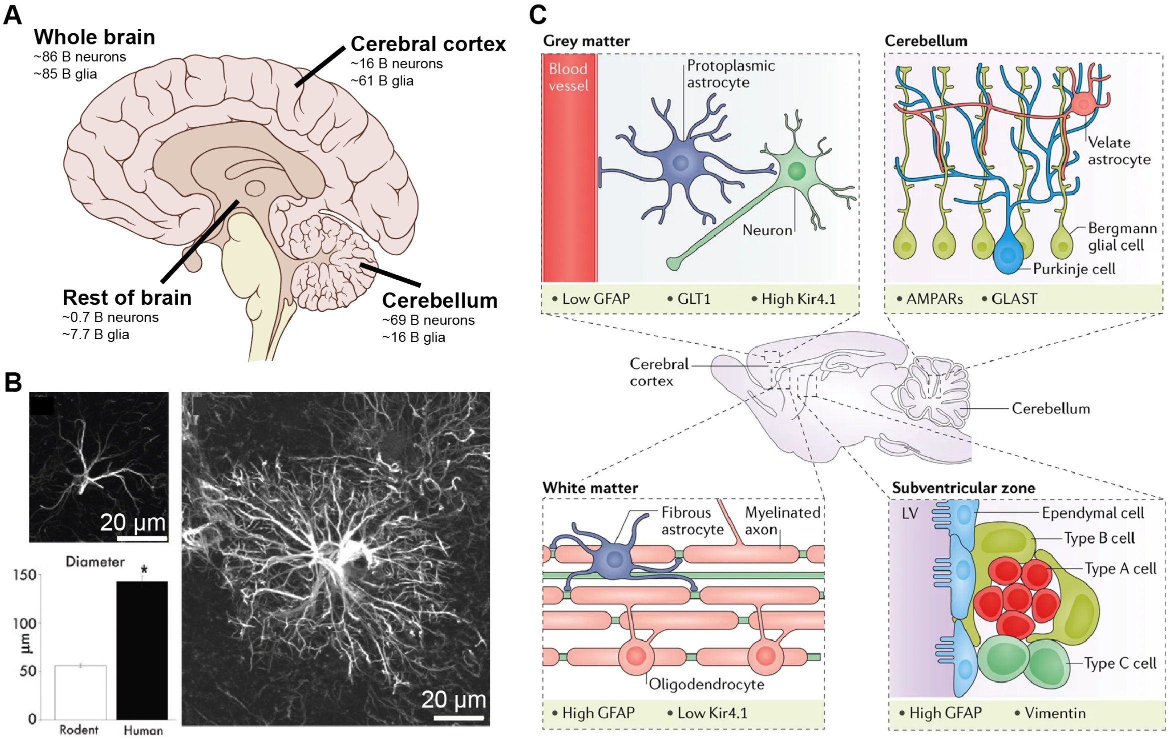
A
Whole brain
~86 B neurons
~85 B glia
Cerebral cortex
~16 B neurons
~61 B glia
Rest of brain
~0.7 B neurons
~7.7 B glia
Cerebellum
~69 B neurons
~16 B glia
B
20 µm
Diameter
150
100
50
0
µm
*
Rodent
Human
20 µm
C
Grey matter
Blood vessel
Protoplasmic astrocyte
Neuron
• Low GFAP
• GLT1
• High Kir4.1
Cerebellum
Velate astrocyte
Bergmann glial cell
Purkinje cell
• AMPARs
• GLAST
Cerebral cortex
Cerebellum
White matter
Fibrous astrocyte
Myelinated axon
Oligodendrocyte
• High GFAP
• Low Kir4.1
Subventricular zone
LV
Ependymal cell
Type B cell
Type A cell
Type C cell
• High GFAP
• Vimentin

Figure 1.1: Heterogeneous distribution and identity of astrocytes in the brain. A) The glia to neuron ratio (GNR) varies between brain areas. Illustration of approximate number of neurons and glia in selected areas of the human brain. B) Human astrocytes (right) are ≈2.5 times bigger in diameter (bottom, left) compared to rodent astrocytes (top, left) as revealed by GFAP labelling. C) Astrocytes exhibit different morphology and molecular markers depending on their locations in the brain. Protoplasmic astrocytes are found in the gray matter, have radial morphology and are in contact with synapses and blood vessels (top, left). Fibrous astrocytes are found in the white matter, have elongated morphology and are in contact with myelinated axons and oligodendrocytes (bottom, left). Bergman glia and velate astrocytes are found in the cerebellum. Bergman glia extend long apical processes who wrap the dendrites of Purkinje cells. Velate astrocytes are like protoplasmic astrocytes and are found particularly around granule neurons (top, right). The lateral ventricles of the subventricular zone are lined with astrocyte-like B cells(bottom, right). Different astrocyte types differentially express molecular markers including GFAP, GLT1, $K_{ir}4.1$, AMPARs and vimentin. GFAP, Glutamate transporter 1 (GLT1), inward rectifying potassium channel 4.1($K_{ir}4.1$). Panel A was modified from wikimedia commons based on [24], panel B was modified from [254] and panel C was taken from [125].

1.1.3 Morphology

The name astrocyte was derived based on the star-like morphology observed when staining the GFAP enriched intermediate filaments [178]. However, more advanced visualization techniques have now revealed that astrocytes exhibit a bushy, spongiform morphology [299] [334] (Figure 1.2 A, B, C, D). Mouse protoplasmic astrocytes consist of a cell body emanating into 4-10 main branches that arborize into thin, nanoscopic processes often referred to as branchlets and leaflets that are devoid of GFAP. These astrocytes have a diameter of ≈40-60 μm occupying a volume of ≈6.6x10μm^3 mostly composed of bracelets and leaflets (≈90-95% of volume). They also extend polarised specialized endfeet that wrap around blood vessels [299] [58] [257] [175]. The territory of a single hippocampal astrocyte territory is estimated to encompass ≈140000 synapses [58] out of which ≈60% are juxtaposed to perisynaptic astrocytic processes (PAPs) [396] [370]. The anatomical and functional relationship between synapses and PAPs was consolidated into the concept of the "tripartite synapse" [14] or "astrocytic cradle" [372]. The intimate relationship between PAPs and synapses allows astrocytes to modulate a multitude of synaptic functions ranging from homeostasis to synaptic plasticity and information processing [14] [372]. PAP coverage of synapses is a dynamic process [38] [280]. Synapses juxtaposed to PAPs tend to be larger [396], suggesting a positive correlation between synaptic strength and PAP coverage of synapses. PAP motility was reported to be enhanced in response to synaptic activity, increasing synaptic coverage and stability [38]. For example, whisker stimulation in adult mice increases astrocyte coverage of synapses in the barrel cortex [116]. In contrast, a recent study [134] suggests that astrocyte processes might withdraw from mature synapses following long-term potentiation (LTP) induction (at least 30-40 min following LTP) thus enhancing glutamate spillover and cross talk between neighbouring synapses. The mechanism, conditions and heterogeneity of PAP mobility is bound to be very important for the functional relationship between astrocytes and neurons. The study of nanoscopic PAPs (Figure 1.2 E, F) is not amenable to diffraction limited optical methods. While most studies so far relied on electron microscopy (often associated with fixation issues [182] and static images), super resolution microscopy techniques [147] [309] [130] and expansion microscopy [389] have potential to "expand" the field. The size, diversity and morphological complexity of astrocytes varies across brain areas (i.e. specialized astrocytes), within areas [194] and between species [253] [254]. For example, human astrocytes occupy a volume 15-20 times larger than rodents (Figure 1.1 B), possess more elaborate processes and have unique astrocyte subtypes [253] [254]. However, the comparative biology of astrocytes between species is not well established yet.

1.1.4 Molecular characteristics

There is still no systematic agreement on how to define astrocytes based on molecular markers. GFAP was the first molecular marker associated with astrocytes. However, GFAP is upregulated in pathology, not all healthy astrocytes express GFAP at concentrations detectable by immunohistochemistry and GFAP is also expressed in cell types other than astrocytes. Thus GFAP expression alone is not sufficient or required

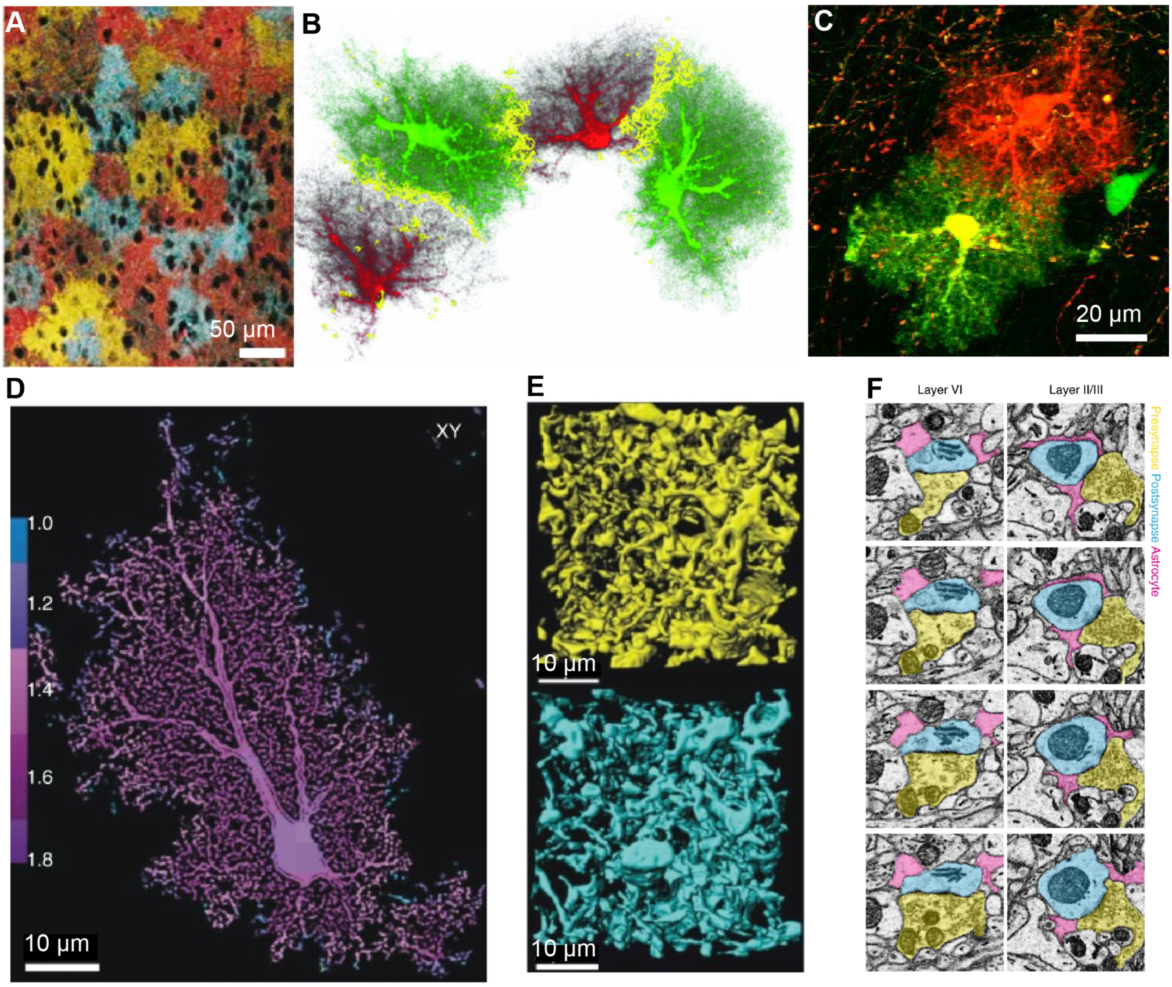

Figure 1.2: Astrocyte morphology. Astrocytes tile the brain with little overlap to each other shown by A) "Brainbow" expression in cortical astrocytes, B) Dye loading of hippocampal, dentate gyrus astrocytes and C) "Traffic light labelling" (tdTomato and eGFP) expression in cortical astrocytes. D) Fine astrocytic process architecture revealed by high resolution optical image of a Lucifer yellow-filled astrocyte. Colour scale represents fractal dimension. E) These nanoscopic processes exhibit high surface area to volume ratio as shown by serial block-face scanning electron microscopy (SBF-SEM) of perisomatic (top) and peripheral (bottom) volumes in Golgi-impregnated astrocytes. F) Astrocyte processes (pink) wrap around presynaptic (yellow) and post-synaptic (blue) synapses as shown by (SBF-SEM) in layer 6 and layer 2/3 of the somatosensory cortex. Panel A was taken from [202]; B was taken from [394]; C is from this thesis; D and E were taken from [334]; F was taken from [194].

for astrocyte identification [175] [234]. Other molecular markers commonly associated with astrocytes include: glutamate transporters GLT-1 and GLAST, connexins (Cx) Cx30 and Cx43, inward rectifying $K_{ir}4.1$ channels, aldehyde dehydrogenase 1 family member L1 (Aldh1L1), glutamate synthetase, water channel aquaporin 4 (AQP4) and the calcium binding protein S100B [373] [175] [234] (Figure 1.1 C). The protein expression profile of astrocytes shows variability within brain areas. For example, Cx30 and Cx43 are enriched within the barrels of the primary somatosensory cortex (S1) compared to septa [146] . Immunohistochemistry and transcriptome analysis revealed layer specific heterogeneity in S1 astrocytes [31] [194]. Also, transcriptomic analysis revealed molecular diversity of astrocytes between different areas [25] [59] [67]. The molecular characteristics of astrocytes is likely regulated by neuronal activity. For example, astrocytes cultured with neurons change their expression of glutamate transporters [279], glutamine synthase [222], connexins [185], and neuropeptide receptors [230]. Prolonged whisker stimulation increases the expression of glutamate transporters in S1 astrocytes [116]. Disturbance of neuronal layers in S1 abolishes the layer specific heterogeneity of astrocytes [31] [194]. The molecular characteristics of astrocytes also change with age [350] [85] and pathology [175] [125]. Therefore, the molecular identity of astrocytes is heterogeneous and dynamic, changing in response to cues in their environment.

1.1.5 Astrocyte networks

Astrocytes interact with all cell types in the central nervous system (CNS). They are connected to each other via gap junctions (Figure 1.3 A) composed primarily of connexins of subtype Cx43 and Cx30 [240]. Cx43 / Cx30 double knockout mice do not exhibit gap-junction mediated K^+ [383] and metabolic [308] communication between astrocytes. Connexins assemble into hemichannels. Hemichannels which dock to each other form gap junctions [391] [56]. Unpaired hemichannels were reported to release gliotransmitters such as ATP [346], glutamate [408] and D-serine [227] in the extracellular fluid. Gap junctions ($\approx$25%) also connect processes from the same astrocyte [302] (reflexive gap junctions, Figure 1.3 A), potentially coupling different subcellular compartments. Gap junctions allow rapid intercellular exchange of ions and small ($\approx$1 kDa) molecules between astrocytes. This is critical for K^+ buffering [383] and calcium wave propagation [105] [143] [114]. Astrocyte gap-junction networks are not random. For example, Cx30 and Cx43 are focused towards the center of S1 [146] (Figure 1.3 B) and olfactory bulb [68] (Figure 1.3 C) functional units [117]. Gap junction communication can be modulated by neurotransmitters and pathology [117]. Astrocytes are also known to communicate to each other through the release of gliotransmitters such as ATP [114].

Astrocytes communicate with microglia to mediate immune responses in the brain [199] [156] and synaptic pruning [315] [46]. They communicate with oligodendrocytes to modulate myelination [96] which could depend on neuronal activity [151]. Astrocytes cooperate with pericytes and neurons to control blood flow in the brain [229]. Finally, astrocytes communicate with neurons. While the interactions between astrocytes and neurons was considered to be homeostatic, a large amount of evidence suggests that astrocytes may be active partners to neurons in information processing in the brain [14] [16] [312] [88] [104]. In this thesis we will focus on astrocyte - neuron interactions.

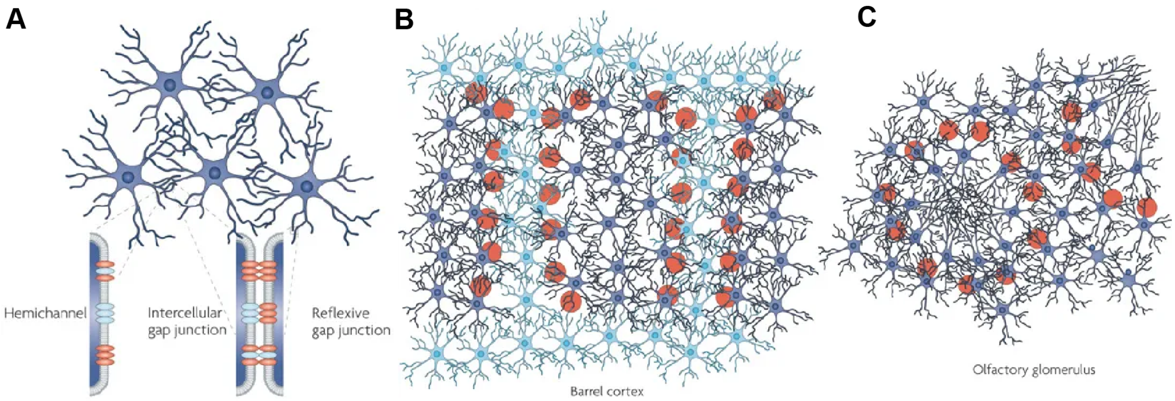

Figure 1.3: Astrocytes are connected to each other via gap junctions. A) Gap junctions connect contacting astrocytes to each other. Gap junctions are composed of paired connexin (Cx) hemichannels. Same astrocyte process can connect with each other forming reflexive gap junctions. B) In the somatosensory cortex, gap junction proteins (Cx30 & Cx43) are more highly expressed in barrel astrocytes (dark blue) compared to septal astrocytes (light blue). C) In the olfactory bulb, glomerular astrocyte cell bodies are found in the periphery extending their processes to the center of the functional unit. Images taken from [117].

1.2 Multifunctional role of astrocytes

1.2.1 Homeostasis

The most well accepted function of astrocytes is regulation of homeostasis. Astrocytes maintain ion homeostasis, regulate the water volume of the brain, maintain the pH, clear excess neurotransmitters (Figure 1.4) and provide metabolic support to neurons (Figure 1.5). While these functions are well accepted, they shouldn't be overlooked, since they play critical roles in brain function and there is still a lot to be learned. The spotlight of current research in astrocytes have been their emerging function as elements of information processing mediated by Ca^{2+} signalling. However, the homeostatic functions of astrocytes are intimately linked to astrocyte Ca^{2+} signalling and can influence neuronal activity.

1.2.2 K^+ homeostasis

When neurons fire action potentials, they release K^+ into the extracellular space which, if not cleared, can result in neuronal hyperexcitability. Astrocytes express a high concentration of K^+ channels and transporters that clear excess extracellular K^+ through uptake and spatial buffering (Figure 1.4 B, top). These include K_{ir}4.1 channels, Na^+/ K^+ ATPases (NKA), inward rectifying, $Na^+/K^+/Cl^-$ (NKCC) co-transporters and K^+/Cl^- co-transporters (KCC) [376] [35]. K^+ uptake uses energy derived from the breakdown of ATP (i.e. NKA) or the electrochemical gradient through co-transporters (i.e. NKCC). Spatial buffering relies on passive transport of K^+ ions from regions of high $[K^+]$ to regions of low $[K^+]$ through K_{ir} channels and the gap-junction coupled net-

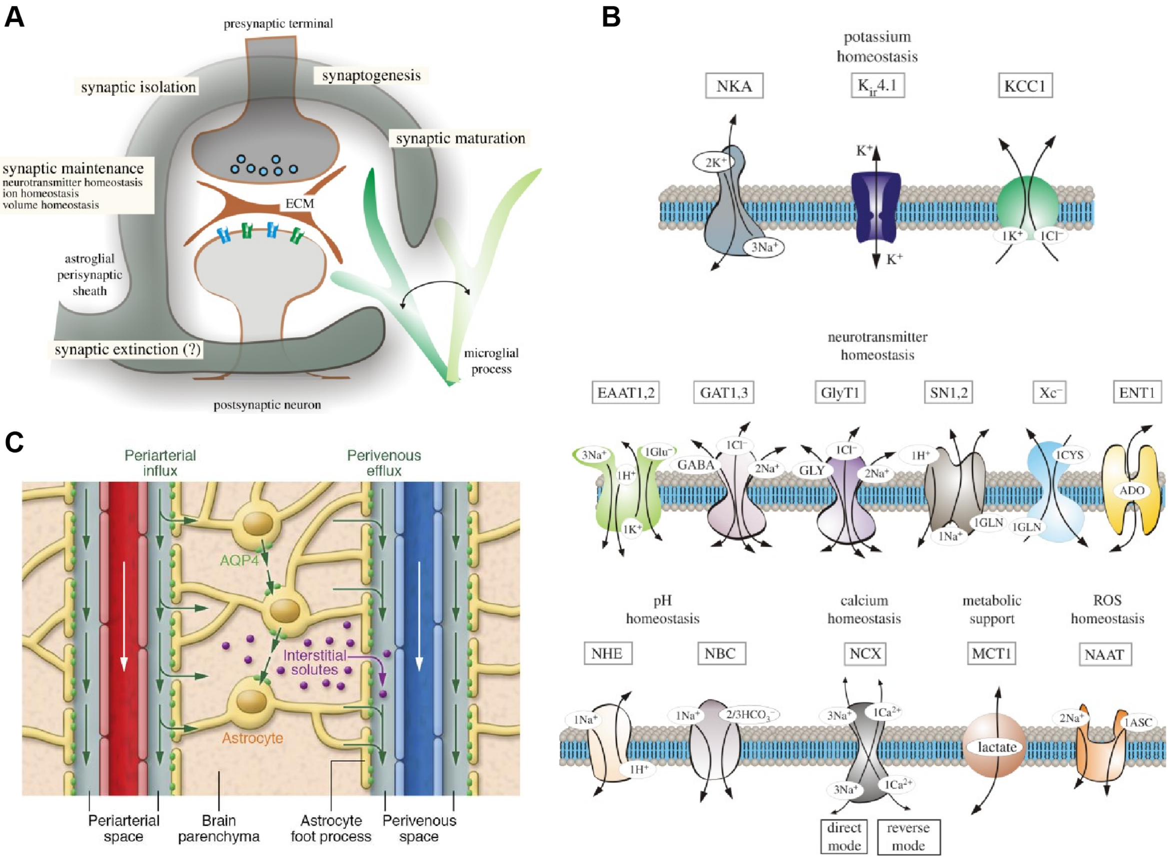
A
presynaptic terminal
synaptic isolation
synaptogenesis
synaptic maturation
synaptic maintenance
neurotransmitter homeostasis
ion homeostasis
volume homeostasis
ECM
astroglial perisynaptic sheath
synaptic extinction (?)
microglial process
postsynaptic neuron
B
potassium homeostasis
NKA
$K_{ir}4.1$
KCC1
$2K^+$
$3Na^+$
K^+
K^+
$1K^+$
$1Cl^-$
neurotransmitter homeostasis
EAAT1,2
GAT1,3
GlyT1
SN1,2
Xc^-
ENT1
$3Na^+$
$1Glu^-$
$1H^+$
$1K^+$
GABA
$1Cl^-$
$2Na^+$
GLY
$1Cl^-$
$2Na^+$
$1H^+$
$1Na^+$
1GLN
1GLN
1CYS
ADO
pH homeostasis
calcium homeostasis
metabolic support
ROS homeostasis
NHE
NBC
NCX
MCT1
NAAT
$1Na^+$
$1H^+$
$1Na^+$
$2/3HCO_3^-$
$3Na^+$
$1Ca^{2+}$
$3Na^+$
$1Ca^{2+}$
direct mode
reverse mode
lactate
$2Na^+$
1ASC
C
Periarterial influx
Perivenous efflux
AQP4
Interstitial solutes
Astrocyte
Periarterial space
Brain parenchyma
Astrocyte foot process
Perivenous space

Figure 1.4: Astrocytes maintain homeostasis in the brain. A) The "astrocytic cradle" or "tripartite synapse" represents the functional and anatomical relationship between astrocytes and neurons at synapses. Astrocyte processes wrap around synapses and play important roles in the function, maturation, maintenance, isolation and elimination of synapses. B) Astrocytes express a plethora of proteins involved in the homeostasis of ions, neurotransmitters, metabolism, pH and reactive oxygen species summarized in this schematic. C) They also express aquaporin (AQP) channels primarily located at their perivascular endfeet, allowing them to maintain water homeostasis and clear waste accumulated in the brain through the glymphatic system. Panel A & B images taken from [372]; C taken from [206].

work of astrocytes [208] [35]. Disturbances to astrocyte mediated K^+ homeostasis can lead to epilepsy [80] and a range of other disorders summarized in [35]. Interestingly, K^+ uptake could also be actively regulated through $[Ca^{2+}]_i$ dependent mechanisms. For example, $[Ca^{2+}]_i$ elevation can increase the activity of Na^+/Ca^{2+} exchangers (NCX), raising $[Na^+]$ that in turn activates Na^+/ K^+ ATPase mediated uptake of K^+ and a decrease in extracellular $[Na^+]$. This leads to neuronal hyperpolarization, reduction in excitatory synaptic activity and a decrease in synaptic failure [385]. Also computer simulations suggest that NCXs are sufficient for the induction of microdomain $[Ca^{2+}]_i$ signals in PAPs [382]. These suggest that astrocytes may be able to modulate neuronal activity through passive and active, $[Ca^{2+}]_i$ dependent, regulation of K^+.

1.2.3 Water homeostasis, aquaporins and the glymphatic system

Astrocytes maintain water homeostasis and regulate extracellular volume in the brain by virtue of high expression of aquaporin (AQP) channels. AQP4 is the most prevalent AQP in astrocytes, predominantly located at perivascular endfeet and, to a lesser extent, processes around excitatory synapses [239]. AQP4 channels were also linked to astrocyte $[Ca^{2+}]_i$ elevations induced by osmotic stress [358]. AQP4 are also critical for the operation of the glymphatic system [150] (Figure 1.4 C). The glymphatic system clears cell waste accumulated in the brain. The system consists of a periarterial cerebrospinal fluid influx route and a perivenous interstitial fluid clearance path, coupled by convective flow facilitated by astrocytic AQP4 channels [155]. Interestingly, AQP4 isoforms (M23) regulate the motility of astrocyte process and glutamatergic synaptic transmission [75]. The position of astrocyte processes in relation to synapses is likely to have diverse effects on synaptic activity depending on the specific proteins expressed at the respective processes (i.e. transporters, channels and receptors).

1.2.4 Neurotransmitter homeostasis

Astrocytes rapidly remove neurotransmitters released by synapses in the extracellular fluid (Figure 1.4 B, middle), and constrain their spill over to nearby synapses [305] (Figure 1.4 A). Astrocytes uptake the majority of glutamate released by synapses ($>$80%) through high affinity excitatory amino acid transporters (EAAT) 1 and 2, optimizing neuronal function and preventing excitotoxicity [213]. Considering that astrocytes can also release glutamate [214] astrocytes may maintain homeostasis by balancing the opposing functions of glutamate uptake and release [213]. Uptaken glutamate is converted to glutamine through the enzymatic action of glutamine synthetase that is expressed in astrocytes but not neurons [218], or used as energy by converting it to a-ketoglutarate used in ATP synthesis [323]. Glutamine transported to neurons is resynthesized to glutamate or gamma aminobutyric acid (GABA) and concentrated into vesicles to be released as a neurotransmitters. This is referred to as the glutamate/GABA-glutamine cycle [28]. Similarly, astrocytes uptake GABA through GABA transporters (GAT) 1 and 3 where it is converted to glutamine or metabolized to succinic semialdehyde [106]. The number, position and distance of EAATs (and

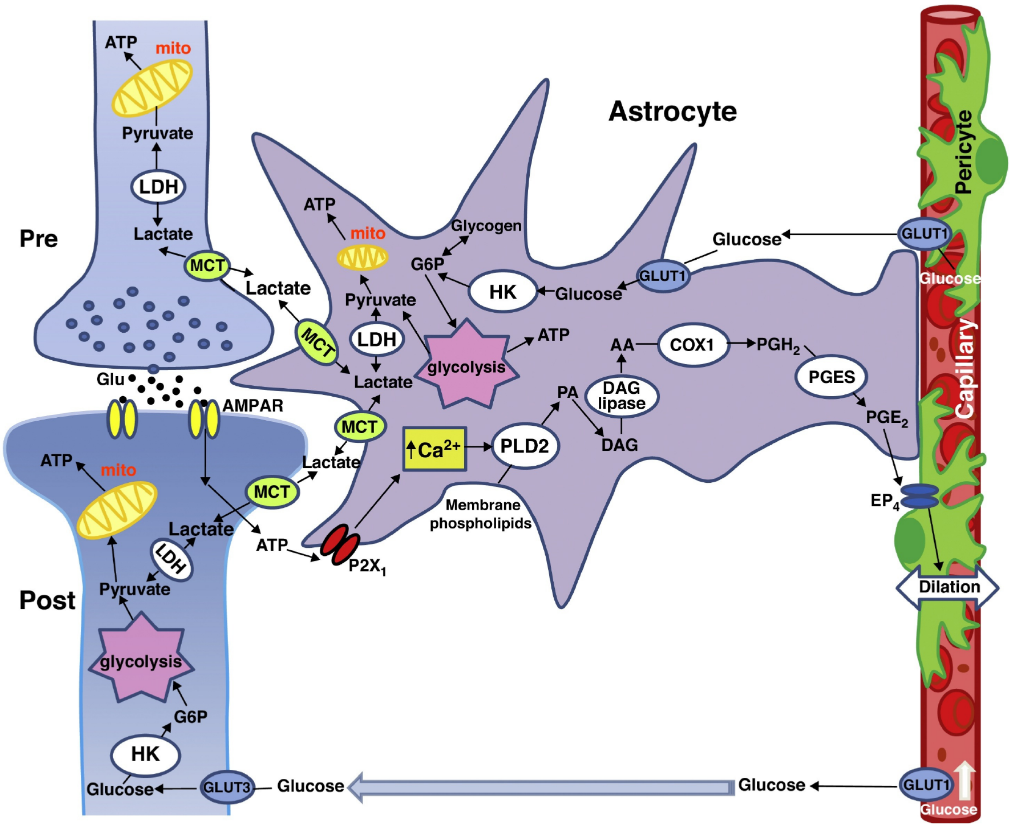
ATP
mito
Pyruvate
LDH
Lactate
Pre
MCT
Lactate
Glu
AMPAR
ATP
mito
Lactate
LDH
Pyruvate
Post
glycolysis
G6P
HK
Glucose
GLUT3
Glucose
Astrocyte
ATP
mito
Glycogen
G6P
HK
Glucose
GLUT1
Glucose
Pyruvate
MCT
LDH
glycolysis
ATP
Lactate
MCT
Lactate
MCT
Ca2+
PLD2
Membrane phospholipids
ATP
P2X1
PA
DAG lipase
DAG
AA
COX1
PGH2
PGES
PGE2
EP4
Dilation
Glucose
GLUT1
Pericyte
Glucose
Capillary
GLUT1
Glucose

Figure 1.5: Astrocyte regulate the energy supply of the brain. Current model on how astrocytes regulate energy supply. Astrocytes regulate the supply of nutrients by modulating the contractility of pericytes. Astrocyte $[Ca^{2+}]_i$ elevation activates an enzymatic cascade that leads to prostaglandin release, relaxing pericytes and dilating blood vessels. Glucose can be taken up by neurons and astrocytes directly and used in glycolysis. In astrocytes glucose can be converted to glycogen for storage. Alternatively, astrocytes can produce lactate and shuttle it to neurons through monocarboxylate transporters (MCT) to use as energy source. For more detailed description of the model see [252]. Image taken from [252].

other transmitter transporters) relative to synapses is likely to be important in synaptic modulation by controlling the spatiotemporal characteristics of neurotransmitter concentration availability at the synapse. For example, surface diffusion of glutamate transporters is modulated by synaptic activity and can influence synaptic transmission [237]. Similarly transient receptor potential cation channel subfamily A member 1 (TRPA1) mediated $[Ca^{2+}]_i$ elevation in astrocytes increase GAT-3 insertion in the membrane thus regulating GABAergic signaling [333]. Thus astrocyte $[Ca^{2+}]_i$ elevation could lead to insertion of transporters near synapses to modulate synaptic activity.

1.2.5 Metabolic support

The human brain consumes ≈20% of the body's energy, mainly to reverse ion fluxes involved in synaptic transmission [128]. Disruption in brain energy supply, quickly leads to cell injury and death. Therefore, it is important to dynamically match energy supply to fluctuating demands. The response of increasing blood flow in response to higher neuronal activity is termed functional hyperaemia [21]. Astrocytes cover blood vessels with specialized endfeet [220] and enwrap synapses, the main energy consumers of the brain, with their fine processes [6] (Figure 1.5). They are thus in a privileged position to regulate functional hyperaemia. Early studies revealed that astrocyte $[Ca^{2+}]_i$ elevation led to dynamic control of microcirculation, mediated by arachidonic acid derivatives [416] [236] [120] [353]. How astrocytes are involved in functional hyperaemia is still under intense investigation and debate, but it seems to involve the coordinated action between multiple cell types [252] (Figure 1.5). One important issue was that somatic Ca^{2+} signals in astrocytes triggered by neuronal activity were too slow to have a causative effect on neurovascular coupling. However, neurovascular coupling might be mediated by faster, inositol trisphosphate receptor (IP3R)-2 independent $[Ca^{2+}]_i$ elevation. Astrocyte $[Ca^{2+}]_i$ elevation (i.e. through ATP-gated P2X1 channels) can trigger an enzymatic cascade leading to the release of prostaglandin E2 acting on pericytes who can relax and dilate capillaries [229]. Diffused glucose then enters both neurons (via GLT3) and astrocytes (via GLT1) to be used for glycolysis [226]. In astrocytes glucose can be converted and stored as glycogen. Pyruvate produced by glycolysis can be used by mitochondria for ATP production or be converted to lactate. According to the lactate shuttle hypothesis, lactate produced by astrocytes can be delivered to neurons (via monocarboxylate transporters) as an energy source [210] but the idea is still controversial [226]. Overall, astrocytes, along with other glia and neurons, play important roles in the regulation of energy supply in the brain. The discovery of fast Ca^{2+} signals in astrocyte processes and *in vivo* preparations may help elucidate the functional role of astrocytes in functional hyperaemia [258]

1.2.6 Perspective

While Ca^{2+} mediated gliotransmission has gained enormous attention and popularity as a means for astrocytes to modulate synaptic activity, the homeostatic functions of astrocytes in regulating synaptic circuits shouldn't be neglected. By mediating K^+ uptake astrocytes control synaptic excitability. The motility of astrocyte processes and recruitment of channels, exchangers and pumps in PAPs could modulate neuronal activity by controlling the rate of transmitter and ion fluxes. Homeostatic processes can also be actively mediated by astrocytic Ca^{2+} signals and in turn can influence neuronal activity. It is thus possible that many of the effects attributed to the Ca^{2+} induced release of gliotransmitters may have been artifacts of astrocytes maintaining homeostasis. Considering that astrocytes are the principal homeostatic cells of the brain, would it be surprising if astrocyte Ca^{2+} signals often triggered by artificial neuronal stimuli, are responses of astrocytes trying to re-establish homeostasis?

1.2.7 Control of synapse form and function

Beyond their homeostatic function, astrocytes are required for the formation and function of synapses. Seminal work by the Barres laboratory revealed that neurons grown in co-cultures with astrocytes had seven times more mature, functional synapses compared

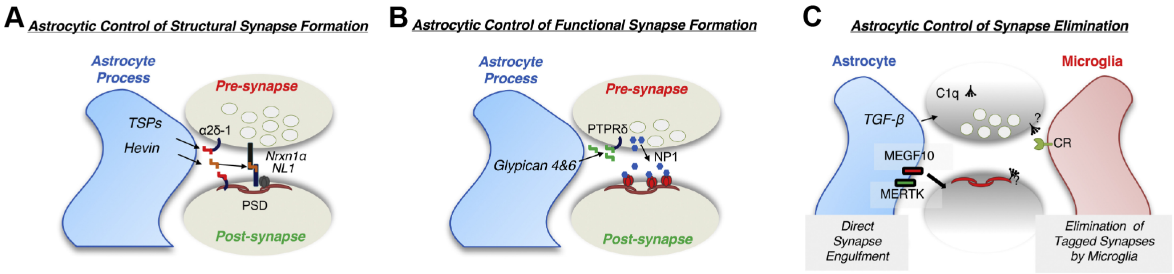
A
Astrocytic Control of Structural Synapse Formation
Astrocyte Process
Pre-synapse
TSPs
Hevin
α2δ-1
Nrxn1α
NL1
PSD
Post-synapse
B
Astrocytic Control of Functional Synapse Formation
Astrocyte Process
Pre-synapse
PTPRδ
Glypican 4&6
NP1
Post-synapse
C
Astrocytic Control of Synapse Elimination
Astrocyte
Microglia
C1q
TGF-β
?
CR
MEGF10
MERTK
Direct Synapse Engulfment
Elimination of Tagged Synapses by Microglia

Figure 1.6: Astrocytes control synaptic form, function and elimination. A) Astrocytes induce the formation of structural synapses by releasing thrombospondins (TSPs) and hevin. B) They can induce functional synapse formation through the release of glypicans and C) eliminate synapses directly through MEGF10 and MERTK mediated phagocytosis or indirectly by tagging synapses for elimination by microglia. Image taken from [6].

to isolated neuron cultures [287] [365]. The role of astrocytes is synapse formation was demonstrated across species and types of synapse [6]. Astrocytes control the formation of synaptic structure, function and elimination by releasing different molecules. For example, releasing thrombospondins [72] and hevin [189] induces structural synapse formation (Figure 1.6 A). These synapses are presynaptically active but postsynaptically silent. Releasing the hevin antagonist SPARC inhibits synapse formation and function [205] [4]. Astrocyte can enhance pre-synaptic function by releasing cholesterol [221] and postsynaptic function by regulating the number (tumor necrosis factor alpha (TNFα)) [343] and localization (Glypicans) [7] of AMPARs (Figure 1.6 B). Astrocytes also regulate synapse elimination directly through phagocytosis [74] and indirectly by tagging synapses for elimination by microglia [315] [46] (Figure 1.6 C). The heterogeneity of astrocytes and the mechanisms of synaptogenic signal release in the control of synaptic development is currently an active frontier in the field. Interestingly, there is *in vitro* evidence suggesting that astrocyte synaptogenic factor release can be regulated by ATP (thrombospondins) [362] and glutamate (SPARC, TNF-a) [159] [342]. Also, the effect on synaptogenic factors could have synapse specific roles [301]. Given that astrocytes are known to respond to neurotransmitters (i.e. ATP and glutamate) with $[Ca^{2+}]_i$ elevations it will be interesting to determine if the release of synaptogenic factors is calcium dependent and to elucidate the mechanisms and conditions of their release *in vivo*.

1.2.8 Reactive astrocytes and pathology

Astrocytes are involved in the coordinated multicellular response to brain trauma, disease and inflammation. Astrocytes respond to pathological conditions and undergo a spectrum of morphological and functional changes; collectively referred to as reactive astrogliosis [338]. Reactive astrocytes were originally characterized by overexpression of GFAP and hypertrophy [36]. It is now becoming evident that astrogliosis is not a binary state, but rather a heterogeneous, graded continuum of context dependent changes in gene expression, morphology and function [9] [228]. Recent collaborative work between the Barres and Steven laboratories [199] revealed two distinct types of reactive astrocytes termed A1 and A2. A1 astrocytes are induced by activated microglial secretion of Il-1α, TNF and C1q cytokines and are lethal to neurons and oligodendrocytes. In contrast, A2 astrocytes upregulate neurotrophic genes and promote neuron survival. Considering the volatile nature of astrocyte identity, gene expression and function during pathological conditions it is worth asking whether experiments assessing physiological aspects of astrocytes in cultures, slices and maybe even *in vivo* are investigating a reactive state of astrocytes. Indeed, Takano et al. [354] showed that astrocytes in slice preparation exhibit observable reactive changes shortly ($\approx$90 mins) after acute slice preparation. Another intriguing question is how different types of reactive astrocytes contribute to pathology and whether selective manipulation of astrocytes using pharmacology or gene therapy can be used to treat disease. Astrocytes are involved in epilepsy, Alzheimer's disease, Huntington's disease, amyotrophic lateral sclerosis, CNS trauma, stroke, infections, cancer, psychiatric disorders, and others [338]. Reactive astrocytes also exhibit aberrant Ca^{2+} signalling generally characterized by increased amplitude, frequency and duration [336]. Astrocytes rapidly respond with $[Ca^{2+}]_i$ elevation to kainate induced epilepsy [138]. Reactive astrocytes display high frequency Ca^{2+} signals and Ca^{2+} waves close to amyloid plaques in Alzheimer's disease model mice *in vivo* [90] [188]. The amplitude of Ca^{2+} signals was higher in the ischemic core compared to the penumbra region in acute stroke models [94]. Additionally, metabotropic glutamate receptors (mGluR5), often implicated in Ca^{2+} induced gliotransmission [260], while normally downregulated with age [350], are upregulated in reactive astrocytes [17] [366] [177]. Other receptors implicated in Ca^{2+} signalling are also upregulated in reactive astrocytes. For example, purinergic P2Y1 receptors [90] [187] [390] and TRP channels (TRPC4) [97] are upregulated during pathology. Reactive astrocytes can in turn release gliotransmitters. For example, they can release tonic GABA though bestrophin-1 channels or GABA transporter reversal [158] [401] [73] and release neurotoxic levels of glutamate [375] [306]. Reactive astrocyte mGluR5 mediated $[Ca^{2+}]_i$ signals may lead to thrombospondin 1 (TSP1) upregulation which contributes to synaptic remodelling and plasticity [177]. Therefore, the reactive state of astrocytes might be involved in Ca^{2+} mediated synaptic modulation by astrocytes. Similarly, the sensitivity of astrocytes to neuronal stimulation might depend on pathology. For example, striatal astrocytes of wild type mice did not respond to cortical stimulation while Huntington's disease model astrocytes responded robustly with Ca^{2+} signals [157]. Since every experimental preparation disturbs the system in some way, different reactive responses might be induced in astrocytes, depending on the specific experimental protocol. It is thus very important to maintain physiological conditions in experimental preparations assessing the functions of (healthy/non-reactive) astrocytes.

1.3 Astrocyte calcium signalling

Astrocytes, just like other glia, are electrically silent [190] as revealed by traditional electrophysiology techniques. Since astrocytes were not amenable to electrophysiological methods used to advance our understanding of neurons, the functional roles of astrocytes were neglected. This changed with the discovery and introduction of calcium dyes that revealed chemical excitability of astrocytes in the form of Ca^{2+} signals [79]. Astrocyte $[Ca^{2+}]_i$ signals are now thought to act in synergy with neuronal activity to process information in the brain [16] [32]. We will explore how Ca^{2+} provides the substrate of astrocyte excitability and its role in information processing.

1.3.1 Calcium: the ubiquitous second messenger

In the furnace of red giants calcium was born through the fusion of helium and argon. 10 billion years after stellar nucleosynthesis and exploding stars, calcium found its way into every cell. Cells evolved to separate their universe by charge, locally decreasing entropy by parsing ions through semi-permeable membranes. Calcium was abundantly available to them (3rd most common metal in nature). Cells possibly evolved to lower intracellular concentration of calcium to avoid the formation of poorly soluble calcium phosphate salts that would interfere with phosphate based bioenergetics. Once cells developed the means to maintain low $[Ca^{2+}]_i$ concentration (≈50-100nM) compared to the extracellular space (≈20000 times higher) they gained an ideal signalling agent. With the development of multicellularity, life already had the machinery available for communication through calcium. As the complexity of signal transduction increased, more numerous and elaborate systems developed to control $[Ca^{2+}]_i$ [77].

The biophysical properties of calcium allow it to be readily accepted by protein sites with irregular geometry. Within the cell, calcium binds to proteins carrying EF hands such as Calmodulin and S100. The binding of Ca^{2+} induces conformational changes in proteins, exposing hydrophobic patches on protein surfaces that allows them to interact with targets. Ca^{2+} is involved in the control of a variety of enzymatic cascades and thus acts as a universal signaling ion. A large number of transporters and exchangers are involved to maintain Ca^{2+} homeostasis. Cytosolic calcium buffers with high affinity to Ca^{2+} bind the ions and limit their diffusion. Ca^{2+} in the cell is typically concentrated in the endoplasmic reticulum (ER) and other organelles such as lysosomes and mitochondria. The movement of Ca^{2+} between the extracellular space and the cell, or between and within intracellular components is referred to as: calcium signals. Physical and chemical cues can trigger calcium signals [285] [49] [61][77] [60].

Mammalian life begins with a global calcium signal sweeping through the egg [233]. Since then, calcium is involved in many aspects of cellular life including embryonic pattern formation, cell differentiation, cell proliferation, transcription factor activation, chemical signalling, and apoptosis [40]. In astrocytes, Ca^{2+} signals are thought to also be involved in the release of "gliotransmitters" i.e. (ATP, glutamate, D-serine) [16], the motility of their processes [38] neurovascular coupling [258], receptor trafficking [333], K^+ homeostasis [385], and others. How can Ca^{2+} elevation regulate so many different processes? The answer likely lies in the versatility of Ca^{2+} signalling mechanisms and an extensive repertoire of calcium sensitive molecular signalling components. The spatio-temporal patterning of calcium signals can recruit different combinations of messenger molecules leading to distinct outputs and interactions with other signaling pathways [40]. Cells use this versatility to regulate a diversity of cellular processes through precise control of Ca^{2+} levels.

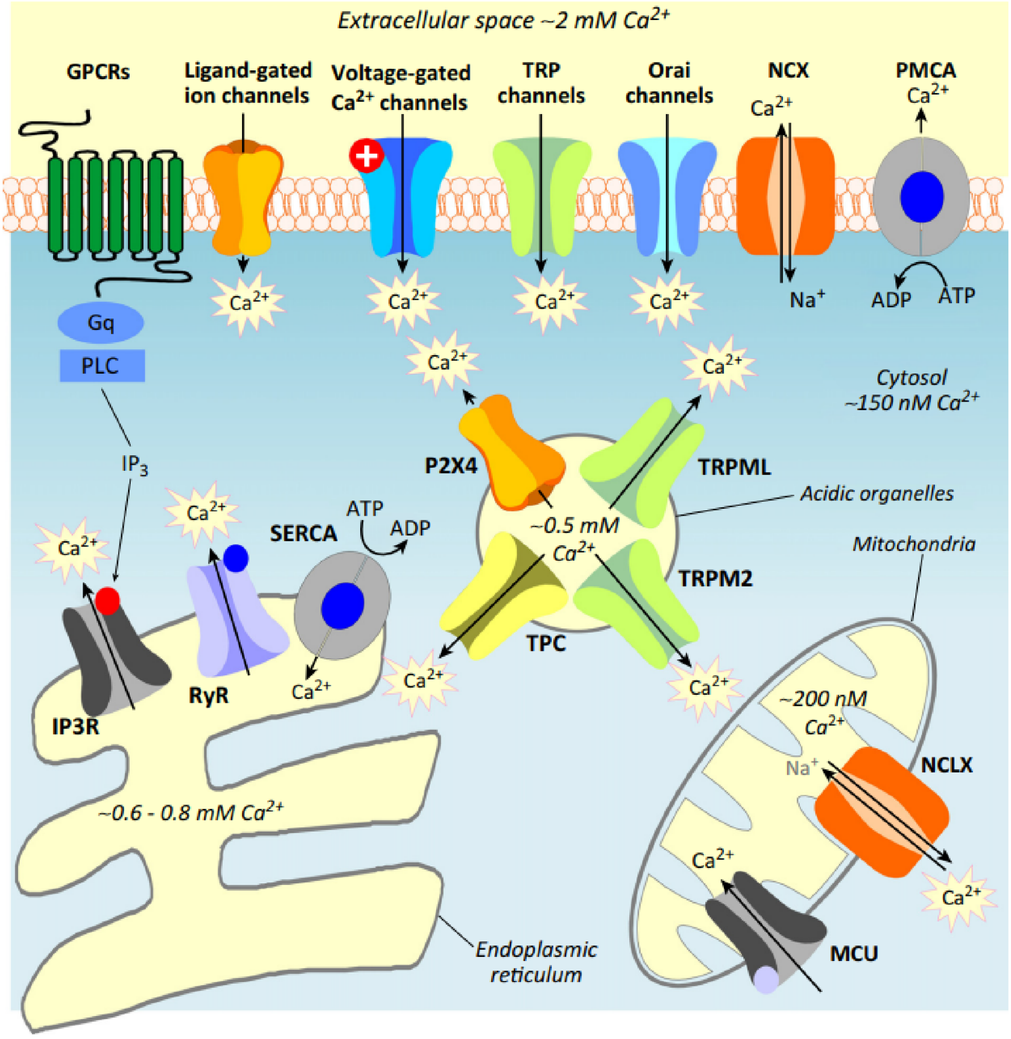
Extracellular space ~2 mM Ca^{2+}
GPCRs
Ligand-gated ion channels
Voltage-gated Ca^{2+} channels
TRP channels
Orai channels
NCX
PMCA
Ca^{2+}
Na$^+$
ADP
ATP
Gq
PLC
IP$_3$
Cytosol ~150 nM Ca^{2+}
P2X4
TRPML
Acidic organelles
~0.5 mM Ca^{2+}
TRPM2
TPC
Mitochondria
SERCA
ATP
ADP
IP3R
RyR
~200 nM Ca^{2+}
NCLX
MCU
~0.6 - 0.8 mM Ca^{2+}
Endoplasmic reticulum

Figure 1.7: Ca^{2+} sources and sinks. The $[Ca^{2+}]_i$ of the cell is dynamically regulated through channels, pumps and transporters expressed in the plasma membrane and organelles of the cell. High $[Ca^{2+}]$ from the extracellular space can enter the cell through: ligand gated ion channels, voltage gated Ca^{2+} channels, TRP ion channels, Orai channels and the reversal of Na$^+$/Ca^{2+} exchangers (NCX). Low cytoplasmic $[Ca^{2+}]$ can be maintained through the expulsion of cytoplasmic Ca^{2+} to the extracellular space through plasma membrane Ca^{2+} ATPase (PMCA) pumps and NCX. Alternatively, cytoplasmic Ca^{2+} can be sequestered within organelles such as the endoplasmic reticulum (ER), acidic organelles (i.e. lysosomes) and mitochondria; for example through plasma membrane Ca^{2+} ATPaseas (PMCAs), mitochondrial calcium uniporters (MCU) and Na$^+$/Li$^+$/Ca^{2+} exchangers (NLCXs). The same organelles can also act as sources of cytoplasmic Ca^{2+}. They can release Ca^{2+} into the cytoplasm through: indirect G-protein coupled receptor (GPCR) mediated opening of inositol trisphosphate receptors (IP3Rs), ryanodine receptors (RYRs), TRP melastatin channels (TRPM) and NCLX among others. Together, Ca^{2+} sources and sinks control the flux of Ca^{2+} and mediate Ca^{2+} signalling in cells. image taken from [335].

1.3.2 Generation of Ca^{2+} signals

Cells generate Ca^{2+} signals using internal and external sources of calcium to increase cytoplasmic $[Ca^{2+}]$ by an order of magnitude. They have mechanisms for increasing (ON mechanisms) and decreasing (OFF mechanisms) $[Ca^{2+}]c$ (Figure 1.8 A, C). The ON mechanisms rely on channels controlling the passage of Ca^{2+} from the extracellular fluid ($\approx$2mM) or intracellular stores ($\approx$0.2-0.8mM) into the cytoplasm ($\approx$150nM) [335]. Ca^{2+} influx into the cell can occur through: a) ligand-gated-ion channels such as ATP-gated P2X channels [251], b) voltage-gated calcium channels [20], c) TRP channels [374], d) store operated Ca^{2+} entry through Orai channels [193], mechanically gated piezo channels [266] and e) Sodium-calcium exchangers (NCX)[378]. Alternatively, stored Ca^{2+} can be released into the cytoplasm by organelles. One of the most well studied mechanism is the G-coupled activation of IP3Rs of the endoplasmic reticulum. This involves the binding of agonists on G-protein coupled receptors (GPCR). GPCRs are classified into four families: Gs, Gi/o, Gq/11 and G12/13 [139]. We will focus on the Gq/11 family. Agonist binding on Gq/11 GPCRs activates inositol triphosphate (IP3) synthesis via the cleavage of phosphatidylinositol bisphosphate (PIP_2) by phospholipase C (PLC). IP_3 diffuses and binds to IP3R receptors of the ER. Binding of both IP_3 and Ca^{2+} triggers IP3R opening and release on Ca^{2+} into the cytosol [50] [39]. GPCR ligands include neurotransmitters and neuromodulators. In astrocytes Gq/11 GPCRs include, noradrenergic receptors [93], muscarinic acetylcholine receptors [356], and metabotropic glutamate receptors (mGluR1 and 5) [53]. Note however that mGluR5 are downregulated with age [350] while other mGluRs found in astrocytes such as the Gi/o mGluR3 that inhibits cyclic AMP production may raise $[Ca^{2+}]_i$ in astrocyte processes [129]. Once the ligand binds it can be amplified. Other organelles and channels, such as mitochondria [2] and lysosomes are also involved in the intricate control of intracellular calcium concentration [335] [295]. A summary of Ca^{2+} sources and sinks in the cell is illustrated in Figure 1.7.

1.3.3 Spatiotemporal organization of Ca^{2+} signals

Once $[Ca^{2+}]_i$ increases in the cytoplasm it binds to $Ca^{2+}+$-binding proteins that function as calcium effectors or buffers (Figure 1.8 A). Buffers (involved in OFF mechanisms) with different kinetics and affinity to Ca^{2+} (i.e. calretinin, calbindin, parvalbumin), fine-tune the spatiotemporal properties of the Ca^{2+} signal [29]. The important role of Ca^{2+} buffers in astrocyte Ca^{2+} signalling is not well explored yet. The small portion of free cytosolic calcium remaining, binds to effector proteins such as calmodulin, synaptotagmin, S100 or annexins [29]. These proteins amplify the diminutive size of Ca^{2+} ions to the scale of proteins. For example, Ca^{2+} can bind to the EF-hand domains of calmodulin (CaM) recruitment sites changing its shape [142]. Since hundreds of proteins contain CaM recruitment sites who can undergo conformational changes when CaM binds Ca^{2+} [77], it is easy to imagine the diverse influence of calcium on cellular processes. Many Ca^{2+} signaling molecules are organized into complexes (Figure 1.8 D) where the effect of Ca^{2+} is localized. These complexes can operate as autonomous units with different properties from their neighbours allowing calcium signals to be spatially organized. The spatial organization of Ca^{2+} signals is very important for rapid responses [29]. The endoplasmic reticulum endowed with IP3Rs distributed on its surface is an important contributor to the spatial organization of Ca^{2+} signals. Stimuli of increasing strength can open single IP3Rs (blips), groups of IP3Rs (Puffs), or trigger a chain reaction of opening neighbouring IP3Rs leading to a calcium wave that can propagate between cells through gap junctions [40]. IP3R2 are enriched in astrocytes [59] and have been the main focus of studying calcium signals in astrocytes.

Additionally, effector proteins operate over a wide temporal spectrum (Figure 1.8 C), ranging from microseconds (i.e. exocytosis) to hours (i.e. fertilization). Regulation of transcription can extend the temporal reach of Ca^{2+} signals even further [29] [77]. Cytoplasmic calcium is rapidly sequestered (OFF mechanisms) by mobile calcium

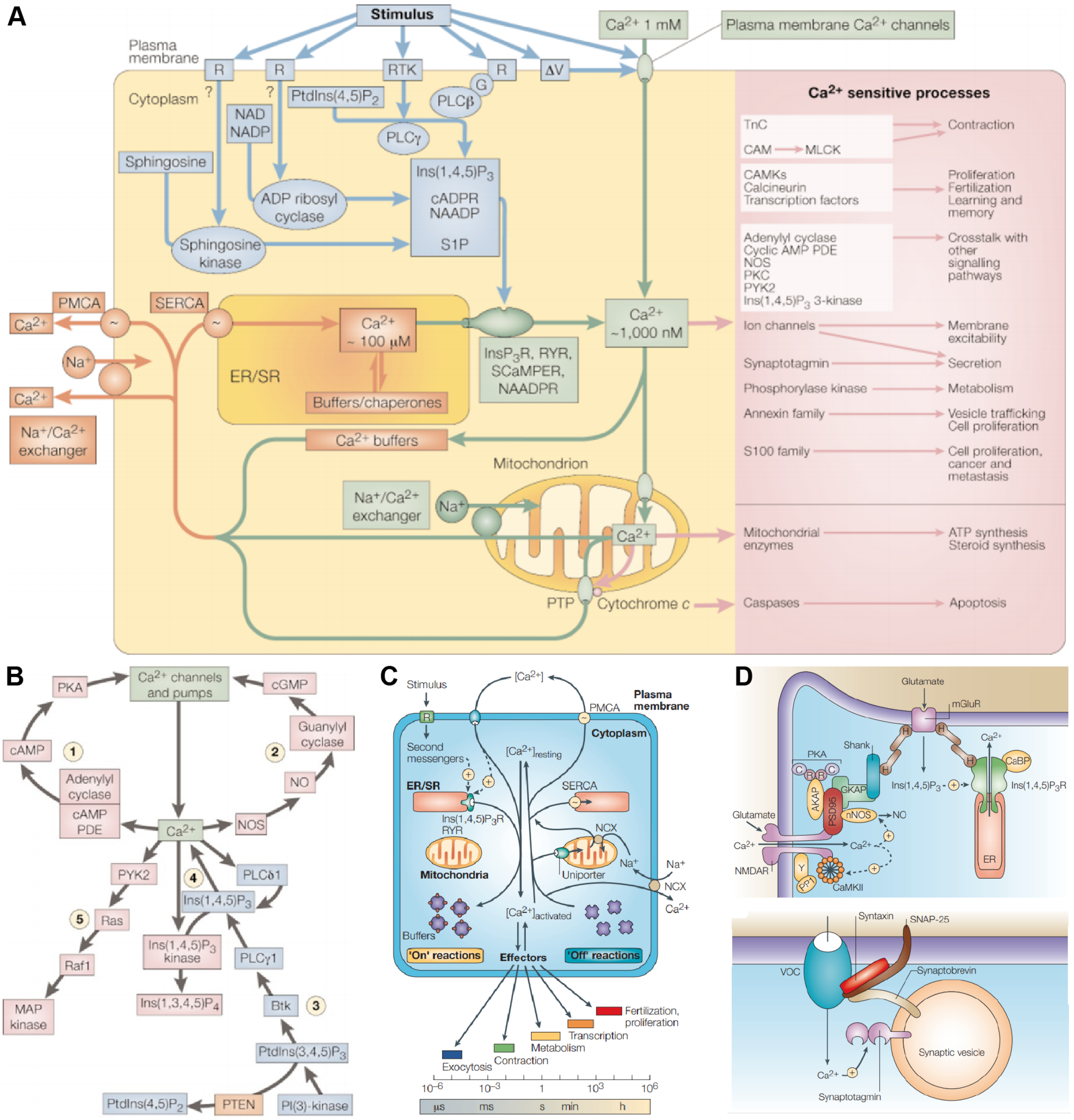
A
Stimulus
Ca2+ 1 mM
Plasma membrane Ca2+ channels
Plasma membrane
R
R
RTK
R
ΔV
Cytoplasm
?
?
PtdIns(4,5)P2
G
PLCβ
NAD
NADP
PLCγ
Sphingosine
Ins(1,4,5)P3
ADP ribosyl cyclase
cADPR
NAADP
Sphingosine kinase
S1P
Ca2+ sensitive processes
TnC
CAM
MLCK
Contraction
CAMKs
Calcineurin
Transcription factors
Proliferation
Fertilization
Learning and memory
Adenylyl cyclase
Cyclic AMP PDE
NOS
PKC
PYK2
Ins(1,4,5)P3 3-kinase
Crosstalk with other signalling pathways
PMCA
SERCA
Ca2+
Ca2+ ~ 100 μM
ER/SR
Na+
Ca2+
Buffers/chaperones
InsP3R, RYR, SCaMPER, NAADPR
Ca2+ ~1,000 nM
Ion channels
Membrane excitability
Synaptotagmin
Secretion
Phosphorylase kinase
Metabolism
Annexin family
Vesicle trafficking
Cell proliferation
S100 family
Cell proliferation, cancer and metastasis
Na+/Ca2+ exchanger
Ca2+ buffers
Mitochondrion
Na+/Ca2+ exchanger
Na+
Ca2+
Mitochondrial enzymes
ATP synthesis
Steroid synthesis
PTP
Cytochrome c
Caspases
Apoptosis
B
PKA
Ca2+ channels and pumps
cGMP
cAMP
1
2
Guanylyl cyclase
Adenylyl cyclase
cAMP PDE
NO
Ca2+
NOS
PYK2
4
PLCδ1
Ins(1,4,5)P3
5
Ras
Raf1
Ins(1,4,5)P3 kinase
PLCγ1
MAP kinase
Ins(1,3,4,5)P4
Btk
3
PtdIns(3,4,5)P3
PtdIns(4,5)P2
PTEN
PI(3)-kinase
C
Stimulus
[Ca2+]
PMCA
Plasma membrane
R
Cytoplasm
Second messengers
[Ca2+]resting
+
+
ER/SR
SERCA
Ins(1,4,5)P3R
RYR
NCX
Mitochondria
Na+
Uniporter
Na+
NCX
Ca2+
[Ca2+]activated
Buffers
'On' reactions
Effectors
'Off' reactions
Fertilization, proliferation
Transcription
Metabolism
Contraction
Exocytosis
10−6
10−3
1
103
106
μs
ms
s
min
h
D
Glutamate
mGluR
H
H
Shank
Ca2+
PKA
C
R
R
C
H
H
CaBP
AKAP
GKAP
PSD95
Ins(1,4,5)P3
+
Ins(1,4,5)P3R
Glutamate
nNOS
NO
Ca2+
Ca2+
+
+
NMDAR
Y
PP1
CaMKII
ER
Syntaxin
SNAP-25
VOC
Synaptobrevin
Synaptic vesicle
Ca2+
+
Synaptotagmin

Figure 1.8: A diverse Ca^{2+} signalling toolkit allows versatile control of cellular processes. (caption next page.)

Figure 1.8: (previous page.) A) Ca^{2+} mobilizing signals (blue) often triggered by stimuli acting on plasma membrane receptors (R) lead to increase in $[Ca^{2+}]_i$ (ON mechanisms; green). ON mechanisms can activate a variety of Ca^{2+} sensitive processes (salmon-red) depending on the context and cell type. The transient elevation of $[Ca^{2+}]_i$ returns to baseline through the action of OFF processes (dark orange) that sequester Ca^{2+} inside organelles or dissipate Ca^{2+} outside of the cell. B) The Ca^{2+} signalling toolkit can interact with other signalling pathways such as the cyclic AMP (1) signalling system, (2) nitric oxide (NO) synthesis system, (3) phosphoinositide 3-kinase (PI3K) system, (4) Ca^{2+} positive and negative feedback interactions and (5) mitogen activated protein kinase (MAPK) interactions. The type and nature of interactions enables flexible, complex non-linear information processing by the cell. C) A tight balance between ON and OFF processes enables Ca^{2+}, acting through effector proteins to influence cells dynamically over a large temporal scale, ranging from μs to hours. D) Also, the components of different Ca^{2+} signalling systems are grouped together into multimolecular complexes, allowing calcium to act differently in space depending on the interacting complexes found there. Two examples of such systems are the NMDA and Inositol trisphosphate receptor (IP3R) complex (top) and synaptic vesicle complex (bottom) of neurons. The complex interaction of Ca^{2+} signals with effector proteins in astrocytes is still in its infancy. Panels A & B were taken from [40]; C & D were taken from [41].

buffers, extrusion from the cell, or through the elaborate network of calcium storing organelles. For example, Ca^{2+} is extruded from the cell by plasma membrane Ca^{2+} ATPase (PMCA) pumps, NCX or mobilized inside the ER by sarco-endoplasmic reticulum ATPase (SERCA) pumps [40].

1.3.4 Diverse types of astrocyte Ca^{2+} signals

The spatiotemporal characteristics of calcium signals established through ON and OFF mechanisms and a complex network of effector proteins are vital for the versatile control of cellular processes. Astrocytes display Ca^{2+} signals with a broad range of spatiotemporal characteristics (Figure 1.9). These include: a) the predominant, spontaneous, highly localized microdomain Ca^{2+} signals observed in branches and branchlets (Figure 1.9) [332] [333] [334] [274] [129] [344] [345] that are independent of neuronal stimulation and are not abolished in IP3R2 KO mice [129] b) localized, microdomain Ca^{2+} signals triggered by neuronal stimulation (Figure 1.10) [92] [261] [47] [344] [345] c) local calcium waves that can occur spontaneously in major branches and somata (Figure 1.9) [129] [157] d) global Ca^{2+} waves encompassing the whole astrocyte that are largely mediated by IP3R2 receptors and can be triggered by intense neuronal stimulation [129] e) synchronous, pan-astrocytic, Ca^{2+} signals triggered by locomotion or startle responses driven by volume transmission of neuromodulators (Figure 1.11 C)[93] [249] [274] [341]. f) localized, mitochondria driven Ca^{2+} signals that can be modulated by neuronal activity [2]. g) Ca^{2+} signals localized to astrocyte endfeet [347] [102] [258] [345]. It is likely that astrocyte nanodomain signals represent another type of Ca^{2+} signaling, however these remain largely unexplored at the moment because of

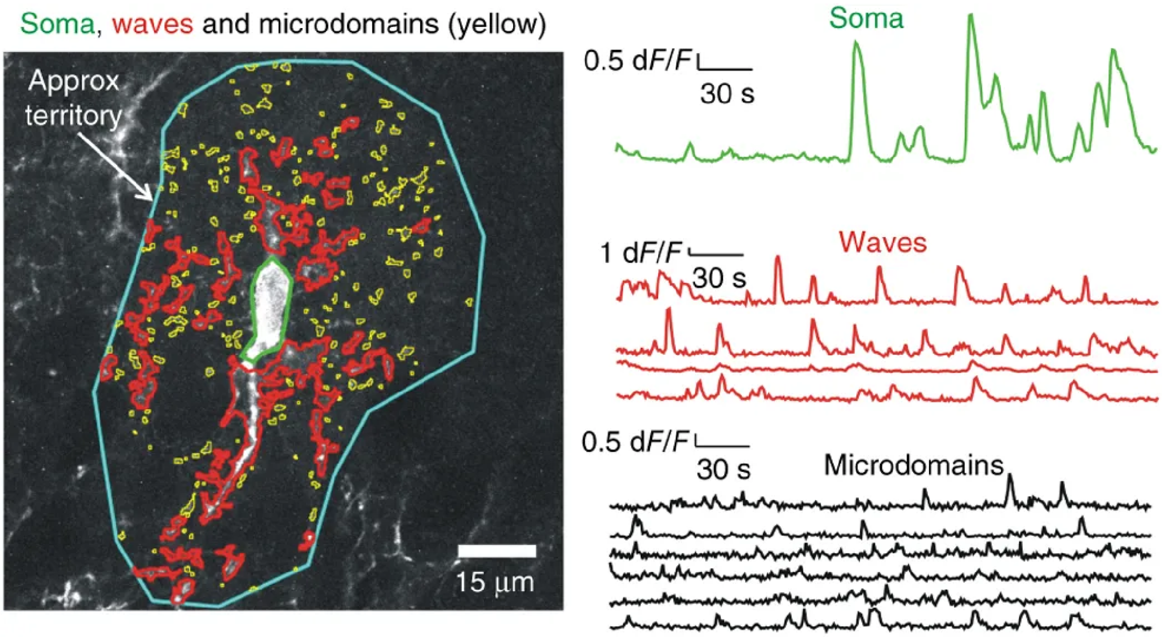

Figure 1.9: Localized Ca^{2+} microdomains in astrocyte processes. Representative image of a hippocampal astrocyte (blue boundary) labelled with cyto-GCaMP6f and traces from three predominant types of astrocyte signals: somatic (green), waves (red) and microdomains (yellow). Astrocytes exhibit a range of Ca^{2+} signals. Image taken from [341].

technical challenges. Astrocyte Ca^{2+} signals of different spatiotemporal characteristics likely mediate diverse astrocyte mechanisms and responses yet to be discovered. While astrocyte Ca^{2+} plays important roles in most aspects of cell and network physiology, we will focus on its role in astrocyte - neuron interactions.

1.4 Astrocyte calcium responses to neuronal activity

1.4.1 Early studies revealed reliable astrocytic Ca^{2+} responses to neuronal stimulation

The active role of astrocyte signalling in information processing was only recently appreciated and actively investigated, largely because of technical developments. Application of Ca^{2+} imaging techniques in the 1990s revealed that astrocytes display $[Ca^{2+}]_i$ elevation in response to neurotransmitters. Cornell-Bell et al. [79] showed that culture hippocampal astrocytes from postnatal rats labelled with fluo-3 respond to glutamate with cytoplasmic $[Ca^{2+}]_i$ elevation in the form of propagating waves. This observation raised the possibility that astrocytes might respond to synaptic glutamatergic activity. Electrical stimulation of mossy fibers in organotypic culture slices triggered calcium waves is CA3 astrocytes [87]. These findings were then supplemented by Porter and McCarthy [291] in acute hippocampal slices loaded with the calcium sensitive dye Calcium Green-1. Electrical stimulation of Schaffer collaterals resulted in $[Ca^{2+}]_i$ elevation in CA1 astrocytes that was inhibited by blocking neuronal activity and mGluRs. These experiments suggested that astrocytes can respond to neuronal glutamate with mGluR mediated $[Ca^{2+}]_i$ elevation. Astrocytes express a variety of transmitter receptors that bind glutamate, GABA, adenosine, ATP, histamine, noradrenaline and acetylcholine [352]. The natural next question was whether astrocytes respond to neurotransmitters associated with these receptors.

A wave of discoveries revealed that astrocytes in brain slices of young rodents respond with $[Ca^{2+}]_i$ elevation to a variety of neurotransmitters released by neurons such as glutamate [272], GABA [165], noradrenaline [192], and acetylcholine [15]. These long lasting somatic Ca^{2+} elevations were triggered by GPCR activation leading to IP3 mediated Ca^{2+} release from the endoplasmic reticulum [276]. Furthermore, the synaptic control of astrocyte Ca^{2+} signals was demonstrated in various brain areas, such as the hippocampus [272] [43] [15]; cortex [282]; cerebellum [123] and retina [246]. A decade of experiments by different groups using a variety of methods in different brain areas made a convincing argument that immature rodent astrocytes reliably respond to neuronal transmitter release with long lasting (10s of seconds) somatic responses *ex vivo*.

The next step was to confirm whether astrocytes respond to neuronal activity under physiological conditions *in vivo*. Once again, this leap in experimental design was enabled by advancements in imaging and indicator labelling; namely two photon microscopy and the development of genetically encoded calcium indicators (GECIs). First, two-photon microscopy combined with bulk loading of calcium dyes pioneered the study of astrocyte signaling *in vivo*. The Nedergaard group [387] used two-photon microscopy in anesthetized adult-mice to monitor Ca^{2+} responses in S1, L2, Fluo-4 AM labelled astrocytes (bulk loaded with SR101 marker) to air-puff whisker stimulation. They found reliable somatic $[Ca^{2+}]_i$ responses in astrocytes following high frequency (5Hz) whisker stimulation. The amplitude of these slow Ca^{2+} responses (peak at $\approx$9s, with onset time $\approx$3s after whisker stimulus) were reduced with mGluR1 and mGluR5 antagonists, reinforcing the idea that astrocytes respond to glutamatergic signalling with $[Ca^{2+}]_i$ elevation. Similar results were observed by other groups. Hirase et al. [140], found that increased neuronal activity was associated with enhanced $[Ca^{2+}]_i$ elevation in Fluo-4 AM labelled astrocytes of the rat barrel cortex (layer I/II). Schummers et al. [325] found that ferret, visual cortex astrocytes loaded with OGB1 and SR101 respond to visual stimuli with spatial receptive fields tuned to feature orientation and spatial frequency similar to neurons. Together, these findings suggested that dye labelled astrocytes respond to neuronal stimuli with robust somatic $[Ca^{2+}]_i$ elevations in anesthetized animals.

1.4.2 Do astrocytes respond with transient elevation of $[Ca^{2+}]_i$ to neuronal activity?

Recent studies have shown weak or a lack of astrocyte responses to sensory stimulation of the somatosensory [93] [250] and visual cortex [274] [48] [18]. It was realized that general anesthetics, used in previous studies, strongly suppressed cortical astrocyte Ca^{2+} signals [359]. Interestingly, blocking synaptic activity (TTX, CNQX, AP5) in the cortex had minor effects on somatic Ca^{2+} signals of astrocytes labelled with the calcium indicator rhod-2 acetoxymethyl in awake animals [359]. It was also found that in awake mice, astrocytes (rhod-2 labelled) don't respond to glutamatergic signals triggered by sensory stimulation [93]. Instead they found that cortical astrocytes respond with widespread Ca^{2+} activity to noradrenergic signals from locus coeruleus (LC) projections by activating astrocytic α_1 adrenergic receptors [93]. The same observation was also made in visual cortex (V1) and cerebellar GCaMP3 labelled astrocytes of awake mice [274]. Interestingly, while V1 astrocytes rarely responded to light stimulation alone, pairing the light stimulus with noradrenaline (NA) release enhanced astrocyte Ca^{2+} responses to the light stimulus. These findings suggested that NA might shift the gain of astrocytes to local synaptic activity. Similarly Bonder & McCarthy [48] found changes in Ca^{2+} elevation in V1 astrocytes labelled with cyto-GCaMP3 and lck-GCaMP6f in response to startle responses (air puff) but not with visual stimulation. Also an extensive study using GECIs, glutamate indicators (iGluSnFR), pharmacogenetic and electrical modulation of neurotransmitter release in the hippocampal mossy fiber astrocytes found no evidence of astrocyte Ca^{2+} microdomain responses to neuronal activity or glutamate release [129]. Similarly, TTX had no effect on astrocyte calcium signals (CA1 of hippocampus and dorsolateral striatum) [67]. Interestingly, the reliability of astrocytic Ca^{2+} responses to electrical stimulation of input neurons increased only during high frequency stimulation in the hippocampus but not in the striatum [67]. In both regions astrocytes responded strongly to $\alpha 1$ adrenoreceptor agonists [67]. Together these reports questioned the role of sensory driven, neurotransmitter induced astrocyte Ca^{2+} stimulation and pointed to neuromodulators as the strong influencers of astrocyte activity. They also suggest possible heterogeneity of responses in different astrocytes that may also depend on the stimulation frequency.

At about the same time, doubt of earlier findings started accumulating. The expression of mGluR5, the Gq-coupled metabotropic receptor commonly thought to generate IP3 and Ca^{2+} release from the endoplasmic reticulum in response to neuronal activity, was found to decrease in mature astrocytes [59]. The mRNA expression of these receptors was undetectable 3 weeks postnatally and mGluR5 agonists didn't induce somatic $[Ca^{2+}]_i$ elevation in adult astrocytes [350]. However, mRNA level may not predict protein level and mGluR5 may be found in astrocyte processes instead of somata [195]. Also, EM studies cast doubt about whether there are calcium stores in thin astrocyte processes apposed to synapses [273]; although these results could have been confounded by fixation conditions. Together these findings questioned the mechanism by which $[Ca^{2+}]_i$ is raised. It was also becoming apparent that the speed of astrocyte $[Ca^{2+}]_i$ elevation was too slow to be involved in fast synaptic processing.

Astrocytes possess functionally independent subcellular compartments. Recent work identified short duration Ca^{2+} signals localized within fine astrocyte processes [123] [249] [332] [261] [92] [333] [334] [164] [18] [258] [341] [2] [47] [201] [344] [345]. Some of the earlier studies using patch mediated dye loading revealed Ca^{2+} transients localized along astrocyte processes in response to supramaximal (bergmann glia [123]) or minimal synaptic stimulation [261] (CA1 of hippocampus). Spontaneous transmitter release triggered brief, localized ($\approx$0.7s, $\approx$4μm) transients in astrocyte processes while action potentials triggered longer lasting, expanded ($\approx$ 3s, $\approx$12μm) events. However, patch loaded dyes dialyze and disturb astrocyte function [245] and they are difficult to load. Patch loading of Ca^{2+} indicators can alter cell physiology [296]. The high dye concentration often needed to study astrocyte microdomain signals [361] potentially buffers these signals. GECIs alleviate some of these challenges. Different strategies have been developed to express GECIs in astrocytes to visualize microdomain Ca^{2+} signals. Kanemaru et al. [164] used transgenic mice expressing the ratiometric Ca^{2+} indicator yellow Cameleon-Nano in astrocytes to reveal localized microdomain Ca^{2+} signalling. Interestingly they also showed that microdomain Ca^{2+} signals were not abolished in IP3R2 KO mice. The Ca^{2+} signals they detected were large ($\approx 10\mu$m) and slow ($\approx$40s to half peak). However, the duration might be an artifact of the indicator used rather than a good estimate of intrinsic Ca^{2+} dynamics. Asada et al. [18] used this ratiometric indicator in combination with 2 photon microscopy to investigate the effect of visual stimuli in V1 astrocyte Ca^{2+} microdomain signals. Visual stimuli didn't change the frequency of Ca^{2+} microdomain events. Instead the size of these events increased with visual stimuli and decreased with the application of TTX.

Single wavelength GECIs can be tethered to the astrocyte membrane (lck-GCaMP), allowing the investigation of near-membrane Ca^{2+} activity [332] [333] [334], [341] [345]. This is important because astrocyte responses to synaptic activity are expected to occur near the membrane and it helps avoid large, global cytoplasmic signals that could mask such responses. These membrane Ca^{2+} events were reduced (to 40%), but not abolished in IP3R2 KO mice. This was in contrast to somatic Ca^{2+} responses which were reduced by $\approx$90% in IP3R2 KO mice [341]. Removing extracellular Ca^{2+} reduced the frequency of Ca^{2+} events at the processes (by 50-75%) but not at the cell body. These findings suggest that the long duration signals observed in somata and thick astrocyte processes are mediated through Ca^{2+} release from internal calcium stores (i.e. ER) while the short duration events observed at astrocyte processes are largely, but not exclusively, mediated by transmembrane entry of Ca^{2+} (i.e. through TRPA1 channels) [333]. Mitochondria are also thought to induce microdomain calcium transients in astrocytes [2]. Astrocyte microdomain calcium transients were colocalized with the position of mitochondria. Microdomain Ca^{2+} transients were reduced with mitochondrial permeability transition pore (mPTP) inhibition (CsA and rotenone) and enhanced with mPTP opening (CAtr). These findings suggest that some astrocyte Ca^{2+} transients are mediated by mitochondria. Increasing neuronal activity with picrotoxin (GABA-A receptor antagonist) increased the number (by $\approx$50%) and frequency ($\approx$60%) of microdomain Ca^{2+} transients who were mediated by mPTP opening. These mitochondrial Ca^{2+} transients may be linked to local metabolic demand.

The idea that astrocytes respond with fast, micrometer scale Ca^{2+} transients to neuronal stimulation *in vivo* is still on the forefront of astrocyte research today. In a recent report, Stobart et al. [345] used a combination of GECIs to label barrel cortex (layer II/III) neurons (RCaMP1.07) and astrocytes (GCaMP6f) simultaneously using two photon excitation microscopy (2P) in awake mice. They revealed a subset ($\approx$8%) of microdomain Ca^{2+} signals that rapidly followed neuronal events ($\approx$120 ms delay) evoked by high frequency (90Hz, 8s) single whisker stimulation (Figure 1.10 B). These events were IP3R2 and neuromodulator (acetylcholine, noradrenaline and serotonin) activity independent. They were only found in preparations with membrane tagged GCaMP (lck-GCaMP6f). Furthermore, advances in 3D imaging used in combination with GECIs expressed in neurons and astrocytes of the adult mouse hippocampus (entorhinal cortex) during minimal or tetanic axon stimulation protocols revealed robust astrocyte microdomain ($\approx$60um^3) Ca^{2+} responses blocked by TTX (Figure 1.10 A)

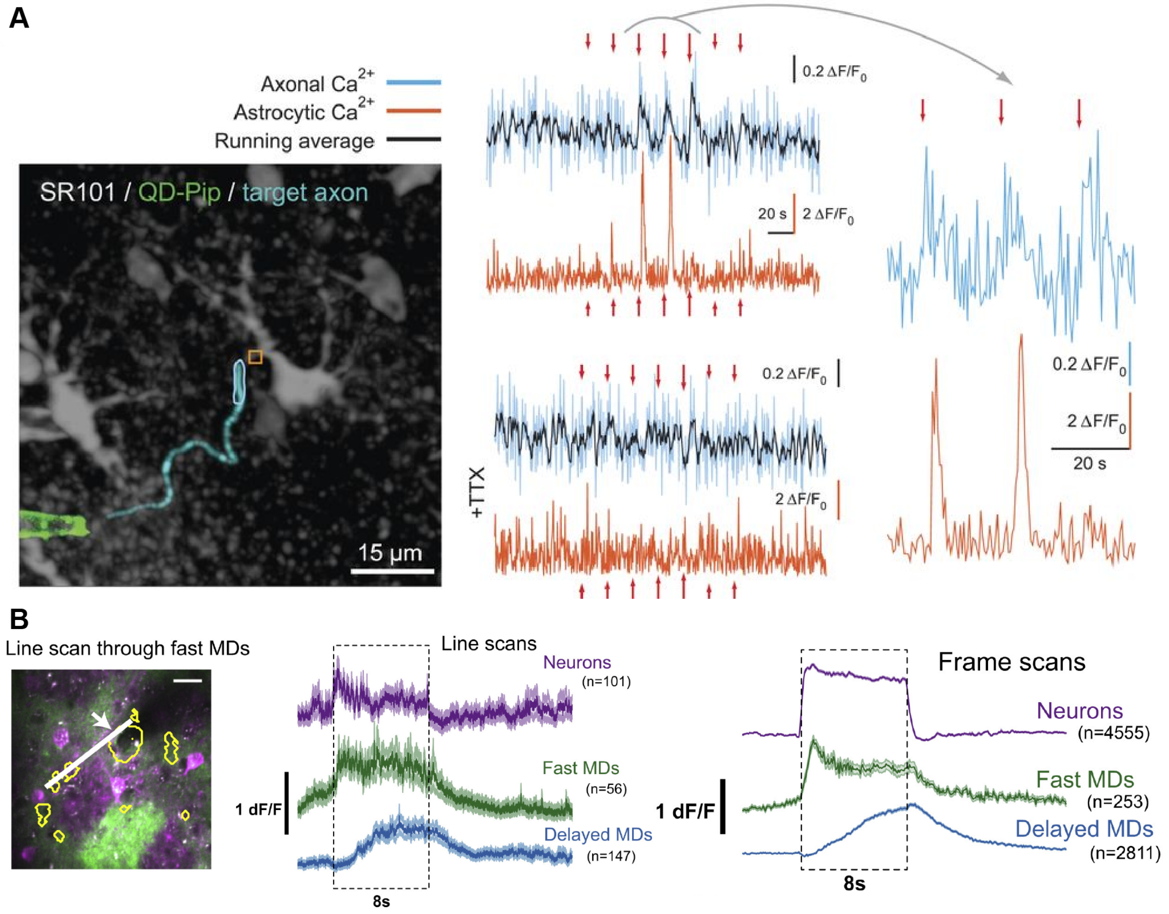

Figure 1.10: Astrocytes responding to neuronal stimulation with Ca^{2+} microdomain signals. A) Minimal stimulation of a jRCaMP6f labelled axon (cyan trace) within the vicinity of a GCaMP6f and SR101 labelled astrocyte with a quantum dot (QD)-coated pipette (green) leads to synchronized Ca^{2+} responses in axons and adjacent astrocytic microdomains in hippocampal slices that are abolished by TTX. Orange arrows represent the onset of stimuli. B) Similar observations were made *in vivo*, in L2/3 of the somatosensory cortex in response to long, high frequency whisker stimulation (90Hz, 8s). A subset of fast Ca^{2+} microdomains (MDs; yellow ROIs; green traces) in lck-GCaMP6f labelled astrocytes respond to whisker stimuli with a similar onset latency as neurons (purple) labelled with RCaMP, as indicated by representative traces during line scans (white arrow on image; middle traces) and frame scans (right traces). Panel A was taken from [47] and panel B images were selected from [345].

[47]. These modern studies support high responsiveness of astrocyte microdomains to neuronal activity. They argue that the reason for conflicting reports was methodological. For example, 2D studies may have missed actively responding regions to neuronal activity that could be resolved in 3D imaging studies or without the use of membrane bound GECIs. Interestingly, Ca^{2+} microdomain activity may be circuit specific. Optogenetic stimulation of paravalbumin or somatostatin expressing interneurons triggered different Ca^{2+} responses in astrocytes [215]. This suggests that astrocytes may respond distinctively to different neuronal populations. While the responsiveness of astrocyte microdomains to physiological neuronal activity and neurotransmitter release is still under debate, recent evidence *in vivo* support the idea that astrocytes respond to minimal neuronal stimulation with fast (timescale of neuronal calcium signals) and possibly circuit specific microdomain Ca^{2+} responses.

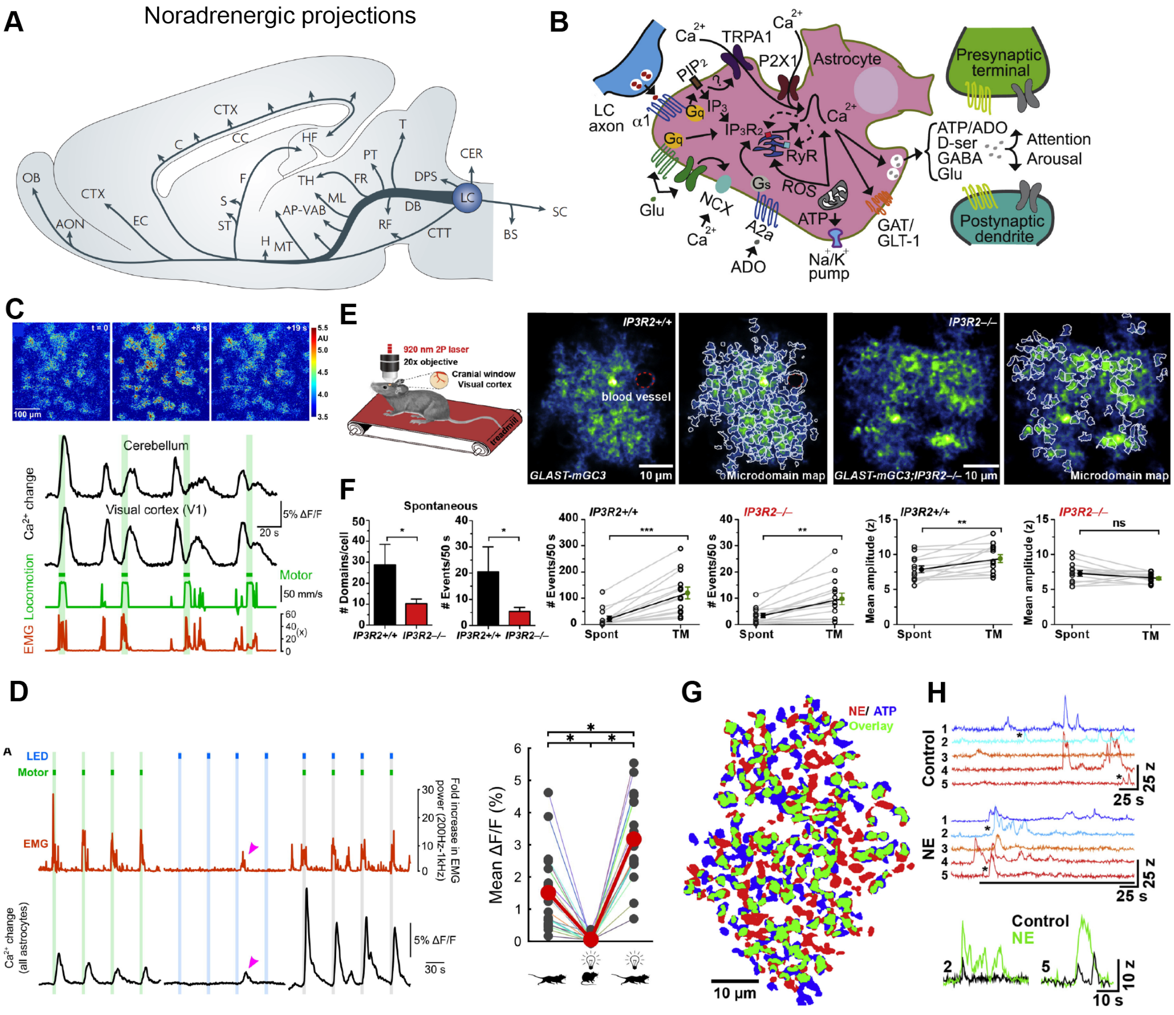

Figure 1.11: Neuromodulators modulate astrocyte Ca^{2+} signalling. (caption next page.)

Figure 1.11: (previous page.) A) The locus coeruleus (LC) sends noradrenergic projections to the whole brain (with the notable exception of the basal ganglia). B) Noradrenaline (NE or NA) can activate astrocytic α_1 receptors that trigger a G-coupled cascade leading to the release of Ca^{2+} from internal stores. Glutamate (Glu) may potentiate the release of Ca^{2+} triggered by noradrenaline through activation of G-coupled receptors or by slowing down the efflux of Ca^{2+} by Na^+/Ca^{2+} exchangers (NCX). Other plasma membrane channels such as TRPA1 and P2X1 and internal stores such as mitochondria might contribute as well. $[Ca^{2+}]_i$ elevation may then trigger the release of gliotransmitters (i.e. ATP, D-serine, GABA and glutamate) and other mechanisms involved that can modulate synaptic activity. C) Locomotion (green trace), associated with increased release of noradrenaline, evokes synchronized $[Ca^{2+}]_i$ elevation in astrocytes of different brain areas including the cerebellum and the visual cortex. D) Enforced locomotion (green or running mouse) in combination with visual stimuli (blue, LED, or light bulb) enhances Ca^{2+} responses in visual cortex astrocytes compared to when these stimuli are presented alone. Note that astrocytes do not respond to visual stimuli alone. E) Locomotion can also trigger Ca^{2+} microdomain signals in astrocytes labelled with membrane tagged GCaMP3 that are not dependent on IP3R2 dependent Ca^{2+} release from the endoplasmic reticulum. F) However, the number of spontaneous microdomains and the frequency of Ca^{2+} events decreases in IP3R2$^{-/-}$ mice. During treadmill rotation (TM), the frequency of event occurrence increased in IP3R2$^{+/+}$ and IP3R2$^{-/-}$ astrocytes but amplitude only increased in IP3R2$^{+/+}$ astrocytes. G) Astrocytes *ex vivo* display distinct Ca^{2+} microdomain patterns in space to after application of NE (red) and ATP (blue) suggesting different microdomains may be physiologically distinct. H) NE promotes synchronized increase in Ca^{2+} microdomains. Panel A was taken from [313]; B from [33]; D & D from [274] and E-H from [2].

1.4.3 Astrocytes respond reliably to neuromodulators

A less controversial idea is that astrocytes reliably respond to neuromodulators with global, long lasting calcium elevations. Noradrenergic neurons in the brainstem locus coeruleus project diffuse axon collaterals throughout the brain, providing a way to exert control of global, brain states through volume transmission (Figure 1.11 A)[313]. Electric stimulation of the LC triggers broad $[Ca^{2+}]_i$ elevation in mouse cortical astrocytes *in vivo* [34]. Aversive stimuli (startle stimuli) and locomotion can induce widespread $[Ca^{2+}]$ elevation in cortical astrocytes (Figure 1.11 C) mediated through α_1 adrenergic receptors [93] [274]. The global release of noradrenaline is thought to increase the gain of astrocytes to local release of synaptic transmitters [274]. Locomotion in combination with visual stimuli synergistically enhances Ca^{2+} response in V1 astrocyte networks (Figure 1.11 D) [274] [337]. Noradrenaline increases the number, size, duration and synchronicity of Ca^{2+} microdomains in single astrocytes (Figure 1.11 E-H) [2]. Noradrenaline is not the only neuromodulator involved in astrocyte Ca^{2+} signalling. Electrical stimulation of nucleus basalis of Maynert (NBM) and medial septum, the predominant sources of cholinergic afferents to the cortex and hippocampus, led to muscarinic receptor (mAChR) dependent $[Ca^{2+}]$ elevation in astrocyte networks of the cortex [356] [69] and hippocampus [243]. Dopamine [368] [154] [404] and serotonin

[320] are also likely implicated in astrocyte Ca^{2+} signalling. Interestingly, ventral midbrain astrocytes respond to dopamine D2 modulation but not to noradrenaline [404] suggesting heterogeneneous sensitivity of different astrocytes to the same neuromodulator. Further work is needed to elucidate the synergistic role of neuromodulators and neurotransmitters acting on astrocytes.

1.4.4 Perspective

A vast number of experiments conducted by different groups using a variety of methods demonstrate that astrocytes respond to neurotransmitters and neuromodulators with $[Ca^{2+}]_i$ elevation. Synthesis of the evidence suggests that astrocytes in *ex vivo* preparations can respond to synaptic neurotransmitter release with $[Ca^{2+}]_i$ elevation. Whether this is the case *in vivo* and under what conditions is still controversial. Astrocyte responses to synaptic neurotransmitter release are likely to occur in the thin processes in the form of fast microdomain Ca^{2+} transients instead of long lasting somatic events. On the contrary, neuromodulators, especially noradrenaline seem to trigger widespread, synchronous Ca^{2+} elevation in astrocyte networks that may increase the gain of astrocytes to sensory stimuli.

It is becoming increasingly clear that the condition of the experimental preparation used is very important to correctly assess astrocytic responses to neuronal activity. We thus summarize the important parameter that an experimenter needs to pay attention to, for studying neuron - astrocyte interactions: 1) Use high quality *in vivo* preparations in awake animals when possible to minimize pathological conditions. 2) Use adult animals to account for age dependent changes in receptor expression 3) Take into account the fast $[Ca^{2+}]_i$ microdomain activity at the fine astrocyte processes, not just the slow $[Ca^{2+}]_i$ activity of the soma. 4) Avoid loading astrocytes with Ca^{2+} dyes or overexpressing GECIs to avoid cell damage, dyalisis and excessive Ca^{2+} buffering 5) Limit the use of non-physiological perturbations as much as possible. For example, use sensory instead of electrical stimuli. 6) Account for possible astrocyte heterogeneity.

1.5 Astrocyte modulation of neuronal activity

Astrocyte Ca^{2+} signalling is important because it is thought to act as a second messenger who can trigger molecular cascades that in turn can modulate neuronal activity and vascular tone. Shortly after the discovery of astrocyte calcium waves in response to neurotransmitters [79], two seminal studies showed independently that $[Ca^{2+}]_i$ increase in cultured astrocytes can evoke $[Ca^{2+}]_i$ elevation in adjacent neurons [267] [244]. Experiments in slices and cultures then showed that astrocytes release glutamate when their $[Ca^{2+}]$ was elevated [267] [272] [43]. These experiments suggested that astrocytes could provide an additional layer in information processing in the brain mediated by astrocytes. An expanded repertoire of signalling molecules released by astrocytes were identified including glutamate, ATP, GABA, and D-serine [16]. These molecules were termed gliotransmitters. The anatomical and functional interaction between astrocytes and neurons was consolidated into the 'tripartite synapse' [14]. Gliotransmission is one of the most exciting and controversial topics in the field at the moment [111] [314].

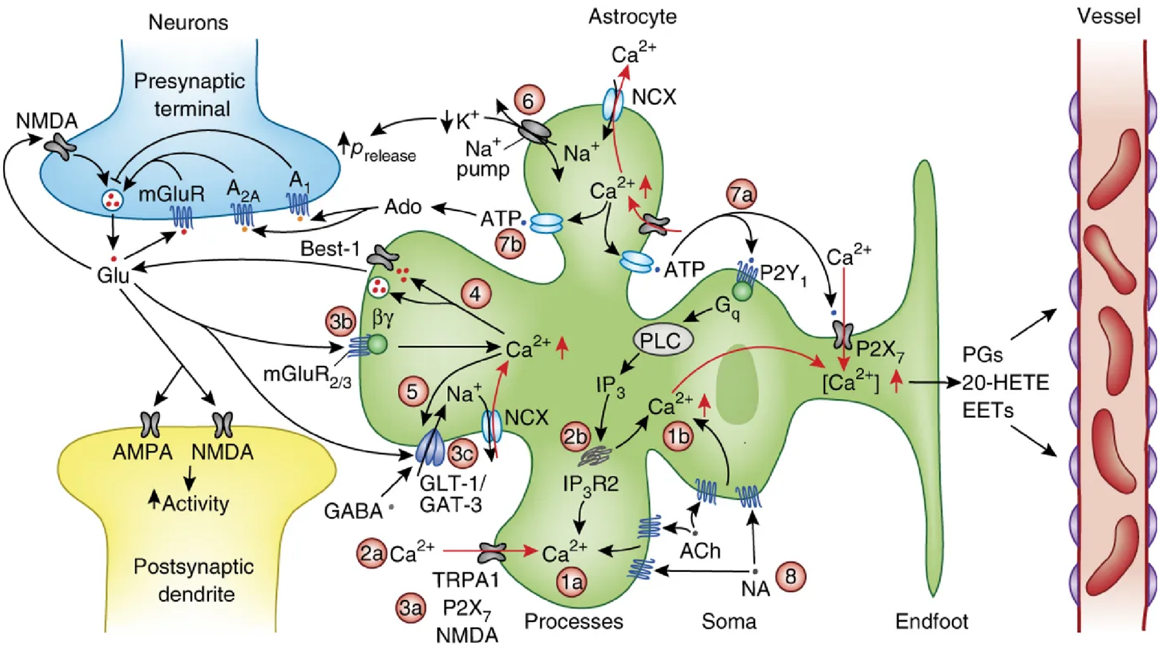
Neurons
Astrocyte
Vessel
Presynaptic terminal
NMDA
mGluR
A2A
A1
Glu
↑p release
↓K+
6
Na+ pump
Na+
Ca2+
NCX
Ca2+
Ado
ATP
7b
7a
Best-1
4
ATP
P2Y1
Ca2+
Gq
PLC
3b
βγ
Ca2+
mGluR2/3
5
Na+
NCX
3c
IP3
Ca2+
2b
1b
P2X7
[Ca2+]
PGs
20-HETE
EETs
AMPA
NMDA
Activity
Postsynaptic dendrite
GABA
GLT-1/
GAT-3
IP3R2
2a
Ca2+
TRPA1
Ca2+
1a
ACh
NA
8
3a
P2X7
NMDA
Processes
Soma
Endfoot

Figure 1.12: Current model of bidirectional communication between astrocytes and neurons. Fast, localized Ca^{2+} signals in astrocytic processes (1a) can be evoked through Ca^{2+} entry from the extracellular space (2a) by the opening of (3a) TRPA1 or neurotransmitter gated channels ,(2b) by release from organelles, (3b) activation of $mGluR_{2/3}$ receptors, or (3c) by reversal of Na^+/Ca^{2+} exchangers (NCX). Subsequently, Ca^{2+} signals may influence neuronal activity by modulating the release of gliotransmitters through (4) ion channels (i.e. Best-1) and exocytosis, (5) altering the expression and mobilization of neurotransmitter transporters, and (6) lowering of extracellular K^+ indirectly through the action of NCX and Na^+ pumps. (7) ATP released from astrocytes may (7a) bind to P2X and P2Y receptors of the same astrocytes triggering widespread Ca^{2+} activity or (7b) is converted to adenosine that can act on presynaptic A_{2A} or A_1 receptors that can increase or decrease neurotransmitter release respectively. (8) Noradrenaline (NA) and acetylcholine (ACh) induce large, synchronous $[Ca^{2+}]_i$ elevation in astrocytes. Image taken from [32].

1.5.1 Mechanisms of gliotransmitter release

The mechanisms of gliotransmitter release can be summarized in two groups, vesicular exocytosis and non-vesicular release. Non vesicular release of glutamate, ATP and D-serine can occur by reversal of excitatory amino-acid transporters (EAATs), volume regulated anion channels (VRACs), gap junction hemichannels (connexins and pannexins) and ATP gated $P2X_7$ receptors. These gliotransmitter can also be released through $P2X_7$ and VRACs in a Ca^{2+} dependent manner when astrocytes swell (i.e. through $[Ca^{2+}]_i$ elevation via ATP acting of P2Y and $P2X_7$ receptors) [126]. Also glutamate and GABA can be released through Ca^{2+} activated bestrophin-1 and TREK channels [264] [198] [398] [409].

For vesicular exocytosis, astrocytes need to have mechanisms for storing gliotransmitters in vesicles and the machinery to promote vesicle fusion to the plasma membrane. Electron microscopy (EM) revealed 30-100 nm vesicles in hippocampal astrocytes resembling those of synapses [45]. Immunostaining suggested that vesicles express vesicular glutamate transporters (VGlut 1-3) [45] [126] and thus can accumulate glutamate. Although astrocytes were shown to lack structurally organized release sites [45] [160], some of the molecular machinery involved in neuronal synaptic transmission was also found in cultured astrocytes (i.e. synaptobrevin II, cellubrevin, syntaxin and SNAP 23) [268] [135]. This suggested that astrocyte vesicles may form SNARE complexes in-situ, similar to neurons. Following SNARE complex formation, a calcium sensor is needed for exocytosis to initiate. Astrocytes express synaptotagmin 4, 7, and 11 [231] [412] [377], thought to trigger vesicular glutamate release in response to $[Ca^{2+}]_i$ elevation.

1.5.2 Modulation of gliotransmitter release

Multiple methods have been used to evoke or inhibit Ca^{2+} dependent gliotransmitter release. Increasing $[Ca^{2+}]_i$ in astrocytes via agonist (i.e. DHPG) activation of metabotropic glutamate receptors (mGluRs) [108] [11], mechanical stimulation [186], uncaging of Ca^{2+} or IP3 within astrocytes [108] [110] [277] or using strong depolarizing pulses [160] [165] modulated neuronal activity. These manipulations provide indirect evidence for gliotransmission acting on neuronal circuits. Stronger evidence for gliotransmitter release was provided by perturbations of the gliotransmitter release machinery. Gliotransmitter release can be inhibited by buffering intracellular calcium (i.e. using BAPTA) [13] [165] [160] [44] or enhanced by bypassing the Ca^{2+} dependent step of exocytosis using a-latrotoxin [269]. Gliotransmitter release can be inhibited by disturbing the SNARE complex in astrocytes using Botulinum and Tetanus Neurotoxins (BoNT and TeNT) to cleave SNARE complex [160] [277] or by inhibiting the formation of the SNARE complex in transgenic mice expressing dominant-negative domain of vesicular SNARE (dnSNARE) in astrocytes [413] [270]. Other, crude methods to inhibit gliotransmission include the inhibition of the tricarboxylic acid (TCA) cycle with fluorocitrine or fluoroacetate [10] [411]. Supplementary evidence in cultured astrocytes using total internal reflection fluorescence microscopy (TIRF) to track labelled vesicles during exocytosis [262] [51] [45], capacitance measurements to assess changes in membrane area during exocytosis [413], amperometric detection of dopamine loaded in vesicles carrying glutamate [71] and the use of sniffer cells expressing ATP or glutamate receptors [262] [45] revealed both kiss-and-run and full-fusion exocytosis leading to quantal-like release of transmitters. Together, these findings provide strong evidence of gliotransmitter release, at least in culture astrocytes.

1.5.3 Role of astrocyte $[Ca^{2+}]_i$ elevation and gliotransmission in neuronal circuits

Astrocyte $[Ca^{2+}]_i$ elevation is thought to trigger the release of gliotransmitters such as glutamate, GABA, ATP and D-serine (Figure 1.13) that in turn bind to neuronal receptors and modulate their activity. Some notable functions of glutamate released by astrocytes include: a) evoke slow inward currents and thus increase neuronal excitability and synchrony of postsynaptic neurons by acting on NMDARs [108] [11] b) increase neurotransmitter release from presynaptic terminals by acting on extrasynaptic NMDARs [13] [160] or mGluRs [110] [277] , c) heterosynaptic depression and d) modulation of LTP [243] and LTD [127]. GABA released from astrocytes is thought to mediate postsynaptic slow outward currents [196] and tonic inhibition [198]. ATP is converted to adenosine in the extracellular space and acts on presynaptic A1 receptors to inhibit transmitter release [270] [329]. D-serine binds to the glycine side of NMDA receptors acting as a co-agonist to glutamate. It is involved in the modulation of LTP and LTD [407] [133] [356]. For an extensive review see [16].

Astrocytes embedded in the same circuit can release multiple gliotransmitters that can exert diverse modulatory effects on neuronal circuits. For example, CA1 astrocytes can release glutamate [165] [108], GABA [196], D-serine [133] and ATP [411] that in turn can have different effects on neuronal signalling. It is likely that individual astrocytes can release multiple gliotransmitters. For example, astrocytes express synaptobrevin II and cellubrevin on distinct vesicle populations. Synaptobrevin II was associated with the release of glutamate and the enhancement of synaptic signalling. Cellubrevin was associated with neuropeptide Y secretion and tonic inhibition of basal synaptic transmission [327]. Interestingly, in single hippocampal astrocytes, short or low frequency stimulation triggers the release of glutamate while prolonged or high frequency stimulation also triggers the release of ATP [81]. These findings suggest that different gliotransmitters can be released from the same astrocyte depending on the nature of neuronal input that in turn can differentially modulate neuronal circuits.

There is also evidence that astrocyte-neuron networks are circuit specific (Figure 1.14). Striatal and hippocampal astrocytes have different Ca^{2+} responses to $G_{i/o}$ GPCR agonists [67], while cortical astrocytes show differential Ca^{2+} responses to optogenetic activation of PV and somatostatin expressing interneurons [215]. Optogenetic activation of visual cortex astrocytes results in differential modulation of PV^+ and SST^+ interneuron activity (Figure 1.14 B) [278]. Ventral midbrain astrocytes respond to dopamine D2 modulation but not to noradrenaline [404]. Subpopulations of dorsal striatum astrocytes selectively respond to one type of medium spiny neuron type but not the other and can release glutamate that acts on NMDARs in homotypic but not heterotypic medium spiny neurons (Figure 1.14 A) [216]. Medial central amygdala astrocytes release ATP in response to endocannabinoid signals to depress basolateral

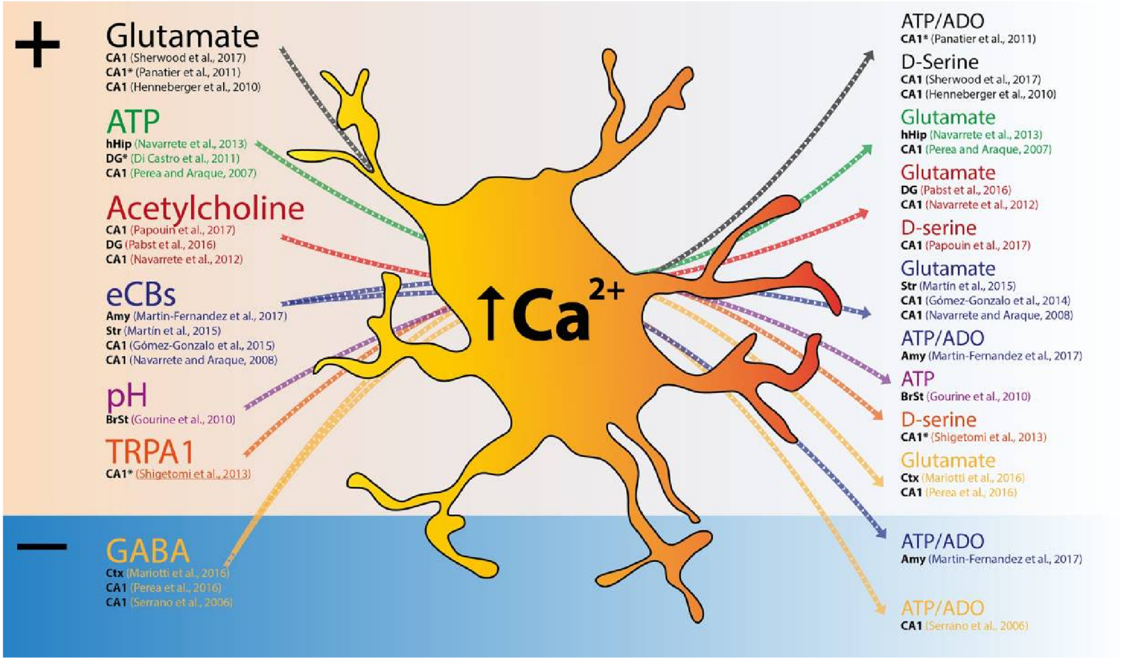
+
Glutamate
CA1 (Sherwood et al., 2017)
CA1* (Panatier et al., 2011)
CA1 (Henneberger et al., 2010)
ATP
hHip (Navarrete et al., 2013)
DG* (Di Castro et al., 2011)
CA1 (Perea and Araque, 2007)
Acetylcholine
CA1 (Papouin et al., 2017)
DG (Pabst et al., 2016)
CA1 (Navarrete et al., 2012)
eCBs
Amy (Martin-Fernandez et al., 2017)
Str (Martín et al., 2015)
CA1 (Gómez-Gonzalo et al., 2015)
CA1 (Navarrete and Araque, 2008)
pH
BrSt (Gourine et al., 2010)
TRPA1
CA1* (Shigetomi et al., 2013)
−
GABA
Ctx (Mariotti et al., 2016)
CA1 (Perea et al., 2016)
CA1 (Serrano et al., 2006)
↑Ca2+
ATP/ADO
CA1* (Panatier et al., 2011)
D-Serine
CA1 (Sherwood et al., 2017)
CA1 (Henneberger et al., 2010)
Glutamate
hHip (Navarrete et al., 2013)
CA1 (Perea and Araque, 2007)
Glutamate
DG (Pabst et al., 2016)
CA1 (Navarrete et al., 2012)
D-serine
CA1 (Papouin et al., 2017)
Glutamate
Str (Martín et al., 2015)
CA1 (Gómez-Gonzalo et al., 2014)
CA1 (Navarrete and Araque, 2008)
ATP/ADO
Amy (Martin-Fernandez et al., 2017)
ATP
BrSt (Gourine et al., 2010)
D-serine
CA1* (Shigetomi et al., 2013)
Glutamate
Ctx (Mariotti et al., 2016)
CA1 (Perea et al., 2016)
ATP/ADO
Amy (Martin-Fernandez et al., 2017)
ATP/ADO
CA1 (Serrano et al., 2006)

Figure 1.13: Functions of astrocyte Ca^{2+} elevation. A diverse array of excitatory (+) and inhibitory (-) signalling molecules can evoke $[Ca^{2+}]_i$ elevation (left) in astrocytes that precedes the release of different gliotransmitters (right) who may exert excitatory or inhibitory effects in contacting neurons. Abbreviations correspond to regions studied: Amy (Amygdala); BrSt (brainstem); CA1 (CA1 region of the hippocampus); Ctx (cortex); DG (dentate gyrus); hHip (human hippocampus); Str (Striatum). The symbol indicates studies describing functional changes to focal $[Ca^{2+}]_i$, instead of global Ca^{2+} signals. Image taken from [124].

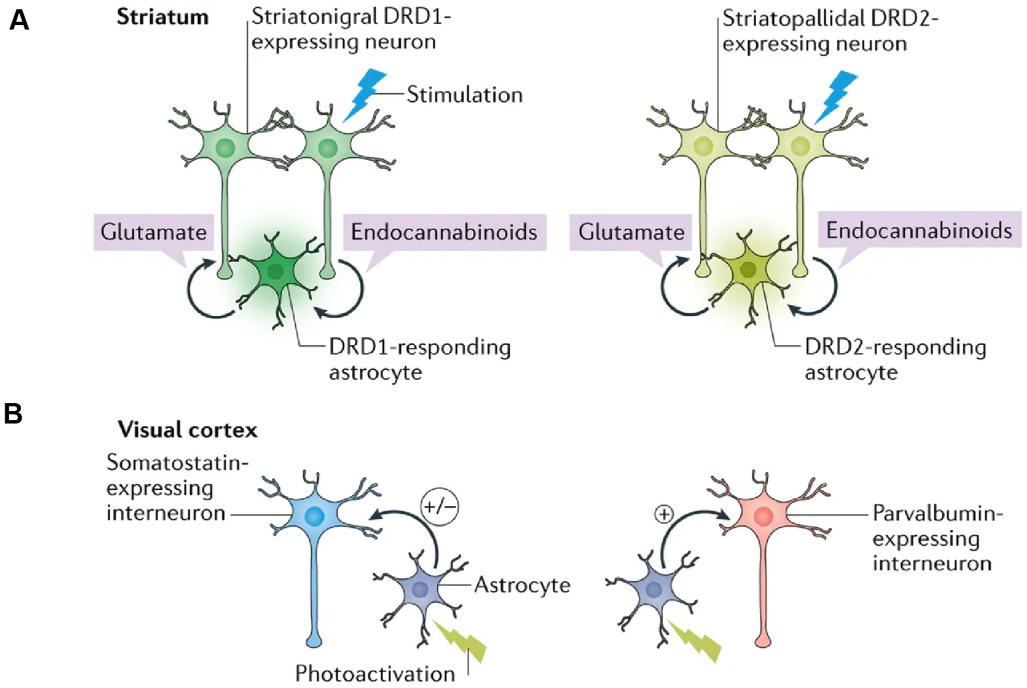
A
Striatum
Striatonigral DRD1-expressing neuron
Stimulation
Glutamate
Endocannabinoids
DRD1-responding astrocyte
Striatopallidal DRD2-expressing neuron
Glutamate
Endocannabinoids
DRD2-responding astrocyte
B
Visual cortex
Somatostatin-expressing interneuron
+/−
Astrocyte
Photoactivation
+
Parvalbumin-expressing interneuron

Figure 1.14: Heterogeneity in astrocyte - neuron interactions. Astrocytes can discriminate between different subtypes of neurons in a brain region and differentially modulate their activity. For example, A) striatal astrocytes, selectively respond to either neurons expressing D1 or D2 dopamine receptors. Stimulation of these neurons evokes the release of endocannabinoids that activate specific astrocyte subpopulations. Astrocytes then selectively modulate synaptic activity only in neurons expressing the same dopamine receptor by releasing glutamate. B) Photoactivation of visual cortex astrocytes increases the spontaneous firing rate of parvalbumin (PV) expressing interneurons while increasing or decreasing the activity of somatostatin (SST) expressing interneurons. Image taken from [125].

amygdala excitatory synapses (A1 activation) and enhance lateral subdivision of central amygdala inhibitory synapses (A_{2A} activation) [217]. These findings suggest that astrocytes respond to neuronal activity with $[Ca^{2+}]_i$ elevation in a circuit specific manner that in turn can modulate distinct neuronal circuits.

In summary, modern findings suggest that astrocyte Ca^{2+} activity and gliotransmitter release depends on the brain area and neuronal circuit they are embedded in, as well as the regime of neuronal activity. A variety of gliotransmitters can be released even by individual astrocytes under different conditions who can target distinct neuronal receptors, leading to specific modulation of synaptic transmission and neuronal circuits.

1.5.4 Controversies

The idea that neuronal activity triggers $[Ca^{2+}]_i$ dependent release of gliotransmitters by astrocytes to modulate neuronal circuits provides a paradigm shift in our thinking on how the brain works. However, there are a lot of controversies challenging the physiological nature and selectivity of methods used to reach such conclusions.

Assessing the role of gliotransmission requires methods that target astrocytes specifically. The challenge is that neurons possess the same receptors as astrocytes. Drugs assumed to evoke $[Ca^{2+}]$ elevation selectively in astrocytes (i.e. DHPG activation of mGluR1 [108] [11]) also affected other cells. To date there are no drugs I am aware of that selectively target astrocytes. Evoking $[Ca^{2+}]_i$ elevation in astrocytes by Ca^{2+} or IP3 uncaging may activate Ca^{2+} gated K^+ channels and the release of K^+ in the extracellular fluid that can depolarize neurons. Blocking gliotransmitter release by sequestering Ca^{2+} (i.e. using BAPTA) dilutes basal calcium levels and perhaps other signalling molecules, while also inhibiting extracellular $[K^+]$ increase through Ca^{2+} gated K^+ channels. Using TeNT, BoNT or dnSNARE mice to block gliotransmitter exocytosis may block the insertion of proteins mediating Ca^{2+} dependent non-exocytotic release of transmitters [126].

mGluR5, suggested to trigger IP3 mediated $[Ca^{2+}]$ elevation and gliotransmitter release are also expressed in neurons and are downregulated in mature astrocytes [59] [350]. Additionally, mGluR5 agonists did not evoke $[Ca^{2+}]$ elevation in mature astrocytes [350] thus suggesting that the machinery thought to trigger transmitter release from astrocytes was absent in adult animals. However, mGluR5 may be found in astrocyte processes [195] [260] and mRNA expression doesn't necessarily predict protein levels. These observations suggest that findings based on studies in immature astrocytes do not necessarily generalize to adult astrocytes.

Knocking down IP3R2 greatly reduced somatic $[Ca^{2+}]$ responses in astrocytes but had no effect on neuronal synaptic activity [286] and had no identifiable effect on animal behaviour evaluated by an extensive battery of behavioural assays [286]. Furthermore, evoking $[Ca^{2+}]_i$ elevation with CNO in astrocytes expressing non-mammalian Gq-coupled, designer receptors exclusively activated by designer drug (DREADD) had no effect on excitatory synaptic activity or neurovascular coupling [112] [48]. These findings suggest that the mechanism of Ca^{2+} elevation is crucial for gliotransmission.

A major innovation in suppressing vesicular release of gliotransmitters *in vivo* was the generation of transgenic mice expressing dnSNARE in astrocytes [413] [270]. However, Fujita et al. [115] found expression of the transgene also in neurons suggesting that the effects attributed to gliotransmitter release could be reinterpreted to be neuronal in origin. Although the topic is still debated and new evidence suggests astrocyte specific expression of dnSNARE [348] [263], the controversy emphasizes the importance of checking transgenic lines for specificity and “leaky” expression.

Interestingly, there is also doubt if there are vesicles associated with gliotransmitter release in astrocytes at all. In a recent study [67] found vesicles in 139 hippocampal and 138 striatal synapses but not in astrocyte processes. Furthermore, they found no significant RNA expression for Ca^{2+} sensitive synaptotagmins or VGluTs in hippocampal and striatal astrocytes suggesting that astrocytes do not have the components necessary for vesicular gliotransmission of glutamate.

Another common controversy is whether D-serine is a gliotransmitter. D-serine synthesis requires the conversion of l-serine into d-serine by serine racemase (SR). The development of SR KO mice [232][37] and other recent studies [397] suggest that it is neurons who synthesized and release D-serine, not astrocytes. The advancement of technology combined with a critical and open mind should clarify whether astrocytes release gliotransmitters or not.

1.6 Methods for investigating astrocyte calcium signals

As we have seen in the previous sections the conditions and methods used to study astrocyte physiology enabled both the greatest discoveries in the field but also fueled most controversies. Any measurement is prone to the observer effect where even mere observation of a phenomenon can disturb the system. Optimal method design relies on disturbing a system just enough to enable measurement of the query of interest without further, unnecessary disturbance. Too much disturbance to biological systems is commonly referred to as pathology or non-physiological conditions. There is no clear definition of what constitutes a physiological preparation or a pathological one, however it should be viewed as a grating. There is no such thing as a fully physiological preparation, but only better approximations of it. Therefore, we try to develop and use the best tools available in optimal configurations to minimize the disturbance to the system and maximize confidence in our measurements.

1.6.1 General principles for optical measurements of Ca^{2+} signals

Here we will focus mostly on how to measure astrocyte $[Ca^{2+}]_i$ dynamics. The general principle involves calcium binding to indicators, such as fluorescent proteins or organic Ca^{2+} indicator dyes, that causes a state transition in said compounds (i.e. conformational change and increase in quantum yield) that can be detected using a fluorescent microscope. The information collected is in the form of photons. The more photons captured the higher signal to noise ratio (SNR) can be achieved for a given signal. Theoretically, we can collect infinite photons by imaging a sample for infinite time.

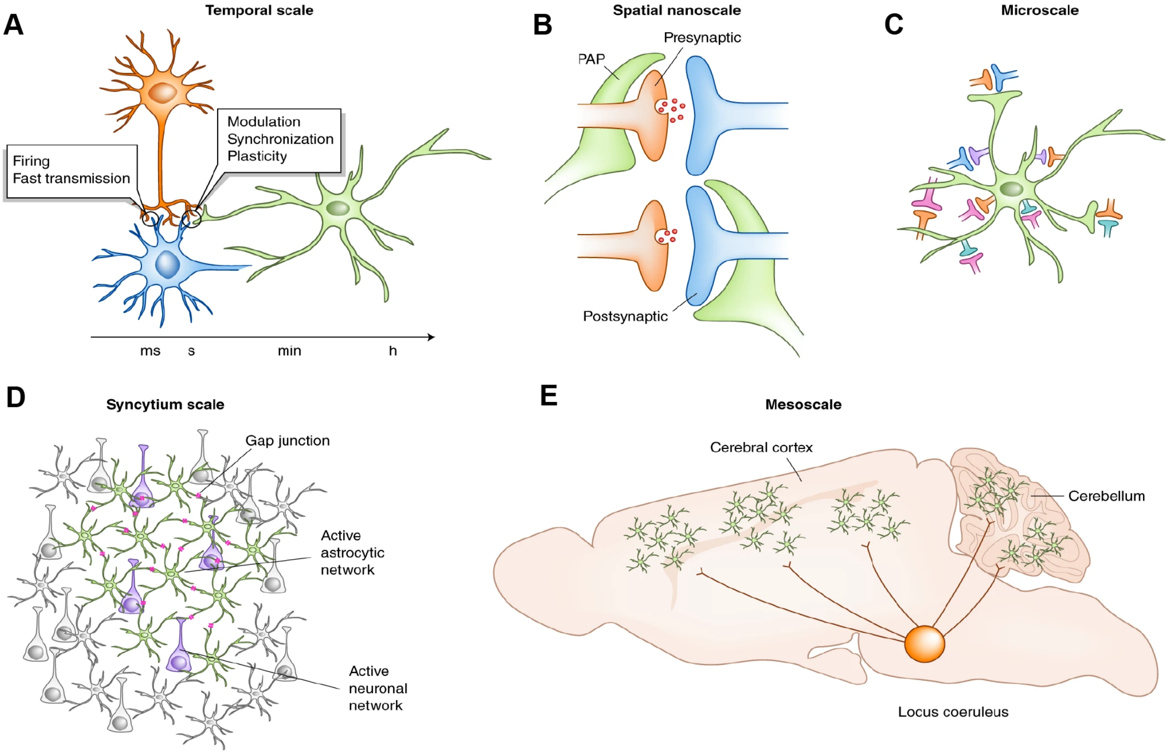
A
Temporal scale
Firing
Fast transmission
Modulation
Synchronization
Plasticity
ms
s
min
h
B
Spatial nanoscale
PAP
Presynaptic
Postsynaptic
C
Microscale
D
Syncytium scale
Gap junction
Active astrocytic network
Active neuronal network
E
Mesoscale
Cerebral cortex
Cerebellum
Locus coeruleus

Figure 1.15: Multiscale spatiotemporal relationship between astrocytes and neurons. Schematic of current perspective on the role of astrocytes at multiple scales. A) Astrocyte - neuron interactions are thought to occur at temporal scales ranging from seconds from minutes, influencing fast (millisecond timescale) synaptic output by tuning the gain of synapses and promoting the synchronization of networks. B) At the spatial nanoscale, perisynaptic astrocytic processes (PAPs) can modulate presynaptic by changing the probability of transmitter release or alter the excitability of postsynaptic terminals. C) At the spatial microscale, astrocytes can modulate multiple synapses within its territory or within the spatial extent of functional microdomains. D) At the syncytium scale, astrocyte networks connected via gap junctions can form dynamic multi-astrocyte domains that can respond to and modulate local neuron network activity. E) At the mesoscale, astrocytes co-ordinated by neuromodulators, such as noradrenaline released from the locus coeruleus, may influence brain states, complex behaviours and cognition. Image taken from [312].

Besides the technical limitations of such a feat, the study of dynamic processes is limited by time. The faster the dynamics of interest the less time is available for collecting photons. Similarly, the longer Ca^{2+} is bound to the indicator the more photons it can emit. However, during binding, Ca^{2+} is buffered and becomes unavailable for cellular processes. Also, longer binding of Ca^{2+} limits the temporal resolution of dynamics that can be investigated. Another way to increase the number of photons collected is the availability of higher concentration of indicators. However, the higher the concentration, more Ca^{2+} is buffered, increasing disturbance to cell physiology. The number of photons collected can also be increased using improved fluorescent indicators or by increasing the power of excitation light. The latter is limited by potential phototoxicity induced damage to the tissue. Alternatively, SNR can be improved by reducing unwanted photons collected (noise). Effective experimental design is an optimization problem taking into account all these variables and the condition of the sample. I will introduce commonly used methods for probing astrocyte Ca^{2+} physiology, with emphasis on the tools used in my study.

1.6.2 Organic Ca^{2+} indicator dyes

Organic Ca^{2+} indicators spearheaded the discovery and early work of astrocyte Ca^{2+} signalling. They are typically available in the form of water soluble, membrane impermeable salts (often dextran conjugated to minimise compartmentalization) or more hydrophobic, membrane permeable acetoxymethyl (AM) esters. Membrane-permeable dyes are typically bulk loaded into tissue to label a large population of cells while cell-impermeable water soluble dyes are typically loaded inside single cells with a patch pipette. Cell permeable dyes (i.e. Fluo4-AM and Oregon Green BAPTA1-AM) can be easily bulk loaded into tissue to label a large population of cells. However, the labelling is not selective to astrocytes thus requiring co-labelling with a cell specific marker, such as sulforhodamine 101 (SR101) dye [248]. However, SR101 should be used with caution since its specificity to astrocytes is questionable [149], it increases neuronal excitability and LTP [166] [149] and can lead to seizures [297]. Furthermore, these bulk loaded dyes are limited to labelling astrocytic somatata and thick processes, excluding their fine distal processes thought to be involved in the tripartite synapse [299]. Hydrophilic dyes can be loaded into single astrocytes (i.e. using a patch pipette), thus avoiding the need of markers such as SR101. They also offer a number of advantages, including precise control over the concentration of dye loaded. While they allow more precise imaging of astrocyte branchlets they still ignore fine distal processes [92] [260]. At the concentration needed to resolve astrocyte Ca^{2+} microdomain activity (up to 0.5mM) they can disturb calcium signalling, dialyze the cell and possibly alter cell physiology [174]. Also, dyes are not ideal for chronic experiments because they wash out over time and need to be reapplied.

1.6.3 Genetically encoded calcium indicators (GECI)

GECIs provide a less invasive way of studying astrocyte Ca^{2+} activity *in vivo* and *in vitro* and can be expressed in many cells without dialyzing them. GECIs are fluorescent proteins derived from GFP or its variant circularly permuted fluorescent proteins, fused with calmodulin and the M13 domain of the myosin light kinase (see figure 2). Calmodulin binds to 4 Ca^{2+} ions undergoing a conformational change binding to M13 (Figure 1.16 C). This leads to rapid de-protonation of the chromophore and bright fluorescence [386]. GECI genes driven by cell type specific promoters (i.e. GFAP or Aldh1l1 for astrocytes) can be selectively expressed in cell types of interest. Low GECI expression leads to low SNR while high expression increases SNR and baseline brightness, but can disturb calcium homeostasis, reduce the signal change and affect cell physiology [360]. Genetic manipulation of cells is usually achieved through viral vector delivery or the generation of transgenic mice. GECI expression can be stable for months [410] thus allowing chronic imaging of astrocytes *in vivo*. The most optimized GECI is the GCaMP scaffold originally engineered by [242]. Variants of increasing sensitivity have since then been developed [70] and used to study astrocytes, GCaMP2 [144], GCaMP3 [361], and GCaMP6 [341]. Additionally, GECIs can be engineered to target subcellular compartments such as the plasma membrane by adding the Lck membrane tethering domain [332] or other organelles [360]. New GECIs are continuously being generated that have improved signal to noise ratio, varied spectral properties and different Ca^{2+} binding affinities promising a bright future for imaging astrocytes labeled with GECIs. Their capacity to target specifically astrocytes, low photobleaching, high SNR, and the capacity to let us non- invasively image Ca^{2+} activity from the thin processes of astrocytes makes them indispensable tools.

1.6.4 Fluorescent microscopy: focus on two photon microscopy

The simplest objective of fluorescent microscopy is to excite fluorophores in a region of interest and collect the emitted photons. When possible, living samples should be studied in their natural habitat to better preserve their physiological characteristics. Biological tissues, such as the brain, are composed of materials with different refractive indices, causing scattering of photons. Scattering leads to the degradation of resolution and contrast. Scattering increases exponentially with the imaging depth [91] [132]. Confocal microscopy partially overcomes some of these issues by introducing a detector pinhole that rejects out of focus photons [78]. However, out of focus excitation is unavoidable and can lead to photodamage. Photodamage refers to the combined effects of photodestruction of the fluorophore (photobleaching) and photodynamic damage of the entire sample mostly mediated by reactive oxygen species (photodamage). Also, the pinhole excludes scattered signal photons emanating from the focus. At increasing imaging depth, photons wasted because of the pinhole and scattering make confocal microscopy prohibitively inefficient for deep tissue imaging [351].

Multiphoton microscopy alleviates a lot of the problems introduced by imaging deep in high scattering tissues. In 2P microscopy, two low energy (infrared) photons are simultaneously (within < 1fs) absorbed by the fluorophore (Figure 1.16 A, top). To deliver the photon flux needed to induce two photon excitation, focused femtosecond pulses ($\approx$150fs) are used. The absorption rate is proportional to the second power of light intensity. The intensity is highest at the focal point, leading to a diffraction-limited focal volume and decreasing quadratically with distance (Figure 1.16 A, bottom) [91] [132] [351]. A schematic of a two photon microscopy setup is illustrated in Figure 1.16 B.

The sample can be scanned quickly using a galvo-scanning mirror, resonant scanning mirror or an acousto-optical deflector. This allows measurements of dynamic signals from many locations simultaneously and establishes the raw temporal resolution of a recording. The light is delivered through an objective. Important factors include: a) numerical aperture (N.A.), that determines the resolution and the angle of photon collection, b) magnification and c) working distance.

Following excitation of the fluorophore, lower energy emitted photons are collected by the objective. Since the excitation volume is limited to focus, emitted photons that are scattered constitute useful signals. In 2P, emitted photons are collected by the objective, separated by frequency through a band-pass filter and amplified using detectors such as photomultiplier tubes (PMT) [91] [132] [351].

As a result, 2P minimizes photodamage by maximizing the probability of detecting signal photons with excitation event and allows for high resolution imaging deep inside tissues (1mm). These properties make 2P an excellent tool for studying astrocytes and neurons *in vivo*. 2P can also be used to perform 3D imaging by vibrating the

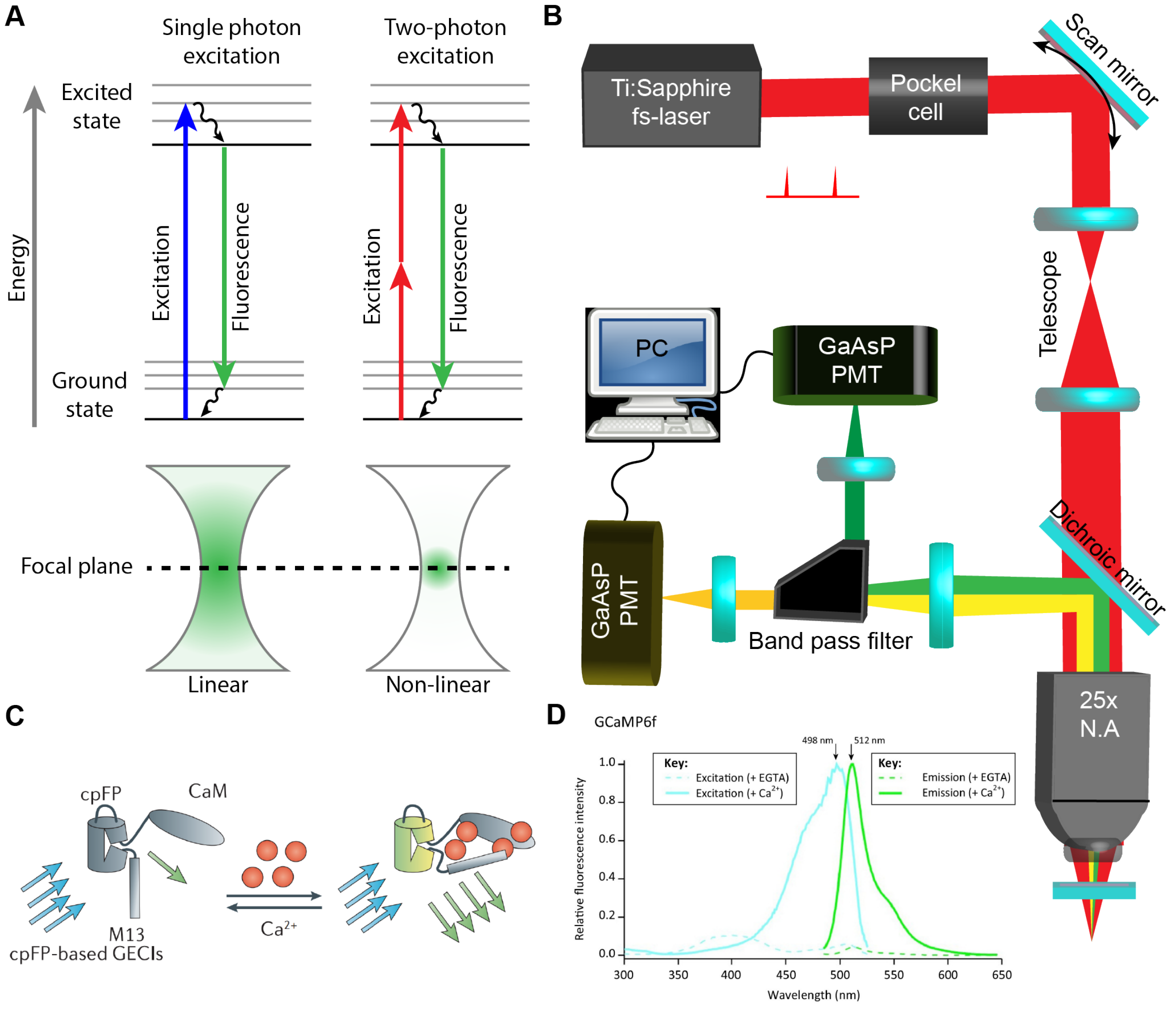
A
Single photon excitation
Two-photon excitation
Excited state
Energy
Excitation
Fluorescence
Excitation
Fluorescence
Ground state
Focal plane
Linear
Non-linear
B
Ti:Sapphire fs-laser
Pockel cell
Scan mirror
Telescope
PC
GaAsP PMT
GaAsP PMT
Band pass filter
Dichroic mirror
25x N.A
C
cpFP
CaM
M13
cpFP-based GECIs
Ca2+
D
GCaMP6f
498 nm
512 nm
Key:
Excitation (+ EGTA)
Excitation (+ Ca2+)
Key:
Emission (+ EGTA)
Emission (+ Ca2+)
Relative fluorescence intensity
0.0
0.2
0.4
0.6
0.8
1.0
300
350
400
450
500
550
600
650
Wavelength (nm)

Figure 1.16: Optical imaging. (caption next page.)

Figure 1.16: (previous page.) A) Schematic comparison between the principle of single photon (1P; left) and two photon (2P; right) excitation fluorescence microscopy. In 1P, a molecule is brought to its excited state by absorbing a single photon (blue). In 2P a molecule is brought to its excited state by simultaneously absorbing two near infrared photons (red). Once in the excited state, vibrational relaxation brings the molecule to its lowest excited state (black arrows), from where it returns to its ground state (green) by emitting a photon of lower energy. 1P is limited by out of focus fluorescence while the non-linear 2P effect minimizes this limitation (bottom). B) Schematic of two-photon microscopy setup. A mode locked femtosecond titanium sapphire laser emits pulsed (100fs) near-infrared light (700-1050nm, red beam) at about 80MHz. The beam is reflected on a pair of computer controlled galvo-scanning mirrors that change the position of the beam in the X-Y plane. The beam then passes through a dichroic mirror to the objective lens and focused at the desired plane in the tissue. The emitted light (yellow-green) is collected by the same objective and separated from the excitation light via the dichroic mirror and a filter. The light is then directed to photomultiplier tubes (PMTs) that amplify and detect the signal. C) Single fluorescent protein, GCaMP indicators are composed of a circularly permuted fluorescent protein (cpFP), calmodulin (CaM) and M13 domain of a myosin light chain kinase. When four Ca^{2+} (red) bind to the CaM-M13 complex during excitation by fluorescence light (blue arrows), the quantum yield of the cpFP increases (green arrows). D) Excitation and emission spectra of GCaMP6f in a solution with free Ca^{2+} or bound to EGTA chelator. Panel C was taken from [180]; D was taken from [335].

objective [118] [47] or holography [406]. The resolution limit of 2P is still diffraction limited, limiting its use when dealing with nanoscopic structures like the thin processes of astrocytes. Super resolution microscopy methods will likely provide new insights into the nanoscopic world of astrocytes by bypassing the diffraction limit [317] [131]. Two-photon microscopy in awake animals requires head-fixation, thus restricting the behaviour of the animal. Imaging during natural behaviour can be benefited with the use of wearable endoscopes [152]. Such endoscopes (especially flexible endoscopes), red shifted GECIs [86] and 3-photon microscopy [145] have the potential to increase the imaging depth limit restricting 2P and thus allow optical investigation of deeper brain structures without removing brain tissue.

1.6.5 Molecular toolkit for probing astrocyte physiology

Molecular manipulation of cells starts by incorporating foreign DNA into cells. This is generally accomplished by generating transgenic mice or using viral vectors. To generate transgenic mice, a linear DNA transgenic construct is injected into the male pronuclei of a newly fertilized mouse egg. Foreign DNA can be inserted into the single cell genome which then replicates with cell division into nearly all cells of the adult mouse. Modified, fertilized eggs are then injected in the oviducts of pseudopregnant female mice who have a chance of producing offspring that carry the transgene. Offsprings are then selected for transgene expression (i.e. using PCR). Transgenic mice offer a reliable way of introducing foreign DNA *in vivo*. It takes a long time (6-9 months) to generate a stable mouse line, but after that it is mostly limited by the reproductive vigor of mice. A faster, more flexible way of introducing transgenes, is using viral vectors. Viruses have been evolving for billions of years to infect cells and exploit their transcription machinery to replicate. Viral DNA can be modified by replacing replication coding sequences with foreign DNA. The necessary viral components are typically produced by cultured cells (typically immortalized HEK293T cells) transfected with plasmids encoding these components. The replication deficient viruses produced by these packaging cells are collected and filtered. These viruses can be used to transduce cells of interest. Sufficient transgene expression typically takes more than one week following delivery, the size of the DNA construct is restricted by the size of the viral capsid and care must be taken regarding safety issues to scientists and possible toxic effects on transduced cells. Typical viruses used in neuroscience include adenovirus, canine adenovirus (CAV), herpes simplex virus (HSV), lentivirus and adeno-associated virus (AAV) [62]. Both transgenic animals and viral strategies have been used to deliver foreign DNA to astrocytes and neurons. The delivery of genes encoding for fluorescent proteins allows visualization of cellular morphology and function. The same strategy can be used to manipulate the function of cells by the insertion of optogenetic receptors such as channelrhodopsin [52], halorhodopsin [393] and melanopsin [224] or chemogenetic receptors such DREADDs [307] [212]. While these approaches proved useful in neuronal manipulation, it is uncertain if they can be trusted in mimicking physiological aspects of astrocyte signalling. These are just some of the many available molecular tools that can be used to monitor and modulate cellular activity. The tool used has to be matched to the problem by considering the strengths and limitations. We will focus on the delivery of AAVs and their potential for studying brain circuits.

1.7 AAV biology

AAVs are small (≈20 nm), icosahedral, non-enveloped, single stranded DNA (ssDNA) parvoviruses often used for gene delivery. AAV is a dependovirus. It requires helper virus genes (of adenovirus or herpes virus) for successful replication and assembly [238]. AAVs have a genome with ≈4.7 kilobase capacity that contains two open reading frames (ORFs). ORFs encode four replication proteins (Rep), three capsid proteins (Cap) and an assembly activating protein (AAP) [3]. Rep and cap encode for replication related proteins and capsid proteins (i.e. VP1, VP2, VP3) respectively. The viral DNA is flanked by two T-shaped inverted terminal repeats (ITRs). ITRs are the only requirements needed to package DNA into the capsid [403]. Recombinant AAV (rAAV) vectors can be produced by replacing the wild type vector genes with genes of interest flanked by ITRs [238]. As a result rAAVs can't replicate. Pseudotyped rAAVs carry ITRs of one serotype in the capsid of a different serotype [294]. For example, AAV2/1 is a pseudotyped rAAV carrying AAV2 ITRs in an AAV1 capsid. Different capsid serotypes exhibit a range of tissue tropisms [19].

AAVs with different serotypes are attached to different cell membrane glycan receptors who dictate their tropism. For example, AAV1 and 5 use sialic acid (SIA) binders [400] [162] while AAV9 uses galactose binders [330]. All three serotypes use the newly

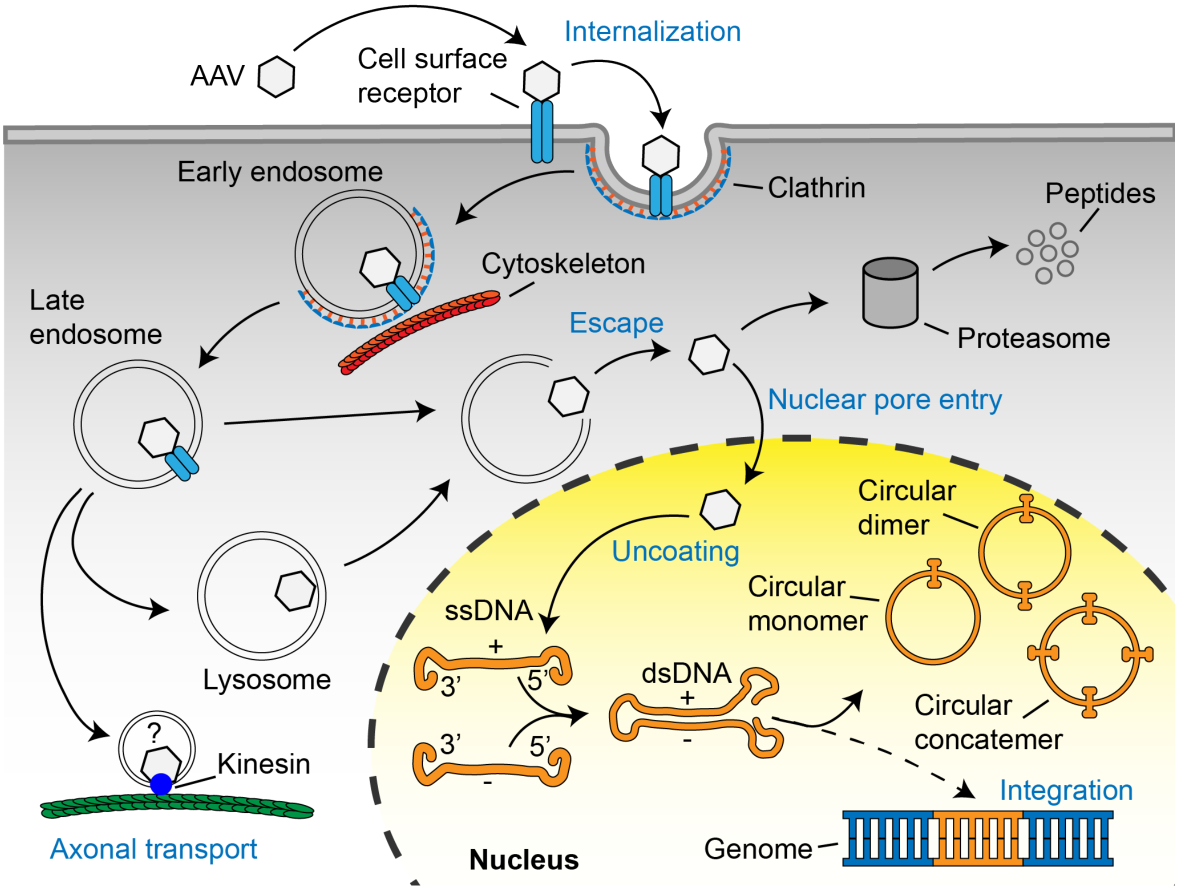
AAV
Cell surface receptor
Internalization
Clathrin
Early endosome
Cytoskeleton
Peptides
Proteasome
Late endosome
Escape
Nuclear pore entry
Lysosome
Uncoating
Circular dimer
Circular monomer
ssDNA
+
3'
5'
3'
5'
-
dsDNA
+
-
Circular concatemer
?
Kinesin
Integration
Axonal transport
Nucleus
Genome

Figure 1.17: Schematic of AAV transduction pathway. Adeno-associated viruses are recognised and bound to glycosylated membrane receptors. This triggers AAV internalization through clathrin-mediated endocytosis. AAVs travel through the cytosol using the cytoskeletal network. Once they are inside the late endosome they can enter the lysosome or tag on kinesin inside an unknown compartment for axonal anterograde trafficking. AAVs escape from endosomes and lysosomes. They can undergo proteolysis by the proteasome or enter the nucleus through the nuclear pore where they are uncoated. There the single stranded DNA (ssDNA) carried by the AAV is converted to double stranded DNA (dsDNA) that can undergo transcription. Inter/intramolecular recombination of inverted terminal repeats (ITRs) leads to the formation of circular episomal monomers, dimers and concatemers that can persist for a long time in the nucleus. Vector genes can also be integrated in the host genome at very low frequencies.

discovered AAV receptor AAVR [349] [288]. AAVs enter cells through clathrin or caveolae-mediated endocytosis [99] [324] [30]. Once inside endosomes AAVs are trafficked through the cytosol using the cytoskeleton [402]. Following endosomal escape AAVs enter the nucleus via the nuclear pore complex [170]. The capsid is likely uncoated in the nucleus since fluorescent-labeled capsids were detected in cell nuclei [328] [30]. The single stranded DNA (ssDNA) strands exposed undergo second strand synthesis [414] and are converted to various forms of double stranded genomes. These include extrachromosomal circular monomers that are converted to high molecular weight concatemers [405]. Concatemers persist in an episomal state and can provide long term transgene expression in non-dividing cells [98] [100] [241]. Interestingly, concatemerization of different independent vector DNA strands can be exploited to expand the small packaging capacity of AAVs [101]. The wtAAV genome can also integrate into the cell DNA because of sequence similarity found within the genomic locus AAVS1 and AAV ITR and Rep [225]. Since the rep gene is removed in the rAAVs genome, integration is vastly reduced [290]. A schematic of the AAV transduction pathway is illustrated in Figure 1.17.

1.7.1 Cell specific gene expression using AAVs

AAVs have evolved to infiltrate cells and exploit the cell transcription machinery for their own benefit. Their capsid serotype allows them to preferentially target different cell types [19]. In rAAVs the rep and cap genes of the wtAAV genome are replaced with artificial constructs [238]. These constructs typically contain a promoter region, a gene of interest we want to express (sometimes flanked by LoxP sites), an enhancer and a regulatory sequence. The promoter can be cell specific, i.e. human synapsin 1 (hSyn) and GFAP for expression in neurons [191] and astrocytes [55] respectively. A promoter can also be general like the cytomegalovirus (CMV) promoter [121] and the strong synthetic CAG promoter [161]. The endogenous diversity of transcription factors and RNA polymerases of different cell types allows these promoters to drive gene expression in defined cell populations [82]. Some genes commonly used in neuroscience research encode for fluorescent proteins such as eGFP, tdTomato or GCaMP allowing researchers to visualise transduced cells. Others include genes encoding for enzymes such as Cre recombinase (Cre). Because Cre can recombine with loxP sites it can be used to selectively activate or inactivate the expression of genes [322]. A common strategy involves the FLEX switch [322]. The FLEX switch (Figure 1.18C) uses separate antiparallel loxP recombination sites that allow homotypic but not heterotypic recombination [197]. Enhancer elements such as the woodchuck hepatitis post-transcriptional regulatory element (WPRE) are typically used to enhance expression [179]. Terminator sequences such as SV40 and rBG are used to terminate transcription [316].

In summary rAAV capsids of different serotypes can be selected to preferentially enter specific cell types. Since their DNA is modified to contain genes of interest instead of the rep and cap genes these viruses can't replicate. Specific promoters can be used to drive gene expression in specific cell types further enhancing the specificity of expression. The Cre-Lox system can also be used to induce conditional activation/inactivation of genes. Continuous developments lead to a greater range of genetic tools that can be delivered by AAVs to interact with cells.

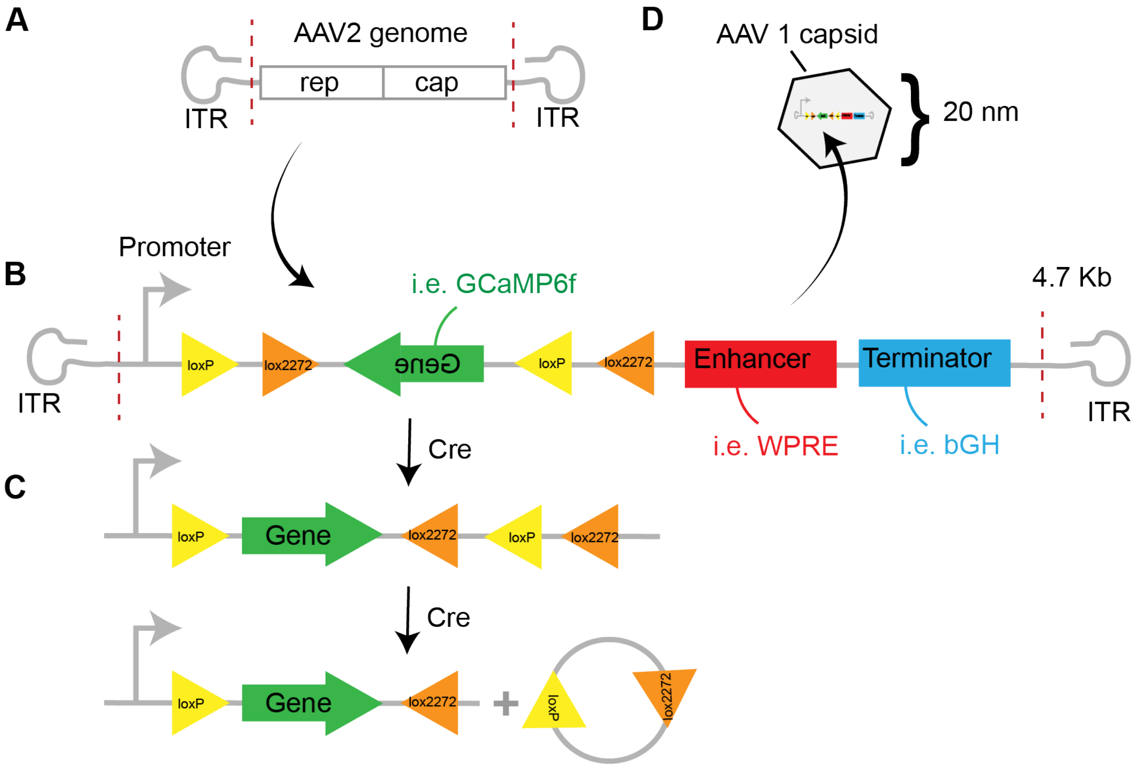
A
AAV2 genome
rep
cap
ITR
ITR
D
AAV 1 capsid
20 nm
B
Promoter
i.e. GCaMP6f
4.7 Kb
ITR
loxP
lox2272
Gene
loxP
lox2272
Enhancer
Terminator
ITR
i.e. WPRE
i.e. bGH
Cre
C
loxP
Gene
lox2272
loxP
lox2272
Cre
loxP
Gene
lox2272
+
loxP
lox2272

Figure 1.18: rAAV construct building strategy for cell specific gene delivery. A) Rep and cap genes are removed from wild type AAVs. B) They are replaced by genes of interest typically consisting of a promoter region (often cell type specific), a gene of interest (i.e. encoding for a fluorescent protein), an enhancer sequence to enhance gene expression and a terminator sequence to regulate gene expression. The gene of interest can be flanked by loxP sites. C) Cre recognises loxP sites and initiates side specific recombination between these sites. loxP sites have an orientation. If two loxP sites are in the same direction the gene will be excised while if they face in opposite directions Cre will induce continuous flipping. Cre recombinase recombines only with two loxP sites with the same spacer sequences. Flanking a gene with a combination of two pairs of loxP sites with different spacer sequences led to the development of the FLEX switch. First recombination with a pair of loxP sites causes inversion of the flanked gene. Next, recombination with the other loxP pair who is now in the same orientation (orange) triggers excision. This results in the permanent rotation of the gene of interest that can now be driven by the promoter. D) The engineered construct is inserted in AAV capsids of specific serotypes to enable preferential entry into nuclei of cell types of interest.

1.7.2 AAVs exhibit anterograde and retrograde properties

AAVs are valuable tools in research and clinical applications because they can transduce non- dividing cells and confer stable, long-term gene expression without causing inflammation or toxicity [42] [119]. Because of these properties rAAVs can be very useful tools for neuronal tracing studies. A very important viral property for tracing is the ability of the vector to travel between synapses. Common viral tools used to map neuronal circuits include the rabies virus that has retrograde transsynaptic properties [392] and the herpes simplex virus that has anterograde transsynaptic properties [364] [203]. However, these tracers are not ideal because they are neurotoxic and spread uncontrollably across multiple synapses [203]. AAVs have been largely overlooked as potential tracers.

AAVs have been known to exhibit anterograde and retrograde properties for about two decades, transducing cells at substantial distance from the injection site [168] [169] [57] [271] [293] [65] [66] [172] [76] [310] [63] [64] [415]. During retrograde transport, viruses are taken up at axon terminals and are transported to the cell body. In anterograde transport viruses enter the cell body and travel through the axon to the terminals where they are released. The released viruses then transduce new nearby cells.

Kaspar et al. [168] discovered that AAV2 injected in the rat brain undergoes retrograde transport. Injecting AAV2 carrying genes encoding for GFP in the hippocampus and striatum resulted in infection of projection neurons in the entorhinal cortex and substantia nigra respectively. They showed that AAV particles are found in entorhinal cortex and substantia nigra neurons by conjugating a fluorophore (Cy3) to the AAV capsid. They also detected viral genomic DNA in the retrograte areas using RT-PCR. The retrograde transport properties of AAVs were later used to expand the range of gene delivery to reverse pathology such as amyotrophic lateral sclerosis [169] and lysosomal disorders [271] [66] in animal models.

Provost et al. [293] detected vector DNA in the optic nerve following subretinal injection of AAV 2, 4 or 5 and in the brain after intravitreal AAV 2 injection. Their findings suggested anterograde transport of AAVs. Experiments were performed on rats, dogs and primates suggesting that anterograde AAV transfer is unlikely to be species dependent. Anterograde AAV transport of AAV 2 was also reported following injection in the rat striatum [76] and primate thalamus [172]. Injecting AAV2 carrying genes encoding for glial cell line-derived neurotrophic factor (GDNF) in the rat striatum led to GDNF expression in the substancia nigra, globus pallidus, entopeduncular nucleus and subthalamic nucleus [76]. Similarly, AAV2 (GDNF and GFP) injections in the primate thalamus led to GDNF and GFP expression in the cingulate, pre-frontal, pre-motor, primary and secondary somatosensory and motor cortices with highest expression in cortical layers III and IV [172].

Castle et al. [63] compared the anterograde and retrograde properties of AAV1, 8 and 9 and found that they exhibit both retrograde and anterograde properties. Using microfluidic primary neuron cultures and dye conjugated AAV9 Castle [64] found that AAV9 undergoes fast anterograde (≈ 2 μm/s) and retrograde transport (≈ 0.8 μm/s) along axon microtubules driven by kinesin-2 and dynein respectively. Recently, Zingg et al. [415] reported that AAV 1 and 9 can be used for anterograde trans-synaptic tagging of neurons. They used four lines of evidence to claim trans-synaptic properties.

They found labelled neurons only at the known upstream areas to the injection site, no labelling was found in cells around axon bundles, no cells were GFAP$^+$ suggesting no transfer to astrocytes and labelled upstream cells were always functionally connected to the neurons of the primary injection site. Zingg [415] also demonstrated that specific neuronal populations can be targeted using an intersectional approach and that anterograde trans-synaptic tagging can be used in conjunction with optogenetics for functional assays.

It is important to note that anterograde and retrograde transport of AAV is low. Novel approaches using *in vivo* directed evolution allowed engineering of retrograde functionality in AAV capsids [184]. This led to the development of rAAV2-retro that could robustly act as a retrograde tracer [357].

In summary, multiple groups and lines of evidence reported that AAVs exhibit anterograde and retrograde properties. These properties can be used for widespread delivery of transgenes in the brain for the treatment of neurological disorders and to facilitate experimental studies of neuronal circuits. There is very little research or evidence suggesting intercellular transport of AAVs to astrocytes. This is quite surprising considering the close proximity of astrocyte processes to synaptic elements and that astrocytes can be directly infected with AAVs.

1.8 The mouse somatosensory system

Neuronal and astrocytic activity are naturally modulated by the behavioural state and sensory experience of the organism. These physiological stimuli bypass the majority of concerns regarding artificial modulation by optogenetics, chemogenetics or electrical stimulation. We will focus on the mouse whisker system (Figure 1.19) as a model for studying astrocyte-neuron interactions.

1.8.1 The whisker somatosensory circuit

Tactile information from facial whiskers allows dark dwelling mice to extract spatial and textural information from their environment. Mice actively scan the environment through back and forth (16Hz) movement of their whiskers (whisking)[339]. Whisker deflection opens mechano-gated ion channels in trigeminal ganglion primary sensory neuron distal axon endings innervating the hair follicles [283]. Trigeminal ganglion neurons are pseudounipolar, with a proximal axon innervating the ipsilateral brainstem trigeminal complex (BTC) [209] and a distal axon innervating only one whisker follicle [417]. Thus, whisker deflection depolarizes trigeminal ganglion neurons who in turn send glutamatergic projections to the BTC. The BTC is divided into the principal sensory nucleus (PrV) and the spinal nucleus (SpV) who is subdivided into the oralis (SpVo), interpolaris (SpVi) and caudalis (SpVc) sub-nuclei [209]. BTC neurons preserve the somatotopic organization of whiskers and form functional clusters termed “barrellets” [369]. Principal trigeminal neurons send glutamatergic projections to the ventral posterior medial (VPM) nucleus of the thalamus. The VPM is also somatotopically laid out into clusters termed “barreloids” [54]. VPM neurons send glutamatergic projections to the primary somatosensory cortex (S1), forming distinct clusters in layer

4, termed “barrels” separated by septa [399]. The majority of VPM axons project to L4, but they also directly innervate L2/3 and the border of L5 and L6 (Figure 1.19 D)[395]. While whisker stimuli are detected reliably by the trigeminal ganglia, the cortex responds with high variability to identical stimuli [12]. The S1 then innervates other cortical and subcortical regions (Figure 1.19 C, E) [284]. The PrV - VPM - S1 circuit in termed the “lemniscal” pathway. An alternative circuit termed the “paralimniscal” pathway involves the interpolaris nucleus projecting to the posterior medial (POM) thalamic nucleus which primarily innervates L1 and L5 of the S1 (Figure 1.19 D)[283]. Together these circuits transmit whisker, sensory information to the cortex for sensorimotor processing (Figure 1.19 B).

1.8.2 Whisker touch increases neuronal activity in barrel cortex

The barrel cortex of the mouse is typically 1 mm thick and is classically subdivided based on cytoarchitecture into six layers. L4 barrel receives the majority of input from the VPM and sends inputs to L2/3 [284]. Whisker contact with an object evokes rapid depolarization in L2/3 neurons but drives action potentials only in 10% of them [84] suggesting sparse coding. This is likely because of fast recruitment of inhibitory interneurons which provide feed-forward and feedback inhibition [284]. During active whisking, inhibitory interneurons exhibit decreased firing rates which likely disinhibit L2/3 excitatory excitatory neurons [363].

Natural whisker stimulation increases S1, L2/3 activity. Head fixed mice presented with a pole show increased activity in L2/3 (and L4) neurons of S1 that is highly correlated to the onset of touch [255] [84] [83] [141]. The larger the force exerted on the whisker the higher the response [256] [281].

1.8.3 VPM drives cortical states

Changes in the activity of the VPM modulates the cortical state. Whisking increases the firing of VPM neurons driving S1 into an active, desynchronized state [367] [235] [292]. Optogenetic stimulation of the thalamus is sufficient to drive an active, desynchronized state in S1 while pharmacological inactivation (muscimol) of the thalamus enhances slow V_m fluctuations [292].

1.8.4 Locomotion modulates sensory responses

Sensory responses are also modulated by the behavioural state of the animal, such as locomotion. For example, locomotion increases spontaneous and evoked activity in the V1 [247] [22] and suppresses excitatory neuron activity in the auditory cortex [321] suggesting that it can have modality specific effects. Using a tactile virtual reality setup Ayaz et al. [23] found that locomotion (Figure 1.19 K) robustly increases S1 neuronal activity (L2/3 and L5) more than whisker touch. Whisker touch during run increased the amplitude and percentage of active S1 neurons more, compared to when these stimuli were presented alone. This suggests modulation of sensory stimuli processing by the behavioural state. L5 neurons respond transiently to whisker touch during run while L2/3 neurons show sustained activity and more cells are recruited (Figure 1.19

J). These suggests that L5 reports changes in touch conditions while L2/3 integrates whisker stimuli continuously.

1.8.5 Astrocytes of the barrel cortex

It is no surprise that neurons in the S1 are involved in processing sensory information from the whiskers. However, the cortex is also tiled with a network of astrocytes and other glia. The astrocyte network in S1 is heterogeneous. Astrocytes within S1 barrels are strongly coupled to each other through enriched expression of gap junction proteins (Cx30 and Cx43) while astrocytes located in the septa are either weakly, or not coupled to the astrocytic network [146]. They also exhibit layer specific morphological and molecular characteristics [31] [194]. For example, L2/3 astrocytes had more extensive process arborizations and ensheathed synaptic clefts more extensively compared to L6 astrocytes [194]. Astrocytes exhibit differential gene expression patterns clustered into layers who are divergent from neuronal laminae [31]. Layer specific diversity of astrocyte is likely neuron dependent since they are abolished when neuronal layers are disturbed in reeler and Dab1 conditional KO mice [194] [31].

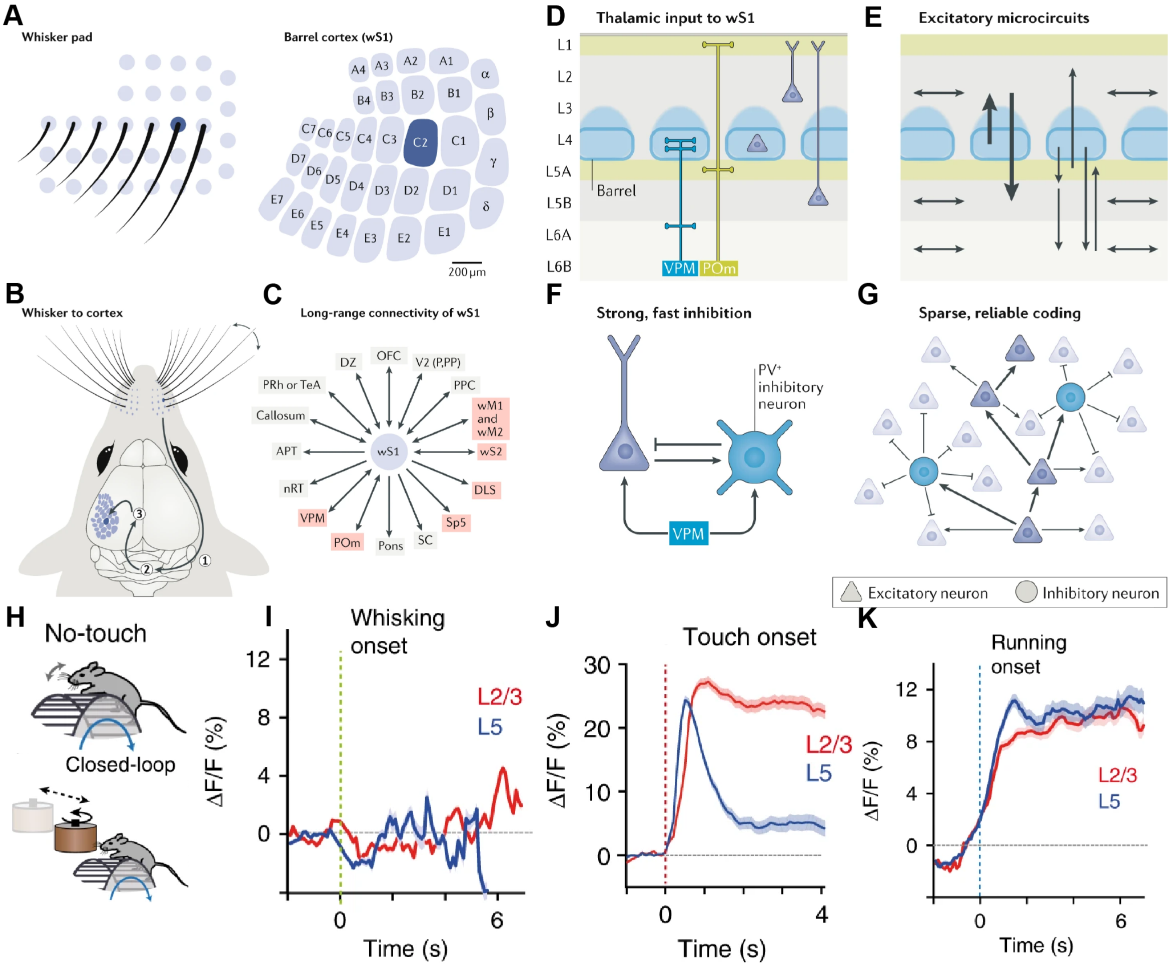
A
Whisker pad
Barrel cortex (wS1)
A4 A3 A2 A1 α
B4 B3 B2 B1 β
C7 C6 C5 C4 C3 C2 C1 γ
D7 D6 D5 D4 D3 D2 D1 δ
E7 E6 E5 E4 E3 E2 E1
200 μm
D
Thalamic input to wS1
L1 L2 L3 L4 L5A L5B L6A L6B
Barrel
VPM POm
E
Excitatory microcircuits
B
Whisker to cortex
1 2 3
C
Long-range connectivity of wS1
DZ OFC V2 (P,PP) PRh or TeA PPC Callosum wM1 and wM2 APT wS1 wS2 nRT DLS VPM Sp5 POm Pons SC
F
Strong, fast inhibition
PV+ inhibitory neuron
VPM
G
Sparse, reliable coding
Excitatory neuron
Inhibitory neuron
H
No-touch
Closed-loop
I
Whisking onset
L2/3
L5
ΔF/F (%)
12 8 4 0
0 6
Time (s)
J
Touch onset
L2/3
L5
ΔF/F (%)
30 20 10 0
0 4
Time (s)
K
Running onset
L2/3
L5
ΔF/F (%)
12 8 4 0
0 6
Time (s)

Figure 1.19: Whisker somatosensory system of mice. (caption next page.)

Figure 1.19: (previous page.) A) The whisker primary somatosensory cortex (wS1) of mice is composed of somatotopically organized 'barrels' (right), each representing an individual whisker (left). B) Whisker deflection activates a cascade of neuronal activity in trigeminal ganglia (1), brainstem (2), thalamus (3) and wS1. C) From there, wS1 neurons project to many cortical and subcortical areas. D) wS1 neurons receive thalamic input from the ventral posterior medial nucleus (VPM) and the posterior medial nucleus (POm). The VPM primarily innervates layer 4 (L4) barrels but also L3 and L6A (blue). The POm sends higher-order inputs to L1 and L5A. E) Extensive excitatory microcircuits send projections between layers in the barrel column (vertical arrows) and across barrel columns (horizontal arrows). F) Both excitatory neurons and inhibitory interneurons receive input from the VPM and are strongly connected to each other. G) The reciprocal connectivity between strong excitatory and inhibitory synapses may mediate reliable, sparse coding in the wS1. H) Mice running on wheels with systems embedded to trigger whisker touch can be used to study the somatosensory system in awake animals. I) Upon whisking (periodic movement of whiskers) onset only a tiny fractions of L2/3 and L5 neurons are activated. J) Both L2/3 and L5 neurons display a sharp initial response to whisker touch. L2/3 neurons exhibit a sustained response to continuous whisker touch while L5 neurons display a transient response. K) Both L2/3 and L5 neurons display sustained activity with (slightly before) the onset of locomotion. APT (anterior pretectal nucleus); DLS, dorsolateral striatum; DZ(dysgranular zone surrounding wS1); nRT(nucleus reticularis of the thalamus); PPC (posterior parietal cortex); OFC (orbitofrontal cortex); PRh (perirhinal cortex); SC (superior colliculus); Sp5 (spinal trigeminal nuclei); TeA (temporal association cortex); wM1 (whisker-related primary motor cortex); wM2 (whisker-related secondary motor cortex); wS2 (whisker-related secondary somatosensory cortex); POm (posterior medial nucleus of the thalamus); VPM (ventral posterior medial nucleus of the thalamus); V2 (P,PP) (secondary visual area). Panels A-G were taken from [284]; H-I from [23].

Recently, astrocytes were also reported to respond to whisker stimulation with $[Ca^{2+}]_i$ elevations in L2/3 of S1 [387] [356] [200] [201] [344][345] but see ([93] [250]) suggesting that they might be involved in aspects of sensory processing. Astrocyte responses were more reliably observed in spatially clustered sensory maps like the mouse S1 compared to V1, suggesting that some of the controversies might be sensory modality dependent [204]. Calcium changes might be different across layers [355] but this remains to be confirmed and better characterized. Slice experiments indicated that L2/3 astrocytes specifically respond to L4 neurons [319] suggesting that astrocytes can discriminate between inputs within anatomical circuits. S1 astrocytes were also shown to exhibit heterogeneous Ca^{2+} responses to optogenetic stimulation of PV+ and STT+ inhibitory interneurons *in vivo* [215]. Stimulating whiskers in mice for 24h doubles the expression of GLT1 and GLAST in the respective barrel column and increases astrocyte enveloping of excitatory dendritic synapses [116]. Therefore, neuronal activity can change functional, molecular and morphological features of S1 astrocytes. The conditions, constraints and effects of astrocyte Ca^{2+} signalling in S1 remains to be explored.

Chapter 2

Anterograde axo-astrocytic AAV transfer to astrocytes

2.1 Motivation

It has been recently realized that astrocytes are heterogeneous cells that may be differentially involved in different neuronal circuits [216] [278]. Viral tracers have been widely used to study neuronal circuits. I hypothesised that viral tracing can be used to label astrocytes embedded in specific neuronal circuits. Recombinant adeno associated viruses (rAAVs) are capable of anterograde and retrograde transport through axons, and have been used to study neuronal circuits [63] [64] [415]. Even though astrocytes are in tight contact with neuronal synapses and can be efficiently transduced by AAVs, the ability of AAVs to transfer through axons to astrocytes was so far unexplored. The objective of this chapter is to investigate the potential of intercellular AAV transfer from neurons to astrocytes.

2.1.1 Hypothesis

- AAV1 injected in the VPM can transfer to the cortex through axons to infect 2nd order astrocytes and neurons in the somatosensory cortex.

2.2 Methods

All experimental procedures were approved by the OIST Institutional Animal Care and Use Committee (IACUC) in an Association for Assessment and Accreditation of Laboratory Animal Care (AAALAC International) accredited facility.

2.2.1 Animals

Male, 1 - 3 month old C57/BL6 mice were used. Mice were housed under reverse light/dark cycle.

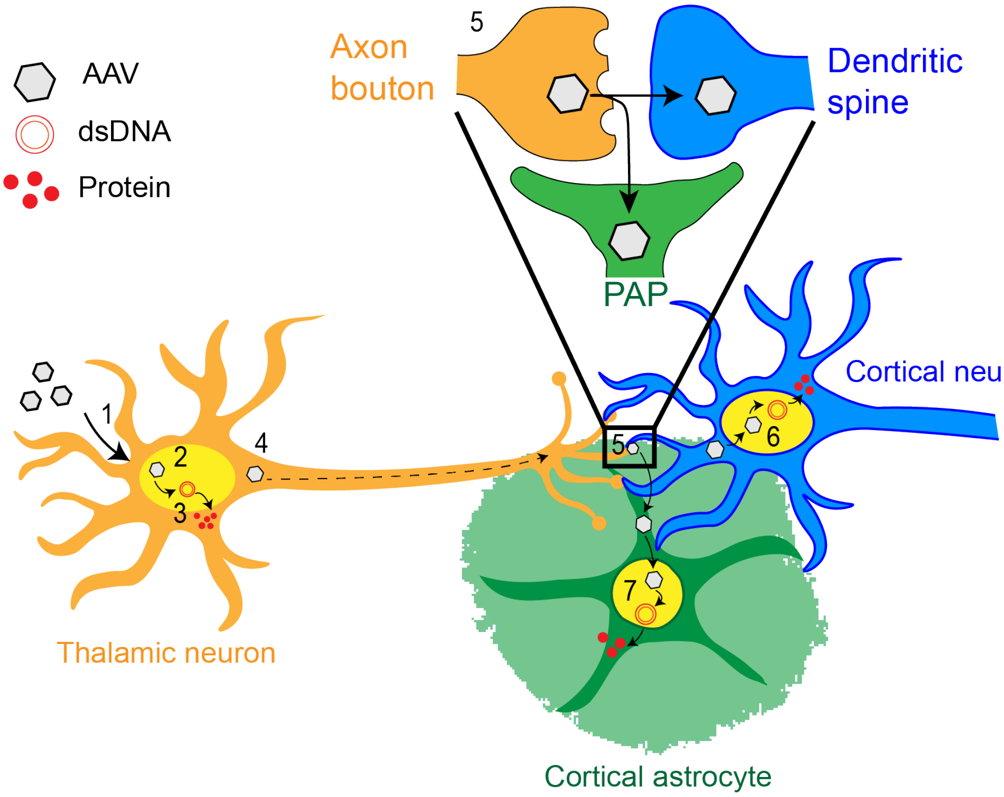
AAV
dsDNA
Protein
5
Axon bouton
Dendritic spine
PAP
1
2
3
4
5
6
7
Cortical neuron
Thalamic neuron
Cortical astrocyte

Figure 2.1: Hypothetical schematic of trans-synaptic AAV transfer to astrocytes and neurons. 1) AAVs enter neurons at the injection site by endocytosis. 2) Some AAV particles transport to the nucleus through the cytoskeleton. 3) They enter the nucleus and release their ssDNA which is converted to dsDNA concatemers. The transgene is transcribed and then translated into proteins. 4) A small number of AAV particles are transported anterogradely along the axons to the terminals. 5) They are then released and enter adjacent postsynaptic dendrites and perisynaptic astrocytic processes (PAPs). Then they enter the nuclei of 6) neurons and 7) astrocytes and release their ssDNA which eventually leads to protein synthesis.

2.2.2 Surgery

Mice were anesthetized by intraperitoneal injection of 0.1 ml/10g 3-mixture anesthetic (Medetomidine: 0.3mg/kg, Midazolam: 4 mg/kg, Butorphanol: 5 mg/kg diluted in 0.9% saline solution). Carprofen (5 μg/g; intraperetoneal), Dexamethasone (2 μg/g; intramuscular) and Buprenorphine (0.1 μg/g; subcutaneous) were administered to reduce inflammation, immune response and pain respectively. Following anesthesia induction the mouse eyes were protected by covering them with mycochlorin eye ointment (Sato Pharmaceutical Co., Ltd). The head hair were removed with a hair trimmer and hair removal cream (Veet). The head of the animal was fixed on a stereotactic apparatus and its skin was sterilized with iodine. If further anesthesia was needed, 1% isoflurane was administered.

A single midline sagittal incision of the skin (head) was performed. The exposed skull was cleaned with the local anesthetic lidocaine. The skin was then pulled and dry fixed with compressed air. Bregma and lambda were used to level the skull. The injection co-ordinates in reference to Bregma were based on the Paxinos reference Atlas [275] and previous calibration injections. The skull was thinned at the desired coordinates using a diamond drill. A sterile glass pipette with a broken tip was used to puncture the thinned skull at the precise coordinates established to minimize the exposure of the brain. Using separate glass pipettes (10-15 μm tip diameter), AAVs were injected in the VPM (1.8 mm posterior, 1.7 mm lateral, 3.5 mm deep) and sometimes in the somatosensory cortex (1.8 mm posterior, 3.2 mm lateral, 0.5 mm deep) as well. AAVs were pressure injected at $\approx$70 nl/ 5 minutes and the pipette was left to rest in the brain for at least 5 minutes before and after injection. After injections, the cut skin was glued back together. Animals were housed individually and allowed to recover for at least one week, unless otherwise stated.

2.2.3 Adeno associated viruses

To assess whether AAV1 tags astrocytes anterograde the injection site, 140 nl (1:1 ratio) AAV2/1.CMV.P1.Cre.rBG (1.2×10^{13} GC/mL) and AAV2/1.hSyn.TurboRFP.WPRE.rBG (3.9×10^{13} GC/mL) (University of Pennsylvania Viral Vector Core) were co-injected in the VPM and 100 nl AAV2/5.GFaABC1D.Flex.Lck.GCaMP6f.WPRE.SV40 (1.0×10^{13} GC/mL) (Sirion Biotech) was injected in the somatosensory cortex.

To assess if a similar intersectional strategy can be used to label neurons, the same combination of AAVs was injected in the VPM, while 100 nl AAV9.Syn.Flex.GCaMP6f.WPRE.SV40 (2.8×10^{13} GC/mL) (University of Pennsylvania Viral Vector Core) was injected in the somatosensory cortex.

To assess whether a cortical injection is necessary and what aspects of the AAV vector are needed to label 2nd order cells; 140 nl (1:1 ratio) of different rAAV combinations were injected only in the VPM:

- AAV2/1.hSyn.TurboRFP.WPRE.rBG and AAV2/1.CAG.GCaMP6f.WPRE.SV40 (1.33×10^{13} GC/mL) (University of Pennsylvania Viral Vector Core).
- AAV2/1.CMV.P1.Cre.rBG and AAV2/1.CAG.Flex.eGFP.WPRE.bGH (9.16×10^{12} GC/mL) (University of Pennsylvania Viral Vector Core).

- AAV2/1.CMV.P1.Cre.rBG and AAV2/1.CAG.Flex.tdTomato.WPRE.rBG (4.65 $\times 10^{13}$ GC/mL) (University of Pennsylvania Viral Vector Core).

A combination of AAVs that induced high contrast, "brainbow"-like labelling, anterograde the injection site were used for cell quantification experiments to aid in the counting of cells, particularly those inside dense thalamocortical projections in layer 4 of S1. I termed this effect 'Traffic light labelling', and it was induced by injecting 70 or 140 nl (1:1:1) AAV2/1.CMV.P1.Cre.rBG, AAV2/1.CAG.Flex.eGFP.WPRE.bGH and AAV2/1.CAG.Flex.tdTomato.WPRE.rBG in the VPM.

2.2.4 Slice preparation and immunohistochemistry

Two weeks after injection (unless otherwise stated) the animals were deeply anesthetized with the 3-mixture anesthetic and transcardially perfused with PBS followed by PLP (4% paraformaldehyde, 0.2% periodate and 1.2% lysine in 0.1M phosphate buffer) fixation. The brains were extracted and stored in PLP at 4°C for a minimum of 48h.

Brains were sliced after all procedures and prepared for confocal microscopy. A vibratome (VT1000S, Leica) was used to cut 100 μm thick coronal brain sections. The slices were mounted on glass slides with Mowiol and stored at 4°C.

I used immunohistochemistry to track AAV capsids by tagging them with an anti-AAV1 antibody. For immunohistochemistry preparation the brains were cryoprotected using 20% sucrose solution in PBS overnight. The brains were then trimmed and embedded in optimal cutting temperature (OCT) compound (Tissue-Tek). The samples were frozen at -80°C for 1 hour. A cryotome (Leica CM3050 S) was used to cut 50 μm thick coronal slices at -15°C which were immediately transferred in wells filled with PBS. The sections were washed in PBS and then incubated in 20% normal goat serum in permeabilization solution (0.3% Triton-X-100, 0.05% sodium azide, PBS) for 1 hour. The serum was replaced with 1:20 mouse Anti-AAV1 monoclonal antibody (Antibodies-online, ABIN933221) diluted in permeabilization solution. The slices were incubated for 24h at 4°C. The samples were washed with PBS and incubated in goat anti-mouse polyclonal secondary antibody Alexa Fluor 488 (abcam, ab150113) 1:200 (diluted in permeabilization solution) for 2-3 hours in the dark at room temperature. The brain slices were washed with PBS, mounted on glass slides with DAPI (VECTASHIELD) and stored at 4°C.

2.2.5 Confocal imaging and analysis

LSM 510 META ConfoCor3 and LSM 710 (Carl Zeis) confocal microscopes were used to image fixed brain slices. LSM 510 was used to capture all images except for antibody-labelled capsid samples in the cortex. For immunostained AAV capsid imaging, LSM 710 was used because an objective with high numerical aperture (N.A.) was needed for high resolution.

For LSM 510, a 488 nm argon laser and a 561nm Diode-Pumped Solid-State (DPSS) laser were used to excite green fluorophores (eGFP, GCaMP6f, Alexa Fluor 488) and red fluorophores (tdTomato, TurboRFP) respectively. A 405 nm Diode was used to excite DAPI.

All data was analyzed using Matlab (R2015b). The normality of distributions was assessed using Kolmogorov-Smirnov test (kstest) with a significance threshold set at $p = 0.05$, and a straight line of the quantile-quantile (QQ) plot (qqplot). Normal distributions from independent samples were compared using an unpaired, two tailed t-test (ttest2) with the significance threshold set to $p < 0.05$.

To compare the relative intensity of the eGFP and tdTomato component of 'Traffic light labelled' cells, confocal images in 100μm thick coronal brain slices from 2 mice were acquired. The intensity parameters of the argon (488nm) and DPSS (561nm) laser were standardized for consistency and to avoid saturation. ROIs of all labelled cells were manually selected in Fiji [318]. The average red and green channel intensities from these ROIs was extracted. ROIs containing saturated pixels were discarded. 1019 cells were used. The extracted red and green ROI intensities were normalized to the minimum and maximum value of the respective channel and set to 0 (minimum) and 1 (maximum) respectively. The values of the red (R): green (G) normalized intensity ratio (G / R + G) for each ROI (cell) where calculated. For example, 0 and 1 means a given ROI is only red (tdTomato$^+$) or green (eGFP$^+$) respectively.

For cell number quantification, 3 image stacks were acquired per mouse composed of 40, 16 bit images with a 409×409 μm field of view, interspaced 1 μm from each other at 1 Airy Unit (AU) using a Plan-apochromat 20x/N.A. 0.8 objective. The 3 stacks were taken from 3 brain slices (1 at the z-plane of the injection tract ± 1) and standardized to be $\approx$1700 μm lateral of the injection track centered on the barrels. All cell bodies were manually counted. The number of cells in all 3 slices were averaged for each mouse. Normal distributions from independent samples were compared using an unpaired, two tailed t-test ($p < 0.05$). 9 brain slices from 4 mice were used to manually count all astrocytes and neurons in 'Traffic light labelled" samples and categorized. Astrocytes were identified and separated from neurons based on their characteristic spongiform morphology. Ambiguous cells were discarded. The remaining classified astrocytes and neurons ($n = 595$) were used to estimate their relative proportions.

For capsid puncta quantification in the cortex tdTomato positive cell bodies of astrocytes and neurons $\approx$1700 μm lateral of the injection site were randomly selected from 3 brain slices per mouse (n=3). A 63x /N.A. 1.46 a-Plan-Apochromat Oil objective was used to acquire 3D image stacks of 67.48×67.48μm field of view (16 bit, 1024 x1024 pixels), 0.7 μm interspaced from each other at 0.84 AU and averaged 8 times. Alexa-fluor 488 and tdTomato were excited using a 488 nm Argon laser and 543 nm Helium-Neon laser respectively. For control, 3D stacks with the same parameters were also taken in the opposite site cortex (1 hour after injection in its ipsilateral VPM). To quantify the number of capsid puncta, images were converted to 8 bits and a 3D gaussian filter of 1 pixel was applied. Standardized brightness, contrast and threshold parameters were established empirically. Fluorescent puncta of 0.1 - 0.5 μm^2 in size were automatically counted using Fiji (analyze particles). The size range parameter was based on empirical observations of puncta sizes since they could be easily identified by eye. Unpaired two tailed t-tests were used to compare the puncta density between a) S1 cell bodies (n=15) vs local background to these cells (n=12; 12 days after injection in ipsilateral VPM) and b) local background vs background of the opposite S1 cortex (n=10), devoid of cell bodies (1 hour after injection in its ipsilateral VPM). The sampling volume was calculated to be equal to the ROI area×(0.7×Number of

Z sections). Puncta density was calculated to be the number of puncta / sampling volume. The significance threshold was set to $p < 0.05$ for all statistical tests.

2.2.6 Whisker removal

To test the hypothesis that AAV transfer to 2nd order cortical cells is activity dependent, the contralateral whiskers to the injected VPM were removed to deprive the mouse of sensory input to the somatosensory circuit. Mice (n=10, 2 months old) were separated into a control (n=5) and an experimental group (n=5). The ipsilateral whiskers to the injected VPM were removed in the control group. All contralateral whiskers to the injected VPM were plucked in the experimental group. Whiskers were first removed right before surgery. Whisker were removed by periodic plucking using tweezers. Whisker regrowth was monitored and any regrowing whiskers were plucked under 1% isoflurane anesthesia. The animals were perfused two weeks after injection. The mean number of S1, 'Traffic light labelled' cells between the two groups was compared using an unpaired, two tailed t-test.

2.2.7 Exosome inhibition

To test if AAV anterograde tagging is exosome dependent I used a protocol based on Dinkins et al. [95] to inhibit exosome production. Dinkins et al. [95] showed that administration of 100 μg GW4869 daily for 5 days in wild type mice reduced the number of exosomes in the brain (detected by the exosome markers Alix and Tsg101). They then reported that injecting 60μg of GW4869 every 2 days for 6 weeks in an Alzheimer's disease mouse model (5XFAD) reduced brain amyloid concentration, serum exosomes and several ceramides. I used Dinkins et al. protocol [95] with modifications in the percentage of DMSO used to dilute the drug. GW4869 (N,N'-Bis[4-(4,5-dihydro-1H-imidazol-2-yl)phenyl]-3,3'-p-phenylene-bis-acrylamide dihydrochloride; molecular weight 577.5 g/mol; Santa Cruz Biotechnology) was diluted and stored in DMSO at 4 mg/mL in 4^oC. Mice (n=10, 2 months old) were separated into a control (n=5) and an experimental group (n=5). The control group was injected with 200 μl of 7% DMSO in 0.9% saline. The experimental group was injected with 200 μl GW4869 diluted to 0.3 mg/mL in 0.9% saline ($\approx$ 60 μg/mouse). Mice in both groups were injected intraperitoneally every day for the first 5 days and then every 48 hours for 2 weeks total (9 injections). The first injection was performed right before surgery. All injections were performed under isoflurane anesthesia. No obvious health problems were observed. The animals were perfused 2 weeks after AAV injection. The mean number of S1, 'Traffic light labelled' cells between the two groups was compared using an unpaired, two tailed t-test.

2.3 Results

2.3.1 AAV1 vectors injected in the VPM mediate astrocytic and neuronal labelling in S1

The long range, thalamocortical projections from VPM to S1 provide a good model to test whether AAV1s transport anterograde through axons to 2nd order astrocytes and neurons. First I tested if injecting AAV1.CMV.Cre in the VPM and AAV1.GFaABC1D.flex.lck.GCaMP6f in the cortex can label astrocytes. In this preparation, AAV1.hSyn.TurboRFP was also co-injected in the VPM as a marker for the projection pathway, to assess if there was any damage at the injection site and check if there are TurboRFP$^+$ cell bodies in the cortex (Figure 2.2 A). The injection co-ordinates were confirmed based on the Paxinos Brain Atlas and by the distinct, dense, barrel like projection pattern of VPM neurons observed in layer 4 of the somatosensory cortex (Figure 2.2). This injection strategy resulted in labelling of S1 astrocytic membranes with lck.GCaMP6f (green; Figure 2.2 A) revealing their cloud like morphology. While dense TurboRFP$^+$ thalamocortical axons could be seen innervating the S1 (red; Figure 2.2 A), no TurboRFP$^+$ cell bodies were found in S1. GCaMP6f$^+$ S1 astrocytes were sparsely distributed in L3 and more densely distributed in L4. A small number of cells with non-astrocytic like morphology were also observed predominantly in layers 5 and 6. Using a similar Cre-Flex intersectional strategy, I tested whether S1 neurons can be selectively labelled. Instead of using the astrocyte specific GFaABC1D promoter, I used AAVs carrying the gene encoding the neuron specific hSyn promoter. Injecting AAV1.CMV.Cre and AAV1.hSyn.TurboRFP in the VPM and AAV9.hSyn.Flex.GCaMP6f in S1 led only to neuronal labelling with GCaMP6f in the cortex (green, Figure 2.2 B). GCaMP6f$^+$ S1 neurons were most densely found in L4 and L6A. I didn't observe TurboRFP labelling in cortical cells.

I then asked whether: a) a double injection strategy (VPM and cortex), b) Cre recombinase or, c) the specific fluorescent protein expressed are needed to label astrocytes and neurons in the cortex . Injecting AAV1.CAG.GCaMP6f and AAV1.hSyn.TurboRFP (Figure 2.2 C) or AAV1.CMV.Cre and AAV1.CAG.flex.eGFP (Figure 2.2 D) in the VPM results in second order cortical astrocytes and neurons labelled with GCaMP6f and eGFP respectively. Therefore, a double injection strategy is not necessary, Cre recombinase is not required and the fluorescent protein expressed doesn't affect whether second order astrocytes and neurons are labeled. Although a double injection strategy is not necessary for the labelling of cortical cells following AAV injection in the VPM, the gene encoding for the fluorescent protein must be driven by a strong promoter (like CAG) for cortical cell to be labelled with a single AAV injection only in the VPM. Once again, the highest density of labelled cortical cells was observed in L4.

Through the above strategies and more than 300 injections with a variety of AAVs I observed reliable ($\approx$100%) labelling of cortical cells following thalamic injection with certain AAV mixtures (i.e. ones demonstrated here). Sparse labelling of cortical cells suggests a small number of AAVs are transferred. Intersectional Cre-FLEX strategies with different promoters can be used with AAVs for anterograde, cell type specific labelling of astrocytes and neurons. AAV1 injected in the VPM led to second order cell labelling in the cortex. However the strong promoter CAG was necessary. The

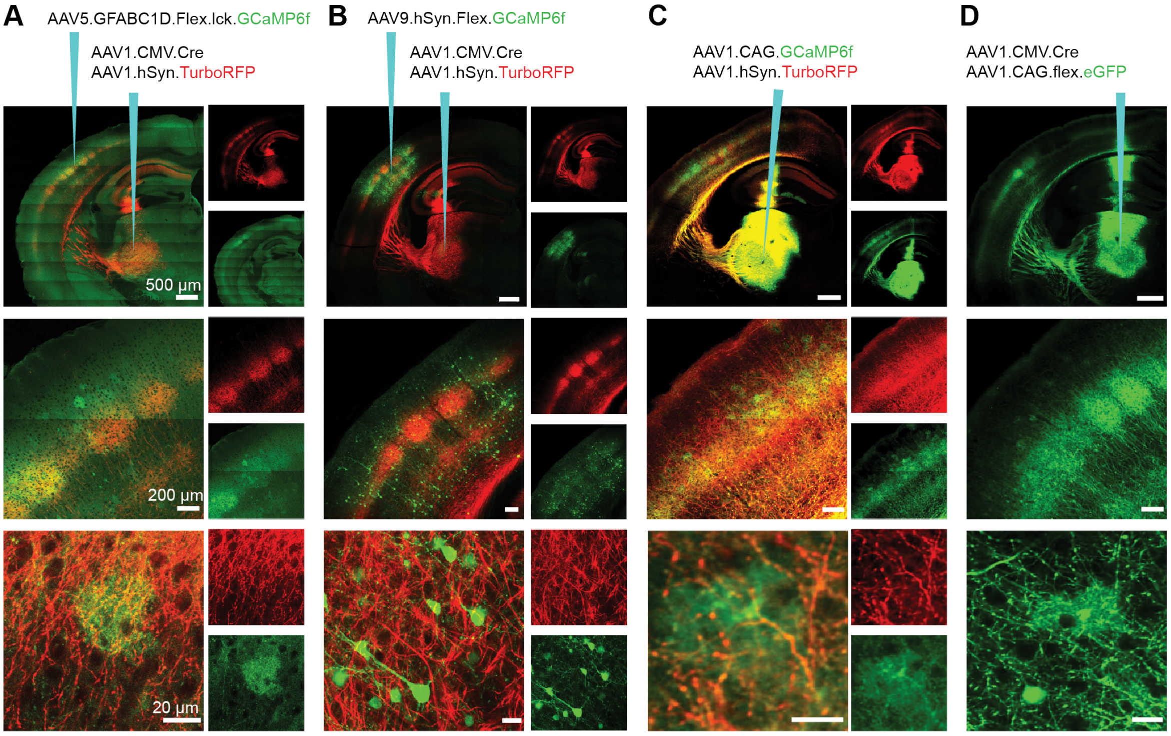
A
AAV5.GFABC1D.Flex.lck.GCaMP6f
AAV1.CMV.Cre
AAV1.hSyn.TurboRFP
B
AAV9.hSyn.Flex.GCaMP6f
AAV1.CMV.Cre
AAV1.hSyn.TurboRFP
C
AAV1.CAG.GCaMP6f
AAV1.hSyn.TurboRFP
D
AAV1.CMV.Cre
AAV1.CAG.flex.eGFP
500 µm
200 µm
20 µm

Figure 2.2: Intercellular AAV transfer injection strategies. Injecting AAV1s carrying genes encoding for fluorescent proteins in VPM results in sparse labelling of astrocytes and neurons in the projecting somatosensory cortex. A) AAV1.CMV.Cre and AAV1.hSyn.TurboRFP injected in the thalamus and AAV5.GFaABC1D.Flex.lck.GCaMP6f injected in S1 cortex. Thalamocortical axons are labelled with TurboRFP and cortical astrocyte membranes are labelled with GCaMP6f. B) AAV1.CMV.Cre and AAV1.hSyn.TurboRFP injected in the thalamus and AAV9.hSyn.Flex.GCaMP6f in the somatosensory cortex. Thalamocortical axons are labelled with TurboRFP and cortical neurons are labelled with GCaMP6f. C) AAV1.hSyn.TurboRFP and AAV1.CAG.GCaMP6f injected in the VPM labels neurons and astrocytes in the somatosensory cortex. D) AAV1.CMV.Cre and AAV1.CAG.Flex.eGFP injected in the VPM labels neurons and astrocytes in the cortex. Thalamic injections of AAV1.hSyn.TurboRFP label VPM neurons but not any cortical cells. All images were taken from fixed brain slices of mice sacrificed two week after injections.

majority of labelled cortical cells were in layer 4, the major projection target of the VPM. A smaller number of labelled thalamocortical axons and cortical cells was found in layers 5, 6 and 2/3. The highest concentration of labelled cells was far (≈1.5 mm) from the injection tract and injection site. Taken together these observations suggest that a small number of AAVs are transferred through thalamocortical axons to cortical astrocytes and neurons.

2.3.2 AAV capsids are found in astrocytes and neurons in the cortex following VPM injection

The next question was whether indeed a small number of AAVs transduce cortical cells following thalamic injection. To test that I tracked AAV capsids periodically using an anti-AAV primary antibody to tag the AAV capsids and a secondary antibody carrying Alexa Fluor 488 to detect where primary antibodies were bound.

First I tested if the antibody labels capsids reliably, and how AAV capsids are distributed at the injection site (VPM). If the anti-VP1 antibody binds to the AAV capsids, then I would expect Alexa Fluor 488 lebelling at the injection site immediately after injection of AAV1. Indeed, injecting an AAV mixture (AAV1.CMV.Cre and AAV1.CAG.Flex.tdTomato) in the VPM of mice followed by perfusion within 1 hour resulted in green, cloud like fluorescence (≈radius = 250 μm; 140nl) only at the injection site. A macroscale and a microscale example can be seen in Figure 2.4 B and Figure 2.3 B respectively. Therefore, in all future experiments using anti-VP1 antibody, two injections were performed in the same mouse: one control (within 1 hour before perfusing the animal serving as a positive control for antibody labelling) and one experimental. Absence of green fluorescence at the control injection site indicated that something went wrong during the experiment and the sample was discarded. A second injection in the opposite VPM to the control was performed to investigate the distribution of AAVs in the VPM 24 hours (Figure 2.3; n = 3 mice) or 12 days (Figure 2.4; n=3 mice) after co-injection of AAV1.CMV.Cre and AAV1.CAG.Flex.tdTomato.

Immediately after injection (≈1h), AAV particles are distributed like a cloud at the injection site (Figure 2.4 B) but do not co-localized with DAPI labelled cell nuclei (Figure 2.3 B). However, 24 hours after AAV injection the opposite picture emerged. Green fluorescent puncta representing AAV capsids (or clusters of capsids) were primarily co-localized with DAPI labelled cell nuclei (Figure 2.3 C). These observations suggested that a large number (not quantifiable) of AAV capsids enter the nuclei of cells within 24 hours after injection.

I then hypothesized that green fluorescent puncta would be present in the cell bodies of tdTomato labelled cells in the cortex following VPM injection of AAV1.CMV.Cre and AAV1.CAG.Flex.tdTomato. A period of 12 days was chosen for this experiment (in contrast to 24 hours of the previous experiment)(Figure 2.4 A) in order to give enough time for tdTomato to be expressed in the cortex, to decrease the chance of any possible damage in the VPM due of prolonged expression and to have relatively low tdTomato expression in the cortex to minimize possible cross talk of the red and green detection channels. The same injection strategy as before was performed. High resolution confocal imaging revealed a small, countable, number of green fluorescent

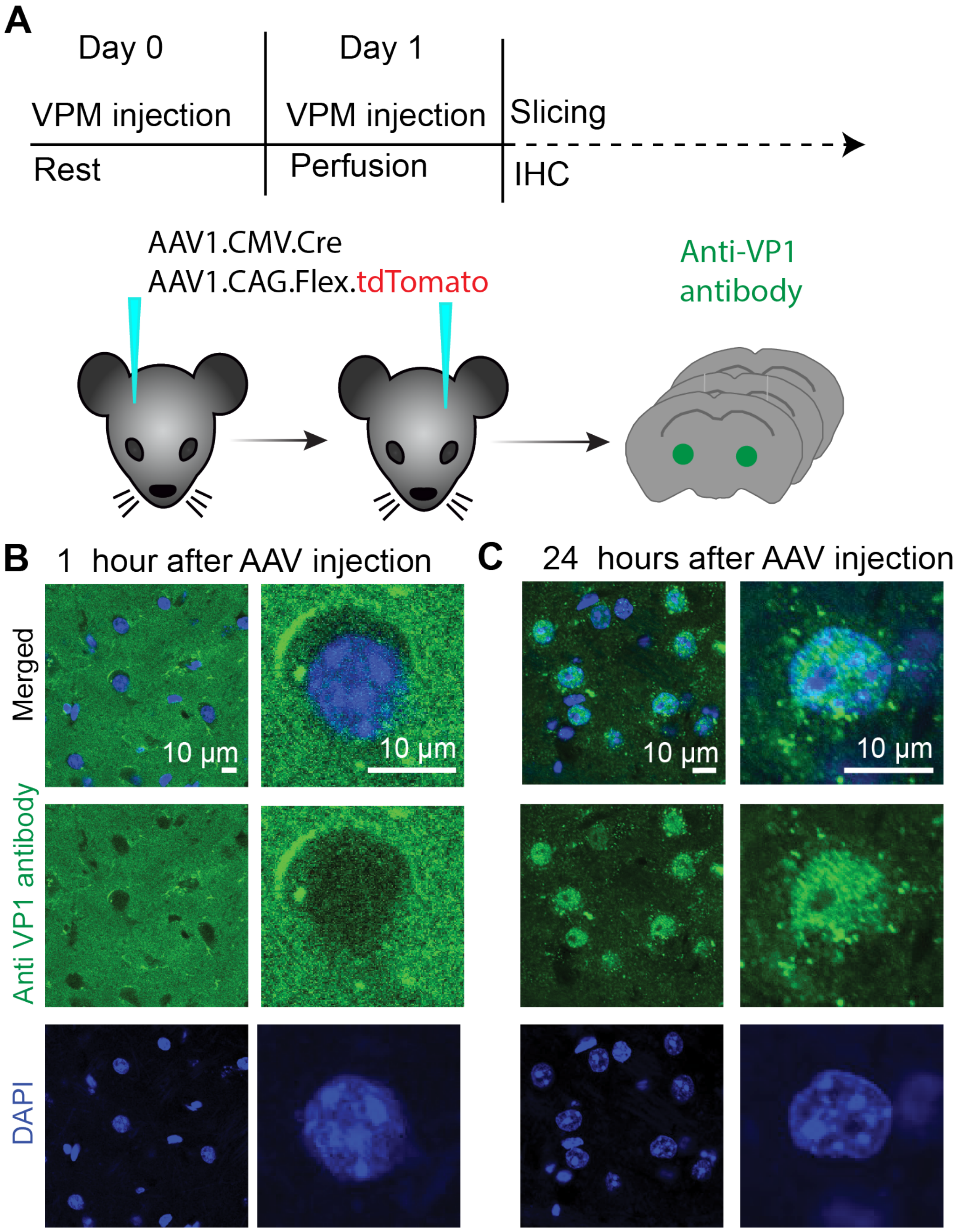
A
Day 0
Day 1
VPM injection
VPM injection
Slicing
Rest
Perfusion
IHC
AAV1.CMV.Cre
AAV1.CAG.Flex.tdTomato
Anti-VP1
antibody
B
1 hour after AAV injection
C
24 hours after AAV injection
Merged
Anti VP1 antibody
DAPI
10 µm
10 µm
10 µm
10 µm

Figure 2.3: AAV capsids enter thalamic cells within 24 hours after injection A) Experimental procedure: AAV1.CMV.Cre and AAV1.CAG.Flex.tdTomato were injected in the left VPM of mice (n=3; Day 0). Following 24 hours of rest (Day 1), the right VPM of the same mouse was injected with the same virus mixture (control) followed by perfusion of the animal within 1 hour from injection. Immunohistochemistry (IHC) was used to label AAV capsids with anti-VP1 antibody in brain slices. B) Confocal images of VPM 1 hour after AAV injection there. Nuclei are stained with DAPI (blue) and AAV capsids are tagged with anti-VP1 antibody (Alexa Fluor 488; green). AAV capsids form a cloud at the injection site but they don't co-localise with cell nuclei. C) Confocal images of VPM 24 hours after AAV injection. AAV capsids (green) co-localize with cell nuclei (blue).

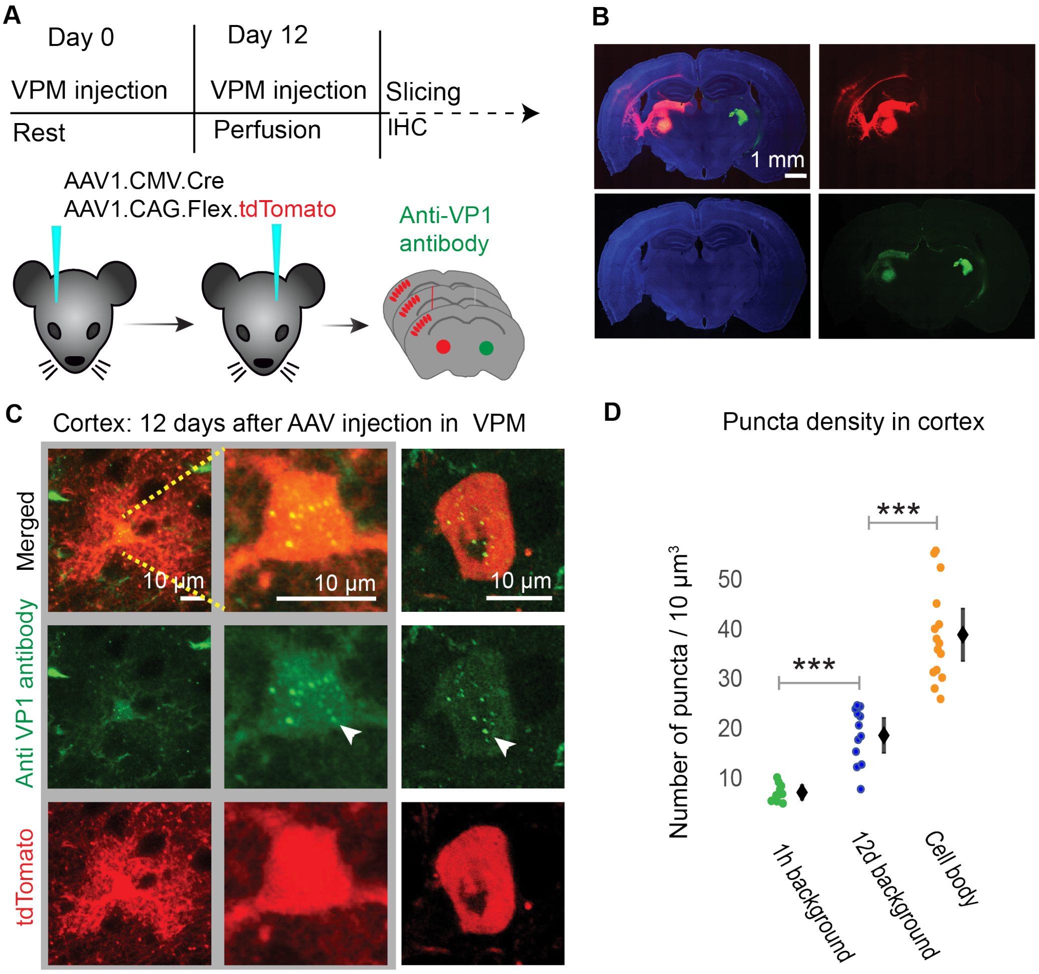
A
Day 0
Day 12
VPM injection
VPM injection
Slicing
Rest
Perfusion
IHC
AAV1.CMV.Cre
AAV1.CAG.Flex.tdTomato
Anti-VP1
antibody
B
1 mm
C
Cortex: 12 days after AAV injection in VPM
Merged
Anti VP1 antibody
tdTomato
10 µm
10 µm
10 µm
D
Puncta density in cortex
Number of puncta / 10 µm³
50
40
30
20
10
***
***
1h background
12d background
Cell body

Figure 2.4: AAV capsids are found in cortical astrocytes and neurons 12 days after injection in the thalamus. A) Experimental procedure: AAV1.CMV.Cre and AAV1.CAG.Flex.tdTomato were injected in the left VPM of mice (n=3; Day 0). Following 12 days of rest (Day 12), the right VPM of the same mouse was injected with the same virus mixture (control) followed by perfusion of the animal within 1 hour from injection. Immunohistochemistry (IHC) was used to label AAV capsids with anti-VP1 antibody in brain slices B) Confocal image of coronal brain slices labelled with tdTomato (red), DAPI (blue) and anti-VP1 antibody (green). 12 days after injection, tdTomato is expressed in the left but not in the right VPM (control). Anti-VP1 antibody tagged AAV capsids in both right and left VPM. C) Confocal images of a S1 astrocyte (left, mid) and neuron (right) in the left cortex labelled with tdTomato (red) and anti-VP1 antibody (green). Green fluorescent puncta can be seen in both astrocytic and neuronal cell bodies (see white arrow). D) Green fluorescent (Alexa Fluor 488) puncta density (number of puncta/ $10\mu m^3$) in the 1 hour background (mean = 8.1 ± 1.0 CI, 1.6 SD, n=10), 12 day background (mean = 19.6 ± 3.0 CI, 5.3 SD, n=12) and tdTomato$^+$ cell bodies (mean = 39.8 ± 4.7 CI, 9.2 SD, n=15) of the cortex. Data is represented as mean ± 95% confidence interval (CI). SD = standard deviation. Unpaired two tailed t-test was used with significance threshold set to $p < 0.05$. *** = $p < 10^{-5}$.

puncta in the cell bodies of tdTomato$^+$ S1 astrocytes and neurons (Figure 2.4 C). Quantification of puncta density (number of puncta / 10 μm^3) from 3D stacks revealed that the mean density of puncta in the cell bodies (mean = 39.8 ± 4.7 CI, 9.2 SD, n = 15) was higher (≈2x; $p < 10^{-5}$) than their local (12d) background (mean = 19.6 ± 3.0 CI, 5.3 SD, n = 12) (Figure 2.4 D). No tdTomato$^+$ cells or distinct green fluorescent puncta clusters were observed in the opposite S1. The mean puncta density of the opposite S1 background (1h background) was significantly ($p < 10^{-5}$) lower (mean = 8.1 ± 1.0 CI, 1.6 SD;), n = 10) than the 12d background (Figure 2.4 D) The 1h background puncta density is more representative of the actual signal noise. The 12d background also contained green fluorescence puncta clusters in tdTomato$^-$ cells and possibly puncta accumulated inside neurites. Also some homogenous labelling of what looked like blood vessels was observed throughout the brain using this antibody that was ignored in the analysis. The data was compared using unpaired, two-tailed t-test with the significance threshold set to $p < 0.05$. (CI = 95% confidence interval, SD = standard deviation).

"Traffic light labelling"

These findings suggest that following AAV injection in the VPM a small number of AAV capsids transport to the ipsilateral cortex and accumulate into neuron and astrocyte cell bodies. Considering that ≈1 week is needed for fluorescent proteins to be produced at visible levels following AAV transduction, anterograde AAV1 transport most likely occures within the first 5 days of VPM injection.

2.3.3 Mechanisms of intercellular AAV transfer

The mechanism of intercellular AAV transfer in unknown. Possible mechanisms might involve exosome release (Figure 2.6) or neuronal activity dependence (Figure 2.7). The general idea was to inhibit exosome production using the drug GW4869 or inhibit glutamatergic input to the VPM by plucking all contralateral whiskers. If these perturbations reduced the number of AAVs transferred from the VPM to the cortex I would expect a reduced number of labelled cells.

First I developed an AAV injection strategy to improve cell counting accuracy. Since the same fluorophores expressed in the VPM are also expressed in the cortex with the highest cell density in the regions of most thalamocortical axon projections (layer 4) it can result in low contrast and therefore high counting errors. I found that injecting AAV1.CMV.Cre, AAV1.CAG.Flex.eGFP and AAV1.CAG.Flex.tdTomato in the VPM leads to a spectrum of sparse, bright green, red and yellow (green + red) astrocytes and neurons (Figure 2.5 B, C). I termed this pattern of labelling “Traffic light labelling” (TLL). Brain slices from 2 mice infected with TLL AAV mixture (VPM, 70nl 1:1:1) were used to test the relative contribution of eGFP and tdTomato in the labelling of cortical cells. Mice were perfused 2 week after AAV injection. All visible cell bodies were manually selected (n=1019 ROIs). Their respective red (R) and green (G) intensity values were extracted and normalized to their respective minimum and maximum (Figure 2.5 E; top, middle). I then calculated the G/(G+R) values of these cells and plotted their probability histogram (Figure 2.5 E; bottom). This analysis

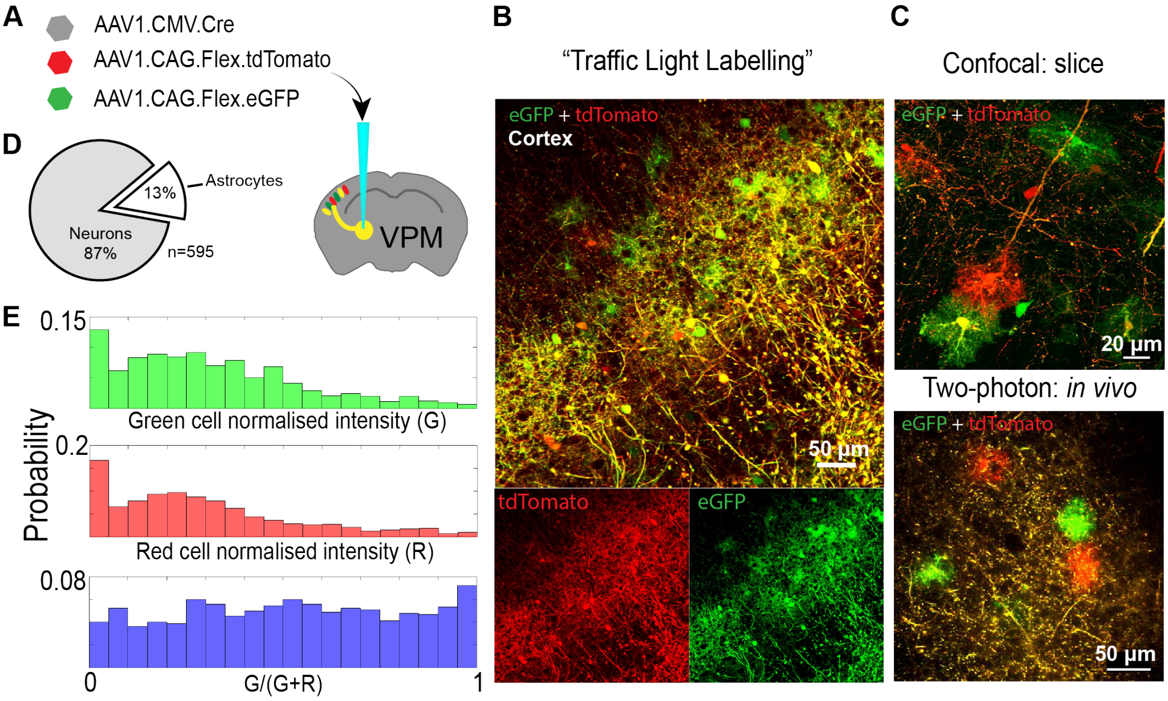
A
AAV1.CMV.Cre
AAV1.CAG.Flex.tdTomato
AAV1.CAG.Flex.eGFP
VPM
D
13%
Astrocytes
Neurons
87%
n=595
E
0.15
Green cell normalised intensity (G)
Probability
0.2
Red cell normalised intensity (R)
0.08
0
G/(G+R)
1
B
"Traffic Light Labelling"
eGFP + tdTomato
Cortex
50 µm
tdTomato
eGFP
C
Confocal: slice
eGFP + tdTomato
20 µm
Two-photon: in vivo
eGFP + tdTomato
50 µm

Figure 2.5: "Traffic light labelling" Injecting a mixture of AAV1.CMV.Cre, AAV1.CAG.Flex.tdTomato and AAV1.CAG flex.eGFP in the VPM results in bright red, green and yellow (red + green) astrocytes and neurons in the cortex. I term this effect "Traffic light labelling". A) Schematic of AAVs injected in the VPM. B) Confocal image of "Traffic light labelled" neurons and astrocytes embedded in yellow thalamocortical axons projecting from the VPM in a fixed brain slice two weeks after injection. C) Confocal (top) and *in vivo* two-photon microscopy image (bottom) of "Traffic light labelled" red and green astrocytes shows their minimally-overlapping domains in the cortex. D) Estimated percentage of astrocytes compared to neurons in the somatosensory cortex using "Traffic light labelling" (n = 595 cells). E) Histogram of the normalized green (G; eGFP; top) and red (R; tdTomato; middle) channel intensity values of labelled cortical cells. G/(R+G) histogram (blue; bottom) of "Traffic light labelled" cells (0 = cell is 100% red, 1 = cell is 100% green). 1019 cells from brain slices of 2 mice.

revealed that some cells are purely red while some others are purely green. However the majority of cells expressed a combination of tdTomato and eGFP. The flat G/(G+R) probability distribution further suggests that a small number of virus particles are delivered to cortical cells from the VPM.

Sorting astrocytes and neurons based on morphology (595 cells, 9 slices, 4 mice), I estimated that 13% of "Traffic light labelled" cells in the somatosensory cortex were astrocytes (Figure 2.5 D). Because of the wide spectrum of colours in the cortex "Traffic light labelling" offers high contrast (to yellow thalamocortical axons) that can be used to count cells in the cortex. "Traffic light labelling" was used to study the exosome (Figure 2.6) and activity dependence (Figure 2.7) of AAV transfer.

Exosome mediated AAV intercellular transport

Exosomes are ≈ 40 - 150 nm diameter extracellular vesicles secreted by most cells. Exosomes are thought to play roles in waste removal [27] and intercellular communication (i.e. they carry proteins, mRNA, lipids) [298]. Their membranes are rich in lipids such as ceramide, sphingolipids and cholesterol [89]

Maguire [211] showed that under normal conditions of AAV production a fraction of AAV particles are associated with exosomes in cell culture media. These exosome-associated AAVs were termed exo-AAVs or vexosomes (vector exosomes). Interestingly exo-AAVs had higher transduction efficiency and showed resistance to neutralizing antibodies compared to conventional AAVs. Maguire's lab later demonstrated that exo-AAVs are capable of efficient transduction in brain astrocytes and neurons [148].

Exosome and AAV pathways are similar. AAVs enter the cell through endocytosis, transfer to the early endosome (EE) followed by entry in the late endosome (LE)/ multivesicular body (MVB) and trans-golgi network (TGN). rAAVs released by endosomes can enter the nucleus through the nuclear pore complex (NPC). AAVs in MVBs can also be targeted for degradation in the lysosome [324]. Similarly, exosomes are formed by the maturation of the early endosome into MVBs. During this process the endosomal membrane invaginates to generate intraluminal vesicles. The vesicles are then released as exosomes through fusion of MVBs to the plasma membrane or targeted for degradation in the lysosome [137].

In neurons, the maturing late endosome can be anterogradely transported along the axon or converted to an MVB. The MVB then fuses with the cell body or dendritic membrane to release intraluminal vesicles as exosomes. MVBs are present in both axons and presynaptic terminals but there is no evidence of its MVB transport along the axon. It is postulated that the maturing late endosome is converted to MVB during its transport [379][181][8][153].

It is likely that viruses would evolve ways to hijack intercellular cargo transport mechanisms for their own proliferation. Other viruses are known to hijack the exosome pathway to aid their spread, infection and pathogenesis [311][176]. Therefore, considering that AAVs can associate with exosomes and that they share similar pathways inside the cell led to the hypothesis that inhibiting exosome production would decrease rAAV intercellular transfer. A summary of this hypothesis is illustrated in Figure 2.6 A.

To investigate if AAV intercellular transfer is exosome dependent I used the neutral

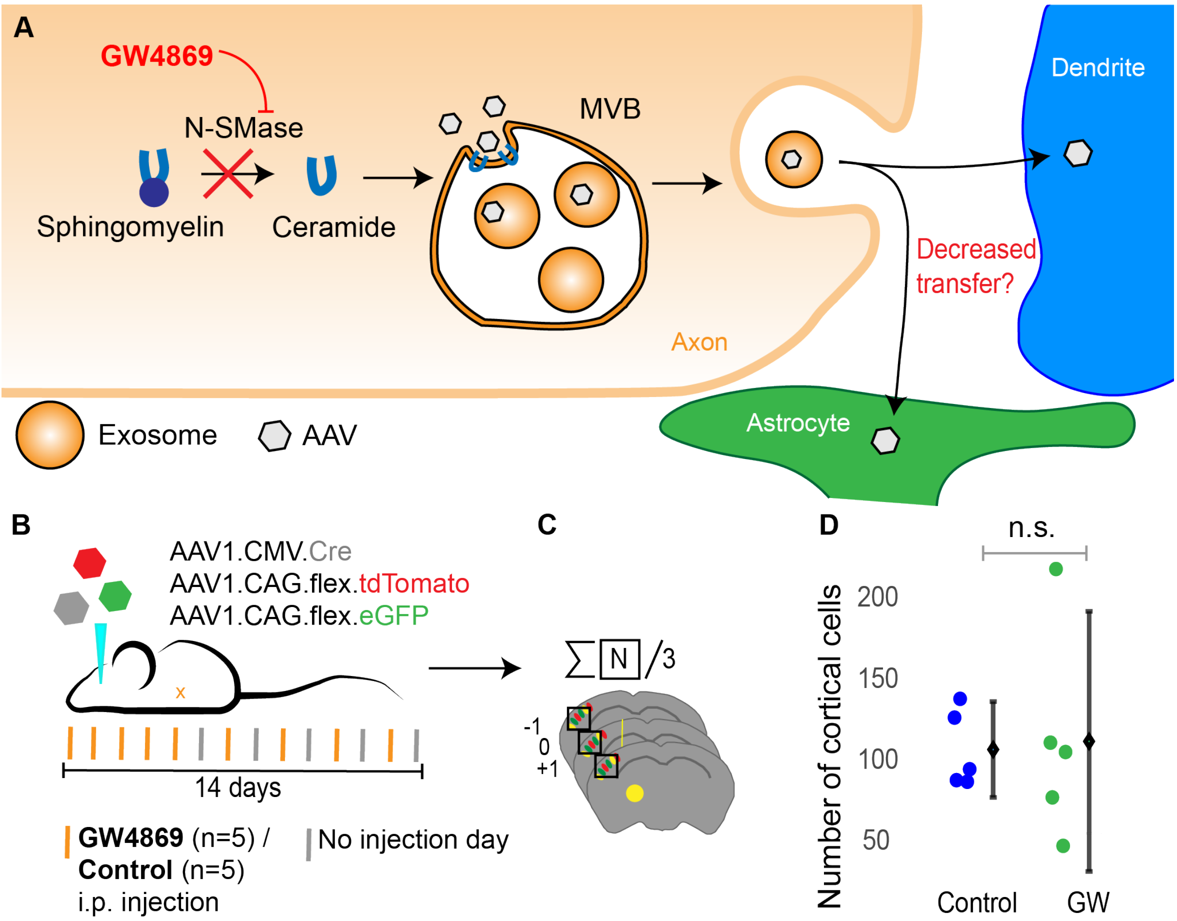
A
GW4869
N-SMase
Sphingomyelin
Ceramide
MVB
Axon
Dendrite
Decreased transfer?
Astrocyte
Exosome
AAV
B
AAV1.CMV.Cre
AAV1.CAG.flex.tdTomato
AAV1.CAG.flex.eGFP
x
14 days
GW4869 (n=5) / Control (n=5) i.p. injection
No injection day
C
∑N/3
-1
0
+1
D
n.s.
Number of cortical cells
200
150
100
50
Control
GW

Figure 2.6: Number of labelled 2nd order cells in S1 was not affected by the exosome inhibitor GW4869. A) Schematic of question: Does inhibiting exosome production using GW4869 reduces the number of 2nd order labelled astrocytes and neurons by intercellular AAV transfer? B) Schematic of experimental procedure: “Traffic light labelling” AAV mixture, is injected in the left VPM of mice (n=10) who were separated into a GW4869 group (n=5) and a control group (n=5). GW4869 or saline mixtures were injected every day for 5 days followed by every 2 days thereafter for 2 weeks in each mouse group respectively. C) The mean number of cortical cells was calculated based on the number of labelled cells found in pre-determined areas (area $\approx 6.7 \times 10^6$ μm^3 /slice; 3 slices) of the S1. D) Comparison between the mean number of cortical cells GW4869 (GW; 108.8 ± 52.5 CI, 59.9 SD) and control (103.6 ± 19 CI, 22.1 SD). Unpaired, two-tail t-test ($p = 0.87$). SD = standard deviation, CI = 95% confidence interval. Data is presented as mean ± CI. Significance threshold set to $p < 0.05$).

sphingomyelin inhibitor GW4869 to inhibit the ceramide-mediated inward budding of MVBs and the release of mature exosomes [183]. I used a protocol based on the work of Dinkins et al. [95] where they tested the effect of the drug in the adult mouse brain.

GW4869 was injected in mice (n=5) every day for 5 days (expected time interval of AAV transfer) followed by 2 day intervals for 14 days total (Figure 2.6 B). Mice were then perfused and their brains were sliced and imaged. I counted and averaged the number of labelled cells in 3 slices per mouse in a cubic area $\approx 6.7 \times 10^6$ μm^3, $\approx$1700 μm lateral the injection site centered on layer 4 (Schematic shown in (Figure 2.6 C). Comparison between the mean number of labelled cortical cells in the GW4869 group (108.8 ± 52.5 CI, 59.9 SD) and control group (103.6 ± 19 CI, 22.1 SD; n=5) revealed no significant difference between the two means (unpaired two tailed t-test, $p = 0.87$) (Figure 2.6 D). This suggests that GW4869 had no significant effect on the number of cortical labelled cells.

Neuronal activity mediated AAV intercellular transport

Another possibility is that intercellular AAV transfer is related to the activity of the infected neurons. I thought that a simple way to chronically decrease the activity of neurons in the VPM is to remove the sensory input (whiskers) associated with it. Early work by Durham & Woolsey [103] using the autoradiographic 2-deoxy-D-glucose showed that whisker plucking in rats results in decreased metabolic activity in the barrel cortex. This can be interpreted as a reduction in neuronal activity. Kelly et al. [173] expanded these findings using extracellular unit recordings of the rat barrel cortex showing that removal of principle whiskers leads to decreased activity in the associated barrel column.

To assess whether intercellular AAV transfer is activity dependent (Figure 2.7 A) I plucked all the whiskers (Figure 2.7 B) contralateral or ipsilateral (control) the injection site (VPM injected with TLL mixture) in two groups of mice ($n = 5$ each) respectively. Two week later the mice were perfused. Confocal imaging of their brain slices revealed no significant difference ($p = 0.35$) between the control (98.6 ± 30.2 CI, 34.3 SD) and experimental group (73.6 ± 31.7 CI, 36.1 SD) (Figure 2.7 D).

2.4 Discussion

2.4.1 A small number of AAV particles is anterogradely transferred to transduce 2nd-order astrocytes and neurons

First, I showed that AAV1s injected in the VPM enter thalamic cell nuclei within 24 hours of injection (Figure 2.3). I demonstrated this using anti-AAV antibodies instead of conjugating a dye to the viral capsid to avoid any possible interference to the natural intracellular and intercellular movement of the virus.

Second, using the same antibody I found punctated antibody labelling inside tdTomato$^+$ cell bodies of cortical astrocytes and neurons 12 days after vector injection in the VPM (Figure 2.4). These findings suggest that AAVs are transferred to the cortical cell bodies. Since cortical cells were tdTomato$^+$ within 12 days of injection, AAVs must have

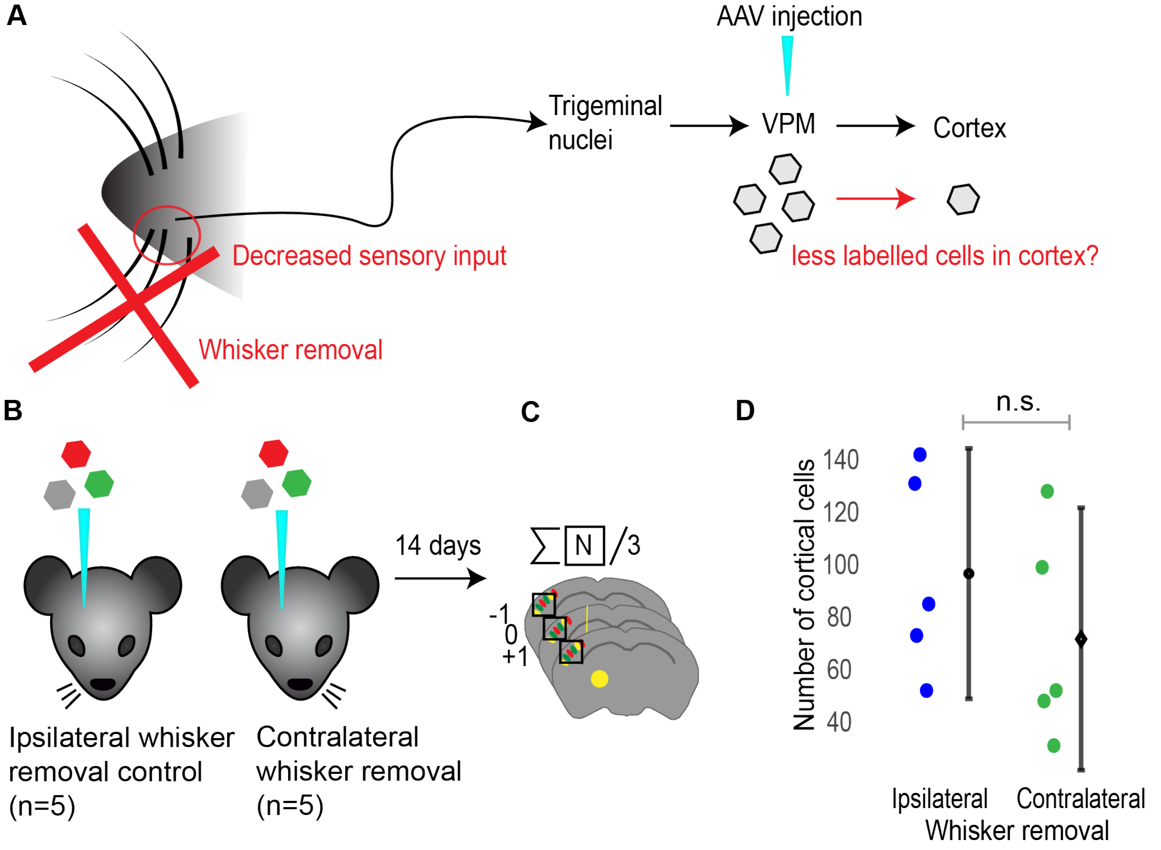
A
AAV injection
Trigeminal nuclei
VPM
Cortex
Decreased sensory input
less labelled cells in cortex?
Whisker removal
B
C
D
Ipsilateral whisker removal control (n=5)
Contralateral whisker removal (n=5)
14 days
∑N/3
-1
0
+1
n.s.
Number of cortical cells
140
120
100
80
60
40
Ipsilateral
Contralateral
Whisker removal

Figure 2.7: Number of labelled 2nd order cells in S1 was not affected by contralateral whisker removal A) Schematic of activity dependent hypothesis of AAV transfer. Removal of contralateral whiskers decreases sensory input to the trigeminal nuclei who in turn projects to the injected VPM. The hypothesis is that the number of viruses transferred from the VPM to the cortex following thalamic injection will decrease with lower neuronal activity resulting in less labelled second order cells. B) Experimental schematic: two groups of mice had either their ipsilateral (n = 5; control) or contralateral (n=5) whiskers to the injected VPM ("Traffic light labelling" AAV mixture) plucked for 2 weeks, followed by perfusion. C) The mean number of cortical cells was calculated based on the number of labelled cells found in pre-determined areas (area ≈6.7×10^6 μm^3 /slice; 3 slices) of the S1. D) Comparison between the mean number of labelled cortical cells in the contralateral whisker removal group (73.6 ± 31.7 CI, 36.1 SD; n=5) and ipsilateral whisker removal control group (98.6 ± 30.2 CI, 34.3 SD; n= 5). Unpaired two-tail t-test, p = 0.35. SD = standard deviation, CI = 95% confidence interval. Data is presented as mean ± CI. Significance threshold set to $p < 0.05$).

transferred soon after infecting VPM neurons to allow time for dsDNA synthesis and tdTomato expression. This is in agreement with findings by Cearley & Wolfe [66] who showed that anterograde and retrograde transfer of dye conjugated AAV9 to second order neurons can occur within less than 24 hours. The early onset of AAV transfer suggests that it didn't take place because of overexpression induced neuronal death at the VPM. The small number of puncta detected in cortical cell bodies compared to the dense antibody labelling in the VPM suggests that only a small number of AAV particles are transferred. It is possible that the puncta detected are capsid fragments that don't carry any DNA. Fluorescence labelling of second order cells suggests that either fluorescent proteins or genetic material (mRNA, DNA) was transferred. Considering the strong expression of fluorescent proteins observed in a minority of cells, DNA transfer through a small number of viral particles seems to be the most likely explanation.

Third, I showed that co-injection of AAV1.CMV.Cre, AAV1.CAG.Flex.tdTomato and AAV1.CAG flex.eGFP in the VPM results in bright, "brainbow" like labelling of S1 astrocytes and neurons (Figure 2.5). Because of the colour pattern observed (red, yellow, green) I termed this effect "Traffic light labelling" (TLL). TLL provides another indication that a small number of AAV particles is anterogradely transferred to 2nd-order cells based on the relative expression of tdTomato and eGFP in these cells (Figure 2.5 E). Thalamocortical axons are co-labelled with tdTomato and eGFP (yellow) suggesting a large amount of eGFP and tdTomato protein delivered there. If intercellular labelling occurred because of protein transfer I would expect a large amount of protein to be delivered to 2nd-order cells so they are detectable with fluorescent microscopy. Unless the cell has a way of sorting out tdTomato from eGFP I would expect that the majority of 2nd-order cells will be co-labelled (yellow). Instead we can observe a mosaic of red, yellow and green cells (Figure 2.5 B, C). Most cells express both eGFP(G) and tdTomato(R) at different proportions resulting in a flat $G/(G+R)$ probability distribution. A gaussian distribution centered on $G/(G+R) = 0.5$ would be expected if a large number of DNA or proteins were delivered. These indirect observations, also support the idea of elevated protein synthesis through a small number of DNA delivered to cells.

2.4.2 Axo-astrocytic AAV transfer offers a flexible toolkit for studying brain circuits

Fourth, I showed a set of injection strategies that can be used for labelling 2nd order astrocyte and neuron of the somatosensory cortex (Figure 2.2). AAV1.CMV.Cre injected in the thalamus and AAV5.GFaABC1D.Flex.lck.GCaMP6f in the somatosensory cortex primarily (a small number of unidentified cell bodies were also detected) labels cortical astrocytes (Figure 2.2 A). Using a similar intersectional approach with AAV9.hSyn.Flex.GCaM6f injected in S1 led to neuronal labelling exclusively (Figure 2.2 B). These observations suggest that intersectional approaches can be used for cell type specific manipulations. Both astrocyte and neuronal labelling is sparse using these strategies even though a large amount of vectors (Flex.GCaMP) are delivered in the cortex. This suggests that Cre recombinase (protein or via AAV mediated DNA expression) is delivered from VPM thalamocortical axons to astrocytes and neurons. Only a small amount of Cre recombinase is needed to recombine with the FLEX system and drive gene expression [340] [381]. Therefore, even if a few AAV Cre encoding vectors transduce cell nuclei, we can still expect strong fluorescence protein expression.

I also found that 2nd order astrocyte and neuron labelling can occur with a single AAV1-injection in the VPM. However a strong general promoter was necessary (CAG). For example AAV1.hSyn.TurboRFP injection in the VPM doesn't induce obvious labelling of cortical cells. It is possible that a large number of ssDNA copies carrying relatively weak promoters are needed for detectable amounts of protein production to occur. In the case of the strong artificial CAG promoters even a small number of ssDNA copies carrying them could be sufficient in producing detectable amounts of fluorescent proteins. This observation is in contrast to what Zingg et al. [415] reported. In their case, injection of AAV1.CAG.eGFP in V1 didn't results in 2nd order cell labelling. This might imply that the propensity of intercellular AAV transfer might depend on the brain area injected (i.e. neuronal subtypes infected and types of synapses involved). Interestingly, Zingg et al. [415] reported no 2nd order astrocyte labelling (using GFAP marker) in the pons and corpus callosum following AAV1.CMV.Cre injection in the V1 of Ai14 (Cre-reporter) mice. This is strange, because Ai14 mice should act as Cre-reporters for astrocytes, since crossing Ai14 mice with hGFAP-CreERT2 mice leads to astrocyte labelling [265]. Again, this might imply that anterograde AAV1 transfer may be neuron type and area specific. I also observed no astrocyte labelling along white matter axon tracts. Instead astrocytes (and neurons) are labelled at the projection sites of these axons (Figure 2.2). For instance we observe more dense neuronal and astrocytic labelling in L4 compared to L2/3 of the somatosensory cortex following AAV injection in the thalamus or an intersectional approach. Also the highest density of 2nd order cell labelling was far (>1mm) from the injection site and injection tract. Therefore, intercellular AAV transfer most likely takes place at axon terminals and is not an artifact of diffusion. It is thus not surprising that Zingg et al. [415] found no astrocyte labelling in the corpus callosum. My results indicate that second order cortical astrocyte and neuron labelling in the cortex by AAVs doesn't require Cre recombinase or a specific fluorophore delivered to the thalamus (Figure 2.2 C, D). This work contradicts the conclusions of Zingg et al. [415] that AAV spread is highly restricted to neuronal structures close to axon boutons since astrocytes are also labelled (at least in the somatosensory cortex). However, my observations reinforce their finding that AAV1 spread is anterograde since astrocytes do not send projections to the VPM, and thus can't be labelled by retrograde AAV transport. Further work is needed to elucidate whether anterograde AAV1 transfer to astrocytes is area and neuron type specific.

Using “Traffic light labelling" I estimated that 13% of labelled cells in the cortex are astrocytes (Figure 2.5 D). This is probably an underestimate since I categorized the cell type based only on morphology. It is likely that some astrocytes were mislabelled as neurons because their distinctive cloud like morphology might have been saturated by the intense thalamocortical axon projections to the barrels despite the use of “Traffic light labelling”. This estimate is likely to be different depending on the serotype and promoters used or the area of injection. The density of neurons and astrocytes in the mouse cortex is estimated to be ≈92000 cells/mm^3 [326] and ≈15696 cells/mm^3 (S100-beta [122]) respectively [171]. Astrocyte cell density is thus ≈15% of the total astrocyte and neuronal cell density (107700 cells/mm^3). Therefore, the cell type labeling pattern observed (13%) reflects the expected percentage of astrocytes to astrocytes and neurons in the cortex (15%). This suggests that AAV1 released by thalamocortical axon terminals enter both neurons and astrocytes in the somatosensory cortex with about equal probability.

Using "Traffic light labelling" (AAV1, 140nl in VPM), ≈100 neurons and astrocytes are expected in 6.7×10^6 μm^3 of somatosensory cortex (mostly in layer 4) to be labelled, which approximates to a density of 15000 cells/mm^3. Compared to the estimate of ≈108000 astrocytes and neurons/mm^3 expected in the mouse cortex [171] I estimate that only 14% of neurons and astrocytes are labelled by "Traffic light labelling" in the somatosensory cortex 2 weeks after AAV1 injection in the VPM. The result is sparse labelling of astrocytes and neurons with highest density in layer 4, the primary projection area of the VPM. Also the number of cortical cells labelled will most likely depend on the injection volume in the thalamus, AAV serotype, titer and vector constract (i.e. promoter, fluorophore, enhancer regions, size). Future AAV capsid discovery and engineering (i.e. directed evolution, rational design, new AAVs discovered and in silico design) has the potential to customize these vectors to optimize their potential to spread and target specific cell types [384], including astrocytes. Such innovations can revolutionize gene therapy and experimental neuroscience targeting astrocytes.

2.4.3 The mechanisms involved in anterograde AAV transfer remain unknown

The mechanisms of AAV release from thalamocortical axons to the cortex remains unidentified. I tested whether AAV transfer could be affected by exosome inhibition (Figure 2.6) or neuronal activity (Figure 2.7). For these experiments I made the assumption that a decrease in AAV transfer from thalamocortical neurons to 2nd order cells in the cortex will result in lower number of labelled cells. To inhibit exosome production I used the drug GW4869 and followed the protocol of Dinkins et al. [95]. I made a few modifications to the original protocol to improve the solubility of the drug (increased DMSO). I wanted to keep the protocol as close to that of Dinkins et al. [95] because I didn't have the means of quantifying the exosome reduction in the tissue following GW4869 administration. Since this important control is missing I can't be confident that my intervention led to the reduction of exosomes. Reduction expectation of serum exosomes and ceramide concentration using GW4869 was based on controls done by Dinkins et al. [95]. In their controls, the normalized percentage of Alix levels (exosome marker using immunoblot) in serum was ≈4 times lower than control. If this is true, I should expect a reduction in labelled cells (not necessarily 4 fold). However the baseline variability in the number of labelled cortical cells (standard deviation ≈60% of mean) is too high to allow accurate assessment of GW4869 induced effects (Figure 2.6 D). A larger sample size is required to accurately assess the effect of exosome inhibition in anterograde AAV transfer. I thus conclude that these results are preliminary and inconclusive. However, I think that this is a promising avenue for further investigation.

To test whether anterograde AAV1 transfer is activity dependent I assumed that chronic whisker removal will lead to lower excitatory input to the contralateral VPM. I didn't use any methods (i.e. electrophysiology) to assess if whisker removal actually decreased neuronal activity in the VPM. I didn't expect to eliminate entirely the activity of VPM neurons following contralateral whisker removal. There is a lot of spontaneous activity in the brain and the VPM receives other inputs as well (i.e. neuromodulators). I found that there was ≈25% reduction in the mean number of labelled cortical cells in the contralateral whisker removal group compared to control. While this reduction could be attributed to reduced neuronal activity in the VPM it can also be explained by random chance (standard deviation ≈50% of mean). A larger sample size and appropriate controls are necessary to more precisely assess the effect of neuronal activity of AAV1 transfer. I thus conclude that the results of these experiments are inconclusive. Further experiments should elucidate the mechanisms of intercellular AAV transfer. Possible mechanisms beyond the ones explored might include: direct phagocytosis of synapses carrying AAVs by astrocytes [74], microvesicle release [223], tunneling nanotubes [259] [1] or cytonemes [331].

2.4.4 Summary

AAV1s injected in the VPM transfer to 2nd-order astrocytes and neurons in the somatosensory cortex of mice. AAV capsid immunolabelling, sparse cell labelling and the heterochromatic nature of "Traffic light labelling" suggest that only a small number of rAAVs are transferred to these 2nd order cells. Since cortical astrocytes are labelled it suggest that AAV transport is anterograde from the VPM instead of retrograde. AAV transfer most likely takes place at synaptic terminals because most labelled 2nd-order cells are found in layer 4 of the somatosensory cortex (main projection site of VPM, barrel cortex) and no labelled cells are found along the thalamocortical tract. It is unlikely that AAVs spread by diffusion because most labelled cortical cells are found far away (>1mm) from both the injection site and injection tract. It is likely that a strong promoter is required to induce high gene expression in 2nd-order cortical cells with AAV injections only in the VPM. Direct AAV injection in the VPM has the advantage of labelling 2nd order cortical cells without injection close to the imaging area, thus minimizing damage there. Using Cre-Flex intersectional approaches with cell specific promoters (i.e. GFaABC1D and hSyn) I can leverage the property of AAVs to transport anterogrately to label specific 2nd-order cell types (astrocytes and neurons) without a very strong promoter (i.e. CAG). The mechanism of AAV transfer remains unknown.

Our findings suggest that anterograde AAV1 transfer can be used to study neuron-astrocyte and neuron-neuron interactions embedded in defined circuits (at least in the thalamocortical - somatosensory circuit). It also provides a way to sparsely label cortical cells for high contrast *in vivo* imaging. A notable implication of these findings is that care should be taken when using AAVs to manipulate cells locally in the brain since the intended effect is likely to spread to distal connected 2nd order astrocytes and neurons. For example chemogenetics is emerging as a popular tool for cell manipulation [307]. Local AAV delivery of genes expressing chemogenetic receptors (i.e. hM4Di, hM3Dq) in neurons locally followed by systemic injection of clozapine N oxide (CNO) will likely also affect astrocytes and neurons in distal connected regions. This may have unintended consequences that may lead to incorrect conclusions. This challenge can likely be alleviated by using AAV serotypes with weak CNS tropism. On the other hand it opens possibilities for anterograde targeting of astrocytes with chemogenetics and optogenetics. The sparse labelling of 2nd order cells limits its application to manipulations targeting a small number of cells. One such application is single astrocyte two-photon *in vivo* imaging. Because of sparse labelling and the lack of fluorescence in superficial cortical layers it should allow for high contrast single cell recordings.

2.5 Summary of findings

- rAAVs injected in the VPM can sparsely transduce astrocytes and neuron in the somatosensory cortex.
- A small number of AAV capsids are found in somatosensory cortex neurons and astrocytes following AAV injection in the VPM.
- Intersectional approaches can be used to target astrocytes or neurons with higher selectivity.

Chapter 3

Single-astrocyte $[Ca^{2+}]_i$ microdomain mapping in behaving mice

3.1 Motivation

Astrocytes are thought to respond to neuronal activity with $[Ca^{2+}]_i$ elevation mostly *ex vivo* [92] [261] [47] and *in vivo* [387] [200] [345]. Astrocyte Ca^{2+} signals in-turn may modulate neuronal activity [16] and local blood flow [229]. The bidirectional communication between neurons and astrocytes suggests that astrocytes may participate in information processing in the brain. However, it is controversial whether astrocytes respond with fast $[Ca^{2+}]_i$ signals to sensory stimuli [93] [250] [274] [48] [18] and dynamically modulate neuronal activity [111] [314] [32] under physiological conditions. Interestingly, some of these studies reported more pronounced astrocyte $[Ca^{2+}]_i$ responses to state dependent, neuromodulatory signalling compared to sensory stimuli and suggested that neuromodulation may increase the gain of astrocytes to local circuit activity [69] [93] [274]. Astrocyte Ca^{2+} signalling is altered with pathology [336] and anesthesia [359]. It is therefore important to preserve physiological conditions. While most studies focused on global, cytosolic calcium signalling, modern studies using membrane tagged genetically encoded calcium indicators (CECIs), revealed a rich spectrum of Ca^{2+} signals primarily at thin astrocytic processes [341] [345] [2]. The spatiotemporal characteristics of $[Ca^{2+}]_i$ signals and their interactions with multimolecular complexes are crucial for the versatile role of Ca^{2+} in cells [40] [77]. Therefore, it is important to account for the spatiotemporal characteristics of astrocytic Ca^{2+} signals since they may elicit different responses. It is also reported that astrocyte signalling may be circuit specific [216] [217] [67] [215] [404] and may be able to release different "gliotransmitters" under different conditions [81] [327]. It is thus important to understand the conditions and constraints of astrocyte calcium signals and their subsequent effects taking into account the conditions of the preparation and the heterogeneity of astrocyte signals, identity and relationship to local neuronal circuits.

Anterograde transfer of rAAVs from neurons to astrocytes (axo-astrocytic transfer; see chapter 2) offers a unique opportunity to investigate neuron astrocyte interactions within a given circuit. Sparse labeling of astrocytes with GECIs enabled by axo-astrocytic AAV transfer, should allow high contrast *in vivo* imaging. My aim was to use this method to study single-astrocyte Ca^{2+} dynamics in the behaving mouse to help elucidate the calcium code of theses cells under physiological conditions, *in vivo*. I chose to study astrocytes embedded in the whisker somatosensory system of the mouse because it is a well studied system [284] and astrocytes were reported to respond to whisker stimuli there [387] [356] [200] [201] [344] [345] [204].

3.1.1 Hypotheses

- Anterograde axo-astrocytic AAV transfer can be used to study single-astrocyte Ca^{2+} microdomains *in vivo*.
- Barrel cortex astrocytes respond to whisker touch stimulation with transient elevation in Ca^{2+} microdomains.
- Barrel cortex astrocytes respond to locomotion with prolonged, synchronized elevation in Ca^{2+} microdomains.
- Barrel cortex astrocyte Ca^{2+} microdomains are correlated to thalamocortical axon activity.
- Astrocyte fine processes exhibit heterogeneous Ca^{2+} activity hotspots that are stable over time.

3.2 Methods

All experimental procedures were approved by the OIST Institutional Animal Care and Use Committee (IACUC) in an Association for Assessment and Accreditation of Laboratory Animal Care (AAALAC International) accredited facility.

3.2.1 Animals

Male, 1 - 6 month old, C57/BL6 wild type mice (n = 6) were housed in reverse light/dark cycles. All experiments were performed during the dark cycle.

3.2.2 Surgery

Mice were anesthetized by intraperitoneal injection (i.p) of 0.1 ml/10g 3-mixture anesthetic (Medetomidine: 0.3mg/kg, Midazolam: 4 mg/kg, Butorphanol: 5 mg/kg diluted in 0.9% saline solution). Carprofen (5 ug/g; i.p), Dexamethasone (2 ug/g; intramuscular) and Buprenorphine (0.1 ug/g) were administered to reduce inflammation, immune response and pain respectively. Following anesthesia the eyes of the mouse were protected by covering them with mycochlorin eye ointment (Sato Pharmaceutical Co., Ltd). The head hair was trimmed and removed with a hair trimmer and hair removal cream (Veet). The animal's head was fixed to a stereotactic apparatus and its skin was sterilized with iodine before cutting it to expose the skull. The skull was cleaned with the local anesthetic lidocaine and leveled by aligning Bregma and Lambda. If further anesthesia was needed, 1% isoflurane was administered.

For chronic window implantation surgeries, a region above the somatosensory cortex and injection site (typically a circle of ≈ 2mm radius) was marked. The skull surrounding it was thinned with a drill. Instead of using forceps to remove the skull, I glued the base of a wooden cotton swab on the bone above the intended craniotomy and gently pulled it to expose the dura without damaging it [303]. Any bleeding was cleared carefully with Carprofen soaked gelfoam (Pfizer). AAVs were injected in the VPM only (n=3) or both VPM and somatosensory cortex (n=3) using glass pipettes (10-15 μm tip diameter). The injection coordinates used were based on the Paxinos brain atlas [275] and previous experiments (see chapter 2) measured from bregma. VPM: 1.8 mm posterior, 1.7 mm lateral, 3.5 mm deep, S1 cortex: 1.8 mm posterior, 3.2 mm lateral, 0.5 mm deep. AAVs were injected at ≈70 nl/ 5 minutes by air pressure application and the pipette was left to rest in the brain for at least 5 minutes before and after injection. A 5 mm diameter glass coverslip was placed directly on top of the craniotomy and fixed to the bone with a thin layer of super glue. A rectangular aluminum head plate was mounted above the glass window and fixed with dental cement (Super-Bond). Super-Bond was also used to cover any exposed skull. The animals were individually housed and allowed to recover for at least one week.

3.2.3 Adeno-associated viruses

To label somatosensory cortex astrocyte membranes with GCaMP6f, I injected 140nl AAV2/1.CMV.P1.Cre.rBG (1.2×10^{13} GC/mL; University of Pennsylvania Viral Vector Core) in the VPM and 140nl AAV2/5.GFaABC1D.Flex.Lck.GCaMP6f.WPRE.SV40 (1.0×10^{13} GC/mL; Sirion Biotech) in the somatosensory cortex.

To label thalamocortical axons and somatosensory cortex astrocytes, I injected 120nl (1:1:1 ratio) AAV2/1.CMV.P1. Cre.rBG (1.2×10^{13} GC/mL), AAV2/1.CAG.Flex. GCaMP6f.WPRE.SV40 (1.33×10^{13} GC/mL) and AAV2/1.hSyn.TurboRFP.WPRE.rBG (3.9×10^{13} GC/mL) (University of Pennsylvania Viral Vector Core) in the VPM.

3.2.4 Two photon imaging in awake animals

One week after surgery animals were habituated by periodic handling and exposure to head-fixation on a vertical, foam treadmill (r = 7.4cm) platform. A whisker stimulus was incorporated to the rotating treadmill in the form of a wooden rod (toothpick) inserted in the foam treadmill so as to periodically intercept the whiskers contralateral the injection site as the animal runs. Animals were briefly anesthetized with 2-3% isoflurane before head fixation and left to rest and recover from anesthesia for ≈10 minutes before two-photon (2P) imaging. 2P *in vivo* microscopy was used to study calcium signalling ≈2 - 3 weeks after injection (depending on the expression of GCaMP6f). A sCMOS camera and infrared light source were used to record behavioural activity (focused on the whisker pad of the animal) and whisker stimulation by the wooden rod. Since the wooden rod intercepting the whiskers also intercepted the light path to the sCMOS camera, the sharp change in light intensity detected by the camera was interpreted as a whisker stimulus. A second infrared camera (Sony) was used for online monitoring of animal behaviour during the experiment. A rotary encoder (E6A2, Omron) synchronized to the imaging setup was used to record the rotation of the treadmill.

In vivo imaging was performed using a custom-built combined wide field and two-photon (2P) microscope (MOM, Sutter Instruments) with a 25x/ N.A. 1.05 water immersion objective with 2 mm working distance (Olympus). A Ti:sapphire femtosecond-pulsed laser (Vision II, Coherent) was used to excite fluorescence at 950 nm (power measured after the objective < 60mW). The back aperture of the objective was underfilled to give an elongated point spread function (PSF) of $\approx$4mm. A resonant scanner was used to acquire images at 30.9 Hz. Fluorescence was detected by two GaAsP photomultiplier tubes (Hamamatsu) in the spectral range of 490–560 nm (green) and 570–640 nm (red) separated by a 565-nm dichroic mirror (Chroma). Commercial software (MScan, Sutter Instruments) controlled the microscope, analog channel acquisition, and behavior camera acquisition. Imaging was done 200 - 300 μm below dura (L 2/3) in the somatosensory cortex with 512×512 pixels and $94\times94\mu m^2$ field of view.

In order to image the same astrocyte repeatedly, I used a 5x/N.A. 0.25 air objective (Zeiss) followed by the 25x objective to map the blood vessel pattern directly above the astrocyte of interest. I used the blood vessel pattern on the brain surface to locate the x, y coordinates of the astrocyte of interest. I could find the same astrocyte by 2P scanning of the z-plane at the x, y coordinates established over consecutive days. This was relatively easy because of sparse labelling and since the approximate depth of the astrocyte was known. I then used the local autofluorescent puncta patterns, shape of astrocyte cloud perimeter and blood vessel perforation of the astrocyte cloud as references to accurately locate the imaging z-plane (1 - 3 days after the first recording).

3.2.5 Data analysis

Behavioural data extraction

To record whisker stimulation, I used the fact that the wooden rod intercepted both the whiskers and the IR light path to the camera (sCMOS). The momentary change in light intensity detected by the camera at the region of the whisker pad contralateral the injection side was translated to a signal. The whisker pad region was manually selected as a ROI in Fiji [318]. I binarized the thresholded light intensity extracted with the sCMOS (0 = no whisker interception, 1 = whisker interception) to detected whisker stimulation events.

The state of the animal was determined as a binary signal: running or resting. Movement of the mouse on the treadmill was extracted from the analog signal of the rotary encoder. If the running mouse stopped moving for less than a threshold of 1.5s and then continued running I considered it a state of continuous running. If the mouse moved less than threshold, its state was defined as at rest. If the wooden rod intercepted the whiskers (manually selected ROI), it was defined as a whisker stimulus. Most often the animal was running when the wooden rod intercepted its whiskers. I define this state as whisker stimulation. Sometimes, the animal would stop and explore the wooden rod with its whiskers during rest. I define that state as whisker exploration.

Preprocessing

Two-photon microscopy movies (30.9 Hz), rotary encoder analog signals and animal behaviour movies were synchronously recorded using MScan software. Proprietary video format files (MDF, Sutter Instruments Inc.) were converted to Tiff using commercial software (MView, Sutter Instrument). Time lapse recordings were preprocessed using Fiji. Movement artifact x, y drift was corrected using the TurboReg plugin (using stiff translation) and a custom macro to automate the process. Videos were then visually inspected to confirm movement artifact correction. A 1 pixel 3D gaussian filter was applied to all 2P image stacks (Fiji). A moving average (bin size = 3) was used to average the recorded video (30.9 Hz) down to 10.3 Hz to increase signal to noise ratio ($\approx$ 1.7x increase).

AQUA processing

AQUA (Automatic Quantification and Analysis) [388] was used for unbiased identification and characterization of astrocyte Ca^{2+} microdomain signals AQUA applies machine learning techniques to model calcium events in a ROI independent, data driven way that does not impose a priori assumptions about the data. All preprocessed time lapse movies used for AQUA processing had a nominal spatial resolution of $\approx$0.18 μm /pixel (optical resolution based on the PSF of the microscope: 1.0 μm; therefore, 5-fold oversampling) and a temporal resolution of 10.3Hz (0.097 seconds/ frame). AQUA performed further preprocessing by applying a Gaussian filter (smoXY = 2 SD). AQUA estimated the standard deviation of the noise (sigma). A conservative ΔF/F threshold was set for signal detection equal to 4 times sigma (thrARScl = 4). Also events with lower ΔF/F than 20% of peak ΔF were discarded (minShow1 = 0.2). AQUA excluded any calcium signals composed of >6 pixels (minSize = 6 pixels) and < 0.2s in duration (seedRemoveNeib = 2). Any events $<2\mu m^2$ (2×PSF) were also subsequently filtered out. No pixels were removed close to the imagining boundary (regMaskGap = 0). A temporal threshold (thrTWScl = 2) was set to discriminate between several events occuring in the same spatial location (defined as delta = thrTWScl×sigma). Voxels (x, y, t) with higher values compared to their spatial and temporal neighbours are termed seeds. To determine whether neighbouring pixels to each seed are similar enough to be included in the signal a growing z-threshold relating to noise is used (thrExtZ = 2). The assigned pixels to seeds form super voxels which in turn can be combined to form super events. This is classified by AQUA using three parameters: rising time uncertainty (cRise = 2), slowest delay propagation (cDelay = 2) and propagation smoothness (gtwSmo = 1). A z-score threshold was set to distinguish events from noise (zThr = 2). AQUA also compensates for possible bleaching that can occur during long recordings. This is done by cutting the video into sub-stacks (cut = 200 frames) to calculate baseline fluorescence (F0) through a moving average filter (movAvgWin = 25 frames). In case of effects like photobleaching AQUA can remove the baseline trend of an event intensity curve and fit it with a polynomial curve (of order correctTrend = 1). Unmentioned parameters were set to default. The same parameters were used for all single-astrocyte membrane microdomain calcium signal analysis. Different parameters were used for axon-astrocyte interactions analysis to match the recording characteristics of the preparation (see axon-astrocyte interaction section).

AQUA was used to extract four event characteristics: size, amplitude duration and frequency of events. Size refers to the maximum spatial extent of the Ca^{2+} signal (in μm^2), amplitude refers to maximum $\Delta F/F$ of the signal, duration refers to the maximum temporal extent of the signal (in seconds) and frequency refers to the number of events detected over time. Each event is described as a 2D binary footprint, whose area (basic.area) represents the event size (μm^2). The peak $\Delta F/F$ of each event (curve.dffMax2) was used a s measure for amplitude ($\Delta F/F$). Duration was calculated as the time between the starting (loc.t0) and stopping frames (loc.t1) of each event.

Statistics

All statistics were performed using Matlab (2015b) or Python (3.7). The normality of the distributions was assessed using the Kolmogorov-Smirnov test (kstest) with a significance threshold set at $p = 0.05$, and a straight line of the quantile-quantile (QQ) plot (qqplot). Normal distributed data was analysed using an unpaired t-test (ttest2; two independent groups), paired t-test (ttest; two paired groups), one-way ANOVA (anova1; multiple independent group comparison) for multiple groups comparison). Non-parametric data was analyzed using the Mann-Whitney U test (ranksum; two independent groups), Wilcoxon signed-rank test (signrank; two paired groups), one-way Kruskal-Wallis (kruskalwallis; multiple independent groups) or Friedman test (friedman; within-group design, multiple groups comparison). To counteract the problem of multiple comparisons I used Tukey's honestly significant difference (HSD) for normally distributed data. For the rest I used the more conservative Bonferroni correction. I sometimes used effect size comparisons between means to give a quantitative assessment about the magnitude of an effect. For parametric data I used Cohen's d (with pooled standard deviations). For nonparametric data I used Cliff's delta. Data was generally plotted as mean ± 95% confidence interval. A non-linear least squares function (Levenberg–Marquardt algorithm) was used to fit exponential functions to data. In all relevant cases, two-tailed tests were used (I never assumed the direction of change) and the significance threshold was set to $p < 0.05$ ($p < 0.05$ = *, $p < 0.01$ = **, $p < 0.001$ = ***).

Astrocyte membrane calcium microdomain signal analysis

I analyzed the membrane calcium activity of 6 astrocytes. Three of these astrocytes were recorded again 1 or 3 days later. For the analysis I included all 9 recordings unless otherwise stated. Mice transitioned between rest and run states during all recordings (Figure 3.1 D). Mice during 3 out of 9 recordings didn't stop to explore the whisker stimulus. Therefore no-data was gathered during whisker exploration state for these astrocytes.

I compared four calcium event characteristics: maximum amplitude($\Delta F/F$), maximum duration (s), maximum size (μm^2) and frequency (number of events/s) during the four behavioural states: rest, run, whisker stimulation (WS) and whisker exploration (WE). I compared the means of event characteristics (between group analysis) for all events (n = 50787) from all astrocyte recordings (n = 9) during rest (n = 29637), run (n= 15123), whiskers stimulation (n=2906) and whisker exploration (n = 3121). To compare frequency of events per voxel, the number of events were normalized to the size of each astrocyte in space (x, y) and time (t). A voxel refers to a 3D cube with x, y, t coordinates. The number of events was divided by the number of voxels in order to assess change in the frequency of events during different states (Figure 3.2 E). 3 astrocyte recordings were excluded when comparing event characteristic during whisker exploration state because the mouse was never in that state. I also compared the mean event characteristics per astrocyte (within group design, paired t-test, Figure 3.3 B, C, D) to control for variability between astrocyte recordings and recording time. All astrocyte recordings (n=9) were used to investigate the probability distributions of event characteristics (amplitude, duration, size) during different states.

To compare event characteristics during state transitions, all recordings were aligned to a transition point. The transition points used were, rest to run (226 transitions: 9s intervals, 4263 Ca^{2+} events), run to rest (177 transitions: 9s intervals, 3089 Ca^{2+} events) and whisker stimulation during run (279 transitions: 6s intervals, 5333 Ca^{2+} events). Transition events were only selected if the behaviour state was stable during the pre and post transition period. For example, during a rest to run transition the animal was at rest for at least 3s continuously followed by at least 6s of continuous running. The onset time (loc.t0) of each event was used to determine the Ca^{2+} characteristics in relation to state transition.

Astrocyte activity maps (heatmaps)

Astrocyte activity maps refer to overall activity patterns observed in astrocytes during long recording times (35 - 106 mins) represented in the form of a heatmap. A heatmap represents the proportion of events in space detected by summing the number of event 2D footprints detected by AQUA in time.

Heatmap generation

Motion corrected, two-photon Ca^{2+} signal recordings of single astrocytes were processed by AQUA. The Ca^{2+} signals were summarized as 2D footprints and binarized to 1. All binarized events were summed in time while maintaining their spatial coordinates to develop activity heatmaps for each astrocyte recording. Some heatmaps were limited to Ca^{2+} events occurring during specific behavioural states (rest, run or all states). In such cases, only frames associated with the respective behavioural state were considered. Real heatmaps (generated from real astrocyte recordings in contrast to random simulations, see below) were normalized to 1 minute and to their respective maximum pixel value unless otherwise stated.

Random Simulations

Simulations of activity heatmaps were created by randomly distributing binarized Ca^{2+} signals onto a mask corresponding to the real, recorded astrocyte. Calcium signals were approximated as ellipses of random orientation, center and eccentricity. These ellipses were incrementally added within the bounds of the astrocyte previously imaged (binarized maximum projection mask). The area of each ellipse was randomly sampled from the corresponding real astrocyte list of event areas. The total area of all ellipses in each random simulation was equal to the total area of real calcium events of their respective astrocyte recording. For example, when the total area of ellipses added to the simulation was equal to the total area of real event 2D footprints then no more ellipses were added to the simulation.

Heatmap comparison

Heatmap hotspot patterns were compared using the total continuous recording, video segments associated with the state of the animal, or subsequences of the respective video recording (splits) for within day or between day comparisons.

Within day: To compare activity heatmaps within same day (i.e. splits, see below) and between their respective random simulations, 2D image cross correlation (Matlab, xcorr2; 512×512 pixels; Pearson's correlation) was used. One of the images was translated to a position (translation vector) of maximum correlation. The maximum correlation coefficient was used as the correlation metric between the images.

Between days: To correlate activity heatmaps between days we created an activity mask to establish the boundaries of cell activity throughout the whole recording. The mask array had binary x, y values where 1 represents an event taking place. 2D cross correlation was used to find the maximum correlation between a stationary sample mask and one translated by a move vector. This allowed us to align the masks of the sample pairs and use 2D correlation between the heatmap pairs.

Splits: Subsequences of continuous video recordings as referred to as splits. 2D correlation between heatmaps generated from 70 minute long recordings and their shorter sub-sequences (split size = 2, 5, 10, 15, 25, 30, 35, 70 minutes) were used to determine what is a reasonable recording time to capture an accurate Ca^{2+} activity map. 70 minute videos were created by trimming out frames beyond the first 70 minutes in 5, >70 minute long recordings.

Similarly, 2D correlation between the activity heatmaps of rest state sequences (splits) of the same astrocyte (within day) were used to determine the stability of heatmaps over individual recordings. The splits were created from 5, 70-minute long astrocyte videos. Each video was split into 3 sequences of equal duration corresponding to the rest state of the animal. Their respective heatmaps were 2D correlated to each other (3 splits/astrocyte correlated, 5 astrocytes, 15 correlations). Alternatively, splits were correlated with the total running activity heatmap of their respective astrocyte (state comparison, 3 correlations / astrocyte, 5 astrocytes). Between day correlation of split heatmaps (n = 12) was obtained from the same astrocytes (n = 2) but during different day recordings (day 0 and day 1, 18 correlations between days).

Axon-astrocyte interactions

To study axon - astrocyte interactions I recorded the calcium activity of thalamocortical axon boutons (n = 8) labelled with GCaMP6f and TurboRFP in contact with individual astrocytes (n = 3 pairs) labelled with GCaMP6f in 3 different mice. Two regions of interest were manually drawn around axon boutons and astrocyte areas with approximately equal size at increasing distance from an axon bouton center (<3 μm, <6 μm) and another one far away from the bouton (>18 μm). The axon-boutons were identified based on their morphology, signaling characteristics and co-labelling with TurboRFP. The axon ROI was based on the maximum projection of the full recording to avoid any possible signal contamination due to uncorrected movement artifacts. Astrocyte territories were selected in the gliapil, avoiding to include axon boutons. The cell body and thick astrocyte processes were ignored in this study. The calcium activity was processed using AQUA. Some AQUA parameters were optimized differently for this preparation. The minimum event size cutoff threshold was set to >0.74 μm (minSize = 4), the spatial smoothing level was set to 1 SD (SmoXY = 1), the active threshold scale was set to 6 SD of noise (thrARScl = 6). Also 50 pixels close to the image border (regMaskGap = 50) were removed. Pearson's cross correlation (xcorr) was used to calculate the maximum correlation coefficient and correlation delay between axon bouton and local astrocyte Ca^{2+} activity initiated within ROIs within a predefined time window from axon signalling (1 and 1.5s) or from astrocyte signalling (1.5s). For correlation delay calculations we used the delay of maximally correlated events per trial. We then calculated the mean of all maximum correlation coefficients and correlation delays for each axon - astrocyte pair.

The axon signals outside the region of the astrocyte were used to investigate changes in axon calcium signalling during behavioural state transitions. These signals were also extracted with AQUA and they represent distinct points of $[Ca^{2+}]_i$ elevation, not distinct axons. The behavioural state transitions investigated and their respective axon Ca^{2+} signals were: rest to run (174 intervals, 8613 events), run to rest (52 intervals, 2274 events) and whisker stimulation during run (756 intervals, 28232 events). I also investigated astrocyte calcium signalling (constrained within ROIs to minimize contamination from axon signalling) changes during whisker stimulation (756 intervals, 6091 events).

3.3 Results

3.3.1 Single-astrocyte Ca^{2+} microdomain 2-photon imaging in awake mice

To achieve sparse astrocyte labelling I leveraged the ability of AAVs to transfer anterogradely via thalamocortical axons to cortical cells (see chapter 2). I injected AAV1.CMV.Cre in the VPM and AAV5.GFaABC1D.Flex.lck.GCaMP6f in the somatosensory cortex (Figure 3.1 A left). This allowed selective labelling of astrocyte membranes because of the GFaABC1D promoter (astrocyte specificity) and lck tag (membrane tagging). Following AAV injections, mice were left to recover for at least a week. I then introduced the mice to the vertical treadmill apparatus with embedded whisker stimulus so they habituate to the setup. When GCaMP6f expression was sufficiently high (typically $\approx$3 weeks post injection) I used *in vivo* two-photon microscopy to record the membrane Ca^{2+} activity of single astrocytes in layer 2/3 of S1 at 30.9 Hz (Figure 3.1 A). Astrocyte microdomain Ca^{2+} activity was automatically extracted using the event based software AQUA (Figure 3.1 B). AQUA enabled us to study astro-

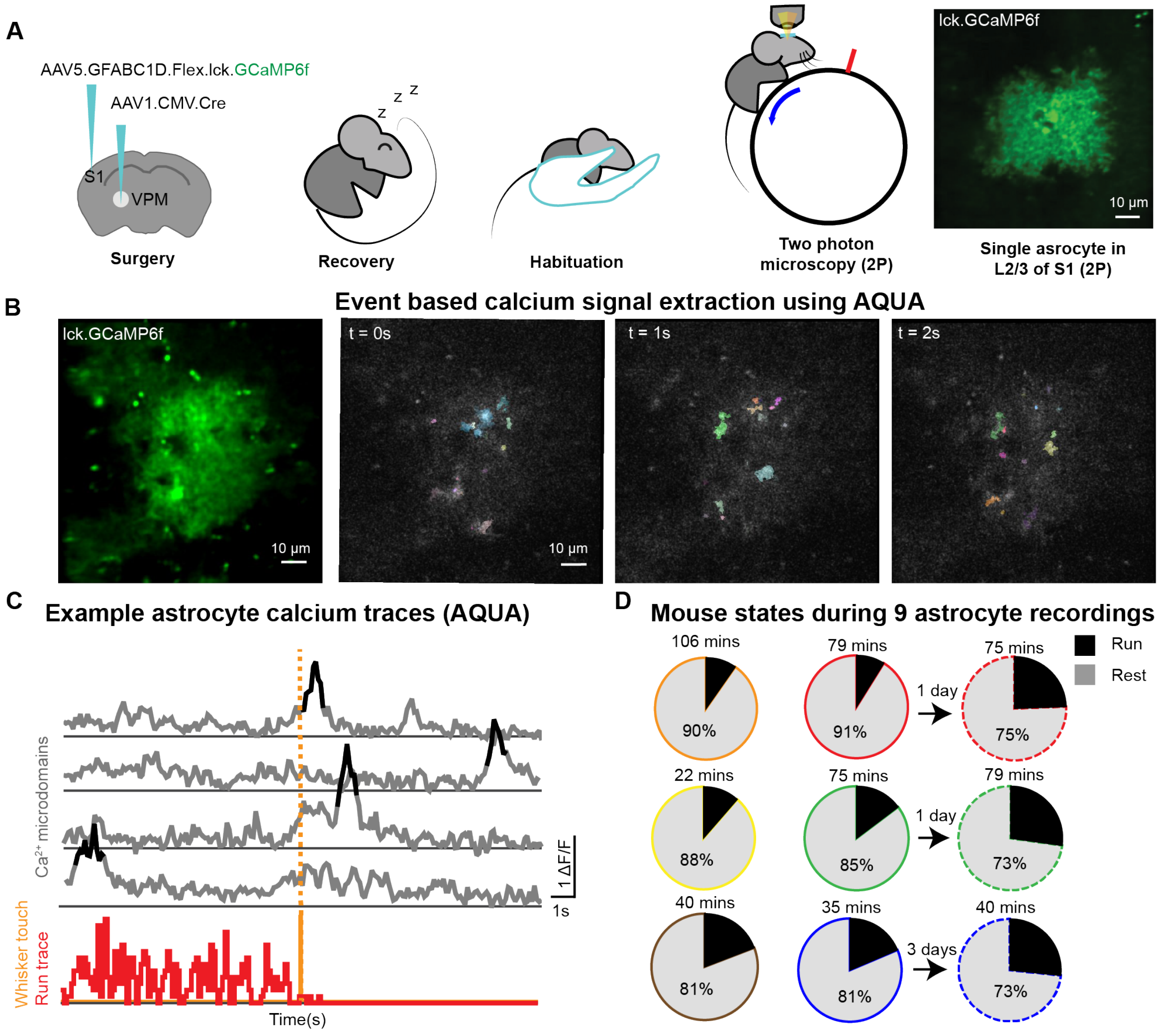

Figure 3.1: Experimental design. A) Double rAAV injection strategy used for sparse labelling of cortical (S1) astrocyte membranes with GCaMP6f. Mice were left to recover and habituate to head-fixation on a cylindrical treadmill embedded with a pole positioned to intersect with whiskers contralateral the injected cortex and VPM. Long duration 2-photon microscopy was used to record single astrocyte calcium signals in the awake mouse free to run on the treadmill. B) Examples of single astrocyte membrane labelling and AQUA processed calcium events represented as coloured 2D footprints. C) Example ΔF/F traces of astrocyte calcium events (black, extracted with AQUA during locomotion (red) and whisker stimulus (orange). D) Total recording duration (over each pie chart) and percentage of time mouse was at rest (gray) and run (black) state ($n = 9$). Each astrocyte ($n = 6$) is represented by a different colour pie chart outline. Same astrocytes recorder on consecutive days ($n = 3$) are represented by dashed lines of the same colour as their first recording.

cyte microdomain calcium activity without using predefined regions of interest (ROIs) in an unbiased way (examples of Ca^{2+} traces extracted shown in Figure 3.1 C). AQUA also enabled us to capture different characteristics of these Ca^{2+} signals such as their frequency, amplitude, duration and size. Since the animal was head-fixed on a rotating treadmill with an embedded whisker stimulus I was able to relate the characteristics of astrocyte Ca^{2+} activity to the behavioural state of the animal.

I investigated Ca^{2+} activity during 4 behavioural states: rest, run, rest with whisker stimulus (whisker exploration) and run with whisker stimulus (whisker stimulation) (Figure 3.2 A). I performed long duration (22 - 106 min) two-photon recordings of 6 astrocytes (3 mice). Three of these astrocytes were recorded again 1 or 3 days after the first recording. I studied the Ca^{2+} activity of all 9 astrocyte recordings while the animal was resting or running (Figure 3.1 D).

3.3.2 State dependent astrocyte Ca^{2+} activity

To get a general understanding of astrocyte Ca^{2+} activity I investigated the mean amplitude, duration, size and frequency (Figure 3.2 B-E) of all microdomains extracted during rest ($n = 29637$), run ($n = 15123$), whisker exploration ($n = 3121$) and whisker stimulation (within 1.5s of whisker stimulus during run, $n = 2906$) states. I used the Mann–Whitney U test to compare calcium event characteristics (amplitude, duration, size; Figure 3.2 B - D). I also estimated the effect size in order to give a quantitative measure of the magnitude of the change using Cliff's delta (delta). I compared calcium signal characteristic changes between rest vs run, rest vs whisker exploration and run vs whisker stimulation. I considered changes significant when $p < 0.05$.

There was a significant ($p < 0.001$) but small (delta = 0.10) decrease in the mean event amplitude (Figure 3.2 B), duration (Figure 3.2 C, $p < 0.001$, delta = 0.09) and size (Figure 3.2 D, $p < 0.05$, delta = 0.03) of events during whisker exploration compared to rest. There was a small (delta = 0.03) but significant ($p < 0.05$) increase in the mean event amplitude and size but not duration during whisker stimulation compared to run states. A significant increase was also observed in the duration ($p < 0.001$, delta = 0.09) and size ($p < 0.001$, delta = 0.12) of events during run compared to rest state. The size and duration of events were correlated (Figure 3.2 F) to each other (Pearson's product moment $r = 0.42$).

I next asked how the probability distribution of the event amplitudes, durations and sizes differ during different states (Figure 3.2 G-I). There appears to be no pronounced difference (confidence interval overlay) in the probability distribution of event amplitudes and durations during the four states (Figure 3.2 G ,H). However, we can observe a small increase in the probability of finding longer duration Ca^{2+} events ($>$ 1.2 s) during run compared to rest where we are more likely to find smaller events. The probability distribution of event durations seems to be composed of two distinct distributions. The probability distribution function of the natural logarithm of event sizes indicates that it is more likely to find larger ($> 5\mu m^2$) events during run compared to rest where it is more likely to find smaller ($< 5\ \mu m^2$) events (Figure 3.2 I). The event size probability function during rest and run can be approximated using exponential functions (Figure 3.2 J). The exponential function approximations for $\log_e$ event sizes indicate a higher time constant of decay during rest (0.54s) compared to run (0.60s).

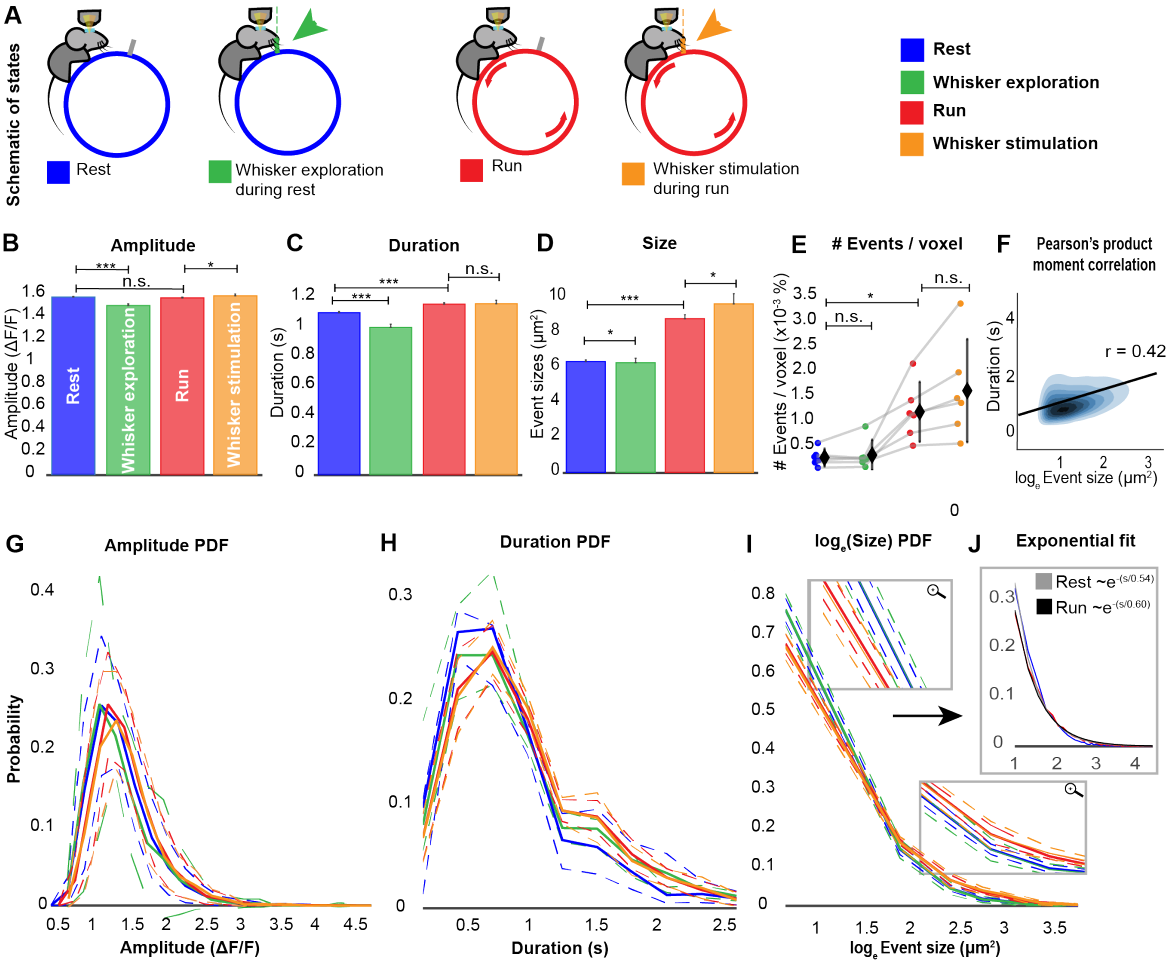

Figure 3.2: State dependent modulation of astrocyte membrane Ca^{2+} signal characteristics. A) Schematic of four behavioural states investigated, rest (blue) = no wheel rotation, whisker exploration (green) = whiskers intercepted by pole while animal is at rest, run (red) = wheel rotation triggered by mouse running, whisker stimulation (orange) = whisker interception by pole while animal is running. B-D) Differences in astrocyte calcium signal characteristics: B) Amplitude ($\Delta F/F$), C) duration (s), D) size (μm^2) during the four behavioural states (mean ± CI, Mann Whittney U test). E) Total number of events per voxel (x,y,t) per astrocyte (connected dots) during the 4 states (black dots = mean number of events per voxel of all astrocytes ± CI; paired, two tailed t-test). F) Pearson's product moment correlation between $\log_e$ event sizes and their durations. G- I) Probability distributions of event: G) amplitudes, H) durations and I) $\log_e$ sizes. Each line represents the distribution of the event characteristic during the 4 behavioural states: rest (blue), run (red), whisker stimulation (orange), whisker exploration (green). Dotted lines represent ± CI. J) Exponential fit of the probability distribution of $\log_e$ event sizes during rest (gray) and run (black). CI = 95% confidence interval. $p < 0.05$ = *, $p < 0.001$ = ***.

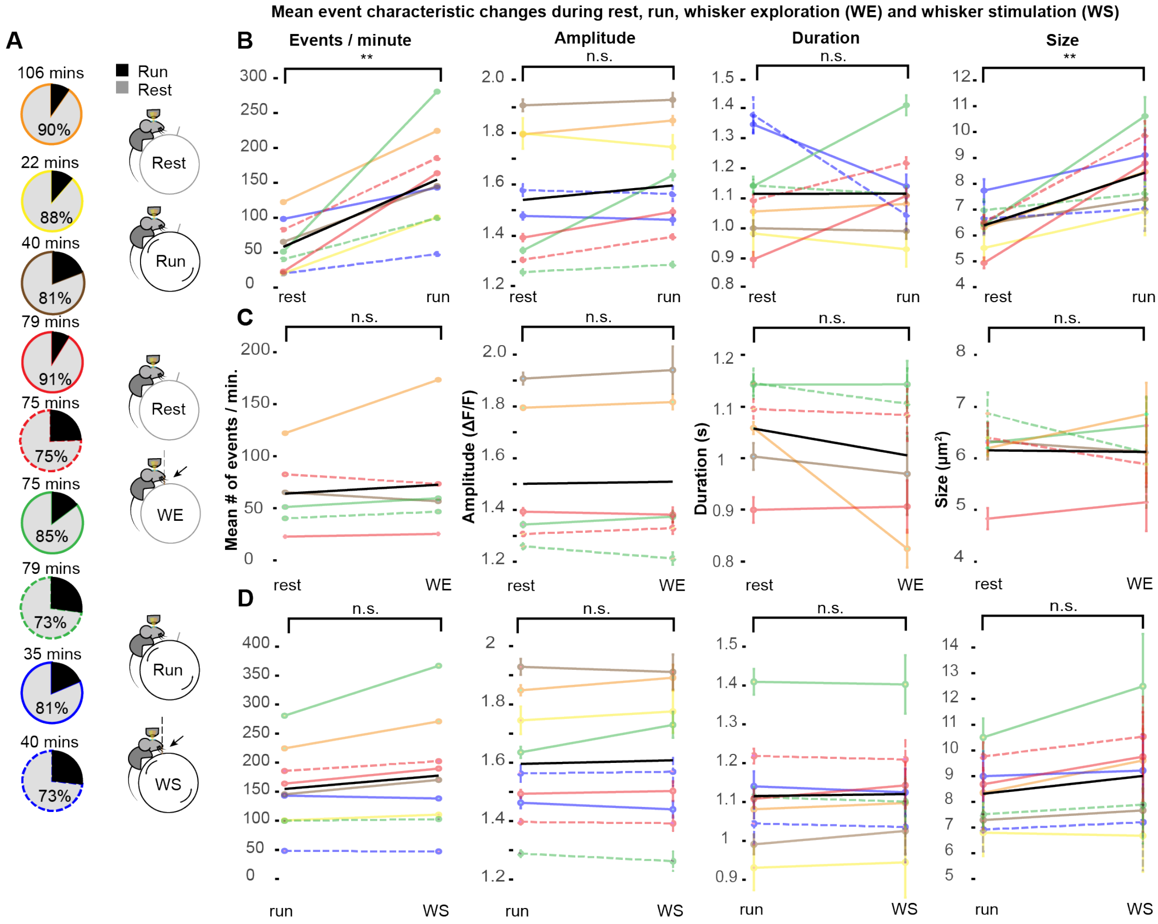

Figure 3.3: State dependent astrocyte Ca^{2+} event characteristics. A) Schematic of astrocyte recordings and behavioural state comparison. Pie chart colour outlines represent individual astrocyte recordings that correspond to lines in B, C and D. B) Mean frequency of events per minute, amplitude ($\Delta F/F$), duration (s) and size (μm^2) changes per astrocyte recording (coloured lines) during rest vs run, C) rest vs whisker exploration (WE), and D) run vs whisker stimulation (within 1.5s from whisker stimulation onset) (WS). Mean of all astrocyte recordings (black line). Dotted lines represent recordings of the same astrocyte (same colour line) on consecutive days. Paired, two tailed t-test, $p < 0.01$ = **, n.s. = non significant ($p > 0.05$).

I then calculated the mean Ca^{2+} event characteristics of each astrocyte during different states. I did that in order to give equal weighting to each astrocyte instead of emphasizing the contribution of longer recordings, like in the previous analysis. Grouping the data this way shows the contribution of individual recordings to the event characteristic mean (Figure 3.3). I compared the mean event characteristics (paired, two tailed t-test) of all the astrocyte recordings to assess general effects of behavioural states on astrocyte Ca^{2+} signalling. I found a large ($d = 1.72$), significant ($p = 0.001$) increase (≈166%, 58 to 154 events/minute) in the mean frequency of events during run compared to rest state (Figure 3.3 B). There was a non-significant increase (≈3.9%, 1.54 to 1.60 $\Delta F/F$, $p = 0.14$) of the mean amplitude of events during run compared to rest. The mean duration of events (1.11 to 1.12, $p = 1$) remained unchanged during rest compared to run state. In contrast, the mean size of events in all astrocytes increased significantly (≈32%, 6.3 to $8.3 \mu m^2$, $p = 0.003$, $d = 1.89$) during run compared to rest state. Therefore, there was a large ($d > 0.8$) increase in the number of Ca^{2+} events and their size, but not in their amplitude and duration during run compared to rest. In contrast, there was no significant change ($p > 0.05$, paired two-tailed t-test) in mean event characteristics during rest compared to whisker exploration (Figure 3.3 C) or run compared to whisker stimulation (within 1.5s of whisker stimulation) (Figure 3.3 D).

3.3.3 Astrocyte Ca^{2+} event changes during state transitions

I then asked how event characteristics change during 3 state transitions (Figure 3.4 A): rest to run (226 intervals, 4263 events), run to rest (177 intervals, 3089 events) and run to whisker stimulus (279 intervals, 5333 events). In all cases the event onset was used to align calcium event characteristics in time. The onset of event characteristics was plotted in time relative to the trigger onset (Figure 3.4) where the trigger was: beginning to run (red lines), stop running (blue lines), or whisker interception during run (orange lines). To compare the frequency of events (number of events/s) over time I used the Friedman test for within-group non-parametric analysis comparing event frequency between 1s time bins before (-1s from onset) and after (all) trigger onset Figure 3.4 B, C, D). To compare event amplitude, duration and size changes I used the Kruskal Wallis test (non-parametric, between-group). I compared the mean magnitude of all events before the trigger condition (representing the baseline) and each individual 1s bin after the trigger onset (Figure 3.4 E-M). Bonferroni post-hoc correction was used in all cases and the significance threshold was set to $p < 0.05$.

The mean frequency of events increased by ≈290% (0.95 to 3.7 events/s) following rest (baseline) to run state transition (Figure 3.4 B). The frequency of events decreased by ≈54% (2.4 to 1.1 events/s) following run (baseline) to rest state transition (Figure 3.4 C). There was a small increase (≈17%, from 2.9 to 3.4 events/s) in the frequency of events following whisker stimulation during run state (Figure 3.4 D). In contrast I found no change in the mean amplitude of events following rest to run (Figure 3.4 E), run to rest (Figure 3.4 F) and whisker stimulation during run (Figure 3.4 G) states. The mean duration of events increased (≈13%, 1.10 to 1.25s) only during rest to run state transitions (Figure 3.4 H) but not during run to rest (Figure 3.4 I) or following whisker stimulation (Figure 3.4 J). Similarly, the mean size of events increased (≈65%, 6.6 to $10.8 \mu m^2$) during rest to run (Figure 3.4 K) but not during run

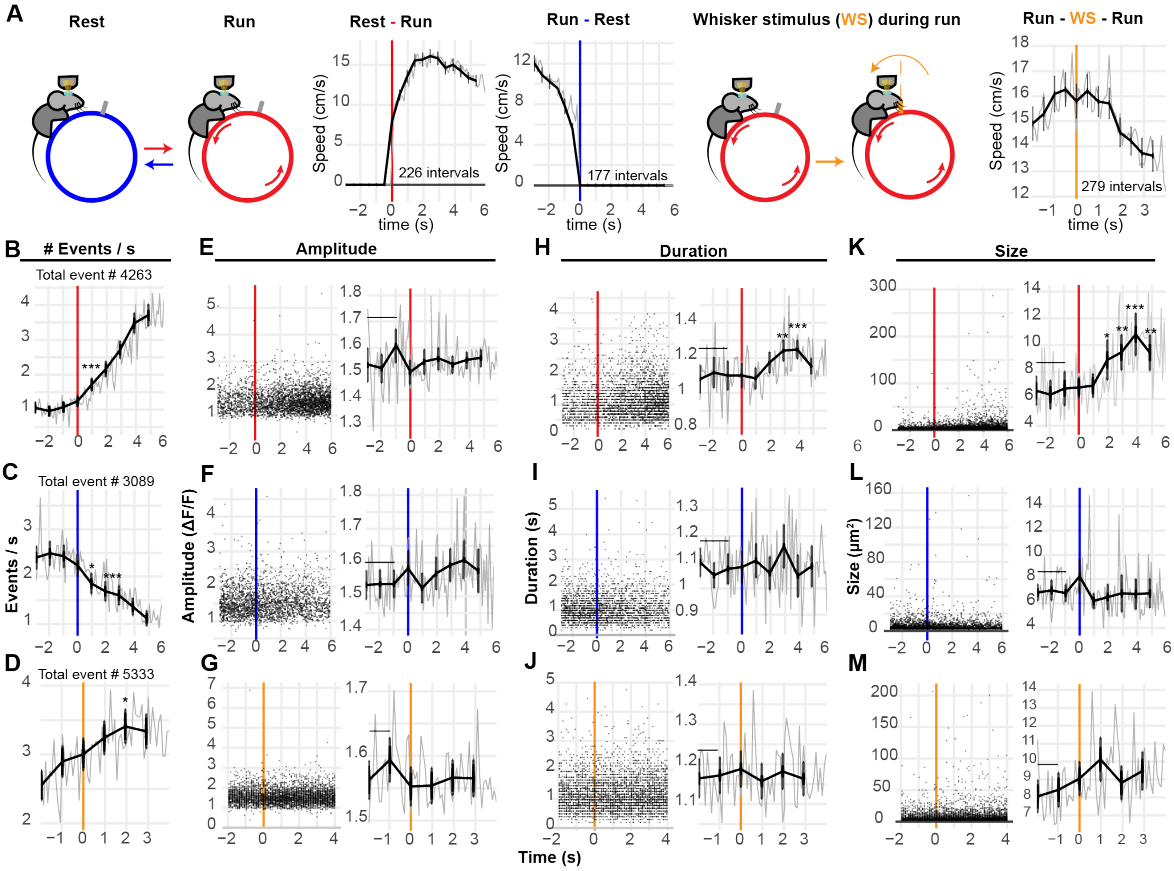

Figure 3.4: Astrocyte Ca^{2+} signal changes during state transitions. A) Schematics of state transitions investigated and their corresponding average running speed traces (gray = raw average, black = 0.5s binned average ± CI): Rest to run (red line), run to rest (blue line) and whisker stimulation (WS) during run (orange line). B) Mean frequency of Ca^{2+} events (number of events/s) during rest to run, C) run to rest and D) whisker stimulation during run (two-tailed, paired Friedman test, bonferroni post hoc). E) Mean (right) amplitude (ΔF/F) of individual Ca^{2+} event maximum amplitudes (left, raw data) during rest to run, F) run to rest transition, G) whisker stimulation during run. H) Mean duration (right) of individual Ca^{2+} event maximum durations (left, raw data) during rest to run, I) run to rest and J) whisker stimulation during run. K) Mean size (right) of individual Ca^{2+} event maximum sizes (left, raw data) during rest to run, L) run to rest transition and M) whisker stimulation during run (two-tailed, unpaired, Kruskal Wallis test, bonferroni post hoc). $p < 0.05$ = *, $p < 0.01$ = **, $p < 0.001$ = ***. Data is represented as mean ± CI. Gray trace = raw average, black trace = 1s bin average. CI = 95% confidence interval.

to rest (Figure 3.4 L) or whisker stimulation (Figure 3.4 M).

3.3.4 Astrocyte Ca^{2+} signals are not random

I then asked whether Ca^{2+} microdomains are randomly distributed in the space of the astrocyte. It is possible that the Ca^{2+} activity of astrocyte processes is heterogeneous allowing microdomains to act as specialized subcellular units. To answer this question all events detected by AQUA were summerd in time while maintaining their spatial characteristics (position and maximum size). If the probability of Ca^{2+} elevation is equal among processes, it should result in a homogeneous distribution of events given an infinite number of events. In other words, given that the probability of a calcium "puff" occurring at any x, y coordinate within the astrocyte territory is equal for all coordinates, then given infinite time (and thus infinite events) all x, y coordinates of the astrocyte should be exposed to the same number of events. Given a limited, but sufficiently large number of events, an approximately homogeneous distribution of calcium events within the astrocyte territory is expected. In contrast, if there are specific parts of the astrocyte that are more active than others, then hotspots of activity within the astrocyte territory are expected.

To test if astrocyte calcium activity is random, I performed >30 minute recordings of astrocyte Ca^{2+} activity in awake animals as previously described. All Ca^{2+} signals extracted (AQUA) were given a value $= 1$, and their duration was set to 1 frame. The spatial characteristics (i.e maximum size and x, y coordinates) of the Ca^{2+} events were maintained. The values of these signals were summed in time to give an activity heatmap and normalized to one minute and to their respective maximum pixel value. The heatmaps tell us how the number of events are distributed in space. Hotspots of greater activity (Figure 3.5 D, E, left) can be clearly seen, strongly suggesting that astrocyte Ca^{2+} microdomain activity is not random.

To test how astrocyte activity heatmaps should look assuming calcium signalling is random we built random simulations of astrocyte calcium activity. The random simulations were based on the real calcium signal characteristics of the respective astrocyte simulated. The shape of calcium events was approximated as ellipses whose size (μm^2) was randomly selected from a list of all real event sizes of the respective astrocyte recording simulated. Ellipses were positioned randomly (random x, y vector) within the astrocyte territory mask until they reached a combined size equal to the total size of real events. The sum of overlaying ellipse territory binary values was used to construct the random activity heatmap. These values were then divided by the respective real astrocyte's recording time and normalized to a period of one minute (Figure 3.5 D, E, right). We can observe that the random simulation heatmap pixel values are more homogenous (Figure 3.5 D, E, right) compared to real astrocyte activity heatmaps (Figure 3.5 D, E, left). I then asked how the frequency of normalized heatmap (real and random) pixel intensity values is distributed (Figure 3.5 F; area under the graph $= 1$, $n = 9$ astrocyte recordings). The frequency of pixel intensity percentile in real heatmaps can be approximated by an exponential (time constant of decay $= 0.18$). The maximum pixel intensity values observed in random simulation heatmaps were $<45\%$ (Figure 3.5 F, top) of the maximum pixel intensity values observed in real heatmaps (Figure 3.5 F, bottom). Pixel values above the 45% intensity threshold can be classified

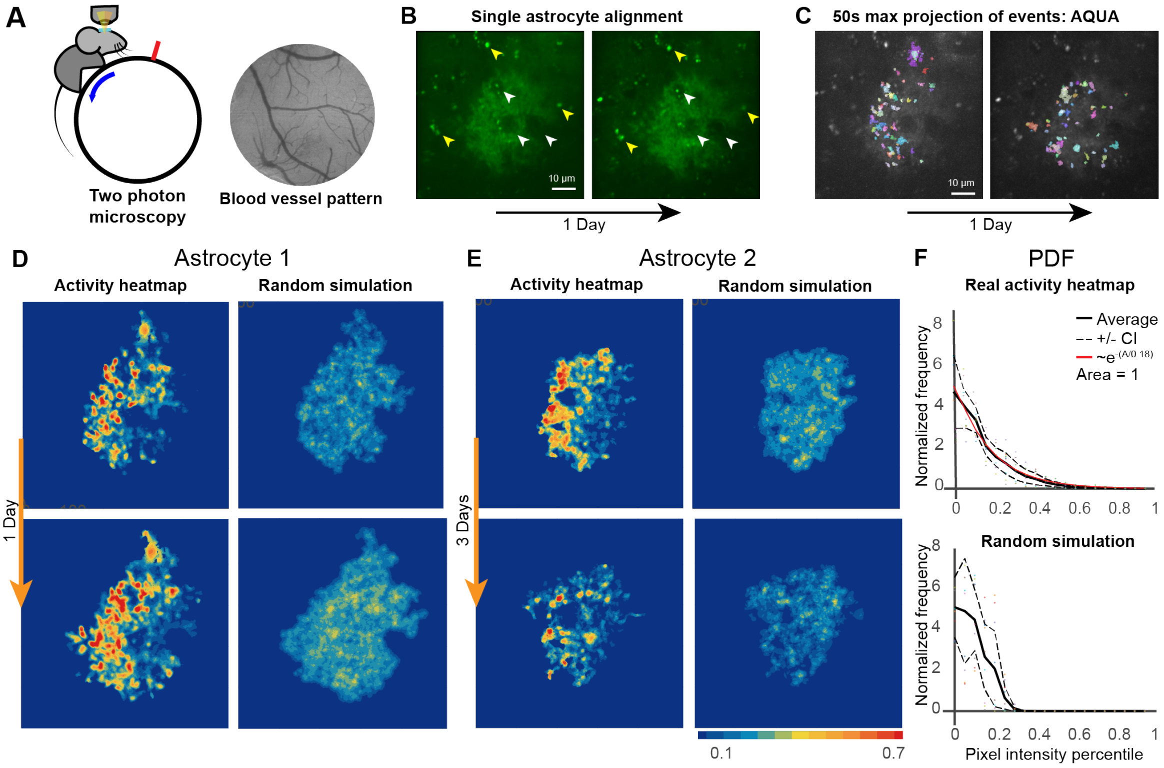

Figure 3.5: Astrocyte calcium activity is not random. A) Single astrocytes were recorded using two photon microscopy in mice free to move on a treadmill (schematic, left). The x, y coordinates of single astrocytes were mapped in relation to the blood vessel pattern obtained using wide-field microscopy (right). B) Z-plane alignment of the same astrocyte between days by aligning morphological features: astrocyte perimeter, blood vessels passing through the astrocyte (white pointers) and autofluorescent puncta patterns (yellow pointers). C). 50s maximum projection of Ca^{2+} signals extracted with AQUA of the same astrocyte recorded over 1 day. D) Astrocyte activity heatmap (all states) during day 0 (top left) and day 1 (bottom left) compared to their respective random simulation heatmaps (right). E) Activity heatmap of a different astrocyte during day 0 (top left) and day 3 (bottom left) compared to their respective random simulation heatmaps (right). All heatmaps are saturated to their 70% maximum pixel value. Random simulation heatmaps are normalized to the same range of pixel values as their respective real heatmap. F) Distribution of normalized heatmap (real: top, random simulation: bottom) mean pixel intensity value frequency ($n = 9$ astrocyte recordings, mean ± CI = black solid line ± black dashed line) and exponential distribution approximation (red line).

as hotspots, or Ca^{2+} activity patterns that aren't attributed to randomness.

3.3.5 Astrocytes display Ca^{2+} activity hotspots that are stable over time

I then asked whether hotspot patterns are stable over time. To test this I recorded again the Ca^{2+} activity of the same astrocytes (n=3) at the same z-plane over one (n=2) or three (n=1) days. To find the same astrocyte over days I used a combination of approaches. I used wide field microscopy to capture the blood vessel pattern of the brain surface above the astrocyte of interest (Figure 3.5 A). Since I knew the approximate depth of astrocytes (z) and position (x, y) relative to the blood vessel pattern on the surface, I could broadly locate the same astrocyte on consecutive days. To find (and align) the same plane of imaging I used the outline of the astrocyte, blood vessel perforation pattern through the astrocyte cloud, and autofluorescent background puncta patterns (Figure 3.5 B). I then performed long duration two-photon imaging of these astrocytes and extracted their Ca^{2+} signals using AQUA (Figure 5 C). Looking at the hotspot patterns of these astrocyte activity heatmaps (whole recording activity pattern) I noticed that the pattern had distinct similarities both between day 1(Figure 3.5 D left) and day 3 (Figure 3.5 E left) recordings.

Given the above observations I wanted to investigate in more detail the stability of this activity pattern (hotspots). First I asked how long a recording should approximately be to accurately capture the heatmap hotspot pattern. This is important since doing continuous, very long (hours) recordings can be an experimental limiting factor. To do that, the activity map was split into temporal segments of increasing duration (split size). Therefore a "split" refers to Ca^{2+} activity heatmap derived from segmented 2P recording. The split heatmaps generated from increasing duration segments (split size) were correlated (pearson's correlation) with their respective 70 minute recording heatmap (Figure 3.6 B). From the average correlation values obtained (5 astrocyte recordings) it can be estimated that ≈20 minute recordings are needed to obtain a heatmap pattern with ≈85% similarity to the full 70 minute long recording heatmap.

If the Ca^{2+} activity pattern of an astrocyte is similar over time and a ≈20 minute recording time is enough to capture this activity map with ≈85% accuracy, then splitting each long recording ($>$ 70 mins) into 3 shorter segments (≈20 mins splits each during rest state) and correlating them to each other should yield a high correlation between them if hotspots stable over time. To test that, astrocyte Ca^{2+} recordings ($>$ 70 mins) during rest state were split into 3 equal size ($>$ 17 mins) heatmaps and compared to each other. Common hotspot patterns could be clearly observed between single recording split heatmaps (Figure 3.6 A, white numbered arrows). Interestingly, similar hotspot patterns were also observed with splits between day recordings (Figure 3.6 A, Rest (split x/3), Day 0 - Day 1) as well as between rest to run (Figure 3.6 A, Rest - Run) and between run states (between days) (Figure 3.6 A, Run, Day 0 - Day 1). The heatmaps of interest were aligned, and their activity profiles were correlated. First, the split heatmaps were correlated with their individual random simulations (n = 15) to get an approximate baseline of the expected correlation coefficient (Figure 3.6 C, random, mean = 0.11, SD = 0.12, CI = 0.06), assuming correlation between random

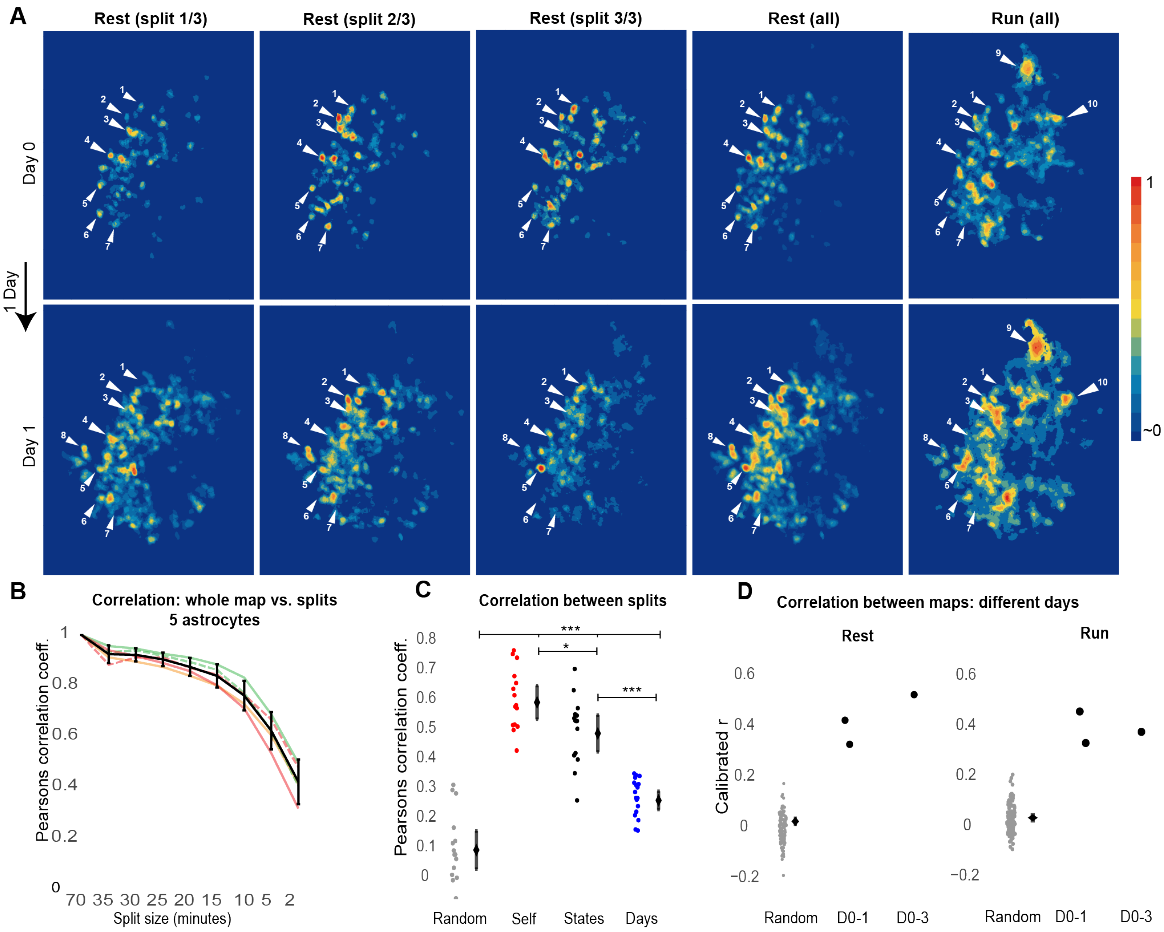

Figure 3.6: Astrocyte activity heatmaps are stable over time. A) Normalised activity heatmaps of the same astrocyte during day 0 (top) and day 1 (bottom) during rest and run states. Activity heatmaps during rest state were split in 3 equitemoral splits (Rest split 1 - 3, $\approx$20 minutes each). Similar hotspot pattern can be observed between different splits, days and states (numbered white pointers indicate examples of these hotspots). All heatmaps were normalized to their maximum pixel value. B) Pearson's correlation between the activity heatmap of astrocyte recordings (n=5, 70 mins each) and different size temporal splits (2-70 mins). C) Pearson's correlation between rest state splits (3 per astrocyte, 5 astrocytes) with: their respective random simulation heatmaps (gray), other splits of same day recordings during rest state (red), run heatmap of same day recordings during run (black) and splits of same astrocyte recordings a day later during rest (blue). Mean ± SD, One-way ANOVA with Tukey's HSD, $p < 0.05 = *$, $p < 0.01 = **$, $p < 0.001 = ***$. D) Pearson's correlation between heatmaps when the mouse is at rest or run state during different days (black dots, D0-1, D0-3) and between 25 random simulations of each recording (total 75 simulations, gray dots, black rhombus = mean ± CI). The correlation value between real heatmaps and their respective random simulations is linearly scaled so the random simulation mean correlation value = 0.

heatmaps. We then quantified the correlation coefficients between real heatmap splits of the same astrocytes (5 astrocytes, 3 splits each, n = 15 comparisons) during single recordings (Figure 3.6 C, Self splits, mean = 0.61, SD = 0.10, CI = 0.06). We then quantified the correlation coefficients of heatmap splits during rest with their respective recording's overall activity heatmap during run state (Figure 3.6 C, state splits, mean = 0.50, SD = 0.11, CI = 0.06). Finally, I correlated the split heatmaps (rest state) of the same astrocyte (2 astrocytes, 3 splits/ astrocyte, day 0 - day 1 recordings, n = 18 comparisons) between days (Figure 3.6 C, Day splits, mean = 0.28, SD = 0.06, CI = 0.03). I used one-way, between-group ANOVA (two-tailed, with Tukey's HSD) to compare the above correlation coefficient values. There was a significantly greater mean Pearson's correlation coefficient for all map comparisons: self splits ($p < 0.0001$, state splits ($p < 0.0001$) and day splits ($p = 0.0001$) compared to random. There was a significant decrease in the mean correlation coefficient (≈0.6 to ≈0.5) of state splits compared to self splits ($p < 0.03$). There was a significant decrease in the correlation between day splits compared to both self splits (≈0.6 to ≈0.3, $p < 0.0001$) and state splits (≈0.5 to ≈0.3, $p < 0.0001$). These results suggest a high correlation between the activity pattern within a recording day that decreases between states and between recording days.

In order to get a better approximation of heatmap similarities between days I compared the total recording heatmap (more averaging in time and therefore a more accurate heatmap pattern) of each astrocyte (n=3) during the same state (Figure 3.5 D) but between different days. For example, the rest state heatmap of day 0 recording vs the rest state heatmap of day 1 recording of the same astrocyte. We compared the correlation values between real heatmaps and 25 random simulations per astrocyte (75 total/ comparison). The correlation values between real heatmaps was calibrated so the mean correlation coefficient of their respective random simulations was = 0. For example, if the mean correlation coefficient of the random simulation for astrocyte 1 was equal to 0.1 and the actual correlation between rest states during different days was 0.5 it would calibrate to mean random simulation correlation = 0 and real correlation = 0.4. This calibration was performed to control for factors other than Ca^{2+} activity that could contribute to an increase in correlation coefficient values (i.e. size of mask). I found that the calibrated correlation coefficient between real heatmaps of all astrocytes during rest (mean $r = 0.43$) and run (mean $r = 0.39$) states (mean r between all states = 0.46) was higher than the full range of random simulation with real heatmap correlation coefficient values above the mean ($r > 0.2$). This observation suggests that there is high similarity between activity heatmaps during either rest or run states between consecutive days of recording.

Together the above findings suggest that astrocyte Ca^{2+} activity is not random. The probability of having a calcium event is higher in some parts of the astrocyte than others. These activity patterns can be extracted over long durations and summarized as activity heatmaps. Heatmaps are stable between days and states suggesting the existence of astrocyte activity maps in the brain.

3.3.6 Axon-astrocyte interaction

Next, I wanted to investigate if astrocyte Ca^{2+} microdomains are correlated to nearby thalamocortical axon activity. To do that, I injected AAV1.CMV.Cre, AAV1.CAG.Flex. GCaMP6f and AAV1.hSyn.TurboRFP in the mouse VPM (Figure 3.7 A). This injection strategy leads to thalamocortical axon labelling with TurboRFP and GCaMP6f (for more details see chapter 2) while cortical astrocytes are labelled only with GCaMP6f. An important feature of this strategy is that there is no injection in the cortex thus alleviating any possible pathological effects triggered by local AAV injections. This strategy also allows for general astrocyte labelling instead of focusing only on membrane calcium activity (no lck tag). Using *in vivo* 2P microscopy in awake mice free to move on a vertical treadmill apparatus embedded with whisker stimuli, I was able to study axon-astrocyte interactions (n= 3 astrocytes, 3 mice) during different states. Axons within astrocyte territories were clearly distinguishable because only axons expressed the TurboRFP marker (Figure 3.7 B). Also the axon bouton calcium activity profile (functional puncta) was starkly contrasting the cloud like morphology of astrocytes.

If axon bouton Ca^{2+} activity (which is associated with neurotransmitter release) triggers Ca^{2+} elevation in nearby astrocytic processes, their Ca^{2+} signals should be correlated to each other. I thus hypothesised that there should be a higher correlation between the Ca^{2+} activity of an axon and its local (near, < 6 μm from bouton center) astrocyte processes compared to processes far away from that axon. To test this hypothesis, ROIs were manually drawn around the maximum z-projection of 8 axon boutons within the astrocyte territory (n = 3 astrocytes). 2 concentric ROIs were manually drawn around each axon bouton with ≈ 3 μm and < 6 μm radius from its center. A third, control ROI of approximately the same size far (>9 μm) from the selected bouton (Figure 3.7 C) was also drawn. Care was taken to avoid selecting axons within astrocytic ROIs to avoid signal contamination. AQUA was then used to extract Ca^{2+} signals initiated within these ROIs (example traces shown in Figure 3.7 D).

Thalamocortical axon and astrocyte Ca^{2+} signalling during behavioural state transitions

First I tested how thalamocortical axon activity changes with state transitions and whisker stimuli. To do that I used all the axons outside the astrocyte territory (Figure 3.7 C, white arrows) so the signal is not contaminated by astrocyte Ca^{2+} activity. I found that during rest to run state transitions (n = 174 intervals) the mean frequency of axon Ca^{2+} events (n= 8613 events) started increasing from rest baseline (mean = 3.8 events / s ± 0.4 SD, 0.3 CI) $\approx$0.5s before the animal started running, reaching a peak event frequency $\approx$0.3s (129% increase; 8.7 events / s) after run onset quickly decaying (within $\approx$0.3s from peak) to the average event frequency (events/ s) during run (5.9 ± 0.6 SD, 0.2 CI; Figure 3.7 E). During run to rest state transitions (n = 52 intervals) the mean frequency of axon Ca^{2+} events (n = 2274 events) started decreasing from run baseline (mean = 7.2 ± 0.9 SD, 1.0 CI) $\approx$1s before the animal stopped running (during deceleration period) down to the baseline resting frequency (47% decrease; mean = 3.8 ± 0.4 SD, 0.2 CI) at t = 0 (Figure 3.7 F). The mean event frequency increased by ≈97% from mean run baseline frequency (5.8 events/s), to 11.4 events/s, 0.2s after the onset of whisker stimulation (WS) during run (754 intervals, 28232 events). Mean run baseline event frequency = 5.8 ± 0.8 SD, 0.2 CI; Figure 3.7 G. A sinusoidal event frequency pattern in time was observed (Figure 3.7 G) presumably because of the repeating whisker stimulation triggered by the rotation of the treadmill (Figure 3.7 I). In contrast, the mean frequency of astrocyte events extracted from all ROIs (n = 35) selected didn't change with whisker stimulation during run state (Figure 3.7 H). These results suggest that thalamocortical axons respond to whisker stimuli and locomotion.

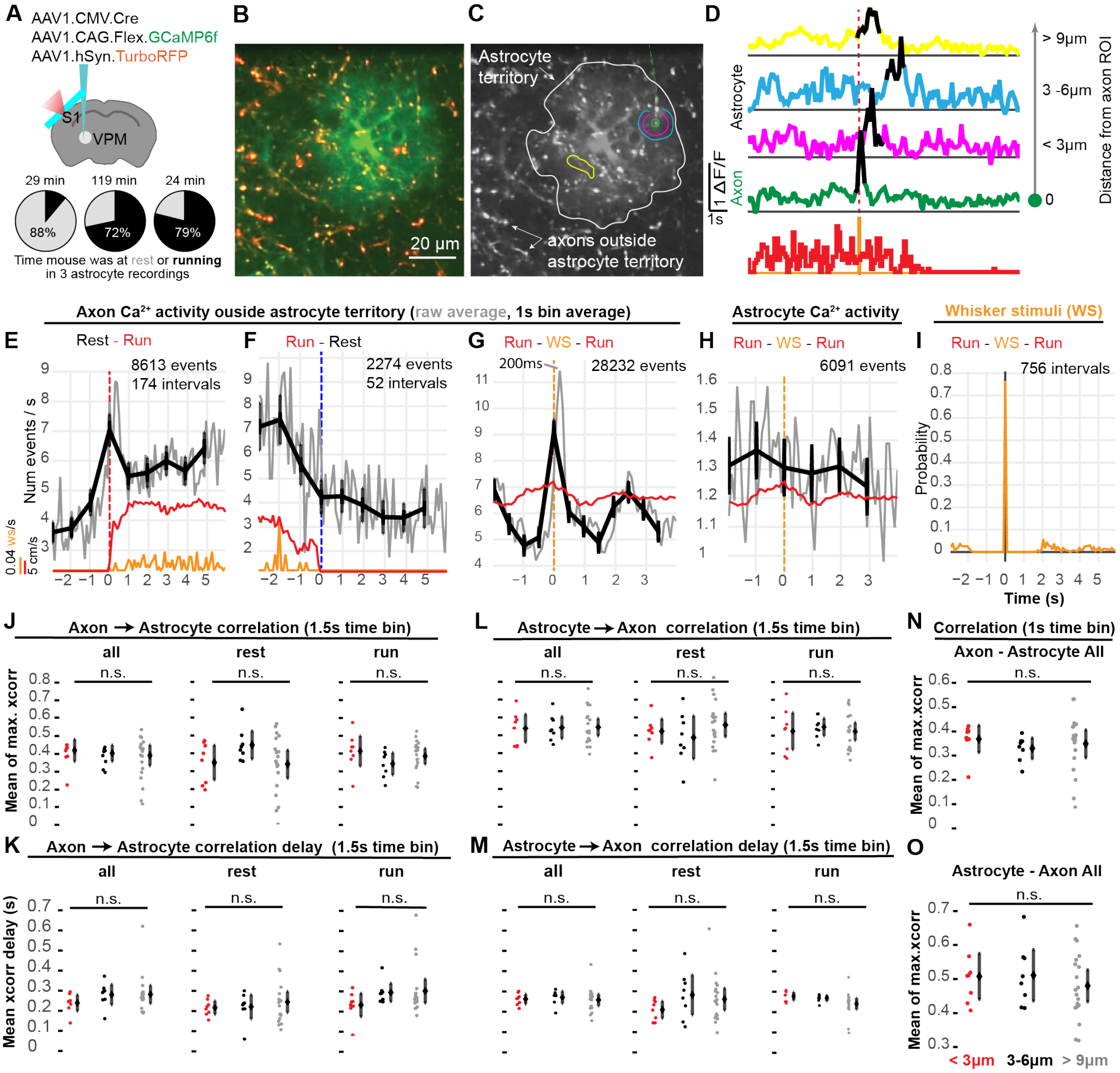

Figure 3.7: Axon-astrocyte interactions (caption next page.)

Figure 3.7: (previous page.) A) Schematic of injection strategy (top) used to study neuron-astrocyte interactions in the somatosensory cortex (S1). I used two photon microscopy in awake mice to study thalamocortical axon - astrocyte interactions in 3 astrocytes from 3 mice (bottom) undergoing rest (gray) and run (black) state transitions with whisker stimulation. B) Layer 2/3 somatosensory cortex astrocyte labelling (green: GCaMP6f) and thalamocortical axons (red: TurboRFP, green: GCaMP6f). C) Schematic of ROI selection for calcium activity extraction with AQUA: Axon (green), nearby astrocyte processes (purple, <3 μm) and light blue (3-6 μm) and far astrocyte processes (yellow, >9 μm). Axons outside astrocyte territory (white) were used to extract axon activity without contamination from astrocyte signals. D) Example of axon (green) and astrocyte signals extracted using AQUA from selected ROIs during locomotion (red) and whisker stimulation (orange). E) Mean number of axon Ca^{2+} events/second (8613 events, outside astrocyte territory during rest to run (red, 174 intervals), F) run to rest (2274 events, 52 intervals) and G) whisker stimulation during run (28232 events, 756 intervals). Mean running speed (Red trace), number of whisker stimuli/ second (orange trace). H) Mean number of astrocyte Ca^{2+} signals seeds per second (6091 events) inside all ROIs ($n = 35$) during whisker stimulation (orange dotted line, 156 intervals) while the animal is running (red trace). I) Distribution or all whisker stimuli during whisker stimulation trials (run - ws - run). WS = whisker stimulation. Raw Ca^{2+} event number/s average = gray, 1s binned average ± CI = black. J) Mean of maximum cross correlation values and K) mean correlation delay (s) between Ca^{2+} signals in selected axon ($n = 8$) and astrocyte process ROIs ($n = 35$) at increasing distance from the selected axon within 1.5s after axon signal onset during different states (rest, run, all states). L) Mean of maximum xcorr. and M) mean xcorr. delay between astrocyte ROIs (at increasing distance from selected axon) and selected axon Ca^{2+} signals within 1.5s following the onset of an astrocyte signal. N) Mean of maximum xcorr between axon and astrocyte signals within a 1s time window from axon signal onset instead of 1.5s like J-M. O) Mean of maximum xcorr. between astrocyte and axon signals within a 1s time window of astrocyte signal onset. All plots are represented as raw means for each axon - astrocyte ROI pair (dots) and their group means (black dots ± CI). Different colour dots represent ROI distance from the selected axon (red = <3 μm: $n = 8$, black = 3-6 μm: $n = 8$, gray = >9 μm: $n = 19$). Between groups comparison, two-tailed Kruskal-Wallis test with bonferroni correction. Significance threshold set at $p < 0.05$.

Correlation between axon and astrocyte calcium signalling at fast timescales ($\leq$1.5s)

Direct observation of simultaneous axon and astrocyte recordings did not reveal obvious correlation between axon and nearby astrocytic process Ca^{2+} activity. In order to give a quantitative description I asked if Ca^{2+} signals in astrocytic processes near (<6 μm) manually selected axon boutons (punctated morphology, co-express TurboRFP) within the astrocyte territory, were more highly correlated than Ca^{2+} signals in processes distant (>9 μm) from the respective bouton. Distal astrocytic processes were used as a control to avoid misinterpretation of correlation values deriving from random Ca^{2+}

signals. Cross-correlation between Ca^{2+} signals of axon boutons ($n = 8$) to Ca^{2+} signals initiated within (detected by AQUA) nearby (<3 μm, 3-6 μm, $n = 8$ each) and distal (>9 μm, $n = 19$) astrocytic process ROIs from the respective bouton revealed no significant difference (Kruskal-Wallis test with bonferroni correction, $p > 0.05$) between their mean correlation values (Figure 3.7 J, all) and correlation delay from the onset of axonal Ca^{2+} signal (Figure 3.7 K, all). Correlations were restricted within a 1.5s time window from the onset of axonal Ca^{2+} signals to account for fast astrocytic responses and to minimize dilution of possible evoked signals with random astrocyte activity. Similarly, there was no significant difference between the mean cross-correlation value (Figure 3.7 N, all) in near and far astrocytic Ca^{2+} microdomains from axon boutons within 1s time window from axon Ca^{2+} signal onset. Similar results were obtained using a range of time windows from axon Ca^{2+} signal onset (not shown). To test if the behavioural state of the animal influences the correlation between active axons and nearby astrocytic process, the same analysis was repeated in data taken during rest or locomotion (run) of mice (Figure 3.7 J, K: rest, run). There was no significant difference ($p > 0.05$) in the mean of maximum correlation value (Figure 3.7 J, rest, run) or cross-correlation delay (Figure 3.7 K, rest, run) in nearby or distant astrocytic Ca^{2+} microdomains to active axon boutons (within 1.5s time window). These results suggest that astrocyte (L2/3, barrel cortex) processes do not reliably respond to nearby (<6 μm) thalamocortical axon Ca^{2+} signals.

I then asked if astrocyte Ca^{2+} signals precede nearby axon Ca^{2+} activity to investigate the possibility of astrocyte signalling triggering presynaptic calcium responses (within $<$1.5s). I found no significant difference ($p > 0.05$) in the mean of maximum xcorr. values (Figure 3.7 L, O) or mean xcorr. delays (Figure 3.7 M) between astrocyte processes at increasing distance from the bouton of interest. Additionally, no significant change in these correlation values was observed during rest or run states (Figure 3.7 L, M: rest, run). Overall, these findings suggest no clear, microscale, bidirectional Ca^{2+} signalling between thalamocortical axon boutons and nearby astrocyte processes.

3.4 Discussion

3.4.1 Anterograde axo-astrocytic rAAV transfer can be used for functional studies in barrel cortex astrocytes

First, I showed that anterograde axo-astrocytic rAAV transfer can be used for functional studies of astrocytes embedded in the thalamocortical circuit. The sparse labelling of L2/3 cortical astrocytes allows high-contrast and long duration (>1hr), *in vivo* two photon imaging of single astrocytes (Figure 3.1). The next step will be to investigate whether other neuron-astrocyte circuits can be probed with axo-astrocytic rAAV transfer or if it is a special property of a subset of circuits including thalamocortical projections. While I focused on astrocyte calcium signalling, it will be interesting to combine axo-astrocytic rAAV transfer with the delivery of other genetically encoded indicators, such as glutamate (i.e. iGluSnFr [219], voltage (GEVIs) [167] and noradrenaline (GRAB$_{NE}$ [109] sensors for future investigations in neuron-astrocyte interactions. Combinations of such sensors and/or dyes (i.e. voltage sensitive dyes such as

ANNINE-6plus [304]) has the potential to refine our understanding of astrocyte-neuron interactions embedded in specific circuits *in vivo*. However, while I tried to use a combination of GECIs (i.e. GCaMP6f & jRGECO delivered by AAVs) to simultaneously label and record Ca^{2+} activity in thalamocortical axons, cortical astrocytes and cortical neurons I observed a "repulsion effect" (not shown in this thesis) between expressed fluorophores that made such a study not possible. Better understanding of rAAV biology, including the interactions between multiple rAAVs, AAV capsid engineering [184] and astrocyte subtype (i.e. take into account the heterogeneity of astrocytes) specific promoters can enhance the potential of axo-astrocytic AAV transfer in functional studies. Studying circuit specific neuron-astrocyte interactions [216] [217] [215] given the functional heterogeneity of astrocytes in distinct circuits [67] has potential to refine our understanding of their bidirectional communication. Axo-astrocytic AAV transfer in combination with *in vivo* functional imaging offers a new way to study circuit specific, neuron astrocyte interactions under physiological conditions.

3.4.2 Unbiased investigation of astrocytic Ca^{2+} microdomains during behaviour

Two photon imaging of single, L2/3 S1 astrocytes labelled with membrane bound GCaMP (lck.GCaMP6f) combined with event based Ca^{2+} signal detection software (AQUA [388]) allowed unbiased extraction of the detected $[Ca^{2+}]_i$ signals. Astrocytes exhibit highly localized microdomain Ca^{2+} signals in their thin astrocytic processes that can be readily investigated using membrane tethered (lck) GCamP [332] [333] [334] [129] [341] [345]. These fast Ca^{2+} microdomains operate at a timescale that may be relevant for subsecond information processing by astrocytes [47] [92] [261] [345]. With these exciting discoveries came the novel challenge of analyzing these signals. Because of the complex spatiotemporal dynamics of these Ca^{2+} signals, ROI based analysis is insufficient in capturing their characteristics. An elegant solution to this problem came with the development of AQUA [388], that enables ROI independent, event based, automatic and unbiased extraction of Ca^{2+} dynamics. Two photon microscopy enables the study of astrocyte signalling in the living animal, under physiological conditions. This is important as many of the earlier findings may have confused physiological responses with pathological ones because of the experimental conditions used [111] [314]. The most physiologically relevant experiments are done in awake conditions since anesthesia is known to disrupt Ca^{2+} signalling in astrocytes [359]. Combination of these innovations with state of the art surgical procedures [303] and fast imaging (30.9Hz) and sparse labelling allowed us to capture single-astrocyte Ca^{2+} microdomain dynamics with a spatiotemporal resolution of $2\mu m^2$ and 0.2s in awake mice even during locomotion.

Head fixed mice on a wheel can be used with 2P to study brain activity in behaving mice. A fundamental questions is whether astrocytes respond to sensory stimuli with fast transient elevation in $[Ca^{2+}]_i$ at their fine processes. I chose the somatosensory circuit as a model system to answer this question because it is well studied [284], it is considered an important, well organized sensory modality in dark dwelling mice (unlike vision) [204] and whisker stimulation was reported to trigger both neuronal [23]

[284] and astrocyte microdomain [345] [Ca^{2+}]$_i$ signals. I developed a simple intermittent whisker stimulation system involving a rod embedded in a cylindrical treadmill mice were free to move on. I avoided air puff stimulation or removal of whiskers to avoid startle (and possibly sound) induced neuronal modulation or a disturbance to the somatosensory system respectively. I avoided any type of artificial stimulation (i.e. electrical stimulation, optogenetics or chemogenetics) since I am not convinced astrocytic responses to such stimuli is physiological (even when delivered to neurons). The intermittent whisker stimulus delivered by the pole contacting whiskers as the mouse run on the cylindrical treadmill provides a transient, natural stimulus the mouse could have experienced in nature. Since there was no sound or visual cues associated with it (experiments were performed in darkness), cross modal interaction was limited. Mice occasionally stopped at their own volition to explore the pole with their whiskers providing another possible state of whisker exploration. Considering that locomotion is thought to increase the gain of astrocytes to sensory stimuli [274] I wanted to investigate if and how astrocyte Ca^{2+} microdomain activity is associated with behaviour state and sensory stimuli. Maybe astrocyte responses to sensory stimuli are situational to the behavioural state of the animal.

3.4.3 Diversity of astrocyte Ca^{2+} microdomain signals

A combination of all of the above techniques revealed a range in amplitude, duration and size (Figure 3.2 G, H, I) of astrocyte [Ca^{2+}] signals. The amplitude of the majority of signals ranged from ≈0.5 to 3 ΔF/F in a skewed probability distribution centered at ≈1 ΔF/F (Figure 3.3 G). The duration of the majority of signals ranged from 0.2s (cutoff point) to ≈2.5s with short duration ($<$ 1s) events being more probable (Figure 3.2 H). Note, a mean Ca^{2+} signal duration of ≈1s is ≈4 times shorter than reported by recent studies investigating Ca^{2+} signals in microdomains reported by lck-GCaMP6f [344] [345]. Also the distribution of event sizes seems to be composed of two distinct distributions (Figure 3.2 H) suggesting that different microdomains may exhibit heterogeneous duration of activity. This may be explained by different sources of calcium elevation, i.e. fast entry through opening of channels allowing extracellular calcium into the cell or release from internal stores. An other explanations might involve different distribution of Ca^{2+} sinks within the cell. The size of the majority of events were at the cutoff point of 2μm^2 with the probability of larger events occurring decreasing exponentially (Figure 3.2 I) suggesting a power law distribution in event size, a characteristic of scale free systems. Thus smaller events are most frequent. If the event size probability distribution follows the same trend for unresolved, nanodomain Ca^{2+} signals then we should expect them to be exponentially more frequent than microdomain Ca^{2+} signals. I believe the reason we observe shorter duration signals than other reports is because I take into account very small events ($>$2μm^2). Since event duration is positively correlated (r = 0.42) to event size (Figure 3.2 F), it is expected that missing smaller events underestimates the lower range of Ca^{2+} signal duration. I therefore show that astrocyte Ca^{2+} microdomains are faster (shorter duration) than generally believed. It would be interesting to assess how these event characteristics change by disturbing specific Ca^{2+} sources or sinks such as ER (IP3R), mitochondria or mobile buffers. The dynamics of single-astrocyte Ca^{2+} signals should aid computational modeling and understanding of the astrocyte Ca^{2+} code.

3.4.4 Locomotion modulates astrocyte Ca^{2+} microdomain signals

I found that during voluntary locomotion, the frequency (number of events/time) size and duration of Ca^{2+} microdomains are increased compared to when the animal is at rest (stationary). Comparing the average of individual calcium signal characteristics I found significant differences between different behaviour states (Figure 3.2 B, C, D). However, when looking at the variability in event characteristics between recordings I realized that the differences shown in Figure 3.2 (B, C, D) can be explained by the variability between recordings. Since Figure 3.2 (B, C, D) shows a biased representation of the data I will refrain from drawing conclusions based on it. To alleviate this bias I gave equal weight to each astrocyte recording and compared the mean event characteristics of each recording during different states to assess general trends (Figure 3.3). I observed the biggest change in the frequency of events. There was approximately a threefold increase in the average number of events/minute and $\approx$32% increase in the average size of events during run compared to rest The average event amplitude and duration was unchanged (Figure 3.3 B). Interestingly, I observed a shift in the probability distributions of event sizes. The probability of having smaller, and shorter duration events is higher during rest, while it is more likely to have larger, longer duration events during locomotion (Figure 3.2 H, I, J). There was no shift in the event amplitudes during different states (Figure 3.2 G). To further assess the effect of locomotion on event characteristics I investigated their changes during state transitions (Figure 3.4). In agreement with my previous findings, I found a sharp increase in the number of Ca^{2+} events/s following the onset of locomotion (peak $\approx$290%, 6s after onset) (Figure 3.4 B). The frequency of events likely decreases to $\approx$2.4 (54%) following a slow onset peak $\leq$6s from run which decreases slowly ($\approx$6s from rest onset) down to a baseline of $\approx$1.1 events/s. I also observed an increase ($\approx$65%) in the mean size of events, reaching a peak $\approx$4s after run onset (Figure 3.4K). Interestingly, the duration of signals also increased (13%) briefly 3-4 seconds following the onset of running (Figure 3.4H). In contrast, there was no change in the mean amplitude of events with the onset or offset of locomotion. Increase in the frequency, duration and amplitude of events starts increasing $\approx$1s from run onset (Figure 3.4 B, H, K). The frequency of events keeps increasing over a longer period of time than the event duration and size. While event duration (with duration decreasing to baseline earlier than size) (Figure 3.4 H, I) and size (Figure 3.4 4 K, L) decrease back to baseline following the initiation of running, the number of events/s decreases but remains 54% higher than baseline during running (Figure 3.4 B, C).

Locomotion is known to be correlated with synchronised global Ca^{2+} activity in cortical astrocytes [93] [274] as well as local synchronization of Ca^{2+} microdomains [2]. Astrocytes exhibit stronger responses to neuromodulators such as noradrenaline compared to sensory stimuli [34] [93] [274] and acetylcholine [356]. Since astrocytes exhibit a variety of GPCRs that bind neuromodulators [59] astrocytes could be targeted directly by these volume transmitters to trigger GPCR mediated Ca^{2+} signals. The large increase in the number of microdomain events/s observed during the onset of voluntary locomotion is similar to the startle induced, fast Ca^{2+} component observed by Srinivasan et al. [341]. Srinivasan et al. [341] found that the fast component (but not the slow component) of Ca^{2+} elevation in astrocyte processes is blocked in IP3R2KO mice and with application of the a1-blocker, prazosin. Similarly, Stobart et al., [345] showed that prazosin and DSP4 (a locus coeruleus neurotoxin) reduced the number Ca^{2+} microdomain activity. It is thus likely that at least the first component in the increase of event frequency observed during voluntary locomotion is mediated by noradrenaline. However that does not exclude synergy with local neuron circuit activity or other neuromodulators. For example, during locomotion the activity of barrel thalamocortical (Figure 3.7 E) and cortical neurons is increased [23]. However the Ca^{2+} activity onset and offset is slower in astrocytes compared to neurons. Increase in neuronal activity is associated with increased metabolic demand and K^+ release in the extracellular fluid. This can trigger Ca^{2+} release from mitochondria in astrocytes [2] and engage in Ca^{2+} mediated K^+ uptake [385]. Also atropine (muscarinic receptor antagonist) is known to decrease Ca^{2+} microdomain activity [345] and cholinergic neurons display increased activity during locomotion [300]. A combination of these factors is likely to modulate changes in the frequency, duration and size of events observed. These slow (multiple seconds) Ca^{2+} responses are unlikely to be involved in fast modulation of neuronal circuits but are better poised in reducing extracellular $[K^+]$ [385], mediate neurotransmitter uptake [237] [333] or be involved in plasticity [38] [356] over longer timescales. Overall, my results are in agreement with previous studies showing that astrocytes reliably respond with slow, transient and synchronized elevations of Ca^{2+} to arousal and locomotion [274] [2]. One notable difference is that I found no change in the amplitude of microdomain Ca^{2+} signals in contrast to Agarwal et al. [2] who found a 20% increase during locomotion. This might be because of the analysis methods used to extract the signals or perhaps there are region specific differences in astrocyte Ca^{2+} dynamics during locomotion (i.e. visual cortex vs somatosensory cortex).

3.4.5 Whisker stimulation does not modulate microdomain Ca^{2+} signals in L2/3 S1 astrocytes

It is well accepted that astrocytes respond with large $[Ca^{2+}]_i$ elevations to neuromodulators during arousal *in vivo*. However, whether astrocytes respond with fast, micrometer scale, Ca^{2+} responses to wired transmission and sensory stimuli in awake animals is not well explored yet [344] [345] [18]. Neuronal activity was shown to trigger astrocyte Ca^{2+} microdomain activity in slices [47] [92] [261], *in vivo* (under anesthesia) in response to optogenetic stimulation of inhibitory interneurons [215], in response to long (8s) high frequency (90Hz) single whisker stimulation in awake animals [345] or air puff and electrical stimulation of the trigeminal nerve [258] [201] during anesthesia. If astrocytes respond to minimal neuronal stimulation (as suggested by [47] [92] [261]) *in vivo* under physiological conditions, using a realistic whisker stimulus should elicit reliable Ca^{2+} responses in astrocyte fine processes. For example, Stobart et al., [345] reported a subpopulation (≈8%) of Ca^{2+} microdomains in S1, L2/3 lck.GCaMP6f labelled astrocytes that respond to whisker stimulation with a short onset latency (≈300ms). On the other hand, Asada et al., [18] reported an increase in the size but not frequency of V1 astrocyte Ca^{2+} microdomains in response to visual stimuli. The (controversial) role of astrocytes as active participants in (ms-s) information processing of the brain should be reflected in fast astrocyte responses to neuronal activity.

I used an intermittent whisker stimulus delivered by a rod attached on a vertical treadmill, whose rotation was determined by the locomotion the mouse. I wanted to avoid stimuli that may evoke cross modal responses (i.e. sound) or startle the animal (air puff). I also wanted to avoid high frequency, single whisker stimuli since they are not an ethologically relevant stimulus to the mouse (as it wouldn't encounter such a stimulus in nature). In combination with the high spatiotemporal resolution and fully automated event based analysis approach should have revealed the response characteristics of S1, L2/3 astrocyte Ca^{2+} microdomains.

Surprisingly, I found no changes in the frequency (number of events/time), amplitude, size or duration of events within 4s of whisker stimulation. First, the probability distribution of event characteristics (amplitude, duration, size) didn't change with whisker stimulation during rest or run (Figure 3.2 G, H, I). Second, the mean number of events/minute, amplitude, duration and size of Ca^{2+} events was unchanged during periods of rest compared to rest with whisker stimulus (Figure 3.3 C) or during periods of run compared to run with whisker stimulus (1.5s) (Figure 3.3 D). The latter was particularly surprising since I expected locomotion to increase the gain to sensory input in the S1 like in V1 [274]. Perhaps the change in astrocytic $[Ca^{2+}]_i$ was very brief and was averaged out in the previous analysis. Third, I didn't find any changes in event size, amplitude or duration (Figure 3.4 G, J, M) in response to whisker stimuli. I found a slow increase in the frequency of events. However, this increase started before the whisker stimulus (Figure 3.4 D) which may be explained by changes in movement speed (see Figure 3.4 A, Run-WS-Run). In addition, since the rate of frequency increase was slow, I support the conservative interpretation that the ambiguous change observed is an artifact of running rather than a genuine response to whisker stimuli. A less conservative interpretation might be that whisker stimuli enhanced the slow Ca^{2+} activity of astrocytes observed during locomotion. Fourth, to ensure that whisker stimulation induces neuronal activity in S1 and to investigate whether the activity of individual thalamocortical axons correlates with local astrocyte Ca^{2+} microdomains I used a new preparation (Figure 3.7). Briefly, I injected a combination of AAV1 vectors only in the VPM (Figure 3.7 A) that I previously showed (Chapter 2) could label both thalamocortical axons and cortical astrocyte with GCaMP6f (Figure 3.7 B). Thalamocortical axons co-expressed TurboRFP, however it was easy to separate them from astrocytes based on their punctated morphology, contrast differences and activity pattern. Extracting Ca^{2+} signals outside the astrocyte territory revealed a sharp increase in thalamocortical axon Ca^{2+} activity with a peak 200ms following whisker stimulation. Correlation between the Ca^{2+} activity of axon boutons with Ca^{2+} signals in astrocytic processes at increasing distance from the selected bouton (Figure 3.7 C) revealed no difference in the mean correlation values or correlation delay between these regions. The time window of correlation was restricted to 1-1.5s since I expect fast astrocytic responses to be within this timeframe. I also investigate a broad range of time windows with the same results (not shown in this thesis). One major limitation of the axon-astrocyte experiment is the use of a single Ca^{2+} indicator that can lead to signal contamination in claimed astrocytic or neuronal signals. Effort has been made to avoid this contamination by choosing sparse boutons and drawing ROIs, but it is still a suboptimal way of performing this analysis. Dual colour GECIs can alleviate this limitation and allow for ROI independent analysis of axon bouton and astrocyte process Ca^{2+} activity at increasing distance from each other, including the overlay to the axon bouton that we ignored. Besides these limitations, visual inspection of the recordings didn't reveal any obvious correlation in their activity. Dual colour GECI labelling didn't work in my hands. In summary, the combined evidence suggest that L2/3 S1 astrocytes do not respond with transient changes in [Ca^{2+}]$_i$ elevation or dynamics to sensory stimuli induced by a pole in awake mice under physiological conditions and are likely not correlated to spontaneous neuronal activity.

One explanation for the conflicting findings might lie in the mode of neuronal stimulation. Perhaps a stronger stimulus is needed to drive micrometer scale Ca^{2+} responses in astrocytic processes of awake animals. For example Stobart et al., [345] used a long, high frequency whisker stimulus (8s, 90Hz, single whisker) to elicit Ca^{2+} microdomain activity. Another possibility is that astrocytes respond with Ca^{2+} nanodomain signals to neuronal activity. Considering the scale of the tripartite synapse is nanoscopic, minimal neuronal stimulation might induce astrocytic [Ca^{2+}]$_i$ elevation contained within nanodomains. Advancements in super resolution microscopy might enable this investigation. Perhaps astrocytes respond with Ca^{2+} signals when their local environment deviates from homeostasis (i.e. thorough abnormal neuronal activity) and it is interpreted as a physiological astrocytic response involved in information processing. It will also be interesting to use different whisker stimuli. For example using wall touch of increasing length to engage whiskers for progressively longer periods. Such experiments can reveal if astrocytes respond to integrated sensory stimulation over time. Interestingly, S1 L2/3 neurons, display sustained activity to wall touch while layer 5 neurons display transient activity in moving mice, suggesting that L2/3 neurons might be integrating tactile stimuli during locomotion [23]. Considering that astrocytes might display circuit-specific functional heterogeneity [216] [217] [67] [215] [404], different sensory conditions might elicit different responses in different astrocytes. It will thus be important to study astrocyte Ca^{2+} microdomain responses to different neuronal circuit modulation.

3.4.6 Thalamocortical axon Ca^{2+} activity increases with whisker stimulation and locomotion

I showed that S1 L2/3 astrocytes respond with Ca^{2+} microdomain characteristic changes to locomotion but not to whisker stimulation. In contrast, thalamocortical axons respond both to whisker stimulation and locomotion. The axonal activity recorded (outside of astrocyte territory) might be slightly contaminated by cortical neurites since cortical neurons are also sparsely labelled with GCaMP6f (but not TurboRFP) using this protocol. Because of sparse labelling cortical neuron neurites are rare in comparison to thalamocortical axons (see example Figure 3.7 B). I found that thalamocortical axons respond with biphasic [Ca^{2+}] elevation to locomotion (Figure 3.7 E) composed of a transient increase from baseline starting before (≈0.5s) the onset of locomotion and reaching a peak ≈0.3s (≈129% increase from rest) after mice started running, followed by a sharp decrease to a sustained running baseline activity ≈44% higher than during rest. VPM axon activity starts decreasing ≈1s before the animal stops running (during deceleration phase) reaching baseline activity approximately as soon as the animal stops (Figure 3.7 F). The animal likely enters a state of higher arousal when it decides to run, leading to neuronal activity preceding the onset of locomotion. These observations are similar to Ca^{2+} activity in S1, L2/3 and L5 neurons in response to the onset of running [23]. Thalamocortical axons respond to whisker stimuli during locomotion with fast, (peak ≈0.2s after whisker stimulus onset) transient increase in Ca^{2+} activity (Figure 3.7 G) similar to what is observed in S1 neurons [23]. The Ca^{2+} activity of axons in the whisker stimulation trace was oscillatory, most likely because of the combined effect of changes in running speed (Figure 3.7 G, red trace) and periodicity in whisker stimuli (Figure 3.7 I). In contrast, astrocytes did not respond with $[Ca^{2+}]$ transients (Ca^{2+} signals initiated in ROIs inside astrocytes devoid of axon boutons) to whisker stimulation (Figure 3.7 H).

3.4.7 Astrocyte Ca^{2+} microdomain activity is not random

Recent work alluded to possible heterogeneity in the Ca^{2+} activity of astrocytic processes [2] [47]. Considering the plethora of inputs, sources and sinks associated with Ca^{2+} signalling, it is unlikely that Ca^{2+} microdomain activity in astrocytes is random. If Ca^{2+} signalling is random then astrocyte process should be equally likely to exhibit Ca^{2+} elevation.

To find if Ca^{2+} signalling is random, I performed long recordings (≈1hr) of Ca^{2+} microdomain activity in lck.GCaMP6f labelled astrocytes, automatically (AQUA) extracted the microdomain signals, binarize their amplitude and duration and summed up all events in time while preserving their maximum size and spatial position. This resulted in activity heatmaps exhibiting high activity hotspots (Figure 3.5, Figure 3.6). This suggested that some parts of the astrocytic territory are more active than others. To visualize and assess how the overall activity profile of an astrocyte would be assuming Ca^{2+} microdomain activity was random we created random simulations using the event characteristics of the real astrocyte simulated (Figure 3.5 D, E right). The distribution of pixel intensity was different between real activity heatmaps (Figure 3.5 F) compared to random simulation heatmaps (Figure 3.5 G). No hotspots are observed in the random simulations of activity. These results thus suggest heterogeneous Ca^{2+} microdomain activity within the territory of a single astrocyte.

This heterogeneity might be associated with the distribution of Ca^{2+} storing organelles such as mitochondria, ER-plasma membrane contacts or lysosomes. Alternatively, hotspot regions might represent areas with increased concentration of Ca^{2+} channels, exchangers and transporters or decreased concentration of Ca^{2+} buffers. Another possibility is that astrocyte Ca^{2+} activity hotspot regions are associated with higher local neuronal circuit activity, thus exhibiting proportional Ca^{2+} responses. This could involve increased uptake of K^+ [385]; gliotransmitter release [16]; metabolic support [252] [2]; neurotransmitter uptake [237] [333] or any combination of the above among others.

3.4.8 Astrocyte Ca^{2+} activity maps in the brain

Since astrocytes exhibit hotspots of higher Ca^{2+} activity, the natural next question was whether the position of activity 'hotspots' is stable over time. First we approximated how long a recording should be to exhibit the characteristic hotspot pattern of a long (<1hr) recording by cutting (splits) recording videos into increasingly shorter segments and comparing it to the total recording heatmap. ≈20 minutes of recording could capture the heatmap pattern with ≈85% accuracy (Figure 3.6 B). Comparing the split heatmaps (during rest state) of the same recordings to each other and the total astrocyte recordings when the animal is at rest or locomotion (Figure 3.6 A) revealed remarkable similarity between hotspot patterns within individual recordings (Figure 3.6 A, C). This suggested that astrocyte hotspot patterns are stable within timescales of minutes to 1 hour. Then I asked if this similarity persists between days. To achieve that I recorded the same astrocyte again 1-3 days after the first recording. I could find the same astrocyte using the blood vessel pattern on the brain surface, the shape of the astrocyte and using autofluorescent signal and blood vessel patterns landmarks at the z-plane of interest. This step is extremely difficult using this method, and virtually impossible to completely control for z-movement artifacts. I could minimize such artifacts through the surgery protocol, an elongation of the PSF to $\approx 4\mu$m by underfilling of the back aperture of the objective, use of heavy optomechanical components for the construction of the treadmill apparatus and training of the animal. Despite these difficulties I was able to record Ca^{2+} activity from the same astrocyte at the same z-plane between days (Figure 3.5 B, D; Figure 3.6 A). I found similarities in the activity heatmaps of the same astrocytes between days (Figure 3.6 A, C, D). The hotspot pattern was more highly correlated in astrocytes within days compared to between days (Figure 3.6 C, D). This is likely because of smaller z-plane offsets in within day recordings and not necessarily because of physiological changes in astrocyte signalling over days. Any z-offset is likely to result in decreased correlation between heatmaps. Future studies should repeat these experiments with 3D imaging (i.e. [47]) or using calcium integrators such as CaMPARI [113] instead of GECIs. These approaches will solve the main problem of z-plane orientation, minimize artifacts and give a more accurate representation of these activity maps. A simpler but less optimal approach might be to use a bessel beam [289] [207]. Despite the limitations of our methods I found that astrocyte calcium activity patterns are stable within single recordings or between day recordings. They are more highly correlated to each other compared to their respective random simulations (Figure 3.6 C, D) and the hotspot pattern can be clearly observed (Figure 3.6 A). Future work should reveal if these hotspots are differentially regulated by different neurotransmitters and neuromodulators. While many of the hotspots were similar between states, there were also notable hotspots that were similar only during locomotion, between days (i.e. arrow 9, Figure 3.6 A). This is line with previous findings *ex vivo* showing that noradrenaline and ATP modulate distinct Ca^{2+} microdomains [2]. Local drug application through a chronic cranial window access port [303] can greatly facilitate this endeavor. It will also be interesting to assess if it is easier to trigger Ca^{2+} signals in these hotspots and if different hotspots mediate heterogeneous functions (i.e. release different gliotransmitters). This might be possible using a combination of light activated calcium channels and holography [136] to stimulate specific parts of the astrocyte at different intensities of illumination.

3.4.9 Summary of findings

- Anterograde axo-astrocytic AAV transfer can be used to study single-astrocyte Ca^{2+} microdomains in behaving mice.
- Astrocytes display rich repertoire of Ca^{2+} microdomain characteristics *in vivo*.
- Barrel cortex astrocytes did not respond to whisker touch stimulation with transient elevation in Ca^{2+} microdomains in awake mice.
- Barrel cortex astrocyte Ca^{2+} microdomains were not correlated to thalamocortical axon activity.
- Thalamocortical axons respond to whisker touch and locomotion with transient and biphasic $[Ca^{2+}]_i$ elevation respectively.
- Barrel cortex astrocytes respond to locomotion with prolonged, synchronized elevation in Ca^{2+} microdomains that exhibit larger size and duration compared to rest state.
- Astrocyte fine processes exhibit heterogeneous Ca^{2+} activity hotspots that are stable over time.

Conclusion

This work provides new methods for studying neuron-astrocyte interactions within specific brain circuits and provides insight about the Ca^{2+} code of astrocytes and its relationship to behaviour, sensory stimuli and neuronal activity under physiological conditions.

First. AAV1 injected in the VPM can transfer anterogradely to S1 astrocytes and neurons. This provides a new toolkit for studying neuron-astrocyte interactions and reinforces the idea that AAV1 can transfer anterogradely to neurons. Also care should be taken when using AAVs to induce local changes in the brain as these viruses may transduce both astrocytes and neurons at projection sites of the injection area. Future studies, focusing on different AAV serotypes injected in different brain regions, should clarify the limits and universality of AAV transfer to astrocytes.

Second. AAV1 anterograde intercellular transfer can be used to sparsely label cortical astrocytes and neurons with fluorescent indicators. Intersectional approaches using combinations of AAVs carrying cell type specific promoters can be leveraged to target astrocytes or neurons with higher specificity. Based on the pattern of fluorescent expression, AAV1 most likely transports to astrocytes and neurons through the 'tripartite synapse'. Sparse labelling enabled by axo-astrocytic AAVs transfer can be used to study single astrocytes within specific neuronal circuits. Future studies should reveal in more detail if axo-astrocytic AAV transport takes place at the tripartite synapse and focus on elucidating the mechanisms of transport. AAV capsid engineering should enhance the efficiency of AAVs to transport to astrocytes.

Third. Anterograde axo-astrocytic AAV transfer can be combined with membrane tagged genetically encoded calcium indicators and *in vivo* two photon microscopy to enable high contrast, long duration (>1 hour) imaging of Ca^{2+} microdomains in single astrocytes of awake mice under physiological conditions. This provides a platform for studying the Ca^{2+} code of single astrocytes under physiological conditions and has the potential of resolving many of the controversies in the field.

Fourth. Astrocytes display rich repertoire of Ca^{2+} microdomain characteristics *in vivo*. Automated, event based analysis of Ca^{2+} microdomains allows unbiased quantification of their characteristics: frequency, amplitude, duration and size. It revealed a rich repertoire of localized, subsecond, μm scale Ca^{2+} signals. Characterization of Ca^{2+} microdomains should help guide computational modeling of astrocyte signalling.

Fifth. Barrel cortex astrocytes respond with Ca^{2+} microdomain signalling to locomotion but not to whisker touch. Analysis of Ca^{2+} microdomain signals of barrel cortex astrocytes in mice free to run on a wheel apparatus embedded with a whisker-touch stimulus revealed an increase in the number, size, and duration of events during locomotion but not with whisker stimulation. This suggests that astrocyte Ca^{2+} microdomains respond to neuromodulators but not to sensory driven, neurotransmitter release. Therefore, these results support the critiques of sensory driven astrocyte responses and add to the growing consensus that astrocytes are responsive to locomotion and arousal. Future studies should clarify under what conditions astrocytes respond to sensory stimuli taking into account possible heterogeneity.

Sixth. Thalamocortical axons respond to whisker touch and locomotion with transient and biphasic $[Ca^{2+}]_i$ elevation respectively. Barrel cortex astrocyte Ca^{2+} microdomains were not correlated to thalamocortical axon activity. Axo-astrocytic AAV transfer can be used to co-label thalamocortical axons and astrocytes with GECIs. Two photon microscopy revealed that thalamocortical axons respond to whisker stimuli with a transient increase in Ca^{2+} activity, and to the onset of locomotion with a biphasic response that starts before the animal begins running. I did not find significant correlation between the Ca^{2+} signals of thalamocortical axon boutons and nearby astrocyte processes. These finding support our previous observations and suggest that barrel cortex astrocytes do not reliably respond with transient Ca^{2+} microdomains to thalamocortical input. Further developments should enable simultaneous recording of axon bouton, dendritic spine and astrocytic process activity with a more diverse array or molecular tools to supplement or disprove our findings.

Seventh. Astrocyte fine processes exhibit heterogeneous Ca^{2+} activity hotspots that are stable over time. This alludes to subcellular specialization and the existence of astrocyte activity maps in the brain. 3D imaging should provide a more accurate and complete representation of these activity maps. Future studies should determine the mechanisms and functional role of these hotspots.

Bibliography

[1] J. Ady, V. Thayanithy, K. Mojica, P. Wong, J. Carson, P. Rao, Y. Fong, and E. Lou. Tunneling nanotubes: an alternate route for propagation of the bystander effect following oncolytic viral infection. *Molecular Therapy-Oncolytics*, 3:16029, 2016.

[2] A. Agarwal, P.-H. Wu, E. G. Hughes, M. Fukaya, M. A. Tischfield, A. J. Langseth, D. Wirtz, and D. E. Bergles. Transient opening of the mitochondrial permeability transition pore induces microdomain calcium transients in astrocyte processes. *Neuron*, 93(3):587–605, 2017.

[3] M. Agbandje-McKenna and J. Kleinschmidt. Aav capsid structure and cell interactions. In *Adeno-Associated Virus*, pages 47–92. Springer, 2012.

[4] D. Albrecht, F. J. López-Murcia, A. P. Pérez-González, G. Lichtner, C. Solsona, and A. Llobet. Sparc prevents maturation of cholinergic presynaptic terminals. *Molecular and Cellular Neuroscience*, 49(3):364–374, 2012.

[5] N. J. Allen and B. A. Barres. Neuroscience: glia—more than just brain glue. *Nature*, 457(7230):675, 2009.

[6] N. J. Allen and C. Eroglu. Cell biology of astrocyte-synapse interactions. *Neuron*, 96(3):697–708, 2017.

[7] N. J. Allen, M. L. Bennett, L. C. Foo, G. X. Wang, C. Chakraborty, S. J. Smith, and B. A. Barres. Astrocyte glypicans 4 and 6 promote formation of excitatory synapses via glua1 ampa receptors. *Nature*, 486(7403):410, 2012.

[8] A. L. Altick, L. M. Baryshnikova, T. Q. Vu, and C. S. Von Bartheld. Quantitative analysis of multivesicular bodies (mvbs) in the hypoglossal nerve: evidence that neurotrophic factors do not use mvbs for retrograde axonal transport. *Journal of Comparative Neurology*, 514(6):641–657, 2009.

[9] M. A. Anderson, Y. Ao, and M. V. Sofroniew. Heterogeneity of reactive astrocytes. *Neuroscience letters*, 565:23–29, 2014.

[10] M. Andersson, F. Blomstrand, and E. Hanse. Astrocytes play a critical role in transient heterosynaptic depression in the rat hippocampal ca1 region. *The Journal of physiology*, 585(3):843–852, 2007.

[11] M. C. Angulo, A. S. Kozlov, S. Charpak, and E. Audinat. Glutamate released from glial cells synchronizes neuronal activity in the hippocampus. *Journal of Neuroscience*, 24(31):6920–6927, 2004.

[12] E. Arabzadeh, E. Zorzin, and M. E. Diamond. Neuronal encoding of texture in the whisker sensory pathway. *PLoS biology*, 3(1):e17, 2005.

[13] A. Araque, V. Parpura, R. P. Sanzgiri, and P. G. Haydon. Glutamate-dependent astrocyte modulation of synaptic transmission between cultured hippocampal neurons. *European Journal of Neuroscience*, 10(6):2129–2142, 1998.

[14] A. Araque, V. Parpura, R. P. Sanzgiri, and P. G. Haydon. Tripartite synapses: glia, the unacknowledged partner. *Trends in neurosciences*, 22(5):208–215, 1999.

[15] A. Araque, E. D. Martın, G. Perea, J. I. Arellano, and W. Buño. Synaptically released acetylcholine evokes ca2+ elevations in astrocytes in hippocampal slices. *Journal of Neuroscience*, 22(7):2443–2450, 2002.

[16] A. Araque, G. Carmignoto, P. G. Haydon, S. H. Oliet, R. Robitaille, and A. Volterra. Gliotransmitters travel in time and space. *Neuron*, 81(4):728–739, 2014.

[17] E. Aronica, E. A. Van Vliet, O. A. Mayboroda, D. Troost, F. H. L. Da Silva, and J. A. Gorter. Upregulation of metabotropic glutamate receptor subtype mglur3 and mglur5 in reactive astrocytes in a rat model of mesial temporal lobe epilepsy. *European Journal of Neuroscience*, 12(7):2333–2344, 2000.

[18] A. Asada, S. Ujita, R. Nakayama, S. Oba, S. Ishii, N. Matsuki, and Y. Ikegaya. Subtle modulation of ongoing calcium dynamics in astrocytic microdomains by sensory inputs. *Physiological reports*, 3(10):e12454, 2015.

[19] D. F. Aschauer, S. Kreuz, and S. Rumpel. Analysis of transduction efficiency, tropism and axonal transport of aav serotypes 1, 2, 5, 6, 8 and 9 in the mouse brain. *PloS one*, 8(9):e76310, 2013.

[20] D. Atlas. The voltage-gated calcium channel functions as the molecular switch of synaptic transmission. *Annual review of biochemistry*, 82:607–635, 2013.

[21] D. Attwell, A. M. Buchan, S. Charpak, M. Lauritzen, B. A. MacVicar, and E. A. Newman. Glial and neuronal control of brain blood flow. *Nature*, 468(7321):232, 2010.

[22] A. Ayaz, A. B. Saleem, M. L. Schölvinck, and M. Carandini. Locomotion controls spatial integration in mouse visual cortex. *Current Biology*, 23(10):890–894, 2013.

[23] A. Ayaz, A. Stäuble, M. Hamada, M.-A. Wulf, A. B. Saleem, and F. Helmchen. Layer-specific integration of locomotion and sensory information in mouse barrel cortex. *Nature communications*, 10(1):2585, 2019.

[24] F. A. Azevedo, L. R. Carvalho, L. T. Grinberg, J. M. Farfel, R. E. Ferretti, R. E. Leite, W. J. Filho, R. Lent, and S. Herculano-Houzel. Equal numbers of neuronal and nonneuronal cells make the human brain an isometrically scaled-up primate brain. *Journal of Comparative Neurology*, 513(5):532–541, 2009.

[25] R. M. Bachoo, R. S. Kim, K. L. Ligon, E. A. Maher, C. Brennan, N. Billings, S. Chan, C. Li, D. H. Rowitch, W. H. Wong, et al. Molecular diversity of astrocytes with implications for neurological disorders. *Proceedings of the National Academy of Sciences*, 101(22):8384–8389, 2004.

[26] J. Bahney and C. S. von Bartheld. Validation of the isotropic fractionator: comparison with unbiased stereology and dna extraction for quantification of glial cells. *Journal of neuroscience methods*, 222:165–174, 2014.

[27] F. Baixauli, C. López-Otín, and M. Mittelbrunn. Exosomes and autophagy: coordinated mechanisms for the maintenance of cellular fitness. *Frontiers in immunology*, 5:403, 2014.

[28] L. K. Bak, A. Schousboe, and H. S. Waagepetersen. The glutamate/gaba-glutamine cycle: aspects of transport, neurotransmitter homeostasis and ammonia transfer. *Journal of neurochemistry*, 98(3):641–653, 2006.

[29] M. Barrige, M. Bootman, and H. Roderick. Calcium signaling: dynamics, homeostasis, and remodeling. *Nature*, 4:517–529, 2003.

[30] J. S. Bartlett, R. Wilcher, and R. J. Samulski. Infectious entry pathway of adeno-associated virus and adeno-associated virus vectors. *Journal of virology*, 74(6): 2777–2785, 2000.

[31] O. A. Bayraktar, T. Bartels, D. Polioudakis, S. Holmqvist, L. B. Haim, A. M. Young, K. Prakash, A. Brown, M. F. Paredes, R. Kawaguchi, et al. Single-cell in situ transcriptomic map of astrocyte cortical layer diversity. *bioRxiv*, page 432104, 2018.

[32] N. Bazargani and D. Attwell. Astrocyte calcium signaling: the third wave. *Nature neuroscience*, 19(2):182, 2016.

[33] N. Bazargani and D. Attwell. Amines, astrocytes, and arousal. *Neuron*, 94(2): 228–231, 2017.

[34] L. K. Bekar, W. He, and M. Nedergaard. Locus coeruleus α-adrenergic–mediated activation of cortical astrocytes in vivo. *Cerebral cortex*, 18(12):2789–2795, 2008.

[35] A. Bellot-Saez, O. Kékesi, J. W. Morley, and Y. Buskila. Astrocytic modulation of neuronal excitability through k+ spatial buffering. *Neuroscience & Biobehavioral Reviews*, 77:87–97, 2017.

[36] L. Ben Haim, M.-A. Carrillo-de Sauvage, K. Ceyzériat, and C. Escartin. Elusive roles for reactive astrocytes in neurodegenerative diseases. *Frontiers in cellular neuroscience*, 9:278, 2015.

[37] M. A. Benneyworth, Y. Li, A. C. Basu, V. Y. Bolshakov, and J. T. Coyle. Cell selective conditional null mutations of serine racemase demonstrate a predominate localization in cortical glutamatergic neurons. *Cellular and molecular neurobiology*, 32(4):613–624, 2012.

[38] Y. Bernardinelli, J. Randall, E. Janett, I. Nikonenko, S. König, E. V. Jones, C. E. Flores, K. K. Murai, C. G. Bochet, A. Holtmaat, et al. Activity-dependent structural plasticity of perisynaptic astrocytic domains promotes excitatory synapse stability. *Current Biology*, 24(15):1679–1688, 2014.

[39] M. J. Berridge. Inositol trisphosphate and calcium signalling mechanisms. *Biochimica et Biophysica Acta (BBA)-Molecular Cell Research*, 1793(6):933–940, 2009.

[40] M. J. Berridge, P. Lipp, and M. D. Bootman. The versatility and universality of calcium signalling. *Nature reviews Molecular cell biology*, 1(1):11, 2000.

[41] M. J. Berridge, M. D. Bootman, and H. L. Roderick. Calcium: calcium signalling: dynamics, homeostasis and remodelling. *Nature reviews Molecular cell biology*, 4 (7):517, 2003.

[42] N. Bessis, F. GarciaCozar, and M. Boissier. Immune responses to gene therapy vectors: influence on vector function and effector mechanisms. *Gene therapy*, 11 (S1):S10, 2004.

[43] P. Bezzi, G. Carmignoto, L. Pasti, S. Vesce, D. Rossi, B. L. Rizzini, T. Pozzan, and A. Volterra. Prostaglandins stimulate calcium-dependent glutamate release in astrocytes. *Nature*, 391(6664):281, 1998.

[44] P. Bezzi, M. Domercq, L. Brambilla, R. Galli, D. Schols, E. De Clercq, A. Vescovi, G. Bagetta, G. Kollias, J. Meldolesi, et al. Cxcr4-activated astrocyte glutamate release via tnfα: amplification by microglia triggers neurotoxicity. *Nature neuroscience*, 4(7):702, 2001.

[45] P. Bezzi, V. Gundersen, J. L. Galbete, G. Seifert, C. Steinhäuser, E. Pilati, and A. Volterra. Astrocytes contain a vesicular compartment that is competent for regulated exocytosis of glutamate. *Nature neuroscience*, 7(6):613, 2004.

[46] A. R. Bialas and B. Stevens. Tgf-β signaling regulates neuronal c1q expression and developmental synaptic refinement. *Nature neuroscience*, 16(12):1773, 2013.

[47] E. Bindocci, I. Savtchouk, N. Liaudet, D. Becker, G. Carriero, and A. Volterra. Three-dimensional ca2+ imaging advances understanding of astrocyte biology. *Science*, 356(6339):eaai8185, 2017.

[48] D. E. Bonder and K. D. McCarthy. Astrocytic gq-gpcr-linked ip3r-dependent ca2+ signaling does not mediate neurovascular coupling in mouse visual cortex in vivo. *Journal of Neuroscience*, 34(39):13139–13150, 2014.

[49] M. D. Bootman. Calcium signaling. *Cold Spring Harbor perspectives in biology*, 4(7):a011171, 2012.

[50] I. Bosanac, J.-R. Alattia, T. K. Mal, J. Chan, S. Talarico, F. K. Tong, K. I. Tong, F. Yoshikawa, T. Furuichi, M. Iwai, et al. Structure of the inositol 1, 4, 5-trisphosphate receptor binding core in complex with its ligand. *Nature*, 420 (6916):696, 2002.

[51] D. N. Bowser and B. S. Khakh. Two forms of single-vesicle astrocyte exocytosis imaged with total internal reflection fluorescence microscopy. *Proceedings of the National Academy of Sciences*, 104(10):4212–4217, 2007.

[52] E. S. Boyden, F. Zhang, E. Bamberg, G. Nagel, and K. Deisseroth. Millisecond-timescale, genetically targeted optical control of neural activity. *Nature neuroscience*, 8(9):1263, 2005.

[53] S. J. Bradley and R. J. Challiss. G protein-coupled receptor signalling in astrocytes in health and disease: a focus on metabotropic glutamate receptors. *Biochemical pharmacology*, 84(3):249–259, 2012.

[54] M. Brecht and B. Sakmann. -dynamic representation of whisker deflection by synaptic potentials in spiny stellate and pyramidal cells in the barrels and septa of layer 4 rat somatosensory cortex. *The Journal of physiology*, 543(1):49–70, 2002.

[55] M. Brenner, W. C. Kisseberth, Y. Su, F. Besnard, and A. Messing. Gfap promoter directs astrocyte-specific expression in transgenic mice. *Journal of Neuroscience*, 14(3):1030–1037, 1994.

[56] R. Bruzzone, T. W. White, and D. L. Paul. Connections with connexins: the molecular basis of direct intercellular signaling. *European Journal of Biochemistry*, 238(1):1–27, 1996.

[57] C. Burger, O. S. Gorbatyuk, M. J. Velardo, C. S. Peden, P. Williams, S. Zolotukhin, P. J. Reier, R. J. Mandel, and N. Muzyczka. Recombinant aav viral vectors pseudotyped with viral capsids from serotypes 1, 2, and 5 display differential efficiency and cell tropism after delivery to different regions of the central nervous system. *Molecular Therapy*, 10(2):302–317, 2004.

[58] E. A. Bushong, M. E. Martone, Y. Z. Jones, and M. H. Ellisman. Protoplasmic astrocytes in ca1 stratum radiatum occupy separate anatomical domains. *Journal of Neuroscience*, 22(1):183–192, 2002.

[59] J. D. Cahoy, B. Emery, A. Kaushal, L. C. Foo, J. L. Zamanian, K. S. Christopherson, Y. Xing, J. L. Lubischer, P. A. Krieg, S. A. Krupenko, et al. A transcriptome database for astrocytes, neurons, and oligodendrocytes: a new resource for understanding brain development and function. *Journal of Neuroscience*, 28(1): 264–278, 2008.

[60] E. Carafoli. Calcium signaling: a tale for all seasons. *Proceedings of the National Academy of Sciences*, 99(3):1115–1122, 2002.

[61] E. Carafoli. Calcium–a universal carrier of biological signals: Delivered on 3 july 2003 at the special febs meeting in brussels. *The FEBS journal*, 272(5): 1073–1089, 2005.

[62] M. Carter and J. C. Shieh. *Guide to research techniques in neuroscience*. Academic Press, 2015.

[63] M. J. Castle, Z. T. Gershenson, A. R. Giles, E. L. Holzbaur, and J. H. Wolfe. Adeno-associated virus serotypes 1, 8, and 9 share conserved mechanisms for anterograde and retrograde axonal transport. *Human gene therapy*, 25(8):705–720, 2014.

[64] M. J. Castle, E. Perlson, E. L. Holzbaur, and J. H. Wolfe. Long-distance axonal transport of aav9 is driven by dynein and kinesin-2 and is trafficked in a highly motile rab7-positive compartment. *Molecular Therapy*, 22(3):554–566, 2014.

[65] C. N. Cearley and J. H. Wolfe. Transduction characteristics of adeno-associated virus vectors expressing cap serotypes 7, 8, 9, and rh10 in the mouse brain. *Molecular therapy*, 13(3):528–537, 2006.

[66] C. N. Cearley and J. H. Wolfe. A single injection of an adeno-associated virus vector into nuclei with divergent connections results in widespread vector distribution in the brain and global correction of a neurogenetic disease. *Journal of Neuroscience*, 27(37):9928–9940, 2007.

[67] H. Chai, B. Diaz-Castro, E. Shigetomi, E. Monte, J. C. Octeau, X. Yu, W. Cohn, P. S. Rajendran, T. M. Vondriska, J. P. Whitelegge, et al. Neural circuit-specialized astrocytes: transcriptomic, proteomic, morphological, and functional evidence. *Neuron*, 95(3):531–549, 2017.

[68] T. I. Chao, P. Kasa, and J. R. Wolff. Distribution of astroglia in glomeruli of the rat main olfactory bulb: exclusion from the sensory subcompartment of neuropil. *Journal of Comparative Neurology*, 388(2):191–210, 1997.

[69] N. Chen, H. Sugihara, J. Sharma, G. Perea, J. Petravicz, C. Le, and M. Sur. Nucleus basalis-enabled stimulus-specific plasticity in the visual cortex is mediated by astrocytes. *Proceedings of the National Academy of Sciences*, 109(41): E2832–E2841, 2012.

[70] T.-W. Chen, T. J. Wardill, Y. Sun, S. R. Pulver, S. L. Renninger, A. Baohan, E. R. Schreiter, R. A. Kerr, M. B. Orger, V. Jayaraman, et al. Ultrasensitive fluorescent proteins for imaging neuronal activity. *Nature*, 499(7458):295, 2013.

[71] X. Chen, L. Wang, Y. Zhou, L.-H. Zheng, and Z. Zhou. “kiss-and-run” glutamate secretion in cultured and freshly isolated rat hippocampal astrocytes. *Journal of Neuroscience*, 25(40):9236–9243, 2005.

[72] K. S. Christopherson, E. M. Ullian, C. C. Stokes, C. E. Mullowney, J. W. Hell, A. Agah, J. Lawler, D. F. Mosher, P. Bornstein, and B. A. Barres. Thrombospondins are astrocyte-secreted proteins that promote cns synaptogenesis. *Cell*, 120(3):421–433, 2005.

[73] H. Chun, H. An, J. Lim, J. Woo, J. Lee, H. Ryu, and C. J. Lee. Astrocytic probdnf and tonic gaba distinguish active versus reactive astrocytes in hippocampus. *Experimental Neurobiology*, 27(3):155–170, 2018.

[74] W.-S. Chung, L. E. Clarke, G. X. Wang, B. K. Stafford, A. Sher, C. Chakraborty, J. Joung, L. C. Foo, A. Thompson, C. Chen, et al. Astrocytes mediate synapse elimination through megf10 and mertk pathways. *Nature*, 504(7480):394, 2013.

[75] S. Ciappelloni, D. Bouchet, N. Dubourdieu, E. Boué-Grabot, B. Kellermayer, C. Manso, R. Marignier, S. H. Oliet, T. Tourdias, and L. Groc. Aquaporin-4 surface trafficking regulates astrocytic process motility and synaptic activity in health and autoimmune disease. *Cell reports*, 27(13):3860–3872, 2019.

[76] A. Ciesielska, G. Mittermeyer, P. Hadaczek, A. P. Kells, J. Forsayeth, and K. S. Bankiewicz. Anterograde axonal transport of aav2-gdnf in rat basal ganglia. *Molecular Therapy*, 19(5):922–927, 2011.

[77] D. E. Clapham. Calcium signaling. *Cell*, 131(6):1047–1058, 2007.

[78] J.-A. Conchello and J. W. Lichtman. Optical sectioning microscopy. *Nature methods*, 2(12):920, 2005.

[79] A. H. Cornell-Bell, S. M. Finkbeiner, M. S. Cooper, and S. J. Smith. Glutamate induces calcium waves in cultured astrocytes: long-range glial signaling. *Science*, 247(4941):470–473, 1990.

[80] D. A. Coulter and C. Steinhäuser. Role of astrocytes in epilepsy. *Cold Spring Harbor perspectives in medicine*, 5(3):a022434, 2015.

[81] A. Covelo and A. Araque. Neuronal activity determines distinct gliotransmitter release from a single astrocyte. *Elife*, 7:e32237, 2018.

[82] P. Cramer. Organization and regulation of gene transcription. *Nature*, 2019.

[83] S. Crochet and C. C. Petersen. Correlating whisker behavior with membrane potential in barrel cortex of awake mice. *Nature neuroscience*, 9(5):608, 2006.

[84] S. Crochet, J. F. Poulet, Y. Kremer, and C. C. Petersen. Synaptic mechanisms underlying sparse coding of active touch. *Neuron*, 69(6):1160–1175, 2011.

[85] G. Dallérac, J. Zapata, and N. Rouach. Versatile control of synaptic circuits by astrocytes: where, when and how? *Nature Reviews Neuroscience*, 19(12):729, 2018.

[86] H. Dana, B. Mohar, Y. Sun, S. Narayan, A. Gordus, J. P. Hasseman, G. Tsegaye, G. T. Holt, A. Hu, D. Walpita, et al. Sensitive red protein calcium indicators for imaging neural activity. *Elife*, 5:e12727, 2016.

[87] J. W. Dani, A. Chernjavsky, and S. J. Smith. Neuronal activity triggers calcium waves in hippocampal astrocyte networks. *Neuron*, 8(3):429–440, 1992.

[88] M. De Pittà, N. Brunel, and A. Volterra. Astrocytes: Orchestrating synaptic plasticity? *Neuroscience*, 323:43–61, 2016.

[89] J. De Toro, L. Herschlik, C. Waldner, and C. Mongini. Emerging roles of exosomes in normal and pathological conditions: new insights for diagnosis and therapeutic applications. *Frontiers in immunology*, 6:203, 2015.

[90] A. Delekate, M. Füchtemeier, T. Schumacher, C. Ulbrich, M. Foddis, and G. C. Petzold. Metabotropic p2y1 receptor signalling mediates astrocytic hyperactivity in vivo in an alzheimer's disease mouse model. *Nature communications*, 5:5422, 2014.

[91] W. Denk and K. Svoboda. Photon upmanship: why multiphoton imaging is more than a gimmick. *Neuron*, 18(3):351–357, 1997.

[92] M. A. Di Castro, J. Chuquet, N. Liaudet, K. Bhaukaurally, M. Santello, D. Bouvier, P. Tiret, and A. Volterra. Local ca 2+ detection and modulation of synaptic release by astrocytes. *Nature neuroscience*, 14(10):1276, 2011.

[93] F. Ding, J. O'Donnell, A. S. Thrane, D. Zeppenfeld, H. Kang, L. Xie, F. Wang, and M. Nedergaard. α1-adrenergic receptors mediate coordinated ca2+ signaling of cortical astrocytes in awake, behaving mice. *Cell calcium*, 54(6):387–394, 2013.

[94] S. Ding, T. Wang, W. Cui, and P. G. Haydon. Photothrombosis ischemia stimulates a sustained astrocytic ca2+ signaling in vivo. *Glia*, 57(7):767–776, 2009.

[95] M. B. Dinkins, S. Dasgupta, G. Wang, G. Zhu, and E. Bieberich. Exosome reduction in vivo is associated with lower amyloid plaque load in the 5xfad mouse model of alzheimer's disease. *Neurobiology of aging*, 35(8):1792–1800, 2014.

[96] H. S. Domingues, C. C. Portugal, R. Socodato, and J. B. Relvas. Oligodendrocyte, astrocyte, and microglia crosstalk in myelin development, damage, and repair. *Frontiers in cell and developmental biology*, 4:71, 2016.

[97] Q. Dong, Q. Liu, R. Li, A. Wang, Q. Bu, K. H. Wang, and Q. Chang. Mechanism and consequence of abnormal calcium homeostasis in rett syndrome astrocytes. *Elife*, 7:e33417, 2018.

[98] D. Duan, P. Sharma, J. Yang, Y. Yue, L. Dudus, Y. Zhang, K. J. Fisher, and J. F. Engelhardt. Circular intermediates of recombinant adeno-associated virus have defined structural characteristics responsible for long-term episomal persistence in muscle tissue. *Journal of virology*, 72(11):8568–8577, 1998.

[99] D. Duan, Q. Li, A. W. Kao, Y. Yue, J. E. Pessin, and J. F. Engelhardt. Dynamin is required for recombinant adeno-associated virus type 2 infection. *Journal of virology*, 73(12):10371–10376, 1999.

[100] D. Duan, P. Sharma, L. Dudus, Y. Zhang, S. Sanlioglu, Z. Yan, Y. Yue, Y. Ye, R. Lester, J. Yang, et al. Formation of adeno-associated virus circular genomes is differentially regulated by adenovirus e4 orf6 and e2a gene expression. *Journal of virology*, 73(1):161–169, 1999.

[101] D. Duan, Y. Yue, and J. F. Engelhardt. Expanding aav packaging capacity with trans-splicing or overlapping vectors: a quantitative comparison. *Molecular therapy*, 4(4):383–391, 2001.

[102] K. M. Dunn, D. C. Hill-Eubanks, W. B. Liedtke, and M. T. Nelson. Trpv4 channels stimulate ca2+-induced ca2+ release in astrocytic endfeet and amplify neurovascular coupling responses. *Proceedings of the National Academy of Sciences*, 110(15):6157–6162, 2013.

[103] D. Durham and T. A. Woolsey. Acute whisker removal reduces neuronal activity in barrels of mouse sml cortex. *Journal of Comparative Neurology*, 178(4):629–644, 1978.

[104] C. A. Durkee and A. Araque. Diversity and specificity of astrocyte–neuron communication. *Neuroscience*, 396:73–78, 2019.

[105] M. K. Enkvist and K. D. McCarthy. Activation of protein kinase c blocks astroglial gap junction communication and inhibits the spread of calcium waves. *Journal of neurochemistry*, 59(2):519–526, 1992.

[106] V. Eulenburg and J. Gomeza. Neurotransmitter transporters expressed in glial cells as regulators of synapse function. *Brain research reviews*, 63(1-2):103–112, 2010.

[107] X. Fan and Y. Agid. At the origin of the history of glia. *Neuroscience*, 385: 255–271, 2018.

[108] T. Fellin, O. Pascual, S. Gobbo, T. Pozzan, P. G. Haydon, and G. Carmignoto. Neuronal synchrony mediated by astrocytic glutamate through activation of extrasynaptic nmda receptors. *Neuron*, 43(5):729–743, 2004.

[109] J. Feng, C. Zhang, J. E. Lischinsky, M. Jing, J. Zhou, H. Wang, Y. Zhang, A. Dong, Z. Wu, H. Wu, et al. A genetically encoded fluorescent sensor for rapid and specific in vivo detection of norepinephrine. *Neuron*, 102(4):745–761, 2019.

[110] T. A. Fiacco and K. D. McCarthy. Intracellular astrocyte calcium waves in situ increase the frequency of spontaneous ampa receptor currents in ca1 pyramidal neurons. *Journal of Neuroscience*, 24(3):722–732, 2004.

[111] T. A. Fiacco and K. D. McCarthy. Multiple lines of evidence indicate that gliotransmission does not occur under physiological conditions. *Journal of Neuroscience*, 38(1):3–13, 2018.

[112] T. A. Fiacco, C. Agulhon, S. R. Taves, J. Petravicz, K. B. Casper, X. Dong, J. Chen, and K. D. McCarthy. Selective stimulation of astrocyte calcium in situ does not affect neuronal excitatory synaptic activity. *Neuron*, 54(4):611–626, 2007.

[113] B. F. Fosque, Y. Sun, H. Dana, C.-T. Yang, T. Ohyama, M. R. Tadross, R. Patel, M. Zlatic, D. S. Kim, M. B. Ahrens, et al. Labeling of active neural circuits in vivo with designed calcium integrators. *Science*, 347(6223):755–760, 2015.

[114] Y. Fujii, S. Maekawa, and M. Morita. Astrocyte calcium waves propagate proximally by gap junction and distally by extracellular diffusion of atp released from volume-regulated anion channels. *Scientific reports*, 7(1):13115, 2017.

[115] T. Fujita, M. J. Chen, B. Li, N. A. Smith, W. Peng, W. Sun, M. J. Toner, B. T. Kress, L. Wang, A. Benraiss, et al. Neuronal transgene expression in dominant-negative snare mice. *Journal of Neuroscience*, 34(50):16594–16604, 2014.

[116] C. Genoud, C. Quairiaux, P. Steiner, H. Hirling, E. Welker, and G. W. Knott. Plasticity of astrocytic coverage and glutamate transporter expression in adult mouse cortex. *PLoS biology*, 4(11):e343, 2006.

[117] C. Giaume, A. Koulakoff, L. Roux, D. Holcman, and N. Rouach. Astroglial networks: a step further in neuroglial and gliovascular interactions. *Nature Reviews Neuroscience*, 11(2):87, 2010.

[118] W. Göbel, B. M. Kampa, and F. Helmchen. Imaging cellular network dynamics in three dimensions using fast 3d laser scanning. *Nature methods*, 4(1):73, 2007.

[119] M. A. Gonçalves. Adeno-associated virus: from defective virus to effective vector. *Virology journal*, 2(1):43, 2005.

[120] G. R. Gordon, H. B. Choi, R. L. Rungta, G. C. Ellis-Davies, and B. A. MacVicar. Brain metabolism dictates the polarity of astrocyte control over arterioles. *Nature*, 456(7223):745, 2008.

[121] S. J. Gray, S. B. Foti, J. W. Schwartz, L. Bachaboina, B. Taylor-Blake, J. Coleman, M. D. Ehlers, M. J. Zylka, T. J. McCown, and R. J. Samulski. Optimizing promoters for recombinant adeno-associated virus-mediated gene expression in the peripheral and central nervous system using self-complementary vectors. *Human gene therapy*, 22(9):1143–1153, 2011.

[122] A. Grosche, J. Grosche, M. Tackenberg, D. Scheller, G. Gerstner, A. Gumprecht, T. Pannicke, P. G. Hirrlinger, U. Wilhelmsson, K. Hüttmann, et al. Versatile and simple approach to determine astrocyte territories in mouse neocortex and hippocampus. *PLoS One*, 8(7):e69143, 2013.

[123] J. Grosche, V. Matyash, T. Möller, A. Verkhratsky, A. Reichenbach, and H. Kettenmann. Microdomains for neuron–glia interaction: parallel fiber signaling to bergmann glial cells. *Nature neuroscience*, 2(2):139, 1999.

[124] S. Guerra-Gomes, N. Sousa, L. Pinto, and J. F. Oliveira. Functional roles of astrocyte calcium elevations: from synapses to behavior. *Frontiers in cellular neuroscience*, 11:427, 2018.

[125] L. B. Haim and D. H. Rowitch. Functional diversity of astrocytes in neural circuit regulation. *Nature Reviews Neuroscience*, 18(1):31, 2017.

[126] N. B. Hamilton and D. Attwell. Do astrocytes really exocytose neurotransmitters? *Nature Reviews Neuroscience*, 11(4):227, 2010.

[127] J. Han, P. Kesner, M. Metna-Laurent, T. Duan, L. Xu, F. Georges, M. Koehl, D. N. Abrous, J. Mendizabal-Zubiaga, P. Grandes, et al. Acute cannabinoids impair working memory through astroglial cb1 receptor modulation of hippocampal ltd. *Cell*, 148(5):1039–1050, 2012.

[128] J. J. Harris, R. Jolivet, and D. Attwell. Synaptic energy use and supply. *Neuron*, 75(5):762–777, 2012.

[129] M. D. Haustein, S. Kracun, X.-H. Lu, T. Shih, O. Jackson-Weaver, X. Tong, J. Xu, X. W. Yang, T. J. O'Dell, J. S. Marvin, et al. Conditions and constraints for astrocyte calcium signaling in the hippocampal mossy fiber pathway. *Neuron*, 82(2):413–429, 2014.

[130] J. P. Heller and D. A. Rusakov. The nanoworld of the tripartite synapse: insights from super-resolution microscopy. *Frontiers in Cellular Neuroscience*, 11:374, 2017.

[131] J. P. Heller, T. Odii, K. Zheng, and D. A. Rusakov. Imaging tripartite synapses using super-resolution microscopy. *Methods*, 2019.

[132] F. Helmchen and W. Denk. Deep tissue two-photon microscopy. *Nature methods*, 2(12):932, 2005.

[133] C. Henneberger, T. Papouin, S. H. Oliet, and D. A. Rusakov. Long-term potentiation depends on release of d-serine from astrocytes. *Nature*, 463(7278):232, 2010.

[134] C. Henneberger, L. Bard, A. Panatier, J. P. Reynolds, N. I. Medvedev, D. Minge, M. K. Herde, S. Anders, I. Kraev, J. Heller, et al. Ltp induction drives remodeling of astroglia to boost glutamate escape from synapses. *bioRxiv*, page 349233, 2019.

[135] R. Hepp, M. Perraut, S. Chasserot-Golaz, T. Galli, D. Aunis, K. Langley, and N. J. Grant. Cultured glial cells express the snap-25 analogue snap-23. *Glia*, 27 (2):181–187, 1999.

[136] O. Hernandez, E. Papagiakoumou, D. Tanese, K. Fidelin, C. Wyart, and V. Emiliani. Three-dimensional spatiotemporal focusing of holographic patterns. *Nature communications*, 7(1):1–11, 2016.

[137] N. P. Hessvik and A. Llorente. Current knowledge on exosome biogenesis and release. *Cellular and Molecular Life Sciences*, 75(2):193–208, 2018.

[138] K. Heuser, C. G. Nome, K. H. Pettersen, K. S. Åbjørsbråten, V. Jensen, W. Tang, R. Sprengel, E. Taubøll, E. A. Nagelhus, and R. Enger. Ca2+ signals in astrocytes facilitate spread of epileptiform activity. *Cerebral Cortex*, 28(11):4036–4048, 2018.

[139] D. Hilger, M. Masureel, and B. K. Kobilka. Structure and dynamics of gpcr signaling complexes. *Nature structural & molecular biology*, 25(1):4, 2018.

[140] H. Hirase, L. Qian, P. Barthó, and G. Buzsáki. Calcium dynamics of cortical astrocytic networks in vivo. *PLoS biology*, 2(4):e96, 2004.

[141] S. A. Hires, D. A. Gutnisky, J. Yu, D. H. O'Connor, and K. Svoboda. Low-noise encoding of active touch by layer 4 in the somatosensory cortex. *Elife*, 4:e06619, 2015.

[142] K. P. Hoeflich and M. Ikura. Calmodulin in action: diversity in target recognition and activation mechanisms. *Cell*, 108(6):739–742, 2002.

[143] T. Höfer, L. Venance, and C. Giaume. Control and plasticity of intercellular calcium waves in astrocytes: a modeling approach. *Journal of Neuroscience*, 22 (12):4850–4859, 2002.

[144] T. M. Hoogland and B. Kuhn. Recent developments in the understanding of astrocyte function in the cerebellum in vivo. *The Cerebellum*, 9(3):264–271, 2010.

[145] N. G. Horton, K. Wang, D. Kobat, C. G. Clark, F. W. Wise, C. B. Schaffer, and C. Xu. In vivo three-photon microscopy of subcortical structures within an intact mouse brain. *Nature photonics*, 7(3):205, 2013.

[146] V. Houades, A. Koulakoff, P. Ezan, I. Seif, and C. Giaume. Gap junction-mediated astrocytic networks in the mouse barrel cortex. *Journal of Neuroscience*, 28(20):5207–5217, 2008.

[147] B. Huang, M. Bates, and X. Zhuang. Super-resolution fluorescence microscopy. *Annual review of biochemistry*, 78:993–1016, 2009.

[148] E. Hudry, C. Martin, S. Gandhi, B. György, D. I. Scheffer, D. Mu, S. F. Merkel, F. Mingozzi, Z. Fitzpatrick, H. Dimant, et al. Exosome-associated aav vector as a robust and convenient neuroscience tool. *Gene therapy*, 23(4):380, 2016.

[149] S. Hülsmann, L. Hagos, H. Heuer, and C. Schnell. Limitations of sulforhodamine 101 for brain imaging. *Frontiers in cellular neuroscience*, 11:44, 2017.

[150] J. J. Iliff, M. Wang, Y. Liao, B. A. Plogg, W. Peng, G. A. Gundersen, H. Benveniste, G. E. Vates, R. Deane, S. A. Goldman, et al. A paravascular pathway facilitates csf flow through the brain parenchyma and the clearance of interstitial solutes, including amyloid β. *Science translational medicine*, 4(147):147ra111–147ra111, 2012.

[151] T. Ishibashi, K. A. Dakin, B. Stevens, P. R. Lee, S. V. Kozlov, C. L. Stewart, and R. D. Fields. Astrocytes promote myelination in response to electrical impulses. *Neuron*, 49(6):823–832, 2006.

[152] A. D. Jacob, A. I. Ramsaran, A. J. Mocle, L. M. Tran, C. Yan, P. W. Frankland, and S. A. Josselyn. A compact head-mounted endoscope for in vivo calcium imaging in freely behaving mice. *Current protocols in neuroscience*, 84(1):e51, 2018.

[153] A. M. Janas, K. Sapoń, T. Janas, M. H. Stowell, and T. Janas. Exosomes and other extracellular vesicles in neural cells and neurodegenerative diseases. *Biochimica et Biophysica Acta (BBA)-Biomembranes*, 1858(6):1139–1151, 2016.

[154] A. Jennings, O. Tyurikova, L. Bard, K. Zheng, A. Semyanov, C. Henneberger, and D. A. Rusakov. Dopamine elevates and lowers astroglial ca2+ through distinct pathways depending on local synaptic circuitry. *Glia*, 65(3):447–459, 2017.

[155] N. A. Jessen, A. S. F. Munk, I. Lundgaard, and M. Nedergaard. The glymphatic system: a beginner's guide. *Neurochemical research*, 40(12):2583–2599, 2015.

[156] M. K. Jha, M. Jo, J.-H. Kim, and K. Suk. Microglia-astrocyte crosstalk: an intimate molecular conversation. *The Neuroscientist*, 25(3):227–240, 2019.

[157] R. Jiang, B. Diaz-Castro, L. L. Looger, and B. S. Khakh. Dysfunctional calcium and glutamate signaling in striatal astrocytes from huntington's disease model mice. *Journal of Neuroscience*, 36(12):3453–3470, 2016.

[158] S. Jo, O. Yarishkin, Y. J. Hwang, Y. E. Chun, M. Park, D. H. Woo, J. Y. Bae, T. Kim, J. Lee, H. Chun, et al. Gaba from reactive astrocytes impairs memory in mouse models of alzheimer's disease. *Nature medicine*, 20(8):886, 2014.

[159] E. V. Jones, Y. Bernardinelli, Y. C. Tse, S. Chierzi, T. P. Wong, and K. K. Murai. Astrocytes control glutamate receptor levels at developing synapses through sparc–β-integrin interactions. *Journal of Neuroscience*, 31(11):4154–4165, 2011.

[160] P. Jourdain, L. H. Bergersen, K. Bhaukaurally, P. Bezzi, M. Santello, M. Domercq, C. Matute, F. Tonello, V. Gundersen, and A. Volterra. Glutamate exocytosis from astrocytes controls synaptic strength. *Nature neuroscience*, 10 (3):331, 2007.

[161] M. Jun-ichi, T. Satoshi, A. Kimi, T. Fumi, T. Akira, T. Kiyoshi, and Y. Ken-ichi. Expression vector system based on the chicken β-actin promoter directs efficient production of interleukin-5. *Gene*, 79(2):269–277, 1989.

[162] N. Kaludov, K. E. Brown, R. W. Walters, J. Zabner, and J. A. Chiorini. Adeno-associated virus serotype 4 (aav4) and aav5 both require sialic acid binding for hemagglutination and efficient transduction but differ in sialic acid linkage specificity. *Journal of virology*, 75(15):6884–6893, 2001.

[163] E. R. Kandel, J. H. Schwartz, T. M. Jessell, D. of Biochemistry, M. B. T. Jessell, S. Siegelbaum, and A. Hudspeth. *Principles of neural science*, volume 4. McGraw-hill New York, 2000.

[164] K. Kanemaru, H. Sekiya, M. Xu, K. Satoh, N. Kitajima, K. Yoshida, Y. Okubo, T. Sasaki, S. Moritoh, H. Hasuwa, et al. In vivo visualization of subtle, transient, and local activity of astrocytes using an ultrasensitive ca2+ indicator. *Cell reports*, 8(1):311–318, 2014.

[165] J. Kang, L. Jiang, S. A. Goldman, and M. Nedergaard. Astrocyte-mediated potentiation of inhibitory synaptic transmission. *Nature neuroscience*, 1(8):683, 1998.

[166] J. Kang, N. Kang, Y. Yu, J. Zhang, N. Petersen, G.-F. Tian, and M. Nedergaard. Sulforhodamine 101 induces long-term potentiation of intrinsic excitability and synaptic efficacy in hippocampal ca1 pyramidal neurons. *Neuroscience*, 169(4): 1601–1609, 2010.

[167] M. Kannan, G. Vasan, C. Huang, S. Haziza, J. Z. Li, H. Inan, M. J. Schnitzer, and V. A. Pieribone. Fast, in vivo voltage imaging using a red fluorescent indicator. *Nature methods*, 15(12):1108–1116, 2018.

[168] B. K. Kaspar, D. Erickson, D. Schaffer, L. Hinh, F. H. Gage, and D. A. Peterson. Targeted retrograde gene delivery for neuronal protection. *Molecular Therapy*, 5 (1):50–56, 2002.

[169] B. K. Kaspar, J. Lladó, N. Sherkat, J. D. Rothstein, and F. H. Gage. Retrograde viral delivery of igf-1 prolongs survival in a mouse als model. *Science*, 301(5634): 839–842, 2003.

[170] J. M. Kelich, J. Ma, B. Dong, Q. Wang, M. Chin, C. M. Magura, W. Xiao, and W. Yang. Super-resolution imaging of nuclear import of adeno-associated virus in live cells. *Molecular Therapy-Methods & Clinical Development*, 2:15047, 2015.

[171] D. Keller, C. Erö, and H. Markram. Cell densities in the mouse brain: a systematic review. *Frontiers in neuroanatomy*, 12:83, 2018.

[172] A. P. Kells, P. Hadaczek, D. Yin, J. Bringas, V. Varenika, J. Forsayeth, and K. S. Bankiewicz. Efficient gene therapy-based method for the delivery of therapeutics to primate cortex. *Proceedings of the National Academy of Sciences*, 106(7): 2407–2411, 2009.

[173] M. K. Kelly, G. E. Carvell, J. M. Kodger, and D. J. Simons. Sensory loss by selected whisker removal produces immediate disinhibition in the somatosensory cortex of behaving rats. *Journal of Neuroscience*, 19(20):9117–9125, 1999.

[174] B. S. Khakh and K. D. McCarthy. Astrocyte calcium signaling: from observations to functions and the challenges therein. *Cold Spring Harbor perspectives in biology*, 7(4):a020404, 2015.

[175] B. S. Khakh and M. V. Sofroniew. Diversity of astrocyte functions and phenotypes in neural circuits. *Nature neuroscience*, 18(7):942, 2015.

[176] G. Khan, W. Ahmed, and P. S. Philip. Exosomes and their role in viral infections. *Novel Implications of Exosomes in Diagnosis and Treatment of Cancer and Infectious Diseases*, pages 76–95, 2017.

[177] S. K. Kim, H. Hayashi, T. Ishikawa, K. Shibata, E. Shigetomi, Y. Shinozaki, H. Inada, S. E. Roh, S. J. Kim, G. Lee, et al. Cortical astrocytes rewire somatosensory cortical circuits for peripheral neuropathic pain. *The Journal of clinical investigation*, 126(5):1983–1997, 2016.

[178] H. K. Kimelberg. The problem of astrocyte identity. *Neurochemistry international*, 45(2-3):191–202, 2004.

[179] R. Klein, B. Ruttkowski, E. Knapp, B. Salmons, W. H. Günzburg, and C. Hohenadl. Wpre-mediated enhancement of gene expression is promoter and cell line specific. *Gene*, 372:153–161, 2006.

[180] T. Knöpfel. Genetically encoded optical indicators for the analysis of neuronal circuits. *Nature Reviews Neuroscience*, 13(10):687, 2012.

[181] K. Koles, J. Nunnari, C. Korkut, R. Barria, C. Brewer, Y. Li, J. Leszyk, B. Zhang, and V. Budnik. Mechanism of evenness interrupted (evi)-exosome release at synaptic boutons. *Journal of Biological Chemistry*, 287(20):16820–16834, 2012.

[182] N. Korogod, C. C. Petersen, and G. W. Knott. Ultrastructural analysis of adult mouse neocortex comparing aldehyde perfusion with cryo fixation. *Elife*, 4:e05793, 2015.

[183] N. Kosaka, H. Iguchi, Y. Yoshioka, F. Takeshita, Y. Matsuki, and T. Ochiya. Secretory mechanisms and intercellular transfer of micrornas in living cells. *Journal of Biological Chemistry*, 285(23):17442–17452, 2010.

[184] M. A. Kotterman and D. V. Schaffer. Engineering adeno-associated viruses for clinical gene therapy. *Nature Reviews Genetics*, 15(7):445, 2014.

[185] A. Koulakoff, P. Ezan, and C. Giaume. Neurons control the expression of connexin 30 and connexin 43 in mouse cortical astrocytes. *Glia*, 56(12):1299–1311, 2008.

[186] A. Kozlov, M. Angulo, E. Audinat, and S. Charpak. Target cell-specific modulation of neuronal activity by astrocytes. *Proceedings of the National Academy of Sciences*, 103(26):10058–10063, 2006.

[187] K. Kuboyama, H. Harada, H. Tozaki-Saitoh, M. Tsuda, K. Ushijima, and K. Inoue. Astrocytic p2y1 receptor is involved in the regulation of cytokine/chemokine transcription and cerebral damage in a rat model of cerebral ischemia. *Journal of Cerebral Blood Flow & Metabolism*, 31(9):1930–1941, 2011.

[188] K. V. Kuchibhotla, C. R. Lattarulo, B. T. Hyman, and B. J. Bacskai. Synchronous hyperactivity and intercellular calcium waves in astrocytes in alzheimer mice. *Science*, 323(5918):1211–1215, 2009.

[189] H. Kucukdereli, N. J. Allen, A. T. Lee, A. Feng, M. I. Ozlu, L. M. Conatser, C. Chakraborty, G. Workman, M. Weaver, E. H. Sage, et al. Control of excitatory cns synaptogenesis by astrocyte-secreted proteins hevin and sparc. *Proceedings of the National Academy of Sciences*, 108(32):E440–E449, 2011.

[190] S. W. Kuffler. The ferrier lecture-neuroglial cells: physiological properties and a potassium mediated effect of neuronal activity on the glial membrane potential. *Proceedings of the Royal Society of London. Series B. Biological Sciences*, 168 (1010):1–21, 1967.

[191] S. Kügler, E. Kilic, and M. Bähr. Human synapsin 1 gene promoter confers highly neuron-specific long-term transgene expression from an adenoviral vector in the adult rat brain depending on the transduced area. *Gene therapy*, 10(4): 337, 2003.

[192] A. Kulik, A. Haentzsch, M. Lückermann, W. Reichelt, and K. Ballanyi. Neuron–glia signaling via $\alpha 1$ adrenoceptor-mediated ca2+ release in bergmann glial cells in situ. *Journal of Neuroscience*, 19(19):8401–8408, 1999.

[193] J. Kwon, H. An, M. Sa, J. Won, J. I. Shin, and C. J. Lee. Orai1 and orai3 in combination with stim1 mediate the majority of store-operated calcium entry in astrocytes. *Experimental neurobiology*, 26(1):42–54, 2017.

[194] D. Lanjakornsiripan, B.-J. Pior, D. Kawaguchi, S. Furutachi, T. Tahara, Y. Katsuyama, Y. Suzuki, Y. Fukazawa, and Y. Gotoh. Layer-specific morphological and molecular differences in neocortical astrocytes and their dependence on neuronal layers. *Nature communications*, 9(1):1623, 2018.

[195] M. Lavialle, G. Aumann, E. Anlauf, F. Pröls, M. Arpin, and A. Derouiche. Structural plasticity of perisynaptic astrocyte processes involves ezrin and metabotropic glutamate receptors. *Proceedings of the National Academy of Sciences*, 108(31):12915–12919, 2011.

[196] K. Le Meur, J. Mendizabal-Zubiaga, P. Grandes, and E. Audinat. Gaba release by hippocampal astrocytes. *Frontiers in computational neuroscience*, 6:59, 2012.

[197] G. Lee and I. Saito. Role of nucleotide sequences of loxp spacer region in cre-mediated recombination. *Gene*, 216(1):55–65, 1998.

[198] S. Lee, B.-E. Yoon, K. Berglund, S.-J. Oh, H. Park, H.-S. Shin, G. J. Augustine, and C. J. Lee. Channel-mediated tonic gaba release from glia. *Science*, 330 (6005):790–796, 2010.

[199] S. A. Liddelow, K. A. Guttenplan, L. E. Clarke, F. C. Bennett, C. J. Bohlen, L. Schirmer, M. L. Bennett, A. E. Münch, W.-S. Chung, T. C. Peterson, et al. Neurotoxic reactive astrocytes are induced by activated microglia. *Nature*, 541 (7638):481, 2017.

[200] B. L. Lind, A. R. Brazhe, S. B. Jessen, F. C. Tan, and M. J. Lauritzen. Rapid stimulus-evoked astrocyte ca2+ elevations and hemodynamic responses in mouse somatosensory cortex in vivo. *Proceedings of the National Academy of Sciences*, 110(48):E4678–E4687, 2013.

[201] B. L. Lind, S. B. Jessen, M. Lønstrup, C. Joséphine, G. Bonvento, and M. Lauritzen. Fast ca2+ responses in astrocyte end-feet and neurovascular coupling in mice. *Glia*, 66(2):348–358, 2018.

[202] J. Livet, T. A. Weissman, H. Kang, R. W. Draft, J. Lu, R. A. Bennis, J. R. Sanes, and J. W. Lichtman. Transgenic strategies for combinatorial expression of fluorescent proteins in the nervous system. *Nature*, 450(7166):56, 2007.

[203] L. Lo and D. J. Anderson. A cre-dependent, anterograde transsynaptic viral tracer for mapping output pathways of genetically marked neurons. *Neuron*, 72 (6):938–950, 2011.

[204] M. López-Hidalgo, V. Kellner, and J. Schummers. Astrocyte calcium responses to sensory input: influence of circuit organization and experimental factors. *Frontiers in neural circuits*, 11:16, 2017.

[205] F. J. López-Murcia, B. Terni, and A. Llobet. Sparc triggers a cell-autonomous program of synapse elimination. *Proceedings of the National Academy of Sciences*, 112(43):13366–13371, 2015.

[206] A. Louveau, B. A. Plog, S. Antila, K. Alitalo, M. Nedergaard, and J. Kipnis. Understanding the functions and relationships of the glymphatic system and meningeal lymphatics. *The Journal of clinical investigation*, 127(9):3210–3219, 2017.

[207] R. Lu, W. Sun, Y. Liang, A. Kerlin, J. Bierfeld, J. D. Seelig, D. E. Wilson, B. Scholl, B. Mohar, M. Tanimoto, et al. Video-rate volumetric functional imaging of the brain at synaptic resolution. *Nature neuroscience*, 20(4):620, 2017.

[208] B. Ma, R. Buckalew, Y. Du, C. M. Kiyoshi, C. C. Alford, W. Wang, D. M. McTigue, J. J. Enyeart, D. Terman, and M. Zhou. Gap junction coupling confers isopotentiality on astrocyte syncytium. *Glia*, 64(2):214–226, 2016.

[209] P. M. Ma and T. A. Woolsey. Cytoarchitectonic correlates of the vibrissae in the medullary trigeminal complex of the mouse. *Brain research*, 306(1-2):374–379, 1984.

[210] P. J. Magistretti and I. Allaman. Lactate in the brain: from metabolic end-product to signalling molecule. *Nature Reviews Neuroscience*, 19(4):235, 2018.

[211] C. A. Maguire, L. Balaj, S. Sivaraman, M. H. Crommentuijn, M. Ericsson, L. Mincheva-Nilsson, V. Baranov, D. Gianni, B. A. Tannous, M. Sena-Esteves, et al. Microvesicle-associated aav vector as a novel gene delivery system. *Molecular Therapy*, 20(5):960–971, 2012.

[212] S. V. Mahler and G. Aston-Jones. Cno evil? considerations for the use of dreadds in behavioral neuroscience. *Neuropsychopharmacology*, 43(5):934, 2018.

[213] S. Mahmoud, M. Gharagozloo, C. Simard, and D. Gris. Astrocytes maintain glutamate homeostasis in the cns by controlling the balance between glutamate uptake and release. *Cells*, 8(2):184, 2019.

[214] E. B. Malarkey and V. Parpura. Mechanisms of glutamate release from astrocytes. *Neurochemistry international*, 52(1-2):142–154, 2008.

[215] L. Mariotti, G. Losi, A. Lia, M. Melone, A. Chiavegato, M. Gómez-Gonzalo, M. Sessolo, S. Bovetti, A. Forli, M. Zonta, et al. Interneuron-specific signaling evokes distinctive somatostatin-mediated responses in adult cortical astrocytes. *Nature communications*, 9(1):82, 2018.

[216] R. Martín, R. Bajo-Grañeras, R. Moratalla, G. Perea, and A. Araque. Circuit-specific signaling in astrocyte-neuron networks in basal ganglia pathways. *Science*, 349(6249):730–734, 2015.

[217] M. Martin-Fernandez, S. Jamison, L. M. Robin, Z. Zhao, E. D. Martin, J. Aguilar, M. A. Benneyworth, G. Marsicano, and A. Araque. Synapse-specific astrocyte gating of amygdala-related behavior. *Nature neuroscience*, 20(11):1540, 2017.

[218] A. Martinez-Hernandez, K. P. Bell, and M. D. Norenberg. Glutamine synthetase: glial localization in brain. *Science*, 195(4284):1356–1358, 1977.

[219] J. S. Marvin, B. G. Borghuis, L. Tian, J. Cichon, M. T. Harnett, J. Akerboom, A. Gordus, S. L. Renninger, T.-W. Chen, C. I. Bargmann, et al. An optimized fluorescent probe for visualizing glutamate neurotransmission. *Nature methods*, 10(2):162, 2013.

[220] T. M. Mathiisen, K. P. Lehre, N. C. Danbolt, and O. P. Ottersen. The perivascular astroglial sheath provides a complete covering of the brain microvessels: an electron microscopic 3d reconstruction. *Glia*, 58(9):1094–1103, 2010.

[221] D. H. Mauch, K. Nägler, S. Schumacher, C. Göritz, E.-C. Müller, A. Otto, and F. W. Pfrieger. Cns synaptogenesis promoted by glia-derived cholesterol. *Science*, 294(5545):1354–1357, 2001.

[222] K. M. Mearow, J. F. Mill, and E. Freese. Neuron–glial interactions involved in the regulation of glutamine synthetase. *Glia*, 3(5):385–392, 1990.

[223] D. G. Meckes and N. Raab-Traub. Microvesicles and viral infection. *Journal of virology*, 85(24):12844–12854, 2011.

[224] S. Mederos, A. Hernández-Vivanco, J. Ramírez-Franco, M. Martín-Fernández, M. Navarrete, A. Yang, E. S. Boyden, and G. Perea. Melanopsin for precise optogenetic activation of astrocyte-neuron networks. *Glia*, 67(5):915–934, 2019.

[225] P. Meneses, K. I. Berns, and E. Winocour. Dna sequence motifs which direct adeno-associated virus site-specific integration in a model system. *Journal of virology*, 74(13):6213–6216, 2000.

[226] P. Mergenthaler, U. Lindauer, G. A. Dienel, and A. Meisel. Sugar for the brain: the role of glucose in physiological and pathological brain function. *Trends in neurosciences*, 36(10):587–597, 2013.

[227] C. Meunier, N. Wang, C. Yi, G. Dallerac, P. Ezan, A. Koulakoff, L. Leybaert, and C. Giaume. Contribution of astroglial cx43 hemichannels to the modulation of glutamatergic currents by d-serine in the mouse prefrontal cortex. *Journal of Neuroscience*, 37(37):9064–9075, 2017.

[228] S. J. Miller. Astrocyte heterogeneity in the adult central nervous system. *Frontiers in cellular neuroscience*, 12:401, 2018.

[229] A. Mishra, J. P. Reynolds, Y. Chen, A. V. Gourine, D. A. Rusakov, and D. Attwell. Astrocytes mediate neurovascular signaling to capillary pericytes but not to arterioles. *Nature neuroscience*, 19(12):1619, 2016.

[230] P. Mittaud, G. Labourdette, H. Zingg, and D. Guenot-Di Scala. Neurons modulate oxytocin receptor expression in rat cultured astrocytes: Involvement of tgf-β and membrane components. *Glia*, 37(2):169–177, 2002.

[231] T. Mittelsteadt, G. Seifert, E. Alvárez-Barón, C. Steinhäuser, A. J. Becker, and S. Schoch. Differential mrna expression patterns of the synaptotagmin gene family in the rodent brain. *Journal of Comparative Neurology*, 512(4):514–528, 2009.

[232] K. Miya, R. Inoue, Y. Takata, M. Abe, R. Natsume, K. Sakimura, K. Hongou, T. Miyawaki, and H. Mori. Serine racemase is predominantly localized in neurons in mouse brain. *Journal of Comparative Neurology*, 510(6):641–654, 2008.

[233] S. Miyazaki, H. Shirakawa, K. Nakada, and Y. Honda. Essential role of the inositol 1, 4, 5-trisphosphate receptor/ca2+ release channel in ca2+ waves and ca2+ oscillations at fertilization of mammalian eggs. *Developmental biology*, 158 (1):62–78, 1993.

[234] A. V. Molofsky, R. Krenick, E. Ullian, H.-h. Tsai, B. Deneen, W. D. Richardson, B. A. Barres, and D. H. Rowitch. Astrocytes and disease: a neurodevelopmental perspective. *Genes & development*, 26(9):891–907, 2012.

[235] J. D. Moore, N. M. Lindsay, M. Deschênes, and D. Kleinfeld. Vibrissa self-motion and touch are reliably encoded along the same somatosensory pathway from brainstem through thalamus. *PLoS biology*, 13(9):e1002253, 2015.

[236] S. J. Mulligan and B. A. MacVicar. Calcium transients in astrocyte endfeet cause cerebrovascular constrictions. *Nature*, 431(7005):195, 2004.

[237] C. Murphy-Royal, J. P. Dupuis, J. A. Varela, A. Panatier, B. Pinson, J. Baufreton, L. Groc, and S. H. Oliet. Surface diffusion of astrocytic glutamate transporters shapes synaptic transmission. *Nature neuroscience*, 18(2):219, 2015.

[238] N. Muzyczka. Use of adeno-associated virus as a general transduction vector for mammalian cells. In *Viral expression vectors*, pages 97–129. Springer, 1992.

[239] E. A. Nagelhus and O. P. Ottersen. Physiological roles of aquaporin-4 in brain. *Physiological reviews*, 93(4):1543–1562, 2013.

[240] J. I. Nagy and J. E. Rash. Connexins and gap junctions of astrocytes and oligodendrocytes in the cns. *Brain research reviews*, 32(1):29–44, 2000.

[241] H. Nakai, S. R. Yant, T. A. Storm, S. Fuess, L. Meuse, and M. A. Kay. Extrachromosomal recombinant adeno-associated virus vector genomes are primarily responsible for stable liver transduction in vivo. *Journal of virology*, 75(15): 6969–6976, 2001.

[242] J. Nakai, M. Ohkura, and K. Imoto. A high signal-to-noise ca 2+ probe composed of a single green fluorescent protein. *Nature biotechnology*, 19(2):137, 2001.

[243] M. Navarrete, G. Perea, D. F. de Sevilla, M. Gómez-Gonzalo, A. Núñez, E. D. Martín, and A. Araque. Astrocytes mediate in vivo cholinergic-induced synaptic plasticity. *PLoS biology*, 10(2):e1001259, 2012.

[244] M. Nedergaard. Direct signaling from astrocytes to neurons in cultures of mammalian brain cells. *Science*, 263(5154):1768–1771, 1994.

[245] W. J. Nett, S. H. Oloff, and K. D. Mccarthy. Hippocampal astrocytes in situ exhibit calcium oscillations that occur independent of neuronal activity. *Journal of neurophysiology*, 87(1):528–537, 2002.

[246] E. A. Newman. New roles for astrocytes: regulation of synaptic transmission. *Trends in neurosciences*, 26(10):536–542, 2003.

[247] C. M. Niell and M. P. Stryker. Modulation of visual responses by behavioral state in mouse visual cortex. *Neuron*, 65(4):472–479, 2010.

[248] A. Nimmerjahn, F. Kirchhoff, J. N. Kerr, and F. Helmchen. Sulforhodamine 101 as a specific marker of astroglia in the neocortex in vivo. *Nature methods*, 1(1): 31, 2004.

[249] A. Nimmerjahn, E. A. Mukamel, and M. J. Schnitzer. Motor behavior activates bergmann glial networks. *Neuron*, 62(3):400–412, 2009.

[250] K. Nizar, H. Uhlirova, P. Tian, P. A. Saisan, Q. Cheng, L. Reznichenko, K. L. Weldy, T. C. Steed, V. B. Sridhar, C. L. MacDonald, et al. In vivo stimulus-induced vasodilation occurs without ip3 receptor activation and may precede astrocytic calcium increase. *Journal of Neuroscience*, 33(19):8411–8422, 2013.

[251] R. A. North. Molecular physiology of p2x receptors. *Physiological reviews*, 82(4): 1013–1067, 2002.

[252] R. Nortley and D. Attwell. Control of brain energy supply by astrocytes. *Current opinion in neurobiology*, 47:80–85, 2017.

[253] N. A. Oberheim, X. Wang, S. Goldman, and M. Nedergaard. Astrocytic complexity distinguishes the human brain. *Trends in neurosciences*, 29(10):547–553, 2006.

[254] N. A. Oberheim, T. Takano, X. Han, W. He, J. H. Lin, F. Wang, Q. Xu, J. D. Wyatt, W. Pilcher, J. G. Ojemann, et al. Uniquely hominid features of adult human astrocytes. *Journal of Neuroscience*, 29(10):3276–3287, 2009.

[255] D. H. O'Connor, N. G. Clack, D. Huber, T. Komiyama, E. W. Myers, and K. Svoboda. Vibrissa-based object localization in head-fixed mice. *Journal of Neuroscience*, 30(5):1947–1967, 2010.

[256] D. H. O'connor, S. A. Hires, Z. V. Guo, N. Li, J. Yu, Q.-Q. Sun, D. Huber, and K. Svoboda. Neural coding during active somatosensation revealed using illusory touch. *Nature neuroscience*, 16(7):958, 2013.

[257] K. Ogata and T. Kosaka. Structural and quantitative analysis of astrocytes in the mouse hippocampus. *Neuroscience*, 113(1):221–233, 2002.

[258] Y. Otsu, K. Couchman, D. G. Lyons, M. Collot, A. Agarwal, J.-M. Mallet, F. W. Pfrieger, D. E. Bergles, and S. Charpak. Calcium dynamics in astrocyte processes during neurovascular coupling. *Nature neuroscience*, 18(2):210, 2015.

[259] M. Panasiuk, M. Rychłowski, N. Derewońko, and K. Bieńkowska-Szewczyk. Tunneling nanotubes as a novel route of cell-to-cell spread of herpesviruses. *Journal of virology*, 92(10):e00090–18, 2018.

[260] A. Panatier and R. Robitaille. Astrocytic mglur5 and the tripartite synapse. *Neuroscience*, 323:29–34, 2016.

[261] A. Panatier, J. Vallée, M. Haber, K. K. Murai, J.-C. Lacaille, and R. Robitaille. Astrocytes are endogenous regulators of basal transmission at central synapses. *Cell*, 146(5):785–798, 2011.

[262] T. Pangršič, M. Potokar, M. Stenovec, M. Kreft, E. Fabbretti, A. Nistri, E. Pryazhnikov, L. Khiroug, R. Giniatullin, and R. Zorec. Exocytotic release of atp from cultured astrocytes. *Journal of Biological Chemistry*, 282(39):28749–28758, 2007.

[263] T. Papouin, J. M. Dunphy, M. Tolman, K. T. Dineley, and P. G. Haydon. Septal cholinergic neuromodulation tunes the astrocyte-dependent gating of hippocampal nmda receptors to wakefulness. *Neuron*, 94(4):840–854, 2017.

[264] H. Park, S.-J. Oh, K.-S. Han, D. H. Woo, H. Park, G. Mannaioni, S. F. Traynelis, and C. J. Lee. Bestrophin-1 encodes for the ca2+-activated anion channel in hippocampal astrocytes. *Journal of Neuroscience*, 29(41):13063–13073, 2009.

[265] Y. M. Park, H. Chun, J.-I. Shin, and C. J. Lee. Astrocyte specificity and coverage of hgfap-creert2 [tg (gfap-cre/ert2) 13kdmc] mouse line in various brain regions. *Experimental neurobiology*, 27(6):508–525, 2018.

[266] T. Parpaite and B. Coste. Piezo channels. *Current Biology*, 27(7):R250–R252, 2017.

[267] V. Parpura, T. A. Basarsky, F. Liu, K. Jeftinija, S. Jeftinija, and P. G. Haydon. Glutamate-mediated astrocyte–neuron signalling. *Nature*, 369(6483):744, 1994.

[268] V. Parpura, Y. Fang, T. Basarsky, R. Jahn, and P. G. Haydon. Expression of synaptobrevin ii, cellubrevin and syntaxin but not snap-25 in cultured astrocytes. *FEBS letters*, 377(3):489–492, 1995.

[269] V. Parpura, F. Liu, S. Brethorst, K. Jeftinija, S. Jeftinija, and P. G. Haydon. α-latrotoxin stimulates glutamate release from cortical astrocytes in cell culture. *FEBS letters*, 360(3):266–270, 1995.

[270] O. Pascual, K. B. Casper, C. Kubera, J. Zhang, R. Revilla-Sanchez, J.-Y. Sul, H. Takano, S. J. Moss, K. McCarthy, and P. G. Haydon. Astrocytic purinergic signaling coordinates synaptic networks. *Science*, 310(5745):113–116, 2005.

[271] M. A. Passini, J. Bu, J. A. Fidler, R. J. Ziegler, J. W. Foley, J. C. Dodge, W. W. Yang, J. Clarke, T. V. Taksir, D. A. Griffiths, et al. Combination brain and systemic injections of aav provide maximal functional and survival benefits in the niemann-pick mouse. *Proceedings of the National Academy of Sciences*, 104 (22):9505–9510, 2007.

[272] L. Pasti, A. Volterra, T. Pozzan, and G. Carmignoto. Intracellular calcium oscillations in astrocytes: a highly plastic, bidirectional form of communication between neurons and astrocytes in situ. *Journal of Neuroscience*, 17(20):7817–7830, 1997.

[273] I. Patrushev, N. Gavrilov, V. Turlapov, and A. Semyanov. Subcellular location of astrocytic calcium stores favors extrasynaptic neuron–astrocyte communication. *Cell calcium*, 54(5):343–349, 2013.

[274] M. Paukert, A. Agarwal, J. Cha, V. A. Doze, J. U. Kang, and D. E. Bergles. Norepinephrine controls astroglial responsiveness to local circuit activity. *Neuron*, 82(6):1263–1270, 2014.

[275] G. Paxinos and K. B. Franklin. *Paxinos and Franklin's the mouse brain in stereotaxic coordinates*. Academic press, 2019.

[276] G. Perea and A. Araque. Glial calcium signaling and neuron–glia communication. *Cell calcium*, 38(3-4):375–382, 2005.

[277] G. Perea and A. Araque. Astrocytes potentiate transmitter release at single hippocampal synapses. *Science*, 317(5841):1083–1086, 2007.

[278] G. Perea, A. Yang, E. S. Boyden, and M. Sur. Optogenetic astrocyte activation modulates response selectivity of visual cortex neurons in vivo. *Nature communications*, 5:3262, 2014.

[279] C. Perego, C. Vanoni, M. Bossi, S. Massari, H. Basudev, R. Longhi, and G. Pietrini. The glt-1 and glast glutamate transporters are expressed on morphologically distinct astrocytes and regulated by neuronal activity in primary hippocampal cocultures. *Journal of neurochemistry*, 75(3):1076–1084, 2000.

[280] A. Perez-Alvarez, M. Navarrete, A. Covelo, E. D. Martin, and A. Araque. Structural and functional plasticity of astrocyte processes and dendritic spine interactions. *Journal of Neuroscience*, 34(38):12738–12744, 2014.

[281] S. P. Peron, J. Freeman, V. Iyer, C. Guo, and K. Svoboda. A cellular resolution map of barrel cortex activity during tactile behavior. *Neuron*, 86(3):783–799, 2015.

[282] O. Peters, C. G. Schipke, Y. Hashimoto, and H. Kettenmann. Different mechanisms promote astrocyte ca2+ waves and spreading depression in the mouse neocortex. *Journal of Neuroscience*, 23(30):9888–9896, 2003.

[283] C. C. Petersen. The functional organization of the barrel cortex. *Neuron*, 56(2): 339–355, 2007.

[284] C. C. Petersen. Sensorimotor processing in the rodent barrel cortex. *Nature Reviews Neuroscience*, 20(9):533–546, 2019.

[285] O. H. Petersen, M. Michalak, and A. Verkhratsky. Calcium signalling: past, present and future. *Cell calcium*, 38(3-4):161–169, 2005.

[286] J. Petravicz, K. M. Boyt, and K. D. McCarthy. Astrocyte ip3r2-dependent ca2+ signaling is not a major modulator of neuronal pathways governing behavior. *Frontiers in behavioral neuroscience*, 8:384, 2014.

[287] F. W. Pfrieger and B. A. Barres. Synaptic efficacy enhanced by glial cells in vitro. *Science*, 277(5332):1684–1687, 1997.

[288] S. Pillay, N. Meyer, A. Puschnik, O. Davulcu, J. Diep, Y. a. Ishikawa, L. Jae, J. Wosen, C. Nagamine, M. Chapman, et al. An essential receptor for adeno-associated virus infection. *Nature*, 530(7588):108, 2016.

[289] T. A. Planchon, L. Gao, D. E. Milkie, M. W. Davidson, J. A. Galbraith, C. G. Galbraith, and E. Betzig. Rapid three-dimensional isotropic imaging of living cells using bessel beam plane illumination. *Nature methods*, 8(5):417, 2011.

[290] S. Ponnazhagan, D. Erikson, W. G. Kearns, S. Z. Zhou, P. Nahreini, X.-s. Wang, and A. Srtvastava. Lack of site-specific integration of the recombinant adeno-associated virus 2 genomes in human cells. *Human gene therapy*, 8(3):275–284, 1997.

[291] J. T. Porter and K. D. McCarthy. Hippocampal astrocytes in situ respond to glutamate released from synaptic terminals. *Journal of Neuroscience*, 16(16): 5073–5081, 1996.

[292] J. F. Poulet, L. M. Fernandez, S. Crochet, and C. C. Petersen. Thalamic control of cortical states. *Nature neuroscience*, 15(3):370, 2012.

[293] N. Provost, G. Le Meur, M. Weber, A. Mendes-Madeira, G. Podevin, Y. Cherel, M.-A. Colle, J.-Y. Deschamps, P. Moullier, and F. Rolling. Biodistribution of raav vectors following intraocular administration: evidence for the presence and persistence of vector dna in the optic nerve and in the brain. *Molecular therapy*, 11(2):275–283, 2005.

[294] J. E. Rabinowitz, F. Rolling, C. Li, H. Conrath, W. Xiao, X. Xiao, and R. J. Samulski. Cross-packaging of a single adeno-associated virus (aav) type 2 vector genome into multiple aav serotypes enables transduction with broad specificity. *Journal of virology*, 76(2):791–801, 2002.

[295] A. Raffaello, C. Mammucari, G. Gherardi, and R. Rizzuto. Calcium at the center of cell signaling: interplay between endoplasmic reticulum, mitochondria, and lysosomes. *Trends in biochemical sciences*, 41(12):1035–1049, 2016.

[296] M. N. Rand, T. Leinders-Zufall, S. Agulian, and J. D. Kocsis. Calcium signals in neurons. *Nature*, 371:291–292, 1994.

[297] R. Rasmussen, M. Nedergaard, and N. C. Petersen. Sulforhodamine 101, a widely used astrocyte marker, can induce cortical seizure-like activity at concentrations commonly used. *Scientific reports*, 6:30433, 2016.

[298] M. Record, K. Carayon, M. Poirot, and S. Silvente-Poirot. Exosomes as new vesicular lipid transporters involved in cell–cell communication and various pathophysiologies. *Biochimica et Biophysica Acta (BBA)-Molecular and Cell Biology of Lipids*, 1841(1):108–120, 2014.

[299] A. M. Reeves, E. Shigetomi, and B. S. Khakh. Bulk loading of calcium indicator dyes to study astrocyte physiology: key limitations and improvements using morphological maps. *Journal of Neuroscience*, 31(25):9353–9358, 2011.

[300] J. Reimer, M. J. McGinley, Y. Liu, C. Rodenkirch, Q. Wang, D. A. McCormick, and A. S. Tolias. Pupil fluctuations track rapid changes in adrenergic and cholinergic activity in cortex. *Nature communications*, 7(1):1–7, 2016.

[301] W. C. Risher, S. Patel, I. H. Kim, A. Uezu, S. Bhagat, D. K. Wilton, L.-J. Pilaz, J. S. Alvarado, O. Y. Calhan, D. L. Silver, et al. Astrocytes refine cortical connectivity at dendritic spines. *Elife*, 3:e04047, 2014.

[302] A. Rohlmann and J. Wolff. Subcellular topography and plasticity of gap junction distribution on astrocytes. In *Gap junctions in the nervous system*, pages 175–192. Springer, 1996.

[303] C. J. Roome and B. Kuhn. Chronic cranial window with access port for repeated cellular manipulations, drug application, and electrophysiology. *Frontiers in cellular neuroscience*, 8:379, 2014.

[304] C. J. Roome and B. Kuhn. Simultaneous dendritic voltage and calcium imaging and somatic recording from purkinje neurons in awake mice. *Nature communications*, 9(1):1–14, 2018.

[305] C. R. Rose, L. Felix, A. Zeug, D. Dietrich, A. Reiner, and C. Henneberger. Astroglial glutamate signaling and uptake in the hippocampus. *Frontiers in molecular neuroscience*, 10:451, 2018.

[306] D. Rossi, F. Martorana, and L. Brambilla. Implications of gliotransmission for the pharmacotherapy of cns disorders. *CNS drugs*, 25(8):641–658, 2011.

[307] B. L. Roth. Dreadds for neuroscientists. *Neuron*, 89(4):683–694, 2016.

[308] N. Rouach, A. Koulakoff, V. Abudara, K. Willecke, and C. Giaume. Astroglial metabolic networks sustain hippocampal synaptic transmission. *science*, 322 (5907):1551–1555, 2008.

[309] S. J. Sahl, S. W. Hell, and S. Jakobs. Fluorescence nanoscopy in cell biology. *Nature reviews Molecular cell biology*, 18(11):685, 2017.

[310] E. A. Salegio, L. Samaranch, A. P. Kells, G. Mittermeyer, W. San Sebastian, S. Zhou, J. Beyer, J. Forsayeth, and K. S. Bankiewicz. Axonal transport of adeno-associated viral vectors is serotype-dependent. *Gene therapy*, 20(3):348, 2013.

[311] G. C. Sampey, S. S. Meyering, M. A. Zadeh, M. Saifuddin, R. M. Hakami, and F. Kashanchi. Exosomes and their role in cns viral infections. *Journal of neurovirology*, 20(3):199–208, 2014.

[312] M. Santello, N. Toni, and A. Volterra. Astrocyte function from information processing to cognition and cognitive impairment. *Nature neuroscience*, page 1, 2019.

[313] S. J. Sara. The locus coeruleus and noradrenergic modulation of cognition. *Nature reviews neuroscience*, 10(3):211, 2009.

[314] I. Savtchouk and A. Volterra. Gliotransmission: beyond black-and-white. *Journal of Neuroscience*, 38(1):14–25, 2018.

[315] D. P. Schafer, E. K. Lehrman, A. G. Kautzman, R. Koyama, A. R. Mardinly, R. Yamasaki, R. M. Ransohoff, M. E. Greenberg, B. A. Barres, and B. Stevens. Microglia sculpt postnatal neural circuits in an activity and complement-dependent manner. *Neuron*, 74(4):691–705, 2012.

[316] N. Schek, C. Cooke, and J. Alwine. Definition of the upstream efficiency element of the simian virus 40 late polyadenylation signal by using in vitro analyses. *Molecular and Cellular Biology*, 12(12):5386–5393, 1992.

[317] L. Schermelleh, A. Ferrand, T. Huser, C. Eggeling, M. Sauer, O. Biehlmaier, and G. P. Drummen. Super-resolution microscopy demystified. *Nature cell biology*, 21(1):72, 2019.

[318] J. Schindelin, I. Arganda-Carreras, E. Frise, V. Kaynig, M. Longair, T. Pietzsch, S. Preibisch, C. Rueden, S. Saalfeld, B. Schmid, et al. Fiji: an open-source platform for biological-image analysis. *Nature methods*, 9(7):676–682, 2012.

[319] C. G. Schipke, B. Haas, and H. Kettenmann. Astrocytes discriminate and selectively respond to the activity of a subpopulation of neurons within the barrel cortex. *Cerebral Cortex*, 18(10):2450–2459, 2008.

[320] C. G. Schipke, I. Heuser, and O. Peters. Antidepressants act on glial cells: Ssris and serotonin elicit astrocyte calcium signaling in the mouse prefrontal cortex. *Journal of psychiatric research*, 45(2):242–248, 2011.

[321] D. M. Schneider, A. Nelson, and R. Mooney. A synaptic and circuit basis for corollary discharge in the auditory cortex. *Nature*, 513(7517):189, 2014.

[322] F. Schnütgen, N. Doerflinger, C. Calléja, O. Wendling, P. Chambon, and N. B. Ghyselinck. A directional strategy for monitoring cre-mediated recombination at the cellular level in the mouse. *Nature biotechnology*, 21(5):562, 2003.

[323] A. Schousboe, S. Scafidi, L. K. Bak, H. S. Waagepetersen, and M. C. McKenna. Glutamate metabolism in the brain focusing on astrocytes. In *Glutamate and ATP at the Interface of Metabolism and Signaling in the Brain*, pages 13–30. Springer, 2014.

[324] B. R. Schultz and J. S. Chamberlain. Recombinant adeno-associated virus transduction and integration. *Molecular Therapy*, 16(7):1189–1199, 2008.

[325] J. Schummers, H. Yu, and M. Sur. Tuned responses of astrocytes and their influence on hemodynamic signals in the visual cortex. *Science*, 320(5883):1638–1643, 2008.

[326] A. Schüz and G. Palm. Density of neurons and synapses in the cerebral cortex of the mouse. *Journal of Comparative Neurology*, 286(4):442–455, 1989.

[327] Y. Schwarz, N. Zhao, F. Kirchhoff, and D. Bruns. Astrocytes control synaptic strength by two distinct v-snare-dependent release pathways. *Nature neuroscience*, 20(11):1529, 2017.

[328] G. Seisenberger, M. U. Ried, T. Endress, H. Büning, M. Hallek, and C. Bräuchle. Real-time single-molecule imaging of the infection pathway of an adeno-associated virus. *Science*, 294(5548):1929–1932, 2001.

[329] A. Serrano, N. Haddjeri, J.-C. Lacaille, and R. Robitaille. Gabaergic network activation of glial cells underlies hippocampal heterosynaptic depression. *Journal of Neuroscience*, 26(20):5370–5382, 2006.

[330] S. Shen, K. D. Bryant, S. M. Brown, S. H. Randell, and A. Asokan. Terminal n-linked galactose is the primary receptor for adeno-associated virus 9. *Journal of Biological Chemistry*, 286(15):13532–13540, 2011.

[331] N. M. Sherer and W. Mothes. Cytonemes and tunneling nanotubules in cell–cell communication and viral pathogenesis. *Trends in cell biology*, 18(9):414–420, 2008.

[332] E. Shigetomi, S. Kracun, M. V. Sofroniew, and B. S. Khakh. A genetically targeted optical sensor to monitor calcium signals in astrocyte processes. *Nature neuroscience*, 13(6):759, 2010.

[333] E. Shigetomi, X. Tong, K. Y. Kwan, D. P. Corey, and B. S. Khakh. Trpa1 channels regulate astrocyte resting calcium and inhibitory synapse efficacy through gat-3. *Nature neuroscience*, 15(1):70, 2012.

[334] E. Shigetomi, E. A. Bushong, M. D. Haustein, X. Tong, O. Jackson-Weaver, S. Kracun, J. Xu, M. V. Sofroniew, M. H. Ellisman, and B. S. Khakh. Imaging calcium microdomains within entire astrocyte territories and endfeet with gcamps expressed using adeno-associated viruses. *The Journal of general physiology*, 141 (5):633–647, 2013.

[335] E. Shigetomi, S. Patel, and B. S. Khakh. Probing the complexities of astrocyte calcium signaling. *Trends in cell biology*, 26(4):300–312, 2016.

[336] E. Shigetomi, K. Saito, F. Sano, and S. Koizumi. Aberrant calcium signals in reactive astrocytes: A key process in neurological disorders. *International journal of molecular sciences*, 20(4):996, 2019.

[337] M. Slezak, S. Kandler, P. P. Van Veldhoven, C. Van den Haute, V. Bonin, and M. G. Holt. Distinct mechanisms for visual and motor-related astrocyte responses in mouse visual cortex. *Current Biology*, 29(18):3120–3127, 2019.

[338] M. V. Sofroniew and H. V. Vinters. Astrocytes: biology and pathology. *Acta neuropathologica*, 119(1):7–35, 2010.

[339] N. J. Sofroniew and K. Svoboda. Whisking. *Current Biology*, 25(4):R137–R140, 2015.

[340] C. Song, Q. B. Do, S. D. Antic, and T. Knöpfel. Transgenic strategies for sparse but strong expression of genetically encoded voltage and calcium indicators. *International journal of molecular sciences*, 18(7):1461, 2017.

[341] R. Srinivasan, B. S. Huang, S. Venugopal, A. D. Johnston, H. Chai, H. Zeng, P. Golshani, and B. S. Khakh. Ca 2+ signaling in astrocytes from ip3r2-/- mice in brain slices and during startle responses in vivo. *Nature neuroscience*, 18(5): 708, 2015.

[342] D. Stellwagen and R. C. Malenka. Synaptic scaling mediated by glial tnf-α. *Nature*, 440(7087):1054, 2006.

[343] D. Stellwagen, E. C. Beattie, J. Y. Seo, and R. C. Malenka. Differential regulation of ampa receptor and gaba receptor trafficking by tumor necrosis factor-α. *Journal of Neuroscience*, 25(12):3219–3228, 2005.

[344] J. L. Stobart, K. D. Ferrari, M. J. Barrett, M. J. Stobart, Z. J. Looser, A. S. Saab, and B. Weber. Long-term in vivo calcium imaging of astrocytes reveals distinct cellular compartment responses to sensory stimulation. *Cerebral Cortex*, 28(1):184–198, 2016.

[345] J. L. Stobart, K. D. Ferrari, M. J. Barrett, C. Glück, M. J. Stobart, M. Zuend, and B. Weber. Cortical circuit activity evokes rapid astrocyte calcium signals on a similar timescale to neurons. *Neuron*, 98(4):726–735, 2018.

[346] C. E. Stout, J. L. Costantin, C. C. Naus, and A. C. Charles. Intercellular calcium signaling in astrocytes via atp release through connexin hemichannels. *Journal of Biological Chemistry*, 277(12):10482–10488, 2002.

[347] S. V. Straub, A. D. Bonev, M. K. Wilkerson, and M. T. Nelson. Dynamic inositol trisphosphate-mediated calcium signals within astrocytic endfeet underlie vasodilation of cerebral arterioles. *The Journal of general physiology*, 128(6):659–669, 2006.

[348] S. Sultan, L. Li, J. Moss, F. Petrelli, F. Cassé, E. Gebara, J. Lopatar, F. W. Pfrieger, P. Bezzi, J. Bischofberger, et al. Synaptic integration of adult-born hippocampal neurons is locally controlled by astrocytes. *Neuron*, 88(5):957–972, 2015.

[349] C. Summerford and R. J. Samulski. Aavr: a multi-serotype receptor for aav. *Molecular Therapy*, 24(4):663–666, 2016.

[350] W. Sun, E. McConnell, J.-F. Pare, Q. Xu, M. Chen, W. Peng, D. Lovatt, X. Han, Y. Smith, and M. Nedergaard. Glutamate-dependent neuroglial calcium signaling differs between young and adult brain. *Science*, 339(6116):197–200, 2013.

[351] K. Svoboda and R. Yasuda. Principles of two-photon excitation microscopy and its applications to neuroscience. *Neuron*, 50(6):823–839, 2006.

[352] J. T PORTER and K. D MCCARTHY. Astrocytic neurotransmitter receptors in situ and in vivo. *Progress in neurobiology*, 51(4):439–455, 1997.

[353] T. Takano, G.-F. Tian, W. Peng, N. Lou, W. Libionka, X. Han, and M. Nedergaard. Astrocyte-mediated control of cerebral blood flow. *Nature neuroscience*, 9(2):260, 2006.

[354] T. Takano, W. He, X. Han, F. Wang, Q. Xu, X. Wang, N. A. Oberheim Bush, N. Cruz, G. A. Dienel, and M. Nedergaard. Rapid manifestation of reactive astrogliosis in acute hippocampal brain slices. *Glia*, 62(1):78–95, 2014.

[355] N. Takata and H. Hirase. Cortical layer 1 and layer 2/3 astrocytes exhibit distinct calcium dynamics in vivo. *PLoS One*, 3(6):e2525, 2008.

[356] N. Takata, T. Mishima, C. Hisatsune, T. Nagai, E. Ebisui, K. Mikoshiba, and H. Hirase. Astrocyte calcium signaling transforms cholinergic modulation to cortical plasticity in vivo. *Journal of Neuroscience*, 31(49):18155–18165, 2011.

[357] D. G. R. Tervo, B.-Y. Hwang, S. Viswanathan, T. Gaj, M. Lavzin, K. D. Ritola, S. Lindo, S. Michael, E. Kuleshova, D. Ojala, et al. A designer aav variant permits efficient retrograde access to projection neurons. *Neuron*, 92(2):372–382, 2016.

[358] A. S. Thrane, P. M. Rappold, T. Fujita, A. Torres, L. K. Bekar, T. Takano, W. Peng, F. Wang, V. R. Thrane, R. Enger, et al. Critical role of aquaporin-4 (aqp4) in astrocytic ca2+ signaling events elicited by cerebral edema. *Proceedings of the National Academy of Sciences*, 108(2):846–851, 2011.

[359] A. S. Thrane, V. R. Thrane, D. Zeppenfeld, N. Lou, Q. Xu, E. A. Nagelhus, and M. Nedergaard. General anesthesia selectively disrupts astrocyte calcium signaling in the awake mouse cortex. *Proceedings of the National Academy of Sciences*, 109(46):18974–18979, 2012.

[360] L. Tian, S. A. Hires, and L. L. Looger. Imaging neuronal activity with genetically encoded calcium indicators. *Cold Spring Harbor Protocols*, 2012(6): pdb–top069609, 2012.

[361] X. Tong, E. Shigetomi, L. L. Looger, and B. S. Khakh. Genetically encoded calcium indicators and astrocyte calcium microdomains. *The Neuroscientist*, 19 (3):274–291, 2013.

[362] M. D. Tran and J. T. Neary. Purinergic signaling induces thrombospondin-1 expression in astrocytes. *Proceedings of the National Academy of Sciences*, 103 (24):9321–9326, 2006.

[363] R. Tremblay, S. Lee, and B. Rudy. Gabaergic interneurons in the neocortex: from cellular properties to circuits. *Neuron*, 91(2):260–292, 2016.

[364] G. Ugolini, H. Kuypers, and P. Strick. Transneuronal transfer of herpes virus from peripheral nerves to cortex and brainstem. *Science*, 243(4887):89–91, 1989.

[365] E. M. Ullian, S. K. Sapperstein, K. S. Christopherson, and B. A. Barres. Control of synapse number by glia. *Science*, 291(5504):657–661, 2001.

[366] A. D. Umpierre, P. J. West, J. A. White, and K. S. Wilcox. Conditional knock-out of mglur5 from astrocytes during epilepsy development impairs high-frequency glutamate uptake. *Journal of Neuroscience*, 39(4):727–742, 2019.

[367] N. Urbain, P. A. Salin, P.-A. Libourel, J.-C. Comte, L. J. Gentet, and C. C. Petersen. Whisking-related changes in neuronal firing and membrane potential dynamics in the somatosensory thalamus of awake mice. *Cell reports*, 13(4): 647–656, 2015.

[368] A. Vaarmann, S. Gandhi, and A. Y. Abramov. Dopamine induces ca2+ signaling in astrocytes through reactive oxygen species generated by monoamine oxidase. *Journal of Biological Chemistry*, 285(32):25018–25023, 2010.

[369] P. Veinante and M. Deschênes. Single-and multi-whisker channels in the ascending projections from the principal trigeminal nucleus in the rat. *Journal of Neuroscience*, 19(12):5085–5095, 1999.

[370] R. Ventura and K. M. Harris. Three-dimensional relationships between hippocampal synapses and astrocytes. *Journal of Neuroscience*, 19(16):6897–6906, 1999.

[371] A. Verkhratsky and A. Butt. The history of the decline and fall of the glial numbers legend. *Neuroglia*, 1(1):188–192, 2018.

[372] A. Verkhratsky and M. Nedergaard. Astroglial cradle in the life of the synapse. *Philosophical Transactions of the Royal Society B: Biological Sciences*, 369(1654): 20130595, 2014.

[373] A. Verkhratsky and M. Nedergaard. Physiology of astroglia. *Physiological reviews*, 98(1):239–389, 2017.

[374] A. Verkhratsky, R. C. Reyes, and V. Parpura. Trp channels coordinate ion signalling in astroglia. In *Reviews of Physiology, Biochemistry and Pharmacology 166*, pages 1–22. Springer, 2013.

[375] A. Verkhratsky, V. Parpura, M. Pekna, M. Pekny, and M. Sofroniew. Glia in the pathogenesis of neurodegenerative diseases, 2014.

[376] A. Verkhratsky, M. Nedergaard, and L. Hertz. Why are astrocytes important? *Neurochemical research*, 40(2):389–401, 2015.

[377] A. Verkhratsky, M. Matteoli, V. Parpura, J.-P. Mothet, and R. Zorec. Astrocytes as secretory cells of the central nervous system: idiosyncrasies of vesicular secretion. *The EMBO journal*, 35(3):239–257, 2016.

[378] A. Verkhratsky, M. Trebak, F. Perocchi, D. Khananshvili, and I. Sekler. Crosslink between calcium and sodium signalling. *Experimental physiology*, 103(2):157–169, 2018.

[379] C. S. Von Bartheld and A. L. Altick. Multivesicular bodies in neurons: distribution, protein content, and trafficking functions. *Progress in neurobiology*, 93(3): 313–340, 2011.

[380] C. S. von Bartheld, J. Bahney, and S. Herculano-Houzel. The search for true numbers of neurons and glial cells in the human brain: A review of 150 years of cell counting. *Journal of Comparative Neurology*, 524(18):3865–3895, 2016.

[381] N. Vrieler, S. Loyola, Y. Yarden-Rabinowitz, J. Hoogendorp, N. Medvedev, T. M. Hoogland, C. I. De Zeeuw, E. De Schutter, Y. Yarom, M. Negrello, et al. Variability and directionality of inferior olive neuron dendrites revealed by detailed 3d characterization of an extensive morphological library. *Brain Structure and Function*, 224(4):1677–1695, 2019.

[382] J. J. Wade, K. Breslin, K. Wong-Lin, J. Harkin, B. Flanagan, H. Van Zalinge, S. Hall, M. Dallas, A. Bithell, A. Verkhratsky, et al. Calcium microdomain formation at the perisynaptic cradle due to ncx reversal: A computational study. *Frontiers in cellular neuroscience*, 13, 2019.

[383] A. Wallraff, R. Köhling, U. Heinemann, M. Theis, K. Willecke, and C. Steinhäuser. The impact of astrocytic gap junctional coupling on potassium buffering in the hippocampus. *Journal of Neuroscience*, 26(20):5438–5447, 2006.

[384] D. Wang, P. W. Tai, and G. Gao. Adeno-associated virus vector as a platform for gene therapy delivery. *Nature Reviews Drug Discovery*, page 1, 2019.

[385] F. Wang, N. A. Smith, Q. Xu, T. Fujita, A. Baba, T. Matsuda, T. Takano, L. Bekar, and M. Nedergaard. Astrocytes modulate neural network activity by ca2+-dependent uptake of extracellular k+. *Sci. Signal.*, 5(218):ra26–ra26, 2012.

[386] Q. Wang, B. Shui, M. I. Kotlikoff, and H. Sondermann. Structural basis for calcium sensing by gcamp2. *Structure*, 16(12):1817–1827, 2008.

[387] X. Wang, N. Lou, Q. Xu, G.-F. Tian, W. G. Peng, X. Han, J. Kang, T. Takano, and M. Nedergaard. Astrocytic ca 2+ signaling evoked by sensory stimulation in vivo. *Nature neuroscience*, 9(6):816, 2006.

[388] Y. Wang, N. V. DelRosso, T. V. Vaidyanathan, M. K. Cahill, M. E. Reitman, S. Pittolo, X. Mi, G. Yu, and K. E. Poskanzer. Accurate quantification of astrocyte and neurotransmitter fluorescence dynamics for single-cell and population-level physiology. *Nature Neuroscience*, 22(11):1936–1944, 2019.

[389] A. T. Wassie, Y. Zhao, and E. S. Boyden. Expansion microscopy: principles and uses in biological research. *Nature methods*, 16(1):33–41, 2019.

[390] M. Wellmann, C. Álvarez-Ferradas, C. J. Maturana, J. C. Sáez, and C. Bonansco. Astroglial ca2+-dependent hyperexcitability requires p2y1 purinergic receptors and pannexin-1 channel activation in a chronic model of epilepsy. *Frontiers in cellular neuroscience*, 12, 2018.

[391] T. W. White and R. Bruzzone. Multiple connexin proteins in single intercellular channels: connexin compatibility and functional consequences. *Journal of bioenergetics and biomembranes*, 28(4):339–350, 1996.

[392] I. R. Wickersham, D. C. Lyon, R. J. Barnard, T. Mori, S. Finke, K.-K. Conzelmann, J. A. Young, and E. M. Callaway. Monosynaptic restriction of transsynaptic tracing from single, genetically targeted neurons. *Neuron*, 53(5):639–647, 2007.

[393] J. S. Wiegert, M. Mahn, M. Prigge, Y. Printz, and O. Yizhar. Silencing neurons: tools, applications, and experimental constraints. *Neuron*, 95(3):504–529, 2017.

[394] U. Wilhelmsson, E. A. Bushong, D. L. Price, B. L. Smarr, V. Phung, M. Terada, M. H. Ellisman, and M. Pekny. Redefining the concept of reactive astrocytes as cells that remain within their unique domains upon reaction to injury. *Proceedings of the National Academy of Sciences*, 103(46):17513–17518, 2006.

[395] V. C. Wimmer, R. M. Bruno, C. P. De Kock, T. Kuner, and B. Sakmann. Dimensions of a projection column and architecture of vpm and pom axons in rat vibrissal cortex. *Cerebral cortex*, 20(10):2265–2276, 2010.

[396] M. R. Witcher, S. A. Kirov, and K. M. Harris. Plasticity of perisynaptic astroglia during synaptogenesis in the mature rat hippocampus. *Glia*, 55(1):13–23, 2007.

[397] H. Wolosker, D. T. Balu, and J. T. Coyle. The rise and fall of the d-serine-mediated gliotransmission hypothesis. *Trends in neurosciences*, 39(11):712–721, 2016.

[398] D. H. Woo, K.-S. Han, J. W. Shim, B.-E. Yoon, E. Kim, J. Y. Bae, S.-J. Oh, E. M. Hwang, A. D. Marmorstein, Y. C. Bae, et al. Trek-1 and best1 channels mediate fast and slow glutamate release in astrocytes upon gpcr activation. *Cell*, 151(1):25–40, 2012.

[399] T. A. Woolsey and H. Van der Loos. The structural organization of layer iv in the somatosensory region (si) of mouse cerebral cortex: the description of a cortical field composed of discrete cytoarchitectonic units. *Brain research*, 17(2): 205–242, 1970.

[400] Z. Wu, E. Miller, M. Agbandje-McKenna, and R. J. Samulski. $\alpha 2$, 3 and $\alpha 2$, 6 n-linked sialic acids facilitate efficient binding and transduction by adeno-associated virus types 1 and 6. *Journal of virology*, 80(18):9093–9103, 2006.

[401] Z. Wu, Z. Guo, M. Gearing, and G. Chen. Tonic inhibition in dentate gyrus impairs long-term potentiation and memory in an alzheimer's disease model. *Nature communications*, 5:4159, 2014.

[402] P.-J. Xiao and R. J. Samulski. Cytoplasmic trafficking, endosomal escape, and perinuclear accumulation of adeno-associated virus type 2 particles are facilitated by microtubule network. *Journal of virology*, 86(19):10462–10473, 2012.

[403] X. Xiao, W. Xiao, J. Li, and R. J. Samulski. A novel 165-base-pair terminal repeat sequence is the sole cis requirement for the adeno-associated virus life cycle. *Journal of virology*, 71(2):941–948, 1997.

[404] W. Xin, K. E. Schuebel, K.-w. Jair, R. Cimbro, L. M. De Biase, D. Goldman, and A. Bonci. Ventral midbrain astrocytes display unique physiological features and sensitivity to dopamine d2 receptor signaling. *Neuropsychopharmacology*, 44 (2):344, 2019.

[405] J. Yang, W. Zhou, Y. Zhang, T. Zidon, T. Ritchie, and J. F. Engelhardt. Concatamerization of adeno-associated virus circular genomes occurs through intermolecular recombination. *Journal of virology*, 73(11):9468–9477, 1999.

[406] W. Yang, J.-e. K. Miller, L. Carrillo-Reid, E. Pnevmatikakis, L. Paninski, R. Yuste, and D. S. Peterka. Simultaneous multi-plane imaging of neural circuits. *Neuron*, 89(2):269–284, 2016.

[407] Y. Yang, W. Ge, Y. Chen, Z. Zhang, W. Shen, C. Wu, M. Poo, and S. Duan. Contribution of astrocytes to hippocampal long-term potentiation through release of d-serine. *Proceedings of the National Academy of Sciences*, 100(25):15194–15199, 2003.

[408] Z.-C. Ye, M. S. Wyeth, S. Baltan-Tekkok, and B. R. Ransom. Functional hemichannels in astrocytes: a novel mechanism of glutamate release. *Journal of Neuroscience*, 23(9):3588–3596, 2003.

[409] B.-E. Yoon and C. J. Lee. Gaba as a rising gliotransmitter. *Frontiers in neural circuits*, 8:141, 2014.

[410] H. A. Zariwala, B. G. Borghuis, T. M. Hoogland, L. Madisen, L. Tian, C. I. De Zeeuw, H. Zeng, L. L. Looger, K. Svoboda, and T.-W. Chen. A cre-dependent gcamp3 reporter mouse for neuronal imaging in vivo. *Journal of Neuroscience*, 32(9):3131–3141, 2012.

[411] J.-m. Zhang, H.-k. Wang, C.-q. Ye, W. Ge, Y. Chen, Z.-l. Jiang, C.-p. Wu, M.-m. Poo, and S. Duan. Atp released by astrocytes mediates glutamatergic activity-dependent heterosynaptic suppression. *Neuron*, 40(5):971–982, 2003.

[412] Q. Zhang, M. Fukuda, E. Van Bockstaele, O. Pascual, and P. G. Haydon. Synaptotagmin iv regulates glial glutamate release. *Proceedings of the National Academy of Sciences*, 101(25):9441–9446, 2004.

[413] Q. Zhang, T. Pangršič, M. Kreft, M. Kržan, N. Li, J.-Y. Sul, M. Halassa, E. Van Bockstaele, R. Zorec, and P. G. Haydon. Fusion-related release of glutamate from astrocytes. *Journal of Biological Chemistry*, 279(13):12724–12733, 2004.

[414] X. Zhou, X. Zeng, Z. Fan, C. Li, T. McCown, R. J. Samulski, and X. Xiao. Adeno-associated virus of a single-polarity dna genome is capable of transduction in vivo. *Molecular Therapy*, 16(3):494–499, 2008.

[415] B. Zingg, X.-l. Chou, Z.-g. Zhang, L. Mesik, F. Liang, H. W. Tao, and L. I. Zhang. Aav-mediated anterograde transsynaptic tagging: mapping corticocollicular input-defined neural pathways for defense behaviors. *Neuron*, 93(1):33–47, 2017.

[416] M. Zonta, M. C. Angulo, S. Gobbo, B. Rosengarten, K.-A. Hossmann, T. Pozzan, and G. Carmignoto. Neuron-to-astrocyte signaling is central to the dynamic control of brain microcirculation. *Nature neuroscience*, 6(1):43, 2003.

[417] E. Zucker and W. Welker. Coding of somatic sensory input by vibrissae neurons in the rat's trigeminal ganglion. *Brain research*, 12(1):138–156, 1969.